



HAL
open science

Experimental study of the influence of protection structures on avalanches and impact pressures

Paolo Caccamo

► **To cite this version:**

Paolo Caccamo. Experimental study of the influence of protection structures on avalanches and impact pressures. Geophysics [physics.geo-ph]. Université de Grenoble, 2012. English. NNT : 2012GRENU043 . tel-01548275

HAL Id: tel-01548275

<https://theses.hal.science/tel-01548275>

Submitted on 27 Jun 2017

HAL is a multi-disciplinary open access archive for the deposit and dissemination of scientific research documents, whether they are published or not. The documents may come from teaching and research institutions in France or abroad, or from public or private research centers.

L'archive ouverte pluridisciplinaire **HAL**, est destinée au dépôt et à la diffusion de documents scientifiques de niveau recherche, publiés ou non, émanant des établissements d'enseignement et de recherche français ou étrangers, des laboratoires publics ou privés.

THÈSE

Pour obtenir le grade de

DOCTEUR DE L'UNIVERSITÉ DE GRENOBLE

Spécialité : **Science de la Terre, de l'Univers et de l'Environnement**

Arrêté ministériel :

Présentée par

Paolo Caccamo

Thèse dirigée par **Florence Naaim-Bouvet**
et codirigée par **Thierry Faug**

préparée au sein **Irstea, U.R. ETNA**
et de **Ecole Doctorale Terre, Univers et Environnement**

Experimental study of the influence of protection structures on avalanches and impact pressures

Thèse soutenue publiquement le ,
devant le jury composé de :

Aronne Armanini

Prof., Università degli Studi di Trento, Rapporteur

Wei Wu

Prof., *BOKU*, Vienna, Rapporteur

Frédéric Dufour

Prof., *L3SR*, Grenoble, Examineur

Nicolas Rivière

Prof., *LMFA*, Lyon, Examineur

Florence Naaim-Bouvet

Dr., Irstea, Grenoble, Directeur de thèse

Thierry Faug

Dr., Irstea, Grenoble, Co-Directeur de thèse



Contents

French summary	i
Contexte	i
Verrous scientifiques	ii
Méthode	iii
Avalanche granulaire impactant un mur	v
Courants de densité impactant un obstacle	viii
Le site expérimental de Tacconnaz	xiii
Perspectives futures	xv
Introduction	1
Avalanche physics	3
Active and passive protection	6
Design of passive protection structures	8
Scientific focal points	13
Dissertation framework	15
1 An inclined granular plane to model dense snow avalanches	17
1.1 Snow avalanches and flow - obstacle interaction	18
1.1.1 The snow flows	19
1.1.2 Granular flows: characteristics and modelling	25
1.1.3 Why use a granular material to model a dense snow avalanche?	31
1.1.4 Avalanche - obstacle interaction	32
1.2 The inclined granular plane: method	37
1.2.1 Experimental device	37
1.2.2 Measurement techniques	41
1.3 The inclined granular plane: results	50
1.3.1 The avalanche dynamics	50
1.3.2 Force on a large obstacle spanning the channel	54
1.3.3 Force on a small obstacle allowing lateral flows	58
1.3.4 The influence zone uphill from the obstacle	66
1.4 The analytical force model	72
1.4.1 Model's equations for steady flows	72
1.4.2 Model's equations for unsteady flows	74
1.4.3 Model's predictions compared to previous discrete numerical simulations	75
1.4.4 Model's predictions compared to experimental results	79
1.5 Conclusions and outlook	83

2	A small-scale water tank to model powder snow avalanches	87
2.1	Present understanding	89
2.1.1	Physical modelling	89
2.1.2	Analytical and numerical models	94
2.1.3	Focus on the bed-erosion process	96
2.1.4	Focus on density	96
2.1.5	Avalanche-obstacle interaction	97
2.2	The water tank: method	100
2.2.1	Froude-scale modelling	100
2.2.2	Experimental device	101
2.2.3	Measurement techniques	106
2.3	The water tank: results	115
2.3.1	Some qualitative considerations	115
2.3.2	Maximum height	116
2.3.3	Front velocity	117
2.3.4	Core velocity	119
2.4	Conclusions and outlook	129
3	The experimental site of Taconnaz	133
3.1	Context and description of the site	135
3.2	The study led to improve the protection system	138
3.2.1	Historical data analysis	138
3.2.2	Physical, analytical and numerical modelling	139
3.2.3	Residual risk analysis	141
3.3	Monitoring of the avalanche path	143
3.3.1	The site equipment	143
3.3.2	Preliminary results	145
3.4	Conclusions	154
	Conclusion	155
	Context	155
	Method	155
	Granular avalanches past a wall	157
	Density currents past an obstacle	159
	The full-scale experimental site of Taconnaz	163
	Future perspectives	164
	Annexe 1: Vectrino technical features	167
	Annexe 2: Caccamo et al., "Small-scale tests to investigate the dynamics of finite-sized dry granular avalanches and forces on a wall-like obstacle", Granular Matter (2012)	171
	Bibliography	183
	List of symbols	200

French summary

Contents

Contexte	i
Verrous scientifiques	ii
Méthode	iii
Avalanche granulaire impactant un mur	v
Courants de densité impactant un obstacle	viii
Le site expérimental de Tacconnaz	xiii
Perspectives futures	xv

Contexte

Depuis que l'homme habite les zones de montagne, les phénomènes naturels représentent des risques naturels. Pendant le dernier siècle la montagne a été le terrain d'un processus d'urbanisation très conséquent. Dans les Alpes, le développement du tourisme en particulier a mené à la construction d'infrastructures, de routes et de voies ferrées afin d'assurer les activités humaines. Cela implique un besoin croissant d'espace constructible. C'est d'abord les zones les plus sûres qui ont été occupées, mais, au jour d'aujourd'hui, le processus d'urbanisation continue et intéresse des zones menacées par les risques naturels et en particulier par la problématique des avalanches de neige. Le pic de développement nécessite une approche plus scientifique dans la conception des structures de protection, inspirée par les avancées obtenues dans les domaines de la mécanique et des géosciences. De plus, la recherche scientifique doit continuer à avancer sur ce sujet afin d'améliorer la connaissance actuelle.

Dans le cadre des risques liés aux avalanches, la prédictibilité de l'aléa, les mesures de protection à mettre en oeuvre, le zonage du risque et l'analyse de la vulnérabilité des ouvrages sont différents niveaux de questionnement qui nécessitent une connaissance fine en amont des processus

physiques mis en jeu. Une quantification correcte de la vulnérabilité physique des structures soumises à l'aléa est conditionnée par une étude approfondie de la dynamique des avalanches et de leur interaction avec un obstacle, représentant des ouvrages de protection ou des bâtiments.

Verrous scientifiques

Ce travail se place dans le cadre d'une étude visant à améliorer la connaissance actuelle sur le comportement de la dynamique d'un écoulement en interaction avec un obstacle. L'approche utilisée est expérimentale. Des avalanches denses et aérosol ont été étudiées. Des configurations simples et plus complexes (la taille de l'obstacle reste toujours égale ou plus grande que la dimension caractéristique de l'écoulement) ont été testées. La modélisation physique en échelle réduite a été couplée aux observations et aux mesures de terrain.

La partie dense d'une avalanche représente le paramètre clé dans le dimensionnement de structures de protection. Grâce aux études menées jusqu'à présent, différents régimes d'écoulement pouvant se produire durant l'interaction avalanche dense - obstacle, sont connus. Ces régimes sont représentés par la formation *(i)* d'une zone morte, *(ii)* d'un ressaut, à l'amont de l'obstacle, ou *(iii)* la formation d'un jet à l'aval. Cependant, l'application de ces régimes aux écoulements granulaires n'est pas encore très claire. Ainsi, le premier verrou scientifique à aborder concerne le rôle de la zone d'influence générée par la présence de la zone morte. Quel est le rôle de cette zone sur le comportement de l'écoulement? Comment la présence de cette zone influence la force exercée sur un obstacle? Deuxièmement, bien que les régimes de zone morte et ressaut soient connus, du point de vue théorique, comme deux régimes indépendants, les expériences à échelle réduite suggèrent que, sous certaines conditions, un régime de zone morte peut évoluer en régime de ressaut. Par conséquent, le deuxième verrou sur lequel l'attention sera concentrée est la transition de régime de zone morte à ressaut. Enfin, l'influence de la géométrie d'un obstacle sur le comportement d'un écoulement est aussi analysée en détail, en utilisant différentes formes d'obstacle et en comparant les résultats obtenus.

Ceux-ci sont les trois principaux verrous scientifiques traités dans le chapitre 1 qui concerne la modélisation physique d'avalanches de neige dense.

Dans le cadre du dimensionnement de structure de protection paravalanche, il est important de considérer le risque résiduel associé à la partie aérosol. L'aérosol, ne pouvant pas être arrêté par un obstacle de type digue, dépassera dans tous les cas l'obstacle. L'objectif généralement réside dans la quantification du risque que ce phénomène représente à l'aval de la structure dépassée. Le défi du chapitre 2 consiste à représenter, le plus précisément possible, un écoulement aérosol impactant un obstacle afin d'analyser son comportement à l'impact. A cause des caractéristiques d'un aérosol, la modélisation physique est complexe et des mesures précises de vitesse de l'écoulement n'ont jamais été accomplies. Nous nous proposons de réaliser des mesures précises de hauteur et vitesse de l'écoulement, afin d'estimer les pressions d'impact. Les mesures de densité représentent aussi un grand challenge à entreprendre.

Un site expérimental à échelle 1 a été instrumenté dans le cadre du projet de thèse et des mesures ont été réalisées afin de fournir des données concernant des vraies avalanches de neige. La description du site et des activités menées est faite dans le chapitre 3. Pour les mesures de ter-

rain, le défi consistait à équiper avec succès des structures de protection de type tas freineur déjà existantes sur le site de Tacconnaz (Chamonix, France). Ceci signifie un système d'acquisition complexe, capable de résister à toute condition météo (très hautes et très basses températures) de supporter des sollicitation très importantes (des pressions jusqu'à 100 t m^{-2}), d'être constamment opérationnel et d'assurer une communication constante entre toutes les composantes du système. Les données acquises fournissent des résultats complémentaires qui sont précieux pour la validation des modélisations analytique, numérique et physique, aux différentes échelles. Le dimensionnement, la mise en place et l'exploitation des données font partie de ce travail de recherche.

Les points cités ci-dessus représentent les principaux verrous scientifiques autour desquels ce travail a été centré. Tous ces points sont développés en détail dans le texte intégral en anglais et résumés synthétiquement dans la suite.

Méthode

L'objectif de la thèse est d'améliorer les connaissances actuelles en terme de dynamique des fluides et d'interaction écoulement-obstacle. Ce travail est réalisé en vue de fournir des entrées pertinentes pour les modèles de calcul de structure, afin de définir et pouvoir quantifier des indices de vulnérabilité physique pour une large gamme d'ouvrages. L'approche proposée est à dominante expérimentale. La première partie concerne les expériences de laboratoire sur des modèles réduits:

- des avalanches denses de neige seiche ont été modélisées par analogie avec les écoulement granulaires. Un dispositif expérimental a été utilisé consistant en un plan incliné avec une pente variable. Les pentes examinées vont de 21° et 33° . Une masse constante (9.2 kg) de billes de verre, sèches, sans cohésion et mono-disperses est stockée dans un réservoir et, à l'ouverture de la vanne, s'écoule le long du canal jusqu'à impacter un obstacle à $x = 1.3 \text{ m}$ (= 1300 fois le diamètre d'une bille). La force, la vitesse et la hauteur de l'écoulement à l'impact sont mesurées;
- des avalanches aérosol ont été reproduites en analogie avec les courants de gravité. Le dispositif expérimental se compose d'un plan incliné avec une pente fixe ($\theta = 13^\circ$) immergé dans une cuve d'eau ($\rho = 1000 \text{ kg m}^{-3}$). Un volume constant (4 litres) d'eau salée à saturation mélangée à du Kaolin ($\rho = 1200 \text{ kg m}^{-3}$) est lâché instantanément par le réservoir. Ce courant de gravité s'écoule et, 1 m à l'aval de la vanne du réservoir, il impacte un obstacle de type digue d'arrêt. La hauteur de l'écoulement, la vitesse de front et la vitesse maximale sont mesurées.

Pour les deux types d'avalanche en modèle réduit (dense et aérosol), les essais de référence ont été réalisés d'abord. L'avalanche s'écoule vers l'aval en absence d'obstacle. Ceci permet de caractériser les propriétés dynamiques de l'écoulement. Ensuite l'obstacle est rajouté et l'interaction écoulement-obstacle peut être étudiée. Les deux dispositifs expérimentaux analysent le comportement de l'écoulement en présence de deux différents types d'obstacle. Dans le canal granulaire, un obstacle de type digue d'arrêt est étudié d'abord et remplacé ensuite par une structure type tas freineur. Également, les expériences dans la cuve d'eau utilisent aussi une digue d'arrêt avec parement amont vertical ($\alpha_{dam} = 90^\circ$ par rapport à la pente du terrain) et une avec parement incliné ($\alpha_{dam} = 32^\circ$).

La deuxième partie de ce travail de thèse concerne les mesures de terrain à l'échelle 1. Un site expérimental a été conçu au sein du système complexe de protection paravalanche de Tacconnaz (Chamonix, France). Ce système existant déjà, trois tas freineurs ont été équipés de capteurs de pression et vitesse afin de mesurer les paramètres caractéristiques d'une vraie avalanche. Les

données de terrain visent à fournir des résultats supplémentaires pour valider la modélisation physique réalisée en laboratoire et, en général, les simulations théoriques et numériques.

Même si les pentes analysées en modèle réduit pour les avalanches denses ($\theta = 21^\circ - 33^\circ$) et aérosols ($\theta = 13^\circ$) et celle du site expérimental ($\theta = 13^\circ$) ne sont pas les mêmes, la similitude du nombre de Froude assure la similitude dynamique des trois différentes approches.

Avalanche granulaire impactant un mur

Les propriétés dynamiques des avalanches de neige dense fournissent les paramètres clé pour la construction de structures de protection comme les digues d'arrêt, digues de déviation et les tas freineurs. Ainsi l'objectif consiste à quantifier la force qu'un écoulement de ce type peut exercer sur un obstacle et à étudier l'influence de cet obstacle sur le comportement de l'écoulement.

Des avalanches de neige dense ont été simulées en modèle réduit à l'aide de billes de verre sèches, sans cohésion et mono-disperses. Ce type de matériau est caractérisé par deux angles distinctifs, θ_{min} et θ_{max} , faisant référence respectivement au frottement associé aux déformations quasi-statiques et aux régimes rapides et collisionnels. En dessous de θ_{min} l'écoulement ralenti jusqu'à s'arrêter, au dessus de θ_{max} l'avalanche granulaire accélère. Entre ces deux valeurs, pour $\theta_{min} < \theta < \theta_{max}$, des conditions d'écoulement uniforme peuvent être atteintes même en présence d'écoulements non stationnaires. Ces deux angles influencent beaucoup la dynamique de l'écoulement. Ils ont été trouvés expérimentalement, respectivement, égaux à 20° et 28° .

Les écoulement non stationnaires sont typiquement composés par trois phases principales: (i) un front dilué, (ii) un corps dense et (iii) une queue.

Écoulements de référence

Les profils de hauteur de l'écoulement (Fig.1.a) montrent typiquement des valeurs qui augmentent rapidement (front), un pic (corps) et ensuite des valeurs qui diminuent (queue). L'angle θ_{max} influence le comportement et fait apparaître deux groupes de courbes, différant dans la phase de diminution des valeurs. Les valeurs de hauteur obtenues pour des pentes proches de θ_{min} représentent un cas particulier pour lequel le frottement (et les effets des parois latérales) devient important, une transition vers l'arrêt se produit et la hauteur maximale de l'écoulement baisse. Pour $\theta_{min} < \theta < \theta_{max}$ les valeurs maximales sont plutôt constantes et elles diminuent linéairement au delà de θ_{max} .

Les profils de vitesse de surface (Fig.1.b) exhibent, de même, deux comportements différents: montée - pic - descente en valeur pour $\theta_{min} < \theta < \theta_{max}$, tandis que pour $\theta > \theta_{max}$ le pic devient un plateau de plusieurs secondes avant de diminuer. Les valeurs maximales augmentent linéairement avec l'angle de la pente.

Les résultats obtenus pour la hauteur d'écoulement et pour la vitesse de surface ont été comparés à une lois d'échelle donnant la vitesse moyenne sur la hauteur \bar{u} en fonction de la hauteur de l'écoulement h pour des régimes uniformes et stationnaires:

$$\bar{u} \propto h^{3/2} (\tan \theta - \tan \theta_{min}) \quad (1)$$

Les résultats (Fig.1.c) confirment que, même en présence d'avalanches granulaires, de volume fini, en conditions non-stationnaires, pour $\theta_{min} < \theta < \theta_{max}$ la loi d'échelle est vérifiée.

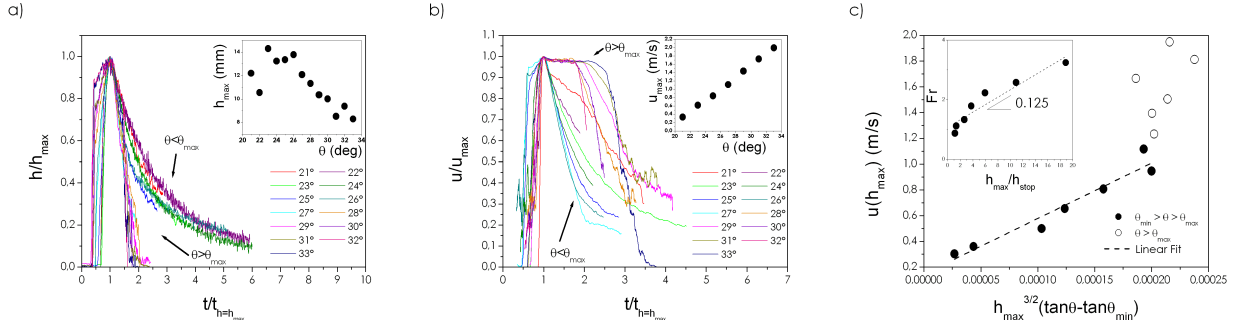


Figure 1: (a) Hauteur de l'écoulement, normalisée par sa valeur maximale h/h_{max} en fonction de $t/t_{h=h_{max}}$. $t_{h=h_{max}}$ est le temps correspondant à la hauteur maximale. (b) Vitesse de surface de l'écoulement, normalisée par sa valeur maximale U/U_{max} en fonction de $t/t_{h=h_{max}}$. (c) Loi d'échelle représentant la vitesse maximale $u(h_{max})$ en fonction de $h_{max}^{3/2}(\tan\theta - \tan\theta_{min})$, pour toutes les pentes testées. Dans l'insert: le nombre de Froude en fonction de la hauteur maximale h_{max} normalisé par la valeur correspondante de h_{stop} dans la plage $[\theta_{min}; \theta_{max}]$.

Mesures de force sur un obstacle large (LO)

Un obstacle large, obstruant la largeur entière de l'écoulement (type digue d'arrêt) a été ajouté au canal et les mesures de force ont été réalisées. Les profils de force ainsi obtenus sont caractérisés par une montée rapide en valeurs, un pic et une phase de diminution qui devient de plus en plus raide en augmentant la pente. Les valeurs maximales de force atteignent le minimum en s'approchant de l'angle θ_{min} (effet du frottement et des parois latérales), elle restent plutôt constantes autour de $\theta_{min} < \theta < \theta_{max}$ et elles augmentent au delà de θ_{max} .

En comparant les valeurs de force maximale $F_{max}^{LO}(\theta)$ avec les contributions hydrostatique ($F \propto \rho gh$) et cinétique ($F \propto \rho u^2$), nous trouvons que, pour des pentes élevées, la force maximale est purement cinétique ($\frac{F_{max}^{LO}}{F_{kin}^{LO}} \simeq 1$) bien que, pour des pentes faibles, la contribution hydrostatique devient importante mais une troisième contribution aussi influence la force totale (Fig.2.a). Nous supposons que cette dernière contribution est due à la présence d'une zone d'influence qui se forme à l'amont de l'obstacle. Plus de détails sur cette zone d'influence seront donné dans la suite. Les profils de force en fonction du temps ne reviennent pas à une valeur nulle. Une force résiduelle constante est mesurée après l'arrêt de l'avalanche. Ceci est du à la présence du dépôt final retenu à l'amont de l'obstacle qui continue à pousser sur son parement. Cette force est associée au dépôt final et tend à augmenter quand la pente du canal diminue, sauf en s'approchant de l'angle θ_{min} où les valeurs de F_{res}^{LO} chutent. A faibles pentes, le frottement joue un rôle important en réduisant le poids du dépôt poussant sur l'obstacle. Un simple modèle basé sur l'équilibre entre le poids du dépôt w et le frottement basal F_f décrit bien le comportement de la force résiduelle, sauf pour des pentes proches de l'angle θ_{min} (Fig.2.c).

Mesures de force sur un obstacle étroit (SO)

L'obstacle large obstruant la largeur entière de l'écoulement a été ensuite remplacé par un obstacle étroit permettant des dépassements latéraux (type tas freineur), et la même procédure de mesures a été répétée.

Il est important de noter que, afin de comparer les forces mesurées sur les deux obstacles, les valeurs sont divisées par la largeur de l'obstacle l_{obs} . Ainsi, dans la suite, nous parlons de force par simplicité mais il est important de se rappeler qu'il s'agit de force par unité de largeur ($\frac{F_i}{l_{obs}}$).

De même que l'obstacle large, la force maximale augmente en général avec la pente. En comparant F_{max}^{SO} aux contributions hydrostatique et cinétique (Fig.2.a), le comportement est similaire à celui de F_{max}^{LO} pour les pentes élevées où la force maximale est purement cinétique ($\frac{F_{max}^{SO}}{F_{kin}^{SO}} \simeq \frac{F_{max}^{LO}}{F_{kin}^{LO}} \simeq 1$). Cependant, le comportement diffère aux pentes faibles où la force maximale exercée sur l'obstacle a été trouvée beaucoup plus élevée que celle mesurée sur le grand obstacle ($\frac{F_{max}^{SO}}{F_{max}^{LO}} = 2 \frac{F_{max}^{LO}}{F_{max}^{LO}}$). Aux pentes faibles, la géométrie de l'obstacle influence la force exercée (Fig.2.b). Ceci est probablement dû à la formation de chaînes de forces agissant dans l'axe de la largeur de l'écoulement qui diminueraient la force exercée sur la structure (effet Janssen) en présence de l'obstacle large.

La force résiduelle F_{res}^{SO} diminue plutôt constamment lorsque la pente augmente et, comme c'était le cas pour l'obstacle large, le modèle analytique, basé sur l'équilibre entre poids du dépôt final et frottement basal, décrit bien le comportement de la force résiduelle, sauf pour $\theta < 24^\circ$, à l'approche de l'angle θ_{min} (Fig.2.c).

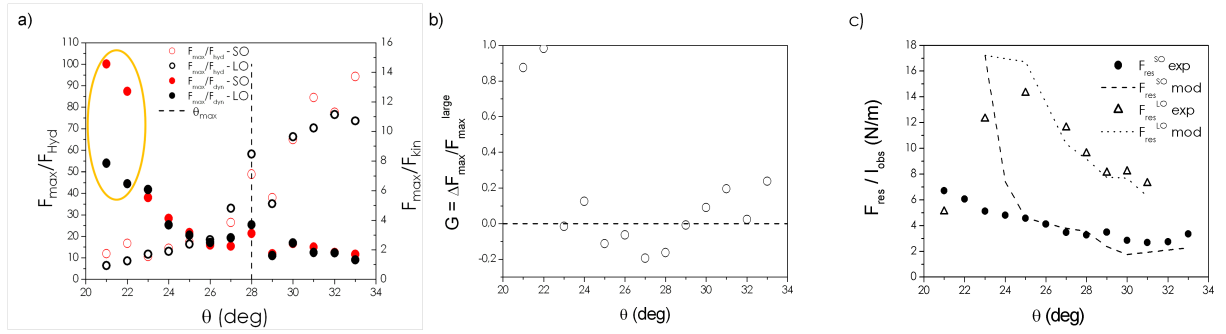


Figure 2: (a) Comparaison entre les valeurs de $\frac{F_{max}}{F_i}$ obtenus avec le grand et le petit obstacle, en fonction de la pente. (b) Nombre adimensionnel G en fonction de la pente. Les résultats confirment que l'influence de la forme de l'obstacle devient importante à des pentes faibles approchant θ_{min} . (c) Comparaison entre les données analytiques et expérimentales de force résiduelle, normalisée par la largeur de l'obstacle, en fonction de la pente, obtenues avec le grand et le petit obstacle.

Transition zone morte - ressaut

À l'impact avec un obstacle, une zone triangulaire quasi-statique se forme à l'amont de l'obstacle et une couche inertielle commence à s'écouler par dessus et dépasse l'obstacle. Ces deux parties composent la zone d'influence, zone qui joue un rôle très important dans la dynamique de l'écoulement. Le comportement de cette zone a été analysé en détail pour une pente fixe de 31° . Une étude a été faite sur l'évolution dans le temps de trois paramètres caractéristiques: l'angle que la surface de la zone d'influence forme avec le fond du canal α_{iz} , la longueur de cette zone L_{iz} , et sa surface S_{iz} . Les résultats obtenus à l'aide d'une technique laser et du traitement d'image montrent un changement de régime. À l'impact avec un obstacle de type mur vertical un régime de zone morte apparaît (zone quasi-statique plus couche inertielle). Les valeurs de α_{iz} , L_{iz} et S_{iz} restent constantes pendant quelques secondes et ensuite la transition arrive (Fig.3.a). Autour de $t^* \simeq 3.2$ s, les valeurs varient rapidement: α_{iz} diminue, et L_{iz} et S_{iz} augmentent. La zone quasi-statique triangulaire prend une forme plutôt trapézoïdale (Fig.3.b), elle remonte vers l'amont dans la direction opposée de l'écoulement et son volume augmente (régime de ressaut) jusqu'à l'arrêt de l'avalanche. Cette transition zone morte - ressaut influence les mesures de force. Une prédiction analytique faite pour les autres pentes montre que le temps t^* auquel la transition se produirait serait plutôt constant quand $\theta > \theta_{max}$, tandis que cette transition ne se

produirait pas en dessous de θ_{max} (Fig.3.c).

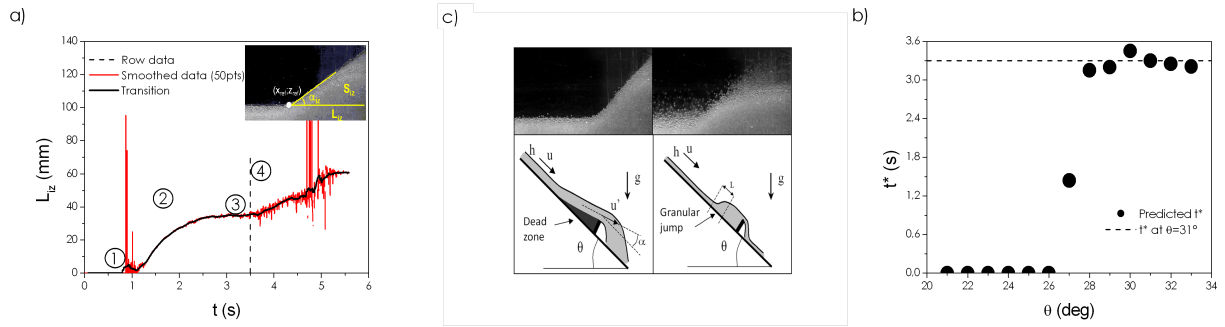


Figure 3: (a) Longueur de la zone d'influence (mesurée comme le montre l'insert), en fonction du temps. Le trait en pointillé correspond à la valeur de t^* calculée théoriquement. (b) Esquisse représentant le régime de zone morte et de ressaut, avec les images respectives correspondant à deux phases différentes de l'écoulement. (c) Temps de transition en fonction de la pente. Les valeurs représentent une prédiction analytique calculée à partir des données acquises durant les essais de référence.

Test sur un modèle analytique de force

Un modèle hydrodynamique moyenné sur la hauteur de l'écoulement a été développé afin de calculer la force normale agissant sur un obstacle de type mur vertical. Les données acquises par les expériences en laboratoire, en présence de l'obstacle large, ont été utilisées pour tester le modèle. Les résultats sont cohérents. Cependant, deux procédures d'ajustement ont été appliquées au modèle afin d'en améliorer la qualité. La fraction volumique $\bar{\phi}(t)$ a été ajustée pour $\theta > \theta_{max}$, tandis que le temps caractéristique de formation de la zone d'influence, τ_{iz} , a été adapté pour des pente proches de θ_{min} ($\theta < 25^\circ$). Bien que des améliorations peuvent encore être apportées, les prédictions du modèle sont en accord avec les résultats issus de la modélisation physique à petite échelle en laboratoire.

Courants de densité impactant un obstacle

Dans la procédure de conception pour des structures de protection paravalanche de type digue d'arrêt, les avalanches aérosol sont sensées dépasser l'obstacle dans tous les cas. L'intérêt, pour ce type d'écoulement, consiste à étudier les caractéristiques de l'écoulement à l'aval de l'obstacle, après l'impact, afin de quantifier le risque résiduel associé à l'avalanche.

Des avalanches aérosol sont modélisées par une solution saline (eau + sel + kaolin) s'écoulant le long d'un canal immergé dans une cuve d'eau.

La hauteur maximale de l'écoulement, sa vitesse de front et sa vitesse maximale sont mesurées. Les essais de référence ont d'abord été réalisés afin de caractériser les paramètres dynamiques

du courant et d'obtenir des valeurs de référence à comparer aux configurations avec obstacle. Il est à noter que, dans la suite:

1. la direction principale de l'écoulement correspond à l'axe des x , parallèle à l'axe du canal et x_0 est fixé en correspondance de la vanne du réservoir;
2. les mesures ont été prises le long du canal, jusqu'à une distance maximale de $x = 1.9$ m;
3. le sens horaire et anti-horaire des rotations sont considérés par rapport à un écoulement descendant de droite vers la gauche;
4. la vitesse maximale, pour une position x donnée correspond à:

$$U_i^+(z) = \frac{1}{n} \sum_1^n u_i^{max}(z) \quad (2)$$

avec

$$u_i^{max}(z) = \max [u_i(z, t)] \quad (3)$$

où $i = x, z$, selon quelle contribution de la vitesse maximale est considérée, et n correspond au nombre d'essais réalisés dans la même position x, z ($n = 3 - 5$).

u_i peut être positif ou négatif, ainsi, par analogie, il est possible de définir

$$U_i^-(z) = \frac{1}{n} \sum_1^n u_i^{min}(z) \quad (4)$$

avec

$$u_i^{min}(z) = \min [u_i(z, t)] \quad (5)$$

$U_i^+(z)$ et $U_i^-(z)$ sont des profils fictifs de vitesse. Ceux-ci représentent les profils de vitesse maximale (et minimale) obtenues sur la hauteur.

$$U_i^{max} = \max (U_i^+(z)) = \max \left[\frac{1}{n} \sum_1^n u_i^{max}(z) \right] \quad (6)$$

$$U_i^{min} = \min (U_i^-(z)) = \min \left[\frac{1}{n} \sum_1^n u_i^{min}(z) \right] \quad (7)$$

U_i^{min} existe seulement si $\min [U_i^-(z)] < 0$.

Quand $t = t_{U_i^{max}}$:

$$V_i^+(z) = \frac{1}{n} \sum_1^n u_i(z)_{(t=t_{U_i^{max}})} \quad (8)$$

Et quand $t = t_{U_i^{min}}$:

$$V_i^-(z) = \frac{1}{n} \sum_1^n u_i(z)_{(t=t_{U_i^{min}})} \quad (9)$$

$V_i^+(z)$ et $V_i^-(z)$ sont de vrais profils parce qu'ils représentent le profil de vitesse instantanée à l'instant où la valeur maximale (minimale) du profil est observée.

5. la norme de la vitesse a été calculée selon

$$u_{xz}(z, t) = \sqrt{u_x(z, t)^2 + u_z(z, t)^2} \quad (10)$$

$$u_{xz}^{max}(z) = \max [u_{xz}(z, t)] \quad (11)$$

$$U_{xz}(z) = \frac{1}{n} \sum_1^n u_{xz}^{max}(z) \quad (12)$$

$$U_{xz}^{max} = \max [U_{xz}(z)] \quad (13)$$

6. la direction de la norme est calculée par rapport aux profils en fonction du temps de $u_x(z, t)$ et $u_z(z, t)$ d'après:

$$\alpha_{xz}^*(z, t) = \arctan \left[\frac{u_z(z, t)}{u_x(z, t)} \right] \quad (14)$$

et, ensuite, cet angle est toujours associé à la norme de la vitesse:

$$\alpha_{xz}^{*,max}(z) = \alpha_{xz} [u_{xz}^{max}(z)] \quad (15)$$

$$\alpha_{xz}(z) = \alpha_{xz} [U_{xz}(z)] \quad (16)$$

$$\alpha_{xz}^{max} = \alpha_{xz} [U_{xz}^{max}] \quad (17)$$

Écoulement de référence

L'avalanche aérosol est composée de 4 litres de solution saline colorée. A l'ouverture du réservoir, le courant de densité commence à s'écouler vers l'aval et il n'impacte pas d'obstacle dans son cours. Les écoulements de référence descendent le canal avec une vitesse plutôt constante. Leur structure turbulente génère une série de tourbillons de différents dimensions tournant dans le sens horaire.

La hauteur maximale de l'aérosol augmente constamment jusqu'à une valeur maximale de $h_{max}^{REF} \simeq 0.24$ m à $x \simeq 1.4$ m et ensuite reste plutôt constante (Fig.4.a).

La vitesse de front est plutôt constante et égale à $u_{fr}^{REF} \simeq 0.28$ m s⁻¹ (Fig.4.b).

La vitesse maximale u_x^{max} diminue de $u_x^{max} \simeq 0.58$ m s⁻¹ ($x = 0.7$ m) à $u_x^{max} \simeq 0.47$ m s⁻¹ ($x = 1.9$ m). La vitesse maximale est généralement plus élevée que la vitesse de front et le rapport $\frac{U_x^{max,REF}}{u_{fr}^{REF}}$ varie entre 1.6 et 1.9 (Fig.4.c).

La vitesse maximale horizontale $V_x^+(z)$ atteint son pic en proximité du sol (fond du canal) et diminue lorsque la coordonnée verticale z augmente. Les valeurs de $V_x^-(z)$ correspondent à l'aérosol qui bouge en direction opposée à la direction principale de l'écoulement. A cause de la structure turbulente de l'aérosol, ce phénomène d'inversion de vitesse se produit pour des valeurs élevées de z , en haut du tourbillon principal tournant en sens horaire. Cependant $|U_x^{min,REF}| \ll |U_x^{max,REF}|$ pour les essais de référence.

La vitesse maximale verticale $V_z^+(z)$ montre un profil semi-elliptique avec le maximum autour de $z = \frac{h_{max}}{2}$ et les minima à $z \simeq 0$ et $z \simeq h_{max}$. A cause de la structure turbulente de l'écoulement, les profils verticaux de $V_z^+(z)$ et $V_z^-(z)$ sont plutôt symétriques. Les valeurs sont en général inférieures aux contributions horizontales.

Le maximum de la norme de la vitesse maximale a été calculé pour chaque position en x étudiée et il a été trouvé jusqu'à 18% supérieur par rapport au maximum de la contribution horizontale de vitesse maximale. U_{xz}^{max} se produit près du sol, pour des faibles valeurs de z et, en conditions de référence, cette valeur est contrôlée par le maximum de la contribution horizontale U_x^{max} .

L'angle associé au maximum de la norme (α_{xz}^{max}) a été calculé et, puisque la contribution horizontale est dominante, cet angle est plutôt faible, $-5^\circ < \alpha_{xz}^{max} < 5^\circ$.

Effets d'une digue d'arrêt avec parement amont vertical ($\alpha_{dam} = 90^\circ$)

Une fois terminés les essais de référence, le premier obstacle (*OBS1*) a été installé dans le canal à une distance de $x = 1$ m. Dans la configuration *OBS1*, l'écoulement impacte le parement vertical de la digue et se disperse complètement. La hauteur du nuage augmente rapidement et le front de l'écoulement se sépare en deux parties: une partie supérieure tournant en sens horaire et s'étalant vers le haut, et une deuxième partie qui génère un nouveau tourbillon tournant en sens anti-horaire. L'impact avec l'obstacle favorise l'incorporation du fluide ambiant par l'écoulement, sa surface augmente et par conséquent sa densité diminue. L'effet de l'obstacle a un rôle important sur les trois paramètres étudiés: la hauteur maximale de l'écoulement, la vitesse de front et la vitesse maximale.

La hauteur maximale, après l'impact, augmente rapidement jusqu'à une valeur $h_{max}^{OBS1} \simeq 0.36$ m ($h_{max}^{OBS1} = 1.5h_{max}^{REF}$) à une distance de $x \simeq 1.7$ m. Les valeurs ensuite diminuent à cause du fait que l'aérosol après s'être dispersé de manière importante, redescend et continue sa course jusqu'à la fin du canal (Fig.4.a).

Suite à l'impact, la vitesse de front chute. Elle atteint un minimum de $u_{fr}^{OBS1} \simeq 0.14$ m s⁻¹ ($u_{fr}^{OBS1} = 0.5u_{fr}^{REF}$) à $x \simeq 1.3$ m et après elle re-augmente pour se stabiliser à une valeur plutôt constante de ($u_{fr}^{OBS1} = 0.78u_{fr}^{REF}$) jusqu'à la fin du canal (Fig.4.b).

La contribution horizontale de la vitesse maximale chute aussi à $x = 1$ m. $U_x^{max,OBS1}$ atteint un minimum de 0.35 m s⁻¹ ($U_x^{max,OBS1} = 0.69U_x^{max,REF}$) qui reste constante jusqu'à la fin du canal. Le rapport $\frac{U_x^{max,OBS1}}{u_{fr}^{OBS1}}$ varie entre 1.4 et 2.3 (Fig.4.a).

A cause de l'impact, la turbulence à l'intérieur de l'avalanche augmente et, par conséquent, la contribution verticale de vitesse maximale et les valeurs négatives de vitesse horizontale augmentent aussi. Juste à l'aval de l'obstacle, à $x = 1.15$ m, la vitesse horizontale négative a été trouvée supérieure par rapport à la contribution positive: $|U_x^{min}| \simeq 2|U_x^{max}|$.

L'augmentation des vitesses verticales implique une augmentation de la norme de la vitesse maximale U_{xz}^{max} . En présence de *OBS1*, le maximum de la norme a été trouvé presque 30% supérieur à la contribution horizontale de vitesse maximale. La valeur de z pour laquelle le maximum de la norme a été enregistré augmente rapidement juste après l'impact, ($x = 1 - 1.2$ m) et il atteint une valeur maximale de $z = 0.18$ m à cause du fait que l'aérosol, suite à l'impact, se disperse violemment. Par conséquent, l'angle associé au maximum de la norme (α_{xz}^{max}) augmente jusqu'à une valeur de 35° juste au niveau de l'arête de l'obstacle ($x = 1$ m). Ensuite cette valeur diminue rapidement.

Effets d'une digue d'arrêt avec parement amont incliné ($\alpha_{dam} = 32^\circ$)

OBS1 a ensuite été remplacé par un deuxième type de structure. *OBS2* représente encore une digue d'arrêt, mais avec son parement amont incliné d'un angle $\alpha_{dam} = 32^\circ$ par rapport à la pente du terrain. En présence de cette deuxième configuration de digue, l'écoulement montre un comportement très différent. L'écoulement ne frappe pas l'obstacle mais il continue plutôt sa course en montant et descendant les parements amont et aval. L'obstacle semble avoir un effet mineur sur la dynamique de l'écoulement.

La hauteur maximale de l'aérosol (Fig.4.a) montre un comportement similaire à celui obtenu en conditions de référence (une première phase de montée en valeurs jusqu'à $h_{max}^{OBS2} \simeq h_{max}^{OBS1} \simeq 0.24$

m pour $x = 1.4$ m et ensuite une valeur plutôt constante).

Un effet légèrement positif est mesuré sur le vitesse de front. Après l'impact, la vitesse de front chute et atteint une valeur de $u_{fr}^{OBS2} \simeq 0.20$ m s⁻¹ ($u_{fr}^{OBS2} = 0.7u_{fr}^{REF}$). Ensuite, l'aérosol re-accélère jusqu'à $u_{fr}^{OBS2} \simeq 0.25$ m s⁻¹ et, après $x = 1.3$ m, il reste constant (Fig.4.b).

A l'impact avec l'obstacle le maximum de la contribution horizontale de la vitesse diminue après $x = 1.1$ m et il diminue jusqu'à une valeur proche de celle obtenue pour $OBS1$ ($U_x^{max,OBS2} \simeq U_x^{max,OBS1} \simeq 0.7U_x^{max,REF}$) à $x = 1.7$ m (Fig.4.c). Le rapport $\frac{U_x^{max,OBS2}}{u_{fr}^{OBS2}}$ varie entre 1.4 et 2.1. Des vitesses horizontales négatives sont encore mesurées à l'aval de l'obstacle mais généralement $|U_x^{min}| < |U_x^{max}|$.

Même si les effets de l'obstacle $OBS2$ sur le comportement de l'écoulement sont faibles par rapports à ceux obtenus avec $OBS1$, à l'impact avec $OBS2$ la différence entre la norme maximale et le maximum de la contribution horizontale de la vitesse maximale reste importante, $U_{xz}^{max} \simeq 1.2U_x^{max}$. Cela signifie que u_x diminue, et que u_z augmente (sûrement à cause de l'inclinaison du parement amont qui agit comme une rampe pour l'écoulement). L'angle associé au maximum de la norme reste assez faible, $-10^\circ < \alpha_{xz}^{max} < 10^\circ$.

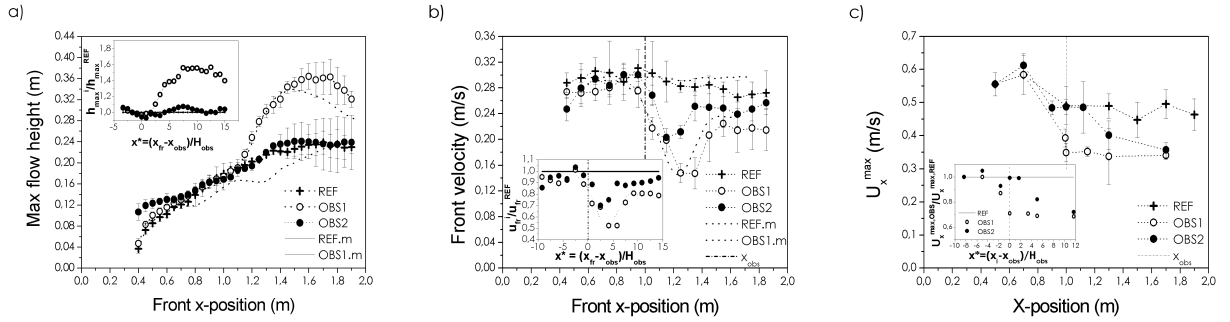


Figure 4: Comportement de (a) la hauteur maximale de l'écoulement h_{max} , (b) la vitesse de front u_{fr} et (c) la vitesse maximale U_x^{max} , obtenu avec les deux techniques utilisées et dans les trois configurations testées ($REF, OBS1, OBS2$). Les trois paramètres sont présentés en fonction de la position le long de l'axe des x . Dans les inserts, les valeurs maximales J_{max}^i ($J = h, u, U_x; i = OBS1, OBS2$) sont normalisées par J_{max}^{REF} , et représentées en fonction de la distance adimensionnelle $x^* = \frac{(x_{fr} - x_{obs})}{H_{obs}}$.

Le site expérimental de Taconnaz

Un nouveau site expérimental a été installé dans le système paravalanche déjà existant de Taconnaz. Ce site vise à recueillir des données relatives à la dynamique d'avalanches déclenchées naturellement et à la vraie échelle. La conception, l'installation et l'interprétation des données font partie de ce travail de recherche.

Les nouvelles installations

Trois tas freineurs ($H_{obs} = 7$ m) ont été équipés avec deux lignes de capteurs de pression et de vitesse, installées à deux hauteurs différentes: ($\frac{1}{3}H_{obs}$ et $\frac{2}{3}H_{obs}$). Les capteurs doivent résister à une gamme de températures entre -30° et 30° , des pressions maximales de 100 t m^{-2} et mesurer des vitesses jusqu'à 60 m s^{-1} . Pour des raisons de sécurité, le bassin de Taconnaz n'est pas accessible pendant l'hiver et par conséquent les trois centrales d'acquisition doivent être reliées entre elles et raccordées à une unité centrale située à l'extérieur du bassin, accessible en permanence.

Le système d'acquisition enregistre en continu sur une mémoire circulaire. Quand un événement est détecté par un des capteurs, un signal est envoyé à la centrale du tas $n^\circ 5$ (voir la numérotation en Fig.3.7.a dans le texte intégral) qui déclenche l'enregistrement synchronisé de tous les capteurs et fournit le temps t_0 , fondamental pour la synchronisation des données. Les 120 s après t_0 et les 60 s avant sont finalement stockés dans une unité de mémoire spécifique. Un système *GSM* permet la consultation de l'unité centrale à distance et le téléchargement des données enregistrées.

Résultats préliminaires: l'avalanche du 29 décembre 2010

Le premier événement, sur le site de Taconnaz, a été enregistré le 29 décembre 2010. A cette occasion, le système d'acquisition et la majorité des capteurs ont bien marché. Le tas $n^\circ 3$ a fourni des données de pression et de vitesse.

Les résultats relatifs à la vitesse (Fig.5.a) concernent seulement la queue de l'écoulement, pour $t > 5$ s, puisque avant $t = 5$ s l'indice de corrélation est trop faible pour que les données soient fiables. Après quelques valeurs dispersées, avec un maximum autour de $18-20 \text{ m s}^{-1}$, on observe une phase continue de valeurs décroissantes.

Un signal complet de pression a été aussi mesuré (Fig.5.a) et il permet un traitement détaillé. Le pic de pression maximale atteint une valeur de $P = 500 \text{ kPa}$ et il consiste en un pic continu et non pas d'une valeur isolée qui atteint la moitié de la valeur estimée pour la pression de projet ($P^{100} = 1000 \text{ kPa}$). Trois vagues impactent successivement l'obstacle. Des gradients de pression ($\frac{\Delta P}{\Delta t}$), jusqu'à 10000 kPa s^{-1} ont été exercés par l'avalanche et ces valeurs diminuent le long des trois vagues.

Des effets de résonance probablement dus à l'impact de blocs isolés peuvent être observés dans le signal de pression. Trois principaux modes de vibration ont été trouvés ($f_n \simeq 600 \text{ Hz}$, $f_n \simeq 1000 \text{ Hz}$ and $f_n \simeq 1600 \text{ Hz}$) et ils dépendent probablement du point d'application de l'impact par rapport au centre du capteur. Ces impacts isolés influencent le signal temporel de pression localement mais leur contribution à l'énergie totale relâchée par l'avalanche (Fig.5.b) est très importante ($\sim 65\%$).

Pour $t > 5$ s, les données de vitesse et de pression sont disponibles et une première interprétation montre que, pour des régimes à faible vitesse, des pressions élevées peuvent encore être exercées. De plus, le coefficient de résistance C_d semble augmenter lorsque le nombre de Froude Fr

diminue (Fig.5.c). Ceci confirme le comportement observé dans la modélisation physique à l'échelle réduite (canal granulaire) et dans les sites expérimentaux, à le vraie échelle, du Col du Lautaret et Vallée de La Sionne.

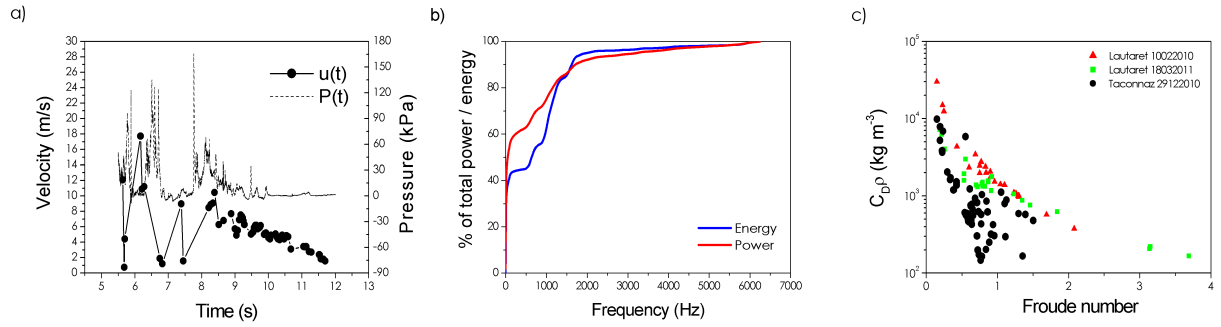


Figure 5: (a) Valeurs de pression (—) et vitesse (●) en fonction du temps. Le pic de pression atteint une valeur proche de 500 kPa. (b) Puissance relative (en rouge) et énergie (en bleu), en fonction de la fréquence f . (c) Coefficient C_D en fonction du nombre de Froude. Les données obtenues sont comparées à celles publiées par *Thibert et al.* (2008) et aux valeurs provenant de deux avalanches récentes au Col du Lautaret et publiées dans *Faug et al.* (2012).

Perspectives futures

Cette thèse a fourni des nouveaux résultats en terme de modélisation physique d'avalanches denses et aérosol. Un nouveau site expérimental a été installé et il commence à fournir des données concernant des avalanches de dimensions extrêmes. De plus, ce travail de recherche ouvre le chemin à des nouveaux défis scientifiques. Les perspectives futures sont présentées ci-dessous.

Modélisation à l'échelle réduite d'avalanches denses

L'étude détaillée de la zone d'influence a montré qu'une transition d'un régime de zone morte à un régime de ressaut peut se produire à l'interaction écoulement - obstacle. Ce résultat met en évidence le rôle important de la zone d'influence et de l'effet que cette transition a sur le comportement de l'écoulement ainsi que sur la force exercée sur un obstacle. Cette étude a été menée pour une pente fixe de 31° et il serait intéressant d'élargir cette analyse à une plus grande gamme de pentes.

Des modèles analytiques existent afin de calculer la force exercée sur un obstacle par une avalanche dense, mais aucun parmi ces modèles considère la transition zone morte - ressaut. Des prédictions analytiques plus précises pourraient être obtenues en implémentant ce nouveau résultat. De plus, l'influence de la géométrie de l'obstacle a été étudiée, à l'aide d'expérience au laboratoire, sur deux types différents d'obstacles (digue d'arrêt et tas freineur). Cependant, actuellement, le modèle analytique développé pour calculer la force normale agissant sur un obstacle est valide seulement pour le cas d'une digue d'arrêt de type mur vertical barrant entièrement l'écoulement. Ce modèle devrait être adapté afin de pouvoir prédire la force exercée sur un obstacle de type tas freineur et de permettre une comparaison avec les résultats issus de la modélisation physique.

Pour ajuster le modèle, une description précise concernant la forme de la zone d'influence devient nécessaire. Une technique laser a été développée dans le cadre de l'étude des forces résiduelles exercées sur un obstacle étroit. Cette technique fournit une reconstruction $3D$ du dépôt de l'avalanche granulaire. Les résultats préliminaires ont montré le potentiel de cette méthode, cependant des divergences avec les résultats expérimentaux existent encore. Cette technique devrait être améliorée afin de disposer d'un outil puissant et fiable pour les mesures.

Les données obtenues ont été moyennées et lissées et la valeur moyenne a été considérée pour l'interprétation des données. Cependant, les signaux de vitesse et de force montrent des fluctuations qui n'ont pas été considérées. En tenant compte de la nature discrète des écoulements granulaires, il serait intéressant de mener une analyse spécifique sur les fluctuations des signaux. Enfin, des simulations numériques discrètes $2D$ ont été réalisées par ailleurs afin de reproduire une avalanche granulaire impactant un obstacle de type mur vertical et elles ont été utilisées pour la comparaison avec les résultats expérimentaux obtenus pour l'obstacle large. Ce type de modélisation ne prend pas en compte les débordements latéraux, ce qui est le cas en présence d'un obstacle de type tas freineur. Ainsi, les simulations numériques discrètes devraient être développées ultérieurement de façon à fournir d'autres données pour comparer et valider les résultats de laboratoire.

Modélisation à l'échelle réduite d'avalanches aérosols

L'influence de deux types d'obstacle sur le comportement de l'écoulement a été testée. Deux obstacles de type digue d'arrêt ont été utilisés: une digue avec parement amont vertical ($\alpha_{dam} = 90^\circ$ par rapport à la pente du terrain) et une digue avec parement incliné ($\alpha_{dam} = 32^\circ$). Cet angle

correspond à l'angle naturel de repos pour une digue en terre et, d'un point de vue de l'ingénierie, il représente la solution la plus simple et la moins chère pour la construction d'une digue. Les résultats montrent que la configuration avec parement amont incliné a un effet mineur sur la dynamique de l'écoulement. Nous supposons l'existence d'un angle seuil $32^\circ < \alpha_{dam}^{thr} < 90^\circ$, au delà duquel le rôle de l'obstacle devient important (décollement visible de l'écoulement du sol). Il serait intéressant, pour des applications pratiques, de mener des nouveaux tests en laboratoire afin d'identifier cet angle seuil α_{dam}^{thr} . L'attention devrait se concentrer sur l'influence que l'angle d'inclinaison du parement, la pente locale du terrain, et la vitesse et la densité de l'écoulement exercent sur la ce seuil.

En particulier, nous avons souligné, tout le long de ce travail, l'importance du paramètre de masse volumique sur le comportement de l'écoulement, sur sa dynamique et dans tous les types de modélisation. Une nouvelle technique a été développée pour la mesure de la densité d'une avalanche aérosol à l'échelle réduite, mais cette méthode ne fournit pas pour l'instant de résultats quantitativement satisfaisants. Ce type de mesure devrait être continué et amélioré, afin de pouvoir, un jour, fournir des valeurs fiables et véridiques aux modèles et se débarrasser des hypothèses lourdes qui influencent la précision des modèles actuels. De plus, comme il a déjà été fait pour les travaux précédents menés en cuve, de la modélisation numérique des expériences en laboratoire devrait être implémentée afin de corriger la distorsion en densité introduite et rendre les résultats obtenus valables pour le cas réel.

En outre, la modélisation physique à l'échelle réduite devrait continuer et, en parallèle avec les écoulements denses, un type de protection permettant le débordement latéraux devrait être testé.

Enfin, ce travail utilise une approche de valeur moyenne, mais en considérant la nature turbulente du phénomène traité, il serait très intéressant de mener une analyse complémentaire visant à une meilleure compréhension des fluctuations en valeurs de hauteur et vitesse de l'écoulement, de façon à mieux connaître les effets de la turbulence sur la dynamique de ce type d'écoulements.

Le site expérimental

Le nouveau site expérimental de Taconnaz a été instrumenté avec des capteurs de pression et vitesse sur trois tas freineurs composant le système de protection actuel. Une première avalanche a atteint les tas durant le premier hiver mais le système n'a pas fonctionné correctement. Le deuxième hiver a fourni la première avalanche enregistrée. Le 29 décembre 2010 le premier jeu de données a été enregistré par les capteurs, montrant que le site est aujourd'hui opérationnel. Le troisième et dernier hiver, deux événements se sont produits mais les deux se sont arrêtés à 1 m à l'amont du premier tas instrumenté. Les premiers résultats ont été analysés mais ils restent pas assez nombreux pour être représentatifs. Par conséquent, les perspectives principales se basent sur l'espoir d'enregistrer le plus possible d'événements dans les années à venir, afin d'agrandir nos bases de données et en permettre une analyse plus consistante.

Des mesures de terrain concernant la hauteur de l'écoulement incident ne sont pas disponibles actuellement. Cependant, ce paramètre est très important pour le calcul du nombre de Froude et pour la comparaison des avalanches mesurées avec celles obtenues dans d'autres site expérimentaux et celles réalisées à l'échelle réduite. Les améliorations futures sur ce site devraient envisager l'installation de capteurs de hauteur.

Contribution à la conception de structures de protection

La force exercée sur un obstacle reste un paramètre clé dans le processus de conception de structures de protection paravalanche. Ce travail de thèse montre que cette force est influencée par (i) une contribution proportionnelle à la vitesse de l'écoulement (force cinétique), (ii) une contribution liée à sa hauteur (force hydrostatique) et (iii) une troisième contribution due au poids apparent de la zone morte qui se forme à l'amont de l'obstacle et qui joue un rôle important sur la définition de la force totale. Bien que ce travail ait fourni des nouveaux résultats, l'étude de la zone morte et de la zone d'influence associée, doit être poursuivie. Le rôle de la zone morte devient important aux pentes faibles, pour des régimes de vitesse basses. La valeur du coefficient C_d , peut augmenter significativement pour des nombres de Froude faibles, ce qui signifie des pressions élevées malgré des vitesses faibles. Les tests en laboratoire montrent cet effet et les mesures de terrain le confirment. Ceci doit être pris en compte lors de la conception des structures de protection paravalanche.

Un autre processus important qui doit être considéré, c'est la transition entre le régime de zone morte et celui de ressaut. Pour l'instant cette transition a été trouvée expérimentalement pour des écoulements granulaires. Les travaux futurs devraient chercher à vérifier ce phénomène dans le cas de vraies avalanches, et les procédures pour la conception de dispositifs de protection devraient en tenir compte.

Un guide européen publié en 2009 décrit les développements récents, pratiques et théoriques, qui visent à améliorer et mettre à jour les principes sur lesquels la conception de structures de protection est basée. Bien que ce guide soit fondé sur une représentation dynamique des caractéristiques d'un écoulement, ces deux sujets (rôle de la zone morte et transition zone morte - ressaut) ne sont pas pris en compte et devraient être inclus dans les futures mises à jour.

De plus, la modélisation physique d'avalanche de neige poudreuse a montré qu'une digue d'arrêt avec parement amont incliné d'un angle $\alpha_{dam} = 32^\circ$ (angle de talus du matériel) est moins efficace sur la dynamique d'un aérosol par rapport à la même digue avec parement vertical ($\alpha_{dam} = 90^\circ$). La configuration expérimentale, avec parement incliné, peut facilement se présenter dans la réalité. Cet angle représente l'angle naturel de talus d'une digue en terre et par conséquent, cette solution est plus facile d'un point de vue de l'ingénierie et moins chère. De plus, le dépôt d'une avalanche accumulé à l'amont d'une digue avec parement vertical peut reproduire des conditions similaires à la configuration étudiée. Les expériences en laboratoire devraient analyser le comportement d'un écoulement de type dense à l'interaction avec une digue d'arrêt à parement incliné. D'un point de vue de l'ingénierie, il serait très intéressant de calculer la hauteur équivalente pour une digue avec parement incliné capable d'atteindre la même efficacité d'une digue à parement vertical de hauteur fixée.

Enfin, pour pouvoir appliquer les résultats issus de l'expérimentation en laboratoire à l'aide de courants de densité en cuve d'eau aux cas réels, des travaux de modélisation numérique devraient être réalisés afin de corriger la distorsion en densité introduite.

L'objectif initial de ce travail étant la synthèse et l'amélioration des connaissances actuelles en terme de interaction écoulement - obstacle, j'espère que ce travail puisse contribuer à une évolution dans la conception des futures structures de protection paravalanche.

Introduction

Contents

Avalanche physics	3
Active and passive protection	6
Design of passive protection structures	8
Scientific focal points	13
Dissertation framework	15

Snow avalanches are rapid gravity-driven flows. Many factors contribute to their formation, but the presence of snow and a terrain slope are the two key ingredients. Generally speaking, *(i)* precipitation provide the snow that forms the snow pack, *(ii)* a provocation (natural or artificial) breaks the equilibrium of the snow-pack and *(iii)* the avalanche is then released and starts flowing downwards, driven by gravity.

Snow avalanches are natural phenomena, such as rockfalls and debris-flows, which have concerned mountainous areas for a very long time. The 20th century witnessed the increase of human presence on mountains, as the urbanisation process started and the interaction between man and mountains changed. Areas which were previously considered as rough and hostile turned out to have a very high potential for human activity, with tourism benefiting the most. The boom of winter activities led to the construction of communication ties to mountain valleys, infrastructures to host people, burgeoning ski resorts and economic activities. Moreover, since mountains have often been used to define country borders, the increase of mass communication and international exchange have also participated in the urbanisation process. Natural phenomena then became natural risks, and a growing need of protecting goods, life and activities arose. This need had always previously existed, but before it had only concerned a few farmers, countrymen and monks who inhabited these remote lands. Prior to the urbanisation boom of the 20th century, man had always tried to protect himself, as Fig.6 shows, by using limited knowledge mainly based on the empirical intuition. The urbanisation boom led man to adopt a



Figure 6: Rudimentary protections developed using a limited knowledge based on empirical intuition. Pictures are taken from: (a) Irstea (PBR), (b) www.imageshack.us and (c) www.avalanches.fr.

more scientific approach based on modern progress in mechanics and geoscience.

This expansion process has not ended, and mountainous areas continue to develop and to expand today as this process started by urbanising the safest zones of mountainous regions, at the present time expansion becomes increasingly challenging because the growing need for space leads to constructions in areas which are clearly threatened by natural hazards.

The spread of human activity throughout mountain slopes has generally been associated with an increase of scientific knowledge and protection effectiveness. However, dramatic accidents such as those in Val d'Isère (France, 1970), Montroc (France, 1999), Evolène (Switzerland, 1999) and Galtur (Austria, 1999), remind us of the unpredictable nature of these natural hazards and the further need for deeper knowledge of this complex phenomena. In particular, in the framework of natural risks connected to snow avalanches, the hazard prediction, the protection measures to be taken, the hazard mapping and the analysis of structures vulnerability, represent some of the main questions that need a prior knowledge about the involved physical processes. An accurate quantification of the physical vulnerability of structures subjected to avalanches requires a detailed study of the flow dynamics and interaction with obstacles.

This PhD work was conducted in the aim of improving current knowledge of these specific aspects. The dynamic of an avalanche is investigated by using an experimental approach for both dense and powder-snow avalanches which focuses on the influence of the flow on a protection structure (exerted pressures) and on the influence of the structure on the flow behaviour. Small-scale laboratory tests were performed on two different experimental devices. Dense snow avalanches were modelled in relation to granular flows and using an inclined channel. The density currents principle was used to reproduce powder snow avalanches by means of a dyed salt solution flowing down a channel immersed in water. Lastly, small-scale laboratory tests are combined with observations and measurements carried out in the field at Tacconnaz.

This chapter provides an overview of the two main subjects that comprise this dissertation: snow avalanches and defence structures. Basic information on the physics of snow avalanches is discussed and different existing form of protection are explained. A discussion of the design of passive-protection structures introduces the main scientific focus points treated through the dissertation. This introduction finishes with the outline of the manuscript.

Avalanche physics

The word *avalanche* is believed to be derived from the Latin term *labi* which means *to slip* [4]. Avalanches generally consist of a snow flow which, once released by the snow pack rupture, rapidly flows downward driven by gravity. After the release, along its flowing path, an avalanche grows, accelerates and then slows down and stops. A typical avalanche path can be separated in three main parts, as stated in the UNESCO Avalanche Atlas [157]:

- the release zone, is the area where the snow pack rupture occurs and the snow starts flowing;
- the flowing zone, generally canalized and steep, is the section where the avalanche can erode or deposit relevant amount of snow, increasing its size and velocity;
- the run-out zone, where the slope suddenly decreases, the flow slows down and stops generating the final avalanche deposit

Several types of classification exist for the various types of avalanches, based on different criteria. A commonly accepted point of view groups snow avalanches into three main families, based on the flow density: (i) dense snow avalanches, (ii) powder snow (or aerosol) avalanches and (iii) mixed avalanches.

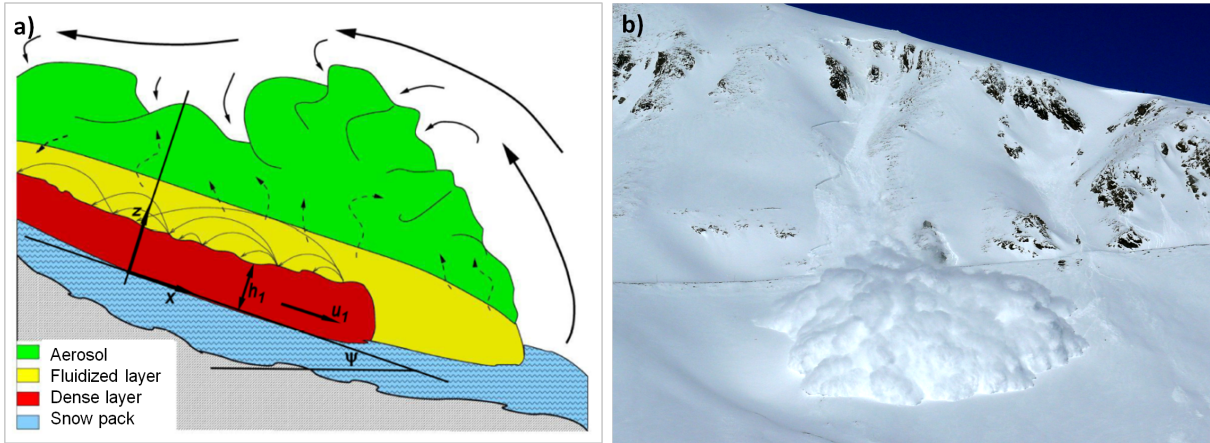


Figure 7: (a) Schematic figure adapted from Issler (2003) [82] showing the different parts that form a mixed dry snow avalanche. (b) Mixed avalanche artificially released at Col du Lautaret. Only the aerosol part is visible but the dense layer, and most likely the fluidised layer as well, flow below it.

1. The dense family includes wet and dry snow avalanches (depending on the water content) and is characterised by high densities ($\rho \simeq 200 - 500 \text{ kg m}^{-3}$). The typical flow velocity ranges between 1 and 30 m s^{-1} , and the mean flow depth is a few meters (in canalised conditions this value can increase significantly) but can nevertheless exert very high pressure upon impact with obstacles (up to 1000 kPa). Wet snow avalanches occur in high air temperatures, when solar radiations are intense, or when the rain brings water to percolation throughout the snow pack. Melted snow (or rain) increases the water content and the avalanche reacts like liquid flow descending at low velocity because of the high friction rate at the sliding surface [103]. Dense flows follow the terrain morphology.
2. Powder snow (or aerosol) avalanches, on the other hand, consist of turbulent suspensions of snow particles in the air. Their density is very low ($\rho \simeq 1 - 10 \text{ kg m}^{-3}$), but the velocity can reach up to 100 m s^{-1} . In aerosol avalanches, turbulence plays a very important role as it takes snow particles from the saltation layer and the snow pack, and carries and holds them in suspension [83]. It also regulates the air entrainment.

3. Mixed avalanches are composed by a dry dense layer flowing at the bottom, combined with a powder snow cloud on top. Figure 7.a illustrates a schematic representation of a mixed avalanche structure, adapted from Issler (2003) [82]. Between the dense layer and the powder cloud on top, a third layer represents an intermediate phase between the dense core and the aerosol outer layer. Current understanding on this layer remains limited as scientists are divided over either a saltation or fluidised layer interpretation. For the sake of clarity in the following discussion, only the term "fluidised" is employed. The density of this third layer ranges between 30 and 200 kg m⁻³ which means lower values than the dense part but too high values to be maintained in suspension by the turbulence. This layer can precede the dense front by many meters and it can attain velocities up to 50 – 60 m s⁻¹. The real-scale measurements conducted since the 1970's in Russia [25], Canada [138] and Japan [113, 142] indicated the presence of a layer of intermediate density between the dense and the aerosol parts of an avalanche. The data from Vallée de La Sionne obtained since 1980 with more recent and accurate sensors confirm it [137]. Figure 7.b shows a mixed avalanche artificially released at Col du Lautaret. Only the aerosol part is visible but the dense layer, and most likely the fluidised layer as well, flow below it.

Pure powder avalanches require steep slopes and generally very cold dry snow conditions, and they are therefore very rare at our latitudes. In the presence of dry snow conditions, after the release, only the dense part of the avalanche starts flowing. The fluidised and suspension layers develop later, depending on the velocity and the air-entrainment rate of the flow. If the aerosol layer does not develop, the avalanche continues flowing downwards as a dense dry snow avalanche. Table 1 is taken from Issler and Naaim (2010) [83] and it summarizes the typical values for the three cited layers.

Table 1: Typical values for the characteristic parameters of an avalanche.

	<i>Dense layer</i>	<i>Fluidized layer</i>	<i>Aerosol</i>
<i>Density (kg m⁻³)</i>	200 – 500	30 – 200	1 – 10
<i>Particle density (kg m⁻³)</i>	300 – 900	300 – 900	900
<i>Volume fraction ()</i>	0.5 – 0.7	0.1 – 0.5	< 0.01
<i>Particle diameter (mm)</i>	1 – 10 ³	1 – 10 ³	< 1
<i>Velocity (m s⁻¹)</i>	1 – 30	20 – 60	20 – 100
<i>Height (m)</i>	0.3 – 3	1 – 5	10 – 100
<i>Pressure (kPa)</i>	10 – 1000	20 – 200	1 – 20
<i>Granular regime</i>	frictional / colli- sional	collisional / iner- tial	macro-viscous / turbulent

Even though this classification is widely accepted in the scientific community today, it is important to note that the boundaries of these layers are not easy to define, and mechanical avalanche properties continuously evolve during motion due to the fragmentation or coalescence of snow particles. An example of these properties is given by compressibility. Even if its behaviour is not perfectly understood, its variation is evidenced by the difference between the snow density in the release area and in the final deposit. Lied et al. (2002) [97] report an increase in density of 43% for an avalanche released at the Ryggfonn test site in Norway, from 300 kg m⁻³ in the release area to 430 kg m⁻³ near the dam.

The design of defence structures against snow avalanches typically takes into account only the dense part which, in spite of its lower velocity, represents the greatest threat in terms of potential damage due to its high density. In most cases, the aerosol layer is supposed to overflow the dam defence structure and is considered to be the residual risk that the avalanche still represents further downhill.

Protecting dams are only one of the many existing defences against avalanche destruction. The following section provides an overview of these different solutions.

Active and passive protection

The most effective way to protect something (buildings, roads, structures...) from natural hazards is to build it far away from natural hazards.

But, as stated at the beginning of this chapter, we currently live in an expanding society. In some ways, risk is accepted at any expense in expanding areas, hence the importance of protection for the ongoing development.

When dealing with snow avalanches, different means of protection can be implemented in order to secure a given place, object or activity. A first distinction can be made based on the protection principle. In order to protect a certain object or structure, *active* protection deals with the release conditions required to prevent the avalanche release or at least to control it. *Passive* protection, on the other hand, aims to control the released avalanche once it arrives in the run-out zone (which generally corresponds to the inhabited area).

Within these two branches, a second distinction must be made between *permanent* and *temporary* actions. The *permanent* protection consists of structures which are fixed, permanently operational and independent from human intervention. *Temporary* solutions, on the other hand, use techniques based on man-made decisions, and they are promptly operative in the case of extreme events and catastrophes. Table 2 summarizes and gives some examples of these types of solutions.

Table 2: Classification of different avalanche defences.

Active protection		Passive protection	
<i>Temporary</i>	<i>Permanent</i>	<i>Temporary</i>	<i>Permanent</i>
Artificial release	Snow nets Snow racks Earthworks Reforestation	Prohibition Alerts Evacuation plans	Breaking mounds Deflecting dams Catching dams Hazard zoning and land planning

Active temporary protection mainly consists of artificial avalanche release (see Fig.8.a). When critical conditions occur, the avalanche can be preventively released in controlled conditions in order to secure the area. *Active permanent* solutions make use of snow nets, snow racks (see Fig.8.b-c), earthworks and reforestation to increase the soil roughness and retain the snow pack. Wind drift control structures such as snow fences, jet roofs and wind baffles can also be used to avoid additional accumulation in the release area from drifting and blowing snow. *Passive temporary* protection consists of defining precise plans for prohibition and crisis management (alert and evacuation). Lastly, *passive permanent* protection is supposed to prevent the avalanche from reaching the element at risk. Different solutions exist:

- breaking mounds, to slow down the incoming flow and dissipate part of its energy (Fig.8.d);
- deflecting dams, to deviate the flow by directing it elsewhere on the lateral side (Fig.8.e);
- catching dams, to stop the flow and store its volume upstream (Fig.8.d);

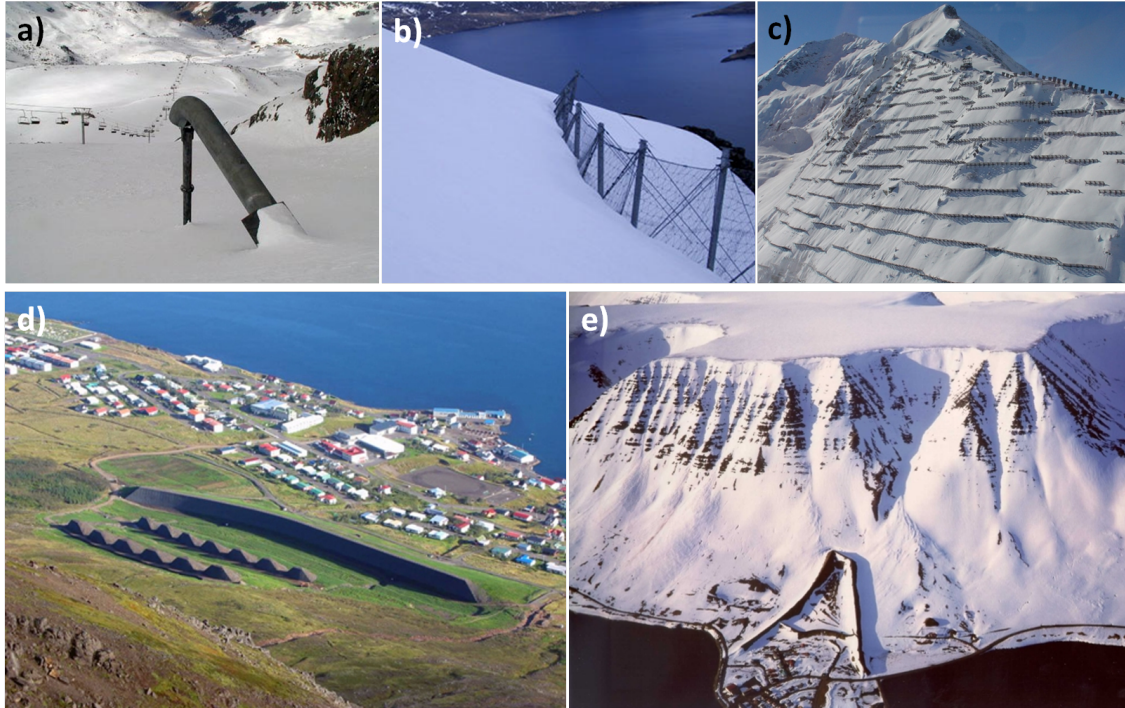


Figure 8: Some examples of protection solutions. (a) Temporary active protection: artificial release using a Gazex (photo from www.toraval.fr). Permanent active protection: (b) snow nets (www.avalanches.fr) and (c) snow racks. Permanent passive protection: (d) breaking mounds and catching dam in Neskaupstadur, Iceland (source SATSIE project, <http://www.leeds.ac.uk/satsie/seynesk.html>) and (e) deflecting dam in Flateyri, Iceland (courtesy of Tomas Johannesson).

- hazard zoning, to define the areas where it is possible to build without any constraint, areas that are suitable for building but only under certain conditions, and areas where construction is not allowed.

All of these solutions can be combined in order to increase the effectiveness of the protection system. Chapter 3 deals with the Taconnaz site which represents an exemplary case for the optimal combination of these solutions.

In this dissertation, we investigate the behaviour of an avalanche flow interacting with passive permanent protections. Catching dams and breaking mounds, in particular, are implemented in small-scale physical simulations.

The next section gives insight into the classic as well as the recent design guidelines for passive permanent structures.

Design of passive protection structures

The content of this section is mainly based on the work published in Barbolini et al. (2009) [13].

Classic design

The devastating effect of rapid mass movements such as snow avalanches can be reduced by placing protection structures that divert, slow down or stop the flow in the avalanche run-out zone. The design of these structures often still refers to rough guidelines, based on practice rather than theory. Several methods exist, among which the most widespread is based on simple point-mass principles advanced by Voellmy in 1955 [158]. Alpine countries have generally adopted this method which is described in detail in Salm et al. (1990) [134], Norem (1994) [116], Lied and Kristensen (2003) [98] and Margreth (2004) [101].

The height of the dam H_{obs} is obtained according to:

$$H_{obs} = h_s + h_f + h_u \quad (18)$$

where h_s is the height of the snow deposited upstream from the obstacle, h_f stands for the flow height (dense core), and h_u represents the expected height due to the kinetic energy of the avalanche. The values of h_s and h_f are estimated from meteorological information (h_s) and considerations on the reference avalanche (h_f), while h_u is calculated, for catching dams, as

$$h_u = \frac{u_1^2}{2g\lambda} \quad (19)$$

where u_1 is the incoming flow velocity, g stands for gravity and λ is an empirical parameter for energy dissipation due to the momentum loss at the impact with the dam. λ is, by construction, greater or equal to the unit. A value larger than 1 means that some of the kinetic energy is dissipated (impact, friction). The expression for the dam height then becomes:

$$H_{obs} = h_s + h_f + \frac{u_1^2}{2g\lambda} \quad (20)$$

which can be written as a function of the Froude number of the flow:

$$\frac{H_{obs}}{h_f} = \frac{h_s}{h_f} + 1 + \frac{Fr^2}{2\lambda} \quad (21)$$

For the case of a deflecting dam, the considerations on h_s and h_f remain but the deflecting angle φ appears ($\varphi = 90^\circ$ for catching dams) in the computation of h_u :

$$h_u = \frac{(u_1 \sin \varphi)^2}{2g\lambda} \quad (22)$$

The values of λ , for catching dams, usually range between 1 – 3. A higher value of λ means a lower dam height and thus this parameter must be chosen cautiously and with respect to the extent of the expected reference avalanche. For deflecting dams, λ is often taken equal to the unit which corresponds to neglect the energy dissipation due to the impact. This choice leads to higher values for the dam height and is considered as a safety measure in order to counterbalance the method uncertainties.

The main drawback to simple point mass models is their neglect of the width of the avalanche and its related 3D effects. From this perspective, a canalised avalanche behaves like an avalanche impacting a dam in an open slope. Another important aspect is not taken into account by these

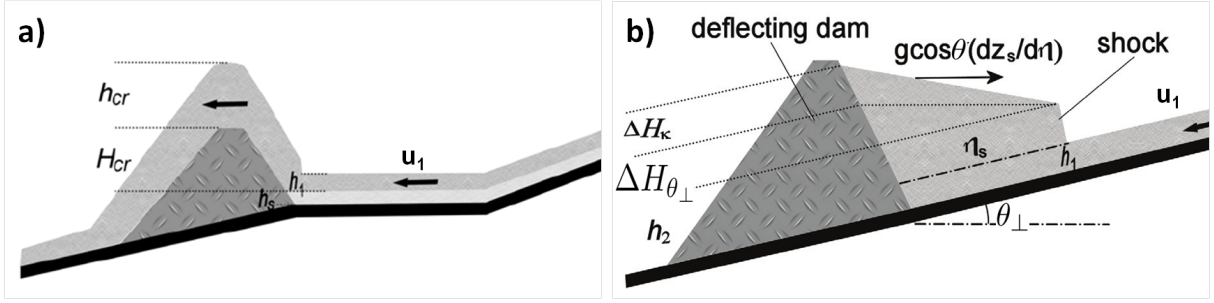


Figure 9: Figures taken from Barbolini et al. (2009) [13]. (a) A schematic figure of supercritical overflow showing the critical dam height H_{cr} and the critical flow depth h_{cr} . (b) Schematic cross-section of a shock formed along a deflecting dam built on a terrain sloping towards the dam.

classic design principles: upon impact with a dam, part of the avalanche volume is trapped upstream from the dam (quasi-static dead zone) and influences the flow behaviour in some ways. Neglecting these effects can lead to inconsistent results.

However, more recent practical and theoretical developments have become available. Although avalanche protection measures were widely implemented in several countries in recent decades, the effectiveness of different types of protective measures remains an open question. During the winter of 1999 several avalanches overran protection dams and demonstrated the need for further research in this field.

New European procedure [13]

The European research projects CADZIE and SATSIE contributed to the improvement of existing avalanche research, and in 2009 a guide for the design of protection dams was published [13]. This book summarises recent theoretical developments and the results of field and laboratory studies. Based on experimental tests and theoretical analyses, the CADZIE and SATSIE projects provided relevant contributions to the knowledge of snow avalanches interacting with obstacles and made it possible to enhance the design criteria for protective measures in avalanche run-out zones. Recent results were combined with traditional design guidelines in order to develop a new framework for the design of protection dams against dry snow avalanches.

This section resumes the main principles on which an effective design should be based. Further details can be found in "*The design of avalanche protection dams. Recent practical & theoretical developments.*", Barbolini et al. (2009) [13].

The proposed guidelines regard catching and deflecting dams and they are based on a consistent dynamic representation of the flow behaviour combined with an accurate description of the terrain and of the structure. No guidelines exist for a standard design of breaking mounds even though they are widely used for avalanche protection. However, several studies were recently conducted and are described in Hákonardóttir (2000) [74], Johannesson and Hákonardóttir (2003) [87], Hákonardóttir et al. (2003c) [77] and Hákonardóttir (2004) [75].

The new criteria for protection dams are based on the concepts of (i) supercritical overflow and (ii) flow-depth downstream from a shock. In most cases, the incoming flow impacts the obstacle in supercritical conditions ($Fr > 1$) and the main objective of the dam design is to prevent a supercritical overflow (see Fig.9.a). If the supercritical overflow is not possible, the dynamics of shallow fluids predicts that a shock occurs upstream from the dam. The second criterion aims to outline a dam height higher than the flow depth downstream from the shock as displayed in Fig.9.b.

In general, the height of the dam H_{obs} , normal to the terrain slope, is calculated as:

$$H_{obs} = h_r + h_s \quad (23)$$

where h_s is the height of the snow upstream from the dam and h_r represents the run-up height which corresponds to:

$$h_r = \max(H_{cr} + h_{cr}, h_2 + \Delta H_{\theta_{\perp}} + \Delta H_{\kappa}) \quad (24)$$

All the parameters involved in the computation of the run-up height h_r respectively stand for: the critical dam height (H_{cr}), the critical flow depth (h_{cr}), the upstream shock height (h_2), the contribution of the terrain slope towards the dam ($\Delta H_{\theta_{\perp}}$) and the height contribution induced by the curvature of the dam axis (ΔH_{κ}). All of these terms are explained later in this section. Guidelines are proposed according to a step-by-step procedure.

1. Firstly, it is necessary to estimate accurately the dynamic characteristics of the incoming flow (h_1 and u_1 with respect to Fig.9) and the height of the snow h_s , deposited on the terrain upstream from the dam.
2. For deflecting dams only, it is necessary to calculate the deflecting angle φ ($\varphi = 90^\circ$ for catching dams).
3. The Froude number of the avalanche must be calculated, according to

$$Fr = \frac{u_1}{\sqrt{gh_1 \cos \theta}} \quad (25)$$

where g stands for gravity and θ is the mean terrain slope upstream from the obstacle.

4. Determine the momentum loss coefficient k_{loss} after fixing α_{dam} , the angle between the upstream dam side and the terrain (see Fig.9.b)

$$k_{loss} = 0.75 \quad \text{if } \alpha_{dam} > 60^\circ \quad (26)$$

$$k_{loss} = 0.75 + 0.1 \frac{(60^\circ - \alpha_{dam})}{30^\circ} \quad \text{for } 30^\circ \leq \alpha_{dam} \leq 60^\circ \quad (27)$$

5. Calculate the contribution of the sum of the critical dam height H_{cr} and the relative critical flow depth h_{cr} given by:

$$\frac{(H_{cr} + h_{cr})}{h_1} = \frac{1}{k_{loss}} + \frac{1}{2} (k_{loss} Fr \sin \varphi)^2 - \frac{1}{2} (Fr \sin \varphi)^{2/3} \quad (28)$$

or, in a dimensionless form:

$$H_{cr} + h_{cr} = \frac{h_1}{k_{loss}} + \frac{(u_1 \sin \varphi)^2}{2g \cos \theta} k_{loss}^2 \left(1 - k_{loss}^{-2} (Fr \sin \varphi)^{-4/3} \right) \quad (29)$$

H_{cr} represents the critical height at which the flow passes from a supercritical ($Fr > 1$) to a subcritical ($Fr < 1$) state upon dam impact. If $H_{obs} < H_{cr} + h_s$ the avalanche overflows the obstacle in supercritical conditions, and this must be prevented. If $H_{obs} < H_{cr} + h_s + h_{cr}$, a shock occurs but the front of the avalanche can still overflow the dam. Thus, it is necessary that

$$H_{obs} > H_{cr} + h_s + h_{cr} \quad (30)$$

6. Calculate the potential shock height h_2 occurring upstream from the obstacle (as represented in Fig.9.b) according to

$$\frac{h_2}{h_1} = \frac{1}{3} \left(2\sqrt{(6Fr_{\perp}^2 + 4)} \cos \delta + 1 \right) \quad (31)$$

where $Fr_{\perp} = Fr \sin \varphi$ and δ is defined as

$$\delta = \frac{1}{3} \left[\frac{\pi}{2} - \tan^{-1} \left(\frac{9Fr_{\perp}^2 - 8}{Fr_{\perp} \sqrt{27(16 + 13Fr_{\perp}^2 + 8Fr_{\perp}^4)}} \right) \right] \quad (32)$$

7. For deflecting dam only, it is necessary to check whether an attached stationary oblique shock is dynamically possible. This can be done by verifying that $\varphi < (\varphi_{max} - 10^\circ)$, where φ is the dam deflecting angle and φ_{max} is defined as

$$\varphi_{max} = \frac{\pi}{2} - \frac{2^{3/4}}{Fr^{1/2}} - \frac{2^{1/4}}{6Fr^{3/2}} \quad (33)$$

If this condition is not fulfilled, the shock height h_2 has to be recalculated from Eq.(31) fixing $\varphi = 90^\circ$.

8. If the terrain normal to the dam axis leans towards the dam, the height of the deflecting dam, derived from the shock dynamics ($H_{obs} = h_s + h_2$), has to take into account the contribution of the terrain slope towards the dam and thus to be increased of a factor

$$\Delta H_{\theta_{\perp}} = \frac{\sqrt{2} \tan \theta_{\perp}}{2Fr \cos \varphi} \quad (34)$$

where θ_{\perp} stands for the terrain slope in the direction normal to the dam axis.

9. If the dam axis is curved, the height of the deflecting dam, derived from the shock dynamics ($H_{obs} = h_s + h_2$), must take into account the centripetal acceleration that is introduced by the flow bending around the curved dam geometry. The dam height must be increased of a factor

$$\Delta H_{\kappa} = \frac{\sqrt{2} (u_1 \cos \varphi)^2}{2Fr \cos \varphi g \cos \theta R_{\kappa}} \xi_{dam} \quad (35)$$

where R_{κ} is the radius of curvature of the dam axis and ξ_{dam} represents the distance along the dam axis measured from its upstream end.

10. Even if the mean slope in the run-out zones is generally low, the vertical dam height slightly differs from the height value normal to the terrain. The dam vertical height H_{obs_v} can then be calculated according to

$$H_{obs_v} = \frac{\cos \theta - \sin \varphi \sin \theta \cot \alpha_{dam}}{1 - \cos^2 \varphi \sin^2 \theta} H_{obs} \quad (36)$$

11. For deflecting dams only, it is very important to evaluate the extent of the region affected by an increase of the run-out distance due to the flow-obstacle interaction.

12. For catching dams only, calculate the necessary storage volume S_{st} per unit width, upstream from the dam, according to

$$S_{st} = \int_{x_0}^{x_1} z_l - (z_s + h_s) dx \quad (37)$$

where z_l is the elevation of a straight line from the top of the dam towards the mountain with a slope in the range $0 - 10^\circ$. This value depends on the water content of the expected avalanche and reflects the friction angle of the unmoving snow. A lower value corresponds to a safety choice. Note that the storage area S_{st} must be larger than the volume of the avalanche divided by its width.

Although some uncertainties remain, we believe that this guide represents an important outcome and that it should serve as the basis for the construction of new protection dams. The main characteristic of this procedure is to be founded on a dynamics-oriented framework rather than on rough guides, based on practice. Important features like shock dynamics and the behaviour of supercritical and subcritical flows are taken into account, and attention is also given to the momentum loss upon impact with the obstacle as well as the channelised effect to which the flow is subjected when hitting a deflecting dam. These are some of the new aspects which make this innovative concept of dam design more consistent and reliable than previous works.

If these considerations are valid for dry snow avalanches, however, the current knowledge of wet snow avalanches is still limited. This type of flows, upon impact with an obstacle, can behave in unpredictable ways. Special attention must be paid to certain aspects in particular:

- many wet flows can drain in the same path and thus the final deposit volume may be higher than the expected design value;
- the deposit height can increase (pile-up phenomena) up to the dam's maximum height, allowing frontal and lateral overflows. In this case, the final deposit height should be used as a design parameter, rather than the incoming flow velocity;
- the flow direction can change without apparent reason, going beyond the control of the protection structure (deflecting dam case);
- a wet snow avalanche can carry very large debris or rocks that may damage the protection structure.

This section has provided an overview of the recent findings in terms of the design of permanent passive protection structures. The next section deals with the scientific focal points treated within this framework. Although structure design is beyond the direct scope of the study, greater understanding of the flow dynamics and the force exerted on a structure will further optimise the dam's design.

Scientific focal points

The previous section highlighted the fundamental role of a dynamics-based strategy to optimise the design of protection structures. This work is placed within the framework of flow investigation that aims to enhance the understanding of its dynamic behaviour. The approach adopted is mainly experimental. Dry dense and aerosol avalanches were studied. Simple and more complex geometrical configurations (where the size of the obstacle is equal or greater than the characteristic dimension of the flow) were considered. Small-scale laboratory tests were combined with observations and measurements carried out in the field.

The dense part of an avalanche determines the main requirements for protection design. The current knowledge on dense avalanches impacting an obstacle is aware of the existence of different flow regimes which can occur, in theory, during the flow-obstacle interaction. These regimes mainly consist of the formation of *(i)* a dead-zone or *(ii)* a granular jump upstream from the obstacle, or *(iii)* the formation of a downstream jet, and they have previously been reproduced individually by physical and numerical simulations. However, the behaviour of these regimes applied to granular flows is still not very well known.

Thus, the first scientific point to tackle is the role of the influence zone generated by the presence of a dead zone. What is the role of this zone on the flow behaviour? How is the force exerted on an obstacle affected by the presence of an influence zone?

Secondly, although the dead-zone and the granular jump regime are theoretically known as two independent regimes, small-scale experiments suggest that, under certain conditions, a dead zone regime can transit into a granular jump regime. Thus, the second important point to focus on is the transition from the dead zone to the granular jump regime.

Lastly, the influence of the obstacle geometry on the behaviour of the flow is also analysed in detail by using different shapes of obstacles and comparing the results.

These are the three main scientific focus points treated in chapter 1 that concern the physical simulation of a dense snow avalanche.

In the design of protection structures, the powder part of an avalanche is considered as residual risk. This aerosol part cannot be blocked by an obstacle and it overflows regardless. Generally the aim is to quantify the risk that this phenomenon still represents downstream from the protection structure. The challenge of chapter 2 therefore consists of a representation, as accurate as possible, of the powder flow impacting an obstacle in order to investigate the flow behaviour upon impact. Due to the characteristics of the aerosol part of an avalanche, physical modelling is complex and precise measurements on the flow velocity have never been achieved. We intend to achieve such accurate measurements of the flow height and velocity in order to estimate the impact pressures. Density measurements also represent a great challenge that must be undertaken.

A full-scale measurement site was equipped in the frame of the PhD project and measurements were taken in order to provide data concerning full-scale avalanches. The description of the site and of the related activities is treated in chapter 3. For the in-situ measurements, the challenge consisted of successfully instrument already existing protection structures with a complex measure system able to operate rough weather conditions (very low and high temperatures), to support very important solicitations (pressures up to 100 ton m^{-2}), to be permanently operational and to ensure constant communication between all the components forming the system. The collected data provide additional results to validate theoretical, numerical and physical modelling on different scales.

The design, the setting up and the data exploitation are part of this research work.

The afore-mentioned points represent the main scientific analysis that the dissertation work was centered around. All of these points are developed in detail in the following chapters. The next section gives a general overview of the dissertation framework and provides the outlines necessary to introduce the reader to the manuscript.

Dissertation framework

This dissertation aims to synthesize and reinforce the existing knowledge of the influence of an obstacle and the forces exerted upon it. The manuscript is structured into three main chapters, each headed by an introduction and finished with a conclusion and outlooks, and a table summarising the main results of the given chapter.

Chapter 1 describes the physical modelling of dense snow avalanches on small-scale model by analogy with granular flows. An overview of current knowledge of snow flow characteristics, combined with granular flow features, highlights some analogies and justifies the choice of a granular material to model dry dense snow avalanches flowing down a channel and interacting with an obstacle. The small-scale model is then described by detailing the experimental device and the measurement techniques that were adopted. Tests were performed first without the obstacle (reference tests) in order to characterise the flow dynamics and, afterwards, two different obstacles were installed and force measurements were taken. The significant role of the influence zone was also investigated through an accurate analysis of its behaviour. Experimental results were validated and interpreted and, consequently, they allowed the validation of an analytical model that was developed in parallel. A description of this model is given and a cross-analysis with results from experimental and numerical simulations is provided to demonstrate the robustness of the model.

Chapter 2 describes the physical modelling of powder snow avalanches on small-scale model by analogy with density currents. An insight on the existing knowledge is given in order to justify the modelling techniques chosen and to set the main objectives. A different experimental set-up (from that employed for dense flows) was used to reproduce aerosol avalanches by using a salty dyed solution flowing down a channel immersed in a water tank. Each test was recorded with lateral video cameras and the behaviour of the flow height, front and maximum velocity were captured by image processing. More precise measurements were also taken by using a *3D* Doppler velocimeter. Results were collected in reference conditions and in the presence of two different types of obstacles. The obtained data were compared in order to analyse the effectiveness of different protection solutions and to quantify the residual risk downstream from the dam.

Chapter 3 details the full-scale experimental site. In Taconnaz (Chamonix, France), a huge avalanche protection system has been in place since 1991. A description of the site, combined with the history of the avalanche path and its catastrophic events, is provided in order to situate the context. Later, in the framework of the renewal of the protection system, three braking mounds were equipped with velocity and pressure sensors and the first data were recorded during the avalanche of December the 29th, 2010. Preliminary results showed a consistent maximum pressure peak up to 50 ton m^{-2} and high pressure values acting upon the obstacle even at low flow regimes combined to the drag enhancement for low velocity values. Although data remain scarce for the moment, they prove that the acquisition system works well.

Finally, the general conclusions of the dissertation resume the work that was accomplished, weigh the successes that were achieved, and examined the problems that were encountered. General insight into future works concludes the dissertation.

Chapter 1

An inclined granular plane to model dense snow avalanches

Contents

1.1	Snow avalanches and flow - obstacle interaction	18
1.1.1	The snow flows	19
1.1.2	Granular flows: characteristics and modelling	25
1.1.3	Why use a granular material to model a dense snow avalanche?	31
1.1.4	Avalanche - obstacle interaction	32
1.2	The inclined granular plane: method	37
1.2.1	Experimental device	37
1.2.2	Measurement techniques	41
1.3	The inclined granular plane: results	50
1.3.1	The avalanche dynamics	50
1.3.2	Force on a large obstacle spanning the channel	54
1.3.3	Force on a small obstacle allowing lateral flows	58
1.3.4	The influence zone uphill from the obstacle	66
1.4	The analytical force model	72
1.4.1	Model's equations for steady flows	72
1.4.2	Model's equations for unsteady flows	74
1.4.3	Model's predictions compared to previous discrete numerical simulations	75
1.4.4	Model's predictions compared to experimental results	79
1.5	Conclusions and outlook	83

Dense snow avalanches are snow flows characterised by high densities ($\rho \simeq 200 - 500 \text{ kg m}^{-3}$) as explained in the introduction. Their typical velocity ranges between 1 and 30 m s^{-1} and the mean flow depth is a matter of several meters, yet because of the very high density, this type of flow can exert huge pressures upon impact with an obstacle (up to 1000 kPa).

This is why the dense avalanche parameters are taken into account for the design of structures subjected to snow avalanches, rather than those of powder snow avalanches.

The aim of this chapter is to investigate dry dense avalanches through small-scale laboratory tests on granular flows in order to study their dynamics, the force that this type of flow can exert upon an obstacle, and the influence of the obstacle on the flow behaviour.

Section 1.1 provides insight into the existing studies at the forefront of dense snow avalanche investigation with a focus on the comparison between flowing snow and granular flows. Section 1.2 describes the experimental set-up that was used and the measurement techniques that were chosen (laser, image processing and force sensors). The results that were obtained, concerning the avalanche dynamics and its interaction with two types of obstacles, are presented in section 1.3. Section 1.4 introduces a hydrodynamics analytical model that was developed in parallel and has been successfully tested through experimental results. Lastly, section 1.5 concludes the chapter.

1.1 Snow avalanches and flow - obstacle interaction

The scientific study of dense snow avalanches is a recent subject. Most of this work dates back to 40 – 50 years ago, the knowledge within this field remains limited and today represents a growing research area. In general, there are three main approaches for treating this phenomenon: *(i)* direct in-situ observation, *(ii)* physical simulation using small-scale models and *(iii)* numerical simulation. In-situ measurements are the most reliable because they deal with real snow avalanches, but they are difficult to handle, weather-dependent, most of the starting parameters cannot be controlled, and they can potentially be dangerous for operators. Physical and numerical simulations are therefore developed simultaneously. They might be able to reproduce real-life events by introducing simplified hypothesis, and they can very well allow the manipulation of various parameters while providing much greater ease-of-use, which also means that tests can be repeated several times and provide a higher amount of data.

The main purpose of this chapter is to study dense snow avalanches through a small-scale model that uses a granular material to reproduce the snow.

This section aims to give a general overview of the existing as well as the already completed work in the field of dense snow avalanches.

A rough description of snow flows will first be provided. Then, granular flows conducted on laboratory tests will be discussed and a parallel to dense snow will be proposed. A summary of existing knowledge concerning the flow - obstacle interaction will conclude the section.

1.1.1 The snow flows

As mentioned in the introductory chapter, avalanches consist of snow flows which, due to the release of a certain volume of snow, start flowing downward as they are driven by gravity.

This section first gives an insight into the characteristics of the snow cover and then describes the standard principles employed for avalanche modeling.

Snow in nature: some physical characteristics

Snow is a complex material. Snow crystals appear during snowfalls; once accumulated on the ground, they form a snow cover consisting of a porous medium composed of air, water vapour, ice, and liquid water [2]. This snow cover is rapidly subjected to a metamorphosing process controlled by physical parameters that characterise the surrounding environment. Wind and temperature variations are the main factors that affect this metamorphosis. This process is related to the asperity's breaking down of the grains' structure that leads to compacting the snow under the load of the upper snow layers. Crystals and grains evolve, from one structure to another, and these transformations are non-reversible. Different metamorphoses lead to different types of snow particles which correspond to different mechanical behaviours of the snow cover. This cover is composed of crystals and grains that belong to five main classes characterised by their state of metamorphism (see Fig.1.1). In general, we use the term "crystals" when referring to classification and falling snow, and the term "grains" when the snow is on the ground (except for fresh snow where the original crystal shape is conserved).

These five classes consist of (i) star-shaped snow crystals and fresh snow, (ii) fine grained snow, (iii) faceted snow crystals, (iv) crystals of depth hoar and (v) rounded wet snow grains. Each class has its own morphological features and particular physical properties [1]. The crystal structure remains perfectly intact only for fresh snow. For other cases, the process of metamorphosis modifies the shape of the particle and the classic star structure is lost. Due to their granular aspect, particles are also called *grains*.

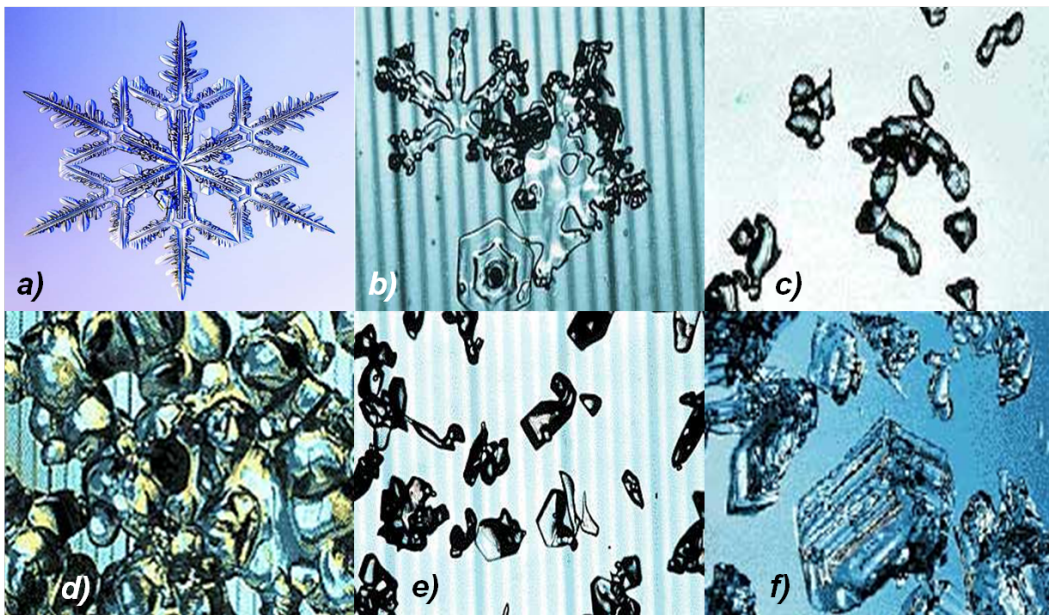


Figure 1.1: Snow crystals: (a) stars (or perfect fresh snow crystals), (b) star-shaped snow crystals, (c) fine grained snow, (d) faceted snow crystals, (e) crystals of depth hoar and (f) rounded wet snow grains.

In the following section, some information is provided for each of these classifications:

- **Stars**

A fresh snow crystal is not subjected to any transformation. Due to negative temperatures and the absence of wind, its original structure is maintained. This structure is characterized by a hexagonal shape generating several groups of crystals. The most familiar one is the common snowflake. It has a dimension of 1 to 5 mm and, because of its interlacing dendrites, it can reach a significant cohesion capacity (through felting cohesion) which makes it holds onto very steep slopes. 90% of its volume is made up of air, which explains its low density (50 to 150 kg m⁻³). Because of the high air content, fresh snow is a very good thermal insulator, and due to its high reflecting capacity (albedo), it can reflect 90% of solar radiation and thus the influence of solar heating is limited on fresh snow cover. Liquid water is not contained in this class of particles, nor in the following four classes. This is a peculiar feature of *dry snow*.

- **Star-shaped snow crystals**

Star-shaped snow crystals can be considered as a sub-division of the star class. This state occurs at the beginning of the metamorphism, and the original crystal structure is still visible. Typically, a snowflake with some broken branches becomes a star-shaped snow crystal. Felting cohesion still exists even if it is weaker than fresh snow. Particles, as their branches break, tend to become fine grained snow, Ice bonds develop between grains where dendrites started breaking. The air content is still high, thus the density is weak (100 to 200 kg m⁻³) and the thermal insulation capacity remains significant. The albedo is similar to the fresh snow case.

- **Fine grained snow**

Fine grained snow consist of small round grains. Due to their size (less than 0.5 mm) and their shape, the contact points between grains facilitate the creation of ice bonds which cause this type of particle to have high sintering cohesion. As grains are bonded together, less air is able to subsist. This means a higher density (200 to 400 kg m⁻³) and a lower insulation power. Due to the small size of the grains, the albedo value remains high.

- **Facetted snow crystals**

Facetted snow crystals are small ($d \simeq 1$ mm) sharp grains characterised by their plane faces. This feature prevents any formation of ice bonds and causes this type of grain to have a very low cohesion rate. The density is about 250 – 350 kg m⁻³ and the albedo decreases due to the dimensions of the grains, which are larger than those of the tiny grains. Thus, solar radiation can rapidly influence the thermal metamorphism of snow cover composed by this type of particle.

- **Crystals of depth hoar**

Crystals of depth hoar have very similar characteristics to the previous ones. They have a peculiar pyramidal shape, but are also sharp with flat faces that provide absolutely no cohesion to other particles. This family of grains, during the formation of an intermediate layer inside the snow cover, greatly facilitates the sliding of the upper layers that generates avalanche releases.

- **Rounded wet snow grains**

Rounded wet snow grains concern humid snow where liquid water partly fills the empty spaces between grains. They have a characteristic round shape with a diameter of several millimetres, a high density (350 to 500 kg/m⁻³) and, due to their significant size, they absorb solar radiation very well. Solar energy can therefore heat them up easily. A low liquid water content increases the grains' cohesion but too high of a value tends to liquefy the medium.

These general characteristics are useful for explaining the basic features of the substance of snow,

which is the main ingredient of snow avalanches. The behaviour of the still, undisturbed snow and the snowpack evolution represent an entire research topic in and of themselves. However closely they are related to snow avalanches, a more detailed analysis is beyond the scope of this report.

Consequently, attention will be focussed on snow avalanches from now on. The next section deals with the modelling of snow avalanches. Their internal structure is set aside as a continuum approach is privileged. Analytical models have existed for ninety years and small-scale and real-scale experiments have been performed more recently.

Avalanche modelling

Previous paragraphs explain how snow is a heterogeneous material characterized by a granular structure. The first avalanche model dates back to 1922. Paul Mougins proposed the consideration of a snow avalanche as one rigid entity sliding down an inclined terrain as it is subjected to a basal friction. Later on, in the 1970s, researchers began to treat avalanches using the Saint Venant equations. As is the case for hydrology, these equations are averaged on the flow depth that can permit to ignore the internal structure details of the flow. This application is valid according to four main principles:

1. the flow height is small with respect to its length or width (shallow water conditions),
2. the density is constant and thus it can be equated to the mean density of the flow ($\rho \simeq \bar{\rho}$),
3. no mass variations over time are taken into account ($\frac{dm}{dt} = 0$). m stands for the total mass and thus the erosion and deposition processes are not considered.
4. normal stresses are proportional ($\sigma_{xx} = k\sigma_{yy}$)

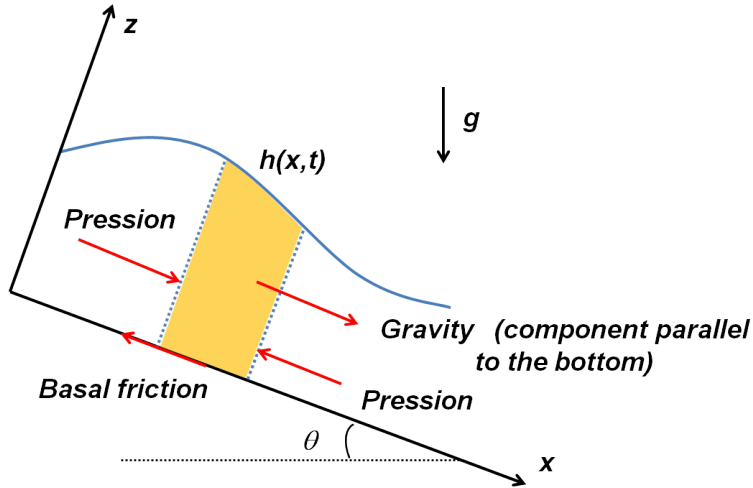


Figure 1.2: Mass and momentum equations averaged on the flow depth are applied to a control volume based on 3 main factors: pressure forces, gravity and basal friction.

Therefore, in relation to a control volume of the flow, as shown in Fig.1.2, the mass and momentum equations averaged on the flow depth become:

$$\frac{\partial h}{\partial t} + \frac{\partial h\bar{u}}{\partial x} = 0 \quad (1.1)$$

$$\bar{\rho} \left(\frac{\partial h\bar{u}}{\partial t} + \beta_u \frac{\partial h\bar{u}^2}{\partial x} \right) = \bar{\rho}gh \cos \theta \left(\tan \theta - \mu^* - k \frac{\partial h}{\partial x} \right) \quad (1.2)$$

where h is the flow height and \bar{u} its mean depth-averaged velocity. β_u represents the Boussinesq coefficient ($\beta_u = \frac{\bar{u}^2}{u^2}$) and k the earth pressure coefficient. As shown in Fig.1.2, the three main factors that act upon the flow block are gravity ($\bar{\rho}gh \sin \theta$), pressure gradient ($\bar{\rho}gh \cos \theta k \frac{\partial h}{\partial x}$) and basal friction ($\bar{\rho}gh \cos \theta \mu^*$). When averaging the equations over the flow depth, in-depth knowledge of the internal structure of the avalanche becomes no longer necessary, on the condition that the friction coefficient μ^* and the related friction law are clearly known. The first model for friction law applied to snow avalanche representation is the Mohr-Coulomb model. This model considers the friction coefficient as a function of the slope, constant and equal to:

$$\mu^*(\bar{u}, h) = \mu = \tan \theta_c \quad (1.3)$$

where θ_c represents a critical slope angle. Beyond θ_c , the avalanche starts flowing, and nothing moves below θ_c . In the 1950s, a new friction model was proposed by Voellmy. It consisted of a revision of the Mohr-Coulomb model, taking into account a constant component of μ^* while introducing an additional factor in order to consider the turbulent dissipation occurring in the flow. This new friction laws became:

$$\mu^*(\bar{u}, h) = \mu_c + \frac{\bar{u}^2}{\xi h} = \mu_c + \frac{g}{\xi} Fr^2 \quad (1.4)$$

μ_c and ξ represent two parameters adjusted with respect to real-scale avalanches [134]. μ_c is related to the type of snow and ξ is related to the flow configuration and the bottom roughness [1]. The Froude number is defined as

$$Fr = \frac{\bar{u}}{\sqrt{gh}} \quad (1.5)$$

and is derived from Eq.(1.2). It consists of a dimensionless number representing the ratio of inertial forces to gravity forces, and it is commonly used to compare flows on different scales. The initial system of equations (Eq.(1.1) and (1.2)) could also be solved in terms of viscosity, instead of friction. The term $\mu_* \rho gh \cos \theta$ could be replaced by $\tau_c + \eta \frac{\bar{u}}{h}$ where τ_c is the yield stress and η the viscosity. However, viscosity is a complex factor when dealing with snow due to its discrete granular structure (except for wet snow [110]) and thus we determined friction to be more conducive to this work. This is actually one of the reasons why, in the following sections, we decided to work with dry granular material.

Although the Voellmy friction model is not the only model, it is actually the most commonly used for this type of modelling. Results from the depth-averaged equations combined with a friction model highly depend on the friction law. The Boussinesq coefficient β_u and the earth pressure coefficient k complete the key parameters required to solve the equation system. Field measurements are needed in order to obtain these parameters. There are two main types of field measurements: in-situ small-scale models using real snow, and real-scale avalanche sites.

i) In-situ small-scale models

There are four main sites, in France (Col du Lac Blanc), Switzerland (Weissfluhjoch), India (Manali) and Japan (Shinjo chute). They consist of experimental chutes equipped with height, velocity and pressure sensors, where real snow flows inside (see Fig.1.3).

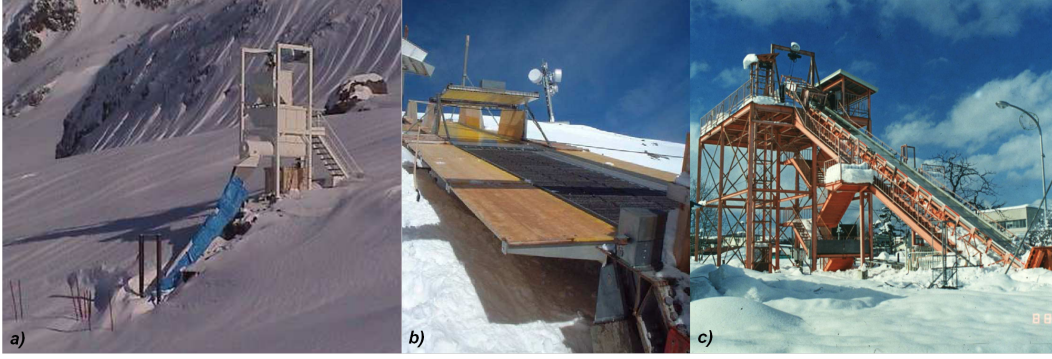


Figure 1.3: Some of the experimental sites for in-situ small-scale models: (a) Col du Lac Blanc, France, (b) Weissfluhjoch, Switzerland and (c) Shinjo chute, Japan (photo courtesy of O. Abe, Shinjo branch, snow and ice research center).

Much work has been conducted on the rheology of dense snow flows [23, 128, 131] at the Col du Lac Blanc site. A chute of ten metres in length with a variable inclination angle (29° - 45°) receives a constant snow flow rate from a supply device. Sensors were installed in order to measure the flow height, the velocity profile, and the normal and shear forces at the bottom. The achieved measurements highlighted three main regimes for constant and steady supply conditions:

1. an *accelerate regime* for slope angles above 42° , associated with an increase of the mean velocity along the channel with a decrease of the flow height ($\frac{\partial \bar{u}}{\partial x} > 0$ and $\frac{\partial h}{\partial x} < 0$);
2. a *decelerating regime* below 33° related to a decrease of the mean velocity and an increase of the flow height along the channel axis ($\frac{\partial \bar{u}}{\partial x} < 0$ and $\frac{\partial h}{\partial x} > 0$);
3. an *uniform regime* between these two critical angles characterized by a constant value of the velocity and depth gradients along the x -axis ($\frac{\partial \bar{u}}{\partial x} = 0$ and $\frac{\partial h}{\partial x} = 0$).

These three regimes are defined by two characteristic angles θ_{min} and θ_{max} . θ_{min} represents the limit between the uniform and the decelerating regimes, while beyond θ_{max} , the uniform regime becomes an accelerating regime. More details on these two angles are given in section 1.1.2.

The in-situ small-scale results of the Col du Lac Blanc [23, 128, 131] were confirmed by Sovilla et al. (2010) [147] with data collected from the deposits of two avalanches released at the Vallée de La Sionne test site. The avalanche deposit height is associated with the h_{stop} function which defines the θ_{min} and θ_{max} angles. More details on this function are provided in section 1.1.2. Small-scale tests at Col du Lac Blanc were filmed and image analysis showed the formation of snow aggregates occurring during the flow. In addition, velocity sensors placed at different heights presented a bi-shaped velocity profile consistent with previous studies [92, 93]. As shown in Fig.1.4, this profile is characterised by a thin, highly sheared basal layer and a much less sheared upper layer.

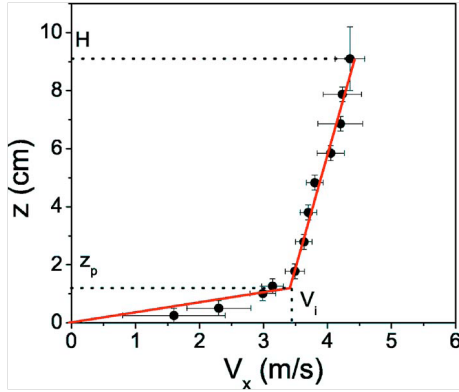


Figure 1.4: Typical bi-sheared velocity profile obtained from in-situ small-scale experiments [128].

ii) Real-scale avalanche triggering

The in-situ study of artificially triggered real-scale avalanches is difficult. Aside from the dangers related to snow avalanches, artificial triggering is dependent on snow and weather conditions which lead to few chances of success and thus few sets of available data. However there are experimental sites in different European countries (France, Italy, Norway, Switzerland), as well as in Russia, the United States and Japan. The French experimental site (see Fig.1.5) is located at the Col du Lautaret (2058 m a.s.l.).

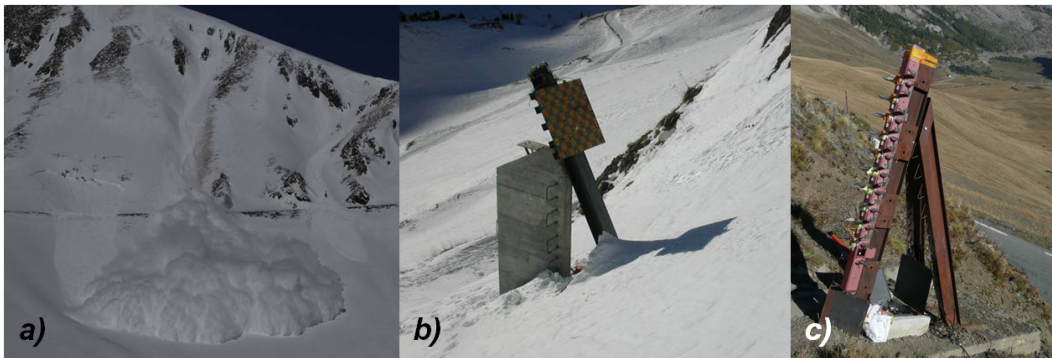


Figure 1.5: French experimental site at the Col du Lautaret: (a) released avalanche, (b) pressure measurements plate and (c) pylon with velocity, height and force sensors.

These sites are equipped for measuring the height of the avalanche $h(t)$, the velocity $u(t)$ and the pressure exerted on an obstacle $P(t)$. Density measurements are difficult to procure (under work at Vallée de La Sionne). Previous studies identified three main parts that form a dense snow avalanche: (i) a very turbulent front, (ii) a dense main body and (iii) a tail [55]. These three parts behave differently during the flow, and their features will be treated in the following sections. Through certain experimental sites, several studies were conducted on the velocity profile of real-scale avalanches [48, 92, 148] and connections were found with the bi-shaped velocity profile obtained from snow chutes [93, 128]. The Froude number of triggered avalanches can be calculated through the flow height and its mean velocity. Typical Froude numbers for dense avalanches of dry snow range from 1 to 5. The avalanche final deposit represents another source of compelling information. The observation of the deposit reveals the presence of snow aggregates of all sizes (from millimetres to metres). These aggregates develop due to shear stress at the bottom of the body phase of the flow. Recent studies [15, 128, 131, 147] showed a link between the flow dynamics and the process of aggregate formation.

All of these results highlighting the formation and presence of aggregates also demonstrate the granular nature of these processes. The next sections deal with granular flows. Some analogies with snow flows are discussed, and then summarized in section 1.1.3.

1.1.2 Granular flows: characteristics and modelling

The last 25 years have been characterised by a constant increase in the use of granular materials to simulate a wide variety of phenomena. Snow avalanches represent one of the research fields that benefitted from the results obtained through the use of granular materials. The main problem with grains is the lack of a constitutive law: under different circumstances, their behaviour can be completely different.

Regardless, previous studies [85] have defined three main regimes related to granular materials: quasi-static, collisional, and dense regimes.

1. *Quasi-static regime* is characterised by slow deformations due to inter-grain contact. Deformations are controlled by grain friction and some strain can develop over long distances forming force networks [42].
2. *Collisional regime*, different from the quasi-static regime, is where deformations occur because of grain excitation that leads to collisions. The kinetic energy is high and constitutive equations are directly derived from the gas kinetic theory [12, 64, 70, 86].
3. *Dense regime*, represents a regime in-between the two previous ones. Due to their fluid-like behaviour, both grain friction and collisions influence the rheology of the material. Temporary force networks can develop. Many studies have been conducted on this subject [50, 63, 119, 120, 122, 143, 144].

The research work presented in this chapter made use of mono-disperse and dry granular material. This implies that all grains have the same size and that cohesion is not relevant.

To handle such a material, we based our work on the results from two important publications: *On dense granular flows* (GDR MiDi, 2004) and *Flows of Dense Granular Media* (Forterre and Pouliquen, 2008).

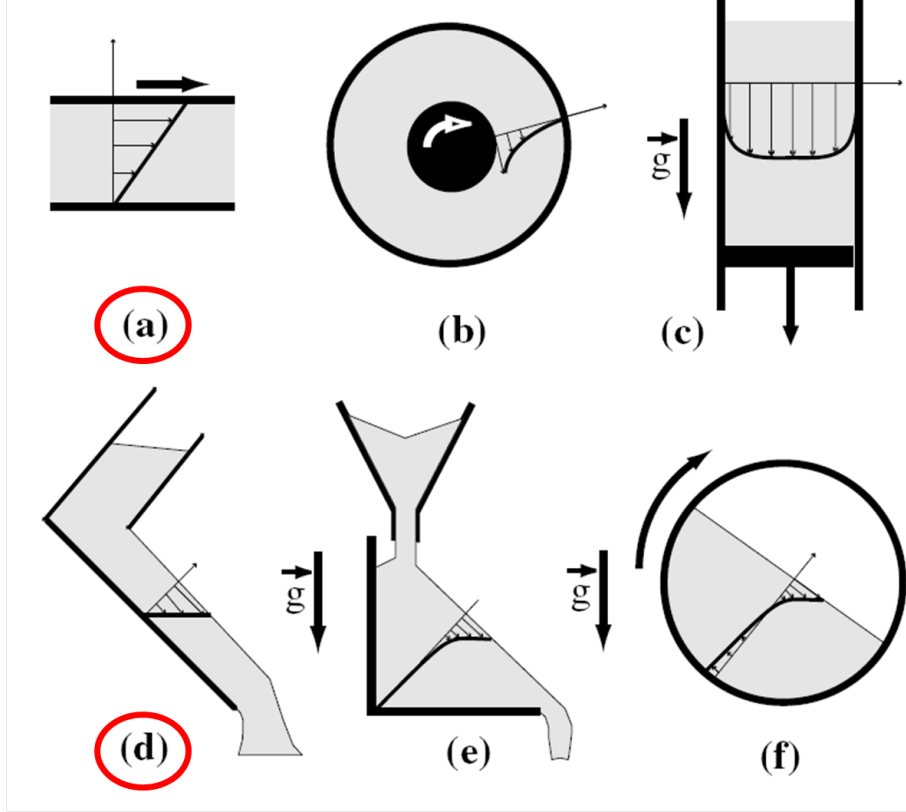


Figure 1.6: Different flow configurations: (a) plane shear, (b) annular shear, (c) vertical chute, (d) inclined plane, (e) heap flow and (f) rotating drum. Images are taken from [63]. Only the two configurations circled in red (a and d) were considered.

In GDR MiDi (2004), several configurations of flow set-ups were considered (see Fig.1.6). Two of them in particular are crucial for this study: a plane shear configuration in order to derive a local rheology for the material, and an inclined plane configuration because it represents the flow condition during experimental tests. The description of these two flow configurations will follow. They are extracted from [63].

a) Plane shear

Fig.1.7.a shows the set-up. The flow is confined between two parallel rough walls at a distance H_{ps} . An horizontal velocity u_H is imposed upon the upper wall in order to start the motion. Gravity is not included and numerical simulations are therefore needed to represent this case. The confining pressure P and the shear rate $\dot{\gamma}$ are controlled, and the strain rate τ and volume fraction ϕ are calculated [43, 44]. A dimensionless number is defined in order to describe the importance of inertia relative to confining forces [63]:

$$I = \frac{\dot{\gamma}d}{\sqrt{\frac{P}{\rho_p}}} \quad (1.6)$$

I is called the *inertial number* and it represents the ratio between two characteristic time scales. A time of macroscopic deformation is associated with the shear rate of the system ($1/\dot{\gamma}$) and a microscopic time scale is related to the rearrangement of particles subjected to a constant pressure ($\sqrt{\frac{d^2\rho_p}{P}}$). I represents the inertia of the system and it defines the three regimes introduced above. Values of $I < 10^{-3}$ correspond to the quasi-static regime. Increasing I causes the

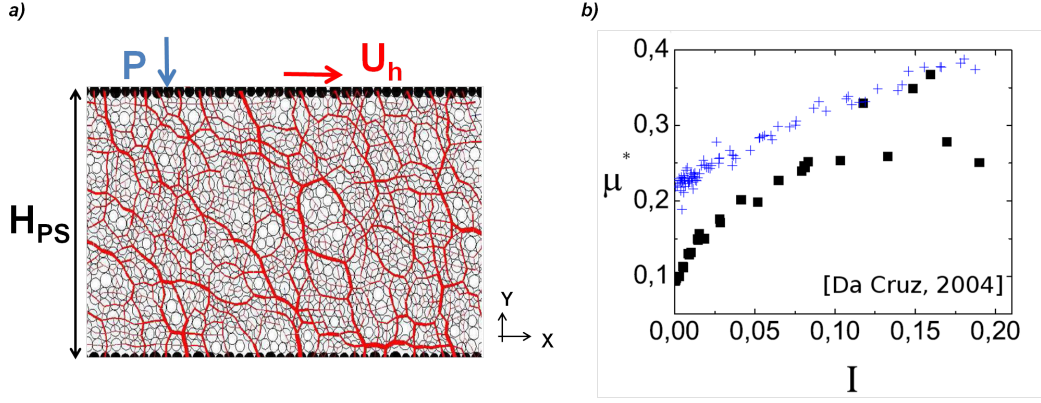


Figure 1.7: (a) Plane shear set-up for discrete numerical simulations. (b) Friction law. Both images are taken from [43].

volume fraction to decrease, grain contact to decrease, and collisions to start occurring. The dense regime is characterised by an inertial number ranging from 10^{-2} to 10^{-1} . $I > 10^{-1}$ that represents the threshold for a collisional regime. Additionally, I influences the strain ratio:

$$\frac{\tau}{P} = \mu^*(I) \quad (1.7)$$

Due to this dependency, two laws can be derived to describe the behaviour of granular materials flowing in a plane shear configuration. A law for volume fraction:

$$\phi \simeq \phi_{max} - a_\phi I \quad (1.8)$$

and a law for friction:

$$\mu^* \simeq \mu_{min}^* + b_\mu I \quad (1.9)$$

where a_ϕ and b_μ are two empirical coefficients and μ_{min}^* corresponds to the friction factor for quasi-static regimes. Fig.1.7.b represents the behaviour of friction as a function of the inertial number. For high values of I (collisional regime), the friction coefficient tends to stabilize at a constant value.

Equation (1.7), combined with the obtained friction law, allows the definition of the shear strain as

$$\tau \simeq \mu_{min}^* P + b \sqrt{\rho_p P} \dot{\gamma} d \quad (1.10)$$

Consequently, as P and τ are constant, $\mu^*(I)$ is constant and thus the inertial number is constant over the flow depth, leading to a linear velocity profile.

b) Inclined plane

In this configuration the granular material flows down a rough incline due to the effect of gravity. Two main parameters influence the flow, the incline slope θ and the flow rate Q .

One of the most relevant features of a granular material is its flow threshold. A horizontal grain layer of initial height h_{start} starts flowing as the plane incline increases beyond a critical angle θ_{start} (flow threshold), and it flows downward until the slope is decreased below a second critical value θ_{stop} . This threshold can be similarly expressed in terms of height. A particle layer of initial height h_{start} flows down an incline at a different fixed slope and the final deposit height h_{stop} is measured. The curve representing h_{stop} as a function of the slope angle defines two angles that are characteristic of granular material, θ_{min} and θ_{max} .

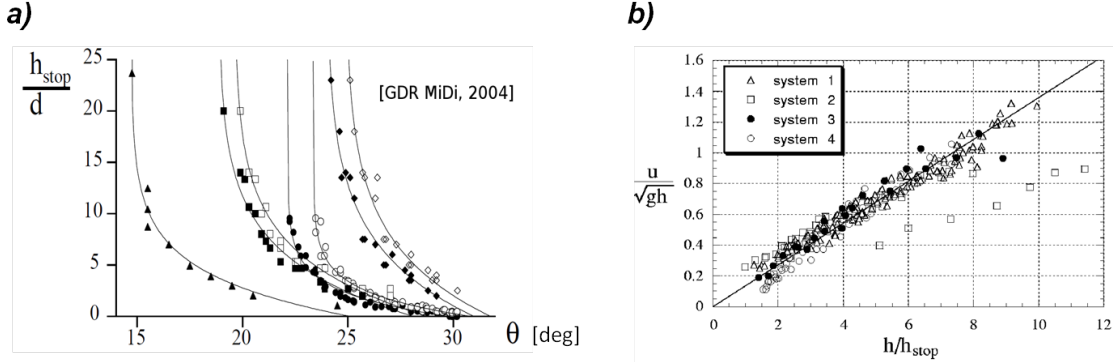


Figure 1.8: Results from laboratory tests: (a) behaviour of $h_{stop}(\theta)$, black symbols, and $h_{start}(\theta)$, white symbols, for different materials. Black triangles result from numerical simulations. (b) Froude number versus the dimensionless flow depth. Data obtained from experiments with different materials and varying slopes [119].

According to Fig.1.8.a, for a chosen granular material, the two angles can be identified. When $h_{stop}(\theta) \rightarrow 0$, θ_{max} is set, the flow enters an accelerating regime, and no final deposit is found on the incline as all the material flows downward. On the contrary, $h_{stop}(\theta) \rightarrow \infty$ represents a stand-still state. The slope is too low to start the motion. θ_{min} is therefore determined. θ_{min} and θ_{max} refer to the effective friction coefficients associated with quasi-static deformation and rapid collisional flows, respectively. Below the θ_{min} angle, the flow slows down and stops, while the granular avalanche accelerates above θ_{max} . Between θ_{min} and θ_{max} the uniform flow condition can be reached.

The experimental curve $h_{stop}(\theta)$ is effectively reproduced by the function

$$\frac{h_{stop}(\theta)}{d} = B \frac{\tan \theta_{min} - \tan \theta}{\tan \theta - \tan \theta_{max}} \quad (1.11)$$

where d is the diameter of the grains and B is a dimensionless value. θ_{min} , θ_{max} and B depend on the granular material and on the bottom roughness [65, 66, 119].

Some observations must be made regarding friction. A constant friction factor (from the Mohr-Coulomb model) is appropriate for a completely smooth incline, but not for a rough bottom. Indeed, if $\mu = \tan \theta = const$, this means that a uniform flow can only be obtained at a single slope angle. However, laboratory tests showed that this is possible within a range of slopes ($\theta_{min} < \theta < \theta_{max}$).

An experimental study [63] was therefore carried out in order to determine a more complex rheology relating the friction coefficient to the height and the mean velocity of the flow ($\mu^* = f(h, \bar{u})$). This would allow the definition of a scaling law for steady and uniform granular flows, as long as measurements of the height and velocity of the flow establish a linear relationship between the Froude number Fr and the ratio h/h_{stop} (see Fig.1.8.b):

$$Fr = \Lambda + \nu \frac{h}{h_{stop}} \quad (1.12)$$

where Λ and ν are empirical coefficients respective to the given material. Additionally, a study concerning the vertical velocity profile inside the flow proved that a Bagnold profile ($u \propto h^{3/2}$) is established (see Fig.1.9.a) for granular flows with a height larger than h_{stop} . This is not the case for shallow flows characterised by a linear velocity profile. Furthermore, tests showed that the volume fraction ϕ is constant with the flow height and that it drops downward, close to the free surface, as shown in Fig.1.9.b.

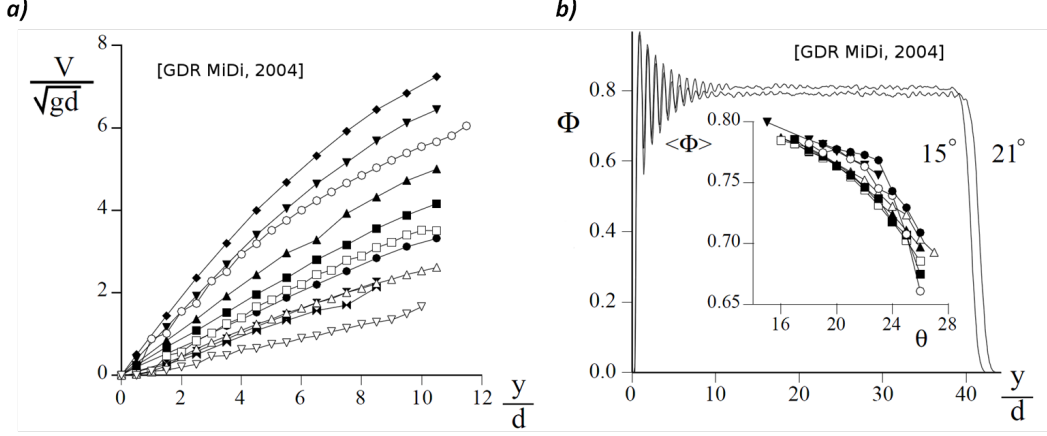


Figure 1.9: (a) Velocity profiles for shallow water flows and (b) volume fraction behaviour over the flow thickness [63].

When applying the local rheology established for the plane shear from the inclined plane configuration, the strain equilibrium associated with a volume fraction constant over the flow height gives:

$$P = \rho_p g \phi (h - z) \cos \theta \quad (1.13)$$

$$\tau = \rho_p g \phi (h - z) \sin \theta \quad (1.14)$$

which leads to a strain ratio $P/\tau = \tan \theta$ controlled by the slope angle. The equation (1.13) combined with the definition of the inertial number (Eq.(1.6)) leads to a shear rate $\dot{\gamma}$:

$$\dot{\gamma}(z, \theta) = I(\theta) \frac{\sqrt{\phi g (h - z) \cos \theta}}{d} \quad (1.15)$$

which, integrated with the flow height, gives a function for the velocity

$$u(z, \theta) = \frac{2}{3} I(\theta) \sqrt{\phi \cos \theta} \frac{[h^{3/2} - (h - z)^{3/2}]}{d} \quad (1.16)$$

If defining a mean velocity $\bar{u} = \frac{1}{h} \int_0^h u(z) dz$, Eq.(1.16) becomes

$$\frac{\bar{u}}{\sqrt{gh}} = \frac{2}{5} I(\theta) \sqrt{\phi \cos \theta} \frac{h}{d} \quad (1.17)$$

Finally, combining Eq.(1.11), Eq.(1.12) and Eq.(1.17), the effective friction μ^* can be written as a function of the inertial number I [88]:

$$\mu^*(I) = \mu_1 + \frac{\mu_2 - \mu_1}{\frac{I_0}{I} + 1} \quad (1.18)$$

where $\mu_1 = \tan \theta_{min}$, $\mu_2 = \tan \theta_{max}$ et $I_0 = \frac{5\nu}{2B\sqrt{\phi \cos \theta}}$. This friction law, as shown in Fig.1.10 reproduces the experimental data very accurately.

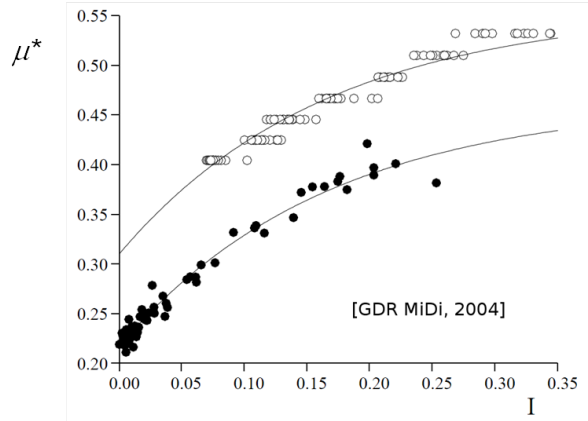


Figure 1.10: Effective basal friction versus the inertial number for the plane shear configuration (●) and the inclined plane (○).

Granular flows: the influence of poly-dispersity and cohesion

Small-scale physical simulations using mono-disperse flows are far from the reproduction of an actual avalanche. Nevertheless, experimental tests introducing poly-dispersity can be very complex. Numerical simulations simplify this task. Rognon et al. [129, 130] studied the influence of cohesion and poly-dispersity on a granular flow.

Modelling a bi-disperse cohesionless flow showed that the range of slope inclines that are able to reach a uniform flow varies and that this influence depends on the dispersity rate. Tests were made using two different sizes of frictional cohesionless disks (corresponding to two-dimensional grains). The dispersity rate is characterised by two dimensionless numbers (D_r and S_r), one related to the surface ratio between the two sizes of disks and the other expressing the areal proportion of large grains. Plus, friction measurements gathered at the bottom of the flow proved that the friction law obtained for mono-disperse flows still works with poly-dispersity:

$$\mu^*(I, S_r, D_r) \simeq \mu_{min}^*(S_r, D_r) - b(S_r, D_r) I \quad (1.19)$$

Other studies have investigated the influence of cohesion in a granular mono-disperse flow [28, 130]. Numerical simulations introduced a cohesion factor represented by an attractive force $N_a(h)$ which is taken into account through the contact law. A dimensionless number is defined to measure the cohesion rate:

$$\eta = \frac{N_c}{Pd} \quad (1.20)$$

where N_c is the maximum value of the attractive force, P represents the normal force acting on grains due to pressure and d is the grains' mean diameter.

As for poly-dispersity, cohesion influences the values of θ_{min} and θ_{max} as well as the local rheology of the flow. The friction law remains valid, but it highly depends on η

$$\mu^*(I, \eta) \simeq \mu_{min}^*(\eta) - b(\eta) I \quad (1.21)$$

Pressure forces increase as the bottom is approached, and the value of η therefore decreases. Its maximum is at the flow surface where the formation of aggregates is maximum.

Figure 1.11 shows the influence of poly-dispersity and cohesion on the velocity profiles.

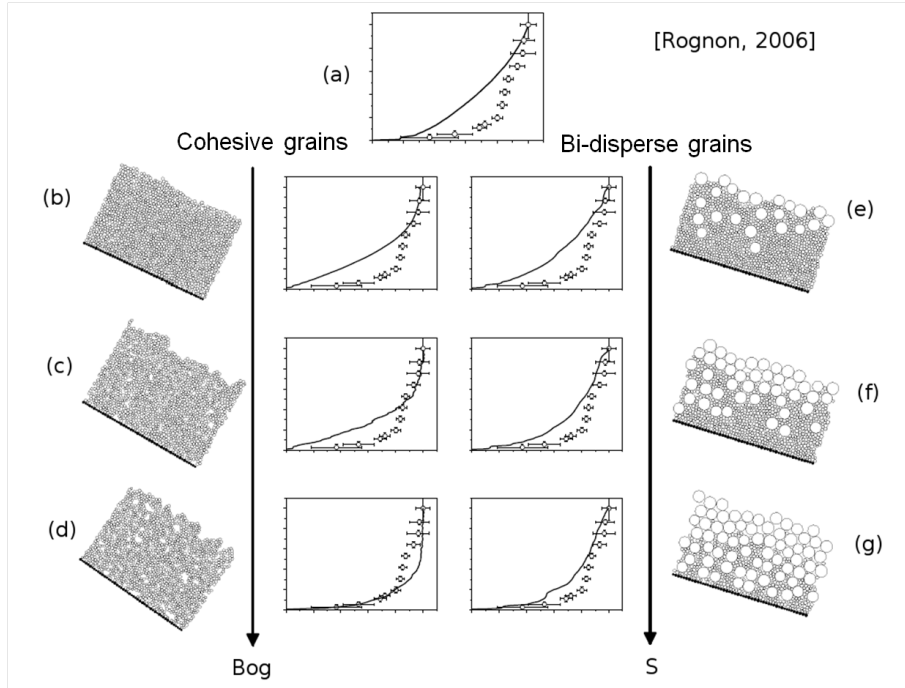


Figure 1.11: Velocity profiles along the flow thickness obtained from small-scale snow experiments (\circ) and numerical simulations ($-$). (a) non cohesive and mono-disperse material compared to: (b), (c) and (d) mono-disperse grains with an increasing cohesion rate, (e), (f) and (g) non cohesive grains with an increasing bi-dispersity rate.

Recently, the work of Marks et al. (2012) [102] represented a promising outcome from the analytical modelling of poly-dispersed flows. These flows are composed of particles of various sizes and the evolution of the grain size distribution throughout the flow is explained through mass and momentum conservation. By coupling this theory with a simple constitutive law, the kinematics of the flow that depend on the dynamics of the grains' sizes can be predicted.

This section described the main features of granular flow behaviour. Some relevant comparisons emerged in relation to snow flows, and they are summarised in the next section.

1.1.3 Why use a granular material to model a dense snow avalanche?

The previous two sections dealt with the characteristics of snow flows and those of granular flows. This section aims to summarise and highlight similarities between the two materials in order to show the reasons that led to the choice of modelling a dense snow avalanche through mono-disperse cohesionless grains. Commonalities can be organised into three categories: visual, rheological and dynamic similarities.

1. **Visual aspect:** when looking at an avalanche deposit (see Fig.1.12), it is obvious that the snow has a natural aptitude to aggregate and create larger particles. These aggregates can be approximated to grains with a diameter varying from centimetres to metres [15, 47].



Figure 1.12: Snow avalanche deposits: (a) image from Ancey (2006) [7], (b) image from Bartelt and McArdell (2009) [15] and (c) photo H. Bellot (Taconnaz, 2010). Observations indicate the granular nature of the snow.

2. ***Rheology:*** as explained in the previous sections, both the granular materials and the snow are characterised by two flow thresholds that correspond to two critical slopes, θ_{min} and θ_{max} . These two angles define the boundaries between decelerating, uniform and accelerating regimes. For granular material, these critical angles are related to the value h_{stop} depending on the slope angle. This correlation (see Eq.(1.11)) was also found for actual snow cases [147].
3. ***Dynamics:*** considering the obtained velocity profiles, tests performed on snow chutes [128, 131] and real-scale avalanche sites [92, 93, 148] yielded a bi-sheared profile. The same type of profile is obtained from numerical simulations when modelling an avalanche through a cohesive or bi-disperse granular flow [128].

As a result of the above considerations and due to similarities existing between the actual snow flows and granular flows, we decided to carry out small-scale experiments using granular material. Although we are aware that this is a simplification, we confined our research to mono-disperse granular beads as has already been done in previous works [54, 57, 75]. The flow interaction with an obstacle complicates matters. Some work has already been carried out with poly-disperse flows but without obstacles [67, 102]. Thus, for the sake of simplicity, mono-dispersed granular beads will be used to simulate small-scale dense snow avalanches interacting with an obstacle. The next section provides insight into present understanding of the flow - obstacle interaction.

1.1.4 Avalanche - obstacle interaction

The study of the interaction between the avalanche flow and an obstacle requires thorough knowledge of avalanche dynamics as well as the structure behaviour. This interaction can be seen from two different points of view: the influence of an obstacle on the flow and, conversely, the influence of the flow on the obstacle. Several studies have been conducted in both fields, combining three common approaches: the in-situ observation, small-scale simulations and numerical modelling. Modelling is often based on shallow water equations and led in relation to water comparisons.

The aim of this section is to give a general overview of these subjects.

The influence of an obstacle on the flow behaviour: flow regimes

As mentioned in the introduction, multiple types of protection structures exist depending on the protection purpose. For permanent-passive protection, different solutions are associated with different flow behaviours affected by the presence of a structure. There are three main solutions:

- **Deviation dams [58, 68, 77, 81, 151]:** aiming to deviate the flow from its natural path, deviation dams cause a rapid change in the flow height and velocity. This variation creates oblique shock waves, treated in accordance with shock wave theory.
- **Breaking (or retarding) mounds [40, 77, 140]:** designed to dissipate the flow energy, breaking mounds can lead to the rise of shock waves, as in the case of deviation dams. Or, if the structure is overcome, a jet can occur. In this case, the flow covers a ballistic trajectory.
- **Catching dams [41, 51, 54, 62, 108]:** more attention will be paid to this scenario as it represents the main configuration considered through small-scale experiments.

The modelling of the flow / obstacle interaction is based on the Saint Venant equations and flow dimensions are therefore averaged through depth. The Froude number is used to characterise the flow and two additional dimensionless numbers are defined to introduce the presence of the obstacle:

$$A_{obs} = \frac{H_{obs}}{h} \quad (1.22)$$

$$Fr_{obs} = \frac{\bar{u}}{\sqrt{gH_{obs} \cos \theta}} \quad (1.23)$$

where A_{obs} refers to the aspect ratio of the obstacle and Fr_{obs} its Froude number ($Fr_{obs}^2 = Fr^2/A_{obs}$).

These three parameters define different flow regimes associated with different flow behaviours (see Fig.1.13):

i) when the Froude number is typically greater than 2 – 3 and $H_{obs} \gg h$ a **granular jump** occurs (Fig.1.13.a). It is possible to define a relationship that describes experimental observations by using the equations for the hydraulic jump combined with the mass and momentum equations [75, 77]:

$$\frac{h_2}{h_1} = \frac{1}{2} \left(\sqrt{1 + 8Fr} - 1 \right) \quad (1.24)$$

From this relationship, it is possible to derive the critical height H_{obs}^{cr} of an obstacle that causes to a hydraulic jump (for frictionless fluids on a horizontal slope and for a fixed incoming flow height h):

$$\frac{H_{obs}^{cr}}{h} = A_{obs}^{cr} = \frac{1}{2} \left(\sqrt{1 + 8Fr} - 1 \right) - Fr^{2/3} \quad (1.25)$$

ii) if $Fr < 1$, the flow is blocked and all the material is stored uphill from the dam.

iii) if Fr is high enough and $H_{obs} < H_{obs}^{cr}$, a quasi-steady **granular jet** occurs [76, 77, 78]. A jet is characterised by high kinetic energy and its trajectory is described by ballistic equations. The influence of the jet on the flow uphill from the obstacle is rather irrelevant while its influence downhill is important (see Fig.1.13.b).

The transition between a granular jump and a downhill jet was previously studied in the frame of debris flows by Armanini and Scotton (1992) [10] and Armanini (1997) [9]. A mixture of granular material and water flows in a tilted flume at the end of which a vertical gate was placed. Two types of impact were observed, related to different viscosities of the mixture: (*i*) a fluid with low internal global viscosity was completely deviated and formed a jet while, (*ii*)

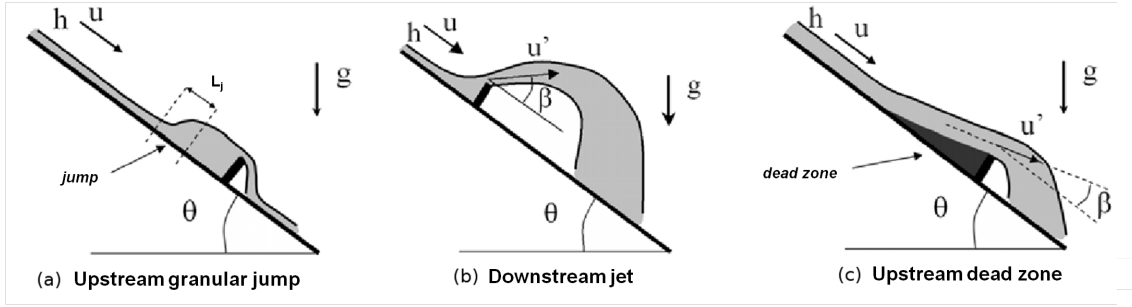


Figure 1.13: Different regimes occurring during the flow-obstacle interaction (sketches are taken from [56]).

when internal friction prevailed, a reflected wave formed and was propelled upwards.

iv) if $H_{obs} \simeq h$, a **dead zone** raises [55]. This condition represents a common situation when dealing with avalanche protection structures such as catching dams, which is why the formation and behaviour of the dead zone uphill from the obstacle is one of the key topics treated in this chapter. The dead zone corresponds to a quasi-static part of the flow blocked uphill from the obstacle which is typically combined with an inertial layer flowing above. Together, these two parts constitute the influence zone (more details are given in section 1.2.2) and characterise a dead zone regime (see Fig.1.13.c). A jet can occur downhill from the obstacle. Laboratory experiments showed that a dead zone regime, under certain conditions, can turn into a granular jump regime. This transition is still not understood very well. A part of this chapter is dedicated to the analysis of the dead zone to granular jump transition and aims to improve current knowledge by providing new experimental results.

Laboratory tests were thus conducted using an obstacle with a height value of the same order of the incoming flow height ($H_{obs} \approx h$). Obtained Froude numbers range from 1 to 7.

The influence of the flow on the obstacle behaviour: impact pressure

To understand what type of influence an avalanche flow can exert on an obstacle, it is necessary to understand the characteristics of the incoming flow and those related to the structure behaviour upon impact. This part only deals with the current knowledge on the incoming flow features since structural mechanics are beyond the scope of this work, and it overall addresses the pressure that the flow can exert on the obstacle during the impact.

The total exerted pressure P can be divided into at least two main contributions. A kinetic contribution P_{kin} related to an inertial regime and depending on the flow velocity, and a gravity contribution P_g related to a quasi-static regime, proportional to g and to the flow height h . Typically:

$$P = C_d P_{kin} + k P_g = C_d \frac{1}{2} \rho u^2 + k \frac{1}{2} \rho g h \quad (1.26)$$

where k is the earth pressure coefficient and C_d stands for the drag coefficient which takes into account the contribution of vertical velocities (generally unknown) and the fluctuations around the mean pressure value.

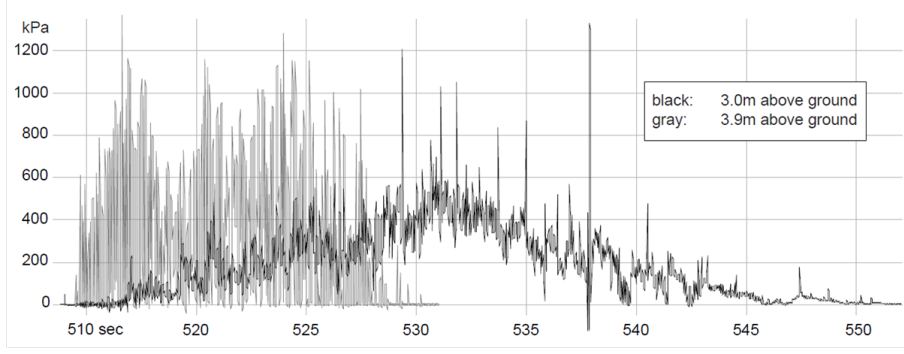


Figure 1.14: Pressure signal obtained at the avalanche experimental site in La Sionne, Switzerland (B. Sovilla).

Figure 1.14 shows a typical time-dependent pressure signal measured during an avalanche. When considering the mean pressure, measured values are rounded. This means that the design pressure can be underestimated because the maximum of the mean pressure will most likely be weaker than the measured maximum value. Some researchers, through comparison to viscous fluids, define an equivalent Reynolds number Re_{eq} for the flow, depending on the equivalent flow viscosity η_{eq} . Therefore, C_d depends on two parameters: the obstacle geometry (size and shape) and the flow regime associated with the equivalent Reynolds number [7, 14, 152]. C_d increases at low regimes of Re_{eq} .

Others function in terms of the Froude number Fr . Figure 1.15 illustrates the influence of the two contributions versus the flow Froude number.

By defining:

$$C_{eq} = \frac{P}{P_{kin}} = C_d + \frac{k}{Fr^2} \quad (1.27)$$

$$k_{eq} = \frac{P}{P_g} = k + C_d Fr^2 \quad (1.28)$$

we traced the C_{eq} and k_{eq} profiles for a case-scenario with $C_d = 1$ and $k = 1$. The graph shows that for high flow regimes (high Fr), the kinetic component is dominant. However, for low Froude numbers, even if the kinetic pressure decreases significantly, the total pressure exerted on the obstacle can still be relevant due to the force of gravity.

The classic design of protection structures is still based on rough guidelines, emphasising practice rather than theory, although recent practical and theoretical developments are available (see Barbolini et al., 2009 for snow avalanches [13]). The kinetic pressure is often considered as the only contribution defining the total pressure. This preliminary sketch highlights how the classic design procedure can underestimate impact pressures.

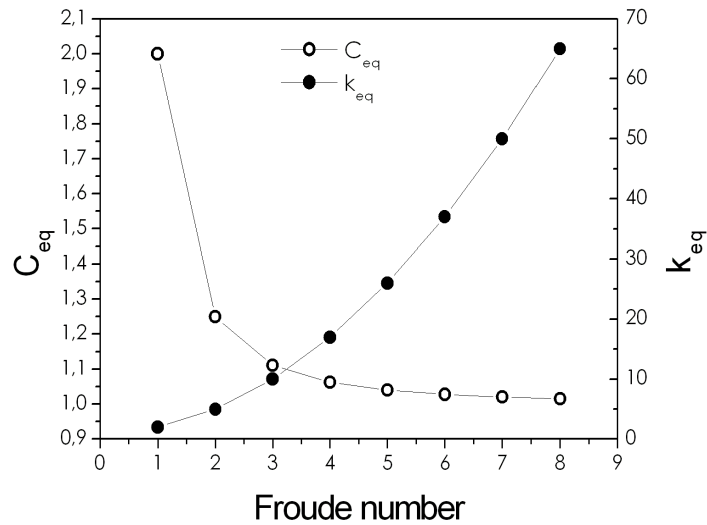


Figure 1.15: Influence of the two typical pressure contributions. The kinetic pressure associated with an inertial regime is dominant at high Froude numbers while the gravity contribution, related to the quasi-static regime, becomes significant for low values of Fr .

The first measurements carried out on real snow avalanches date back to the 1980s [89, 104, 112, 113, 117, 138] and they enhanced the understanding of avalanches' internal structure. More recent studies [14, 59, 62, 152] focussed on the analysis of C_d .

In the framework of granular material, the first studies are from Wieghardt [160, 161]. Recently, some work was conducted regarding granular flows in diluted and collisional regimes [96, 159]. Chanut [36] concentrated his attention on the forces induced by a granular flow impacting a wall when a dead zone is formed.

This work was led in the continuation of the PhD thesis of Chanut (2010) [36]. It deals with forces exerted by an avalanche upon impact with a wall-like protection structure and the effects of the obstacle on the flow regimes. Details are given throughout the following sections.

Section 1.2 describes the small-scale model set-up and the measurement techniques that were employed. Section 1.3 presents the results. Reference tests were performed first, and force measurements were then taken in the presence of two different wall geometries. Maximum and residual values were investigated and associated with different flow regimes. Finally, a detailed analysis of the influence zone behaviour was conducted. Section 1.4 introduces an analytical model to predict the force acting on a wall during the avalanche flow. This model was developed in relation to numerical simulations and is corroborated by laboratory experiment results. Section 1.5 concludes the chapter.

1.2 The inclined granular plane: method

This section deals with the granular incline plane developed at Irstea to study dense snow avalanches interacting with obstacles. Section 1.1.2 showed how granular materials can be used to carry out small-scale tests. By introducing certain assumptions, starting parameters can be controlled and simulations can be repeated as many times as needed. Section 1.2.1 describes the experimental device used for tests. Section 1.2.2 deals with the techniques chosen to gather measurements of the flow height, velocity, and impact force, as well as to investigate the behaviour of the influence zone.

1.2.1 Experimental device

In this section we consider the experimental device to include not only the incline that was used for tests, but also the granular material modelling the avalanche as well as the main tools necessary for gathering measurements. A description of all of these components is given in the following section.

The inclined plane

The experimental device shown in Fig.1.16.*a* was set-up in the framework of Chanut's PhD thesis (2010) [36]. It consists of an inclined plane on which a channel was mounted. The channel has a length of 1.3 m, its walls are made of Plexiglas, and its bottom is covered with sandpaper in order to provide some roughness ($d_{rough} \simeq 0.25$ mm). The width and the inclination of the channel can vary. The width was fixed at 0.25 m for all of the tests executed, and the slopes investigated ranged from 21° to 33° . Two pulley systems allow control of the plane incline and the opening of the reservoir gate. On top of the channel, a reservoir stores the granular material. The releasing system, as shown in Fig.1.16.*b*, is composed of two contiguous gates, one which is fixed and imposes the release height of the flow ($h_{rel}=35d$), and a sliding one that opens the reservoir and releases the granular avalanche. The opening time corresponds to $t = t_0$ and an electrical switch synchronises all measurements to t_0 .

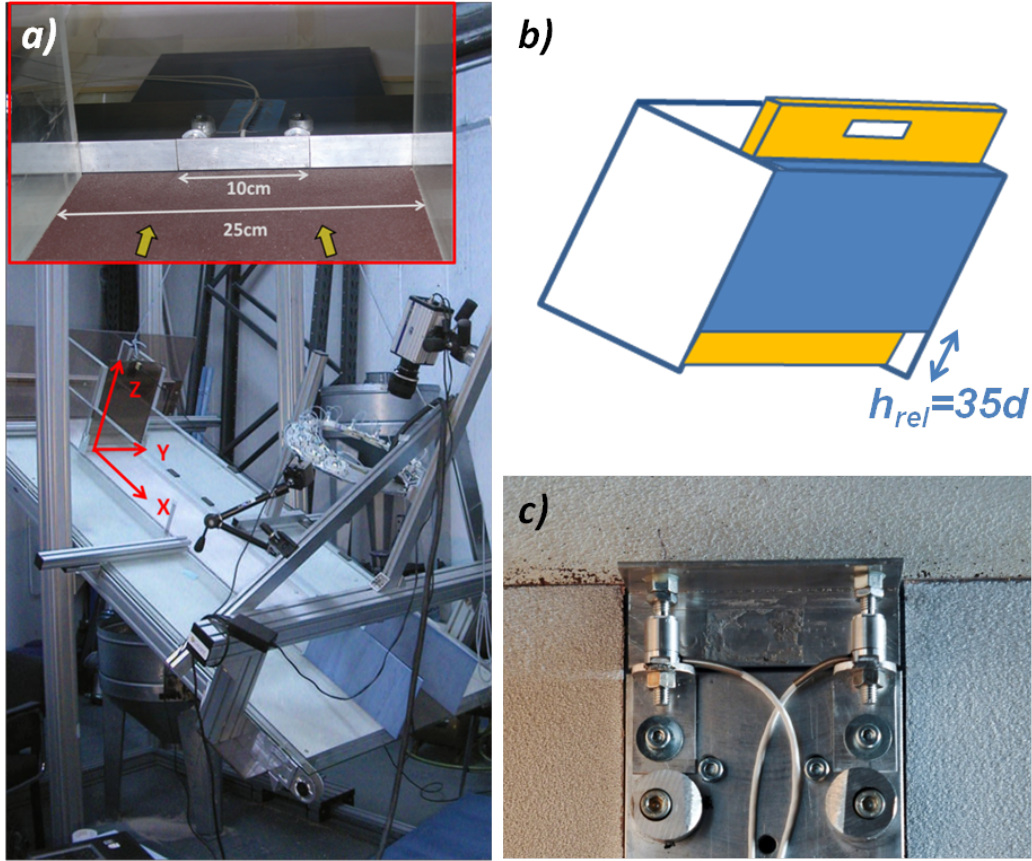


Figure 1.16: (a) Experimental device overview. The insert shows the wall-like obstacle: the wall spans the entire width of the channel, but only the central 10 cm are connected to the force sensors (and not in contact with the rest of the structure). Yellow arrows indicate the direction of the incoming flow. The reference system XYZ illustrated here will be maintained all throughout the chapter. (b) Reservoir releasing system. (c) Detail of the obstacle-sensors set-up. The obstacle in the picture represents the small obstacle (8 cm) allowing lateral flows.

The granular material

The granular material consists of mono-dispersed glass beads with a mean diameter of $d_{beads}=1$ mm ($d_{beads}=4d_{rough}$) and a density of $\rho_{beads}=2450$ kg m⁻³. The beads' mass is constant and equal to 9.2 kg. By analogy to previous numerical simulations, 9.2 kg is the mass of glass beads corresponding to the number of beads implemented in discrete numerical simulations. A volume fraction of 0.6 is assumed. This value is associated to a stand-still state as is the case for the beads in the reservoir.

As introduced in Section 1.1.2, granular materials are characterised by the two frictions angles θ_{min} and θ_{max} [63, 119]. These angles are defined by the function $h_{stop}(\theta)$, which is presented in Fig.1.17, and they were experimentally found equal to 20° and 28°, respectively.

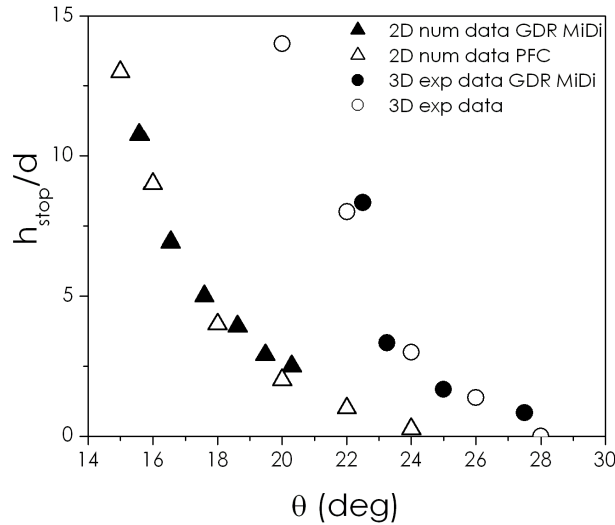


Figure 1.17: Function $h_{stop}(\theta)$. Triangles represent numerical results while circles stand for data obtained experimentally. θ_{min} and θ_{max} , for 3D laboratory conditions, were found equal to 20° and 28° , respectively.

This research aims to investigate the behaviour of granular avalanche dynamics on slopes ranging from $\theta=21^\circ$ (an angle very close to θ_{min}) up to $\theta=33^\circ$ (larger than θ_{max}) for each degree, in order to investigate both the dense uniform and the accelerating regime. Measurements were taken mainly on the flow velocity, the flow height, forces that the flow can exert upon impact with an obstacle, and on the uphill flow behaviour. An obstacle can be mounted at the end of the channel in order to measure the induced forces, and additional tools were required to take measurements. The measurement techniques are detailed in Section 1.2.2. In the following section, we describe the most important instruments necessary for carrying out and gathering the measurements.

High frequency video camera

Two different high frequency video cameras were utilised. Initially, an IDT XS-3 video camera was available. Due to the camera's features, image sequences were recorded at a very high frequency but stored on an internal memory device relatively small for the test's purpose. The higher the acquisition frequency was, a larger amount of data was recorded and the acquisition time available was therefore shorter. The highest acquisition frequency that was used is $f_{ac}=350$ fps for high slope inclines where the flow duration did not exceed 6 s. At low inclines, however, the flow duration reached 15 – 20 s, which limited the acquisition frequency at $f_{ac}=150$ fps. The maximum recording time is also function of the image size. The optimal size, in terms of measurement needs, was found to equal 10×10 cm ($\simeq 950 \times 950$ pix) for velocity and height measurements. A new video camera was later purchased. It consists of a Baumer *HXC13 – C* high frequency video camera. Its main advantage is the new wiring technology that allows data transfer between the camera and the computer in real time, which means much larger memory storage. Consequently, shorts as longer flows were recorded at an acquisition frequency fixed at $f_{ac}=350$ fps which allows a good compromise between a sufficient amount of data recorded and a reasonable size for the files obtained. Image sequences that are too heavy require a very long time to run treatment programs. Additionally, the new video camera allows better image resolution and a larger field of view which, in the case of the PIV method (see section 1.2.2), yields a better velocity profile. Cameras were placed looking down, normal to the channel bottom, or

side-angled pointing at the flow through the Plexiglas walls.

Laser

A class 3 Vector VLL laser was used to measure the flow height. VLL stands for Variable Line Length and this feature is its main advantage. Because of the VLL, by adjusting the laser distance from the surface, it is possible to double the length of the line varying the fan angle to spread the light from 30° ($L_{line}=1$ m) up to 80° ($L_{line}=2$ m). Plus, its small size ($L_{laser}=67$ mm, $d_{laser}=14$ mm) allows it to easily integrate the experimental set-up.

Obstacle

To measure the forces exerted on a structure by the flow, two different types of obstacles were considered. They both consist of a flat wall-like aluminium obstacle, one spanning the entire channel width (catching dam type) and the other allowing lateral flow (braking mound type). The two obstacles are 0.025 m high, 0.002 m wide, and the length is 0.25 m and 0.08 m, respectively. Two force sensors are connected to the obstacle on the downhill side.

Special attention is required for the obstacle set-up. In order to avoid problems related to natural frequencies during the flow/obstacle interaction, a detailed study was previously done on the structure vibration modes [36].

A system composed of the obstacle plus the two sensors was considered and modelled as a beam leaning on two springs as shown in Fig.1.18.a. Assuming that only small deformations occur, the equation for natural vibration frequencies can be written as:

$$f_n = \frac{(\beta_n L)^2}{2\pi} \sqrt{\frac{E\Psi}{\rho L^4}} \quad (1.29)$$

where β_n is the wave number ($\beta_n=(\frac{\rho\omega_n^2}{E\Psi})^{1/4}$), L is the beam length, E its Young modulus, Ψ the momentum of inertia and ρ is the material density. Equation (1.29) is derived from the equilibrium equation of the material strength theory setting the boundary conditions on the bending momentum M and the shear force N equal to:

$$M = E\psi \frac{\partial x^2}{\partial y^2} = 0 \quad (1.30)$$

$$N = \frac{dM}{dx} = E\psi \frac{\partial x^3}{\partial y^3} = k_s x \quad (1.31)$$

where k_s is the material stiffness coefficient.

Equation (1.29) leads to three main choices: the type of sensors, the shape of the obstacle, and its composition (more details can be found in [36]).

The XFTC300 sensors were chosen because of their elevated stiffness coefficient ($k_s=5 \times 10^{-6}$ N m⁻¹) and precision (MR = measure range = 0 – 20 N; linearity $\leq 0.005MR$; hysteresis $\leq 0.005MR$). A rectangular L -shape was chosen for its high momentum of inertia (3 times higher than a simple rectangular flat-shaped obstacle). With respect to Eq.(1.29), a high value of Ψ leads to high vibration frequencies. Since particles can impact the obstacle at very high frequency, we set the frequency threshold at $f_n > 2$ kHz. Lastly, three different materials were considered for the obstacle composition: carbon fiber, steel, and aluminium. Figure 1.18.b shows the frequency behaviour of the system *beam + XFTC300 sensors* as a function of the beam length.

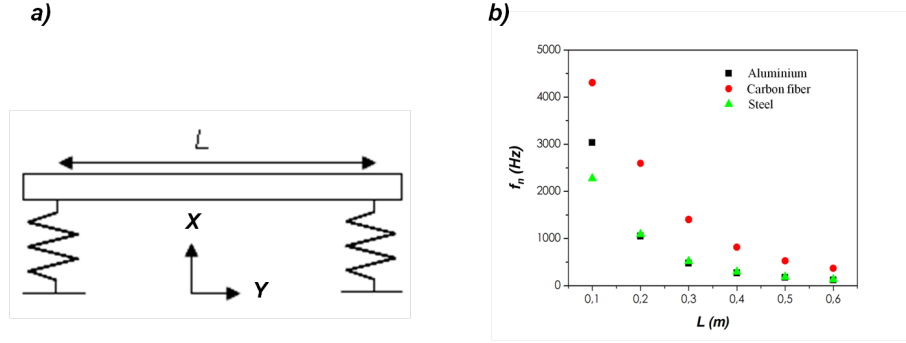


Figure 1.18: (a) Sketch representing the system *obstacle + force sensors*. Numerical simulations reproduced it by using a beam leaning on two springs. (b) Frequency behaviour of the system as a function of the beam length for three different materials.

As previously mentioned, the channel width is 0.25 m. In the case of a large obstacle spanning the whole width of the channel, only the carbon fiber provides a natural frequency higher than 2 kHz for a beam length of 0.25 m. But in order to deal with a material that is cheaper and easier to handle, we decided to adopt an obstacle made of aluminium. The inset in Fig.1.16.a shows how the wall spanning the channel has a central part of a length of 10 cm which is connected to the two force sensors, while the rest of the structure only blocks the incoming flow without contributing to the force computation. The small obstacle allows lateral flows. The same type of obstacle was used (aluminium, L -shaped) but its length was fixed at 0.08 m.

Force sensors

Two XFTC300 force sensors measured the forces exerted upon the obstacle on the axis of the flow with an acquisition frequency of 1 kHz. The XFTC300 series was specifically developed to measure tension and/or compression in static and dynamic applications. The miniature size and light-weight structure facilitate testing where these conditions are necessary. The sensor device is fitted with a fully temperature compensated Wheatstone bridge that is equipped with high stability micro-machined silicon strain gauges. The assembly of the whole structure (obstacle + sensors) is very precise. The obstacle consists of an L-shape beam. Sensors are connected to the bottom platform and to the back side of the obstacle. No other contact was allowed between the obstacle and the rest of the channel. The separation distance l must be $0 < l < 1$ mm to prevent beads from going through and getting stuck. These details avoid parasite momentum which could skew the measurement. Furthermore, sensors were mounted in order to visualise the force acting on the obstacle during the installation procedure. This means that the initial off-set value was set to zero.

1.2.2 Measurement techniques

To study the dynamic behaviour of a dense snow avalanche on a small-scale laboratory model, four different types of measurements were taken. They measure the height of the flow, its mean surface velocity, the forces that can be exerted on an obstacle and the evolution of the influence

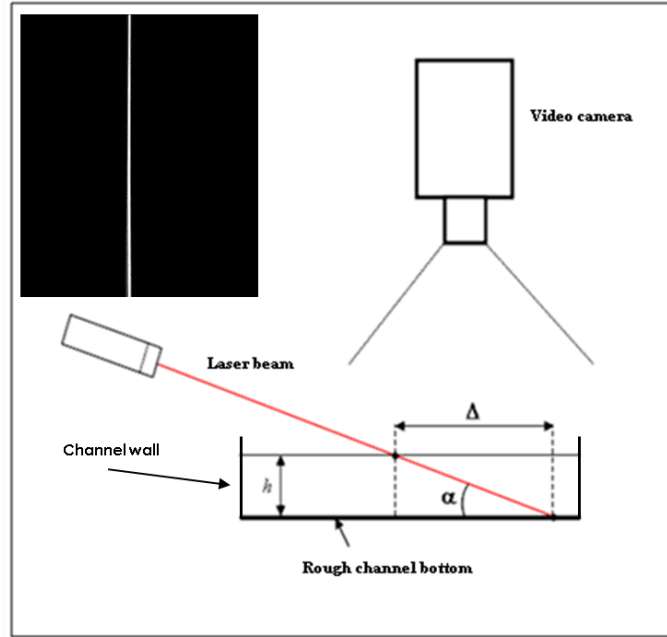


Figure 1.19: Sketch representing the laser technique principle. The inset shows a typical image obtained from laser measurements at $t = t_0$. The main flow direction is normal to the sketched surface.

zone occurring uphill. This section deals with the measurement techniques, the assumptions and calibrations required, and measure uncertainties.

Flow height measurement

Flow height measurement utilised a laser technique. By installing a laser along the channel (see Fig.1.19), a laser beam was projected along the axis and deviated by the transit of the incoming flow (see Fig.1.20.c). As shown in [63] and through cited publications, the line deviates towards the light source and its deviation Δ is proportional to the height h of the flow depending on

$$h = \Delta \tan \delta \quad (1.32)$$

where δ is the angle between the laser beam and the channel bottom. A downward facing video camera, normal to the channel axis, recorded the flow at an acquisition frequency of 350 fps. A Matlab routine handled the image treatment. As the inset of Fig.1.19 shows, tests were performed in a dark environment in order to obtain black images with only the white laser line visible. The programme converted sequences in gray scale images assigning a value between 0 (black) and 255 (white) to each pixel. The resulting laser line had a width of several pixels due to the laser's characteristics, and because beads reflected and deviated the incoming light. Consequently, a gaussian filter was first applied to the image to treat all of the irregularities in the intensity values. The maximum intensity pixel of each line was then detected and the position of the laser line was attributed to these pixels. The step-by-step process is shown in Fig.1.20.a. By providing an accurate calibration, this treatment associated a height value to a deviation measure. The calibration procedure entailed measuring the deviation of the laser line at four different well-known heights. Samples were made by piling up three PVC plates that were 8 mm thick (see Fig.1.20.b) and recording the position of the laser line. This procedure provided a range of calibration thickness from 0 – 24 mm which largely covered the flow heights obtained (the maximum measured flow heights were approximately 20 mm). The calibration accuracy depends on the images' resolution and the thickness of the laser beam in terms of

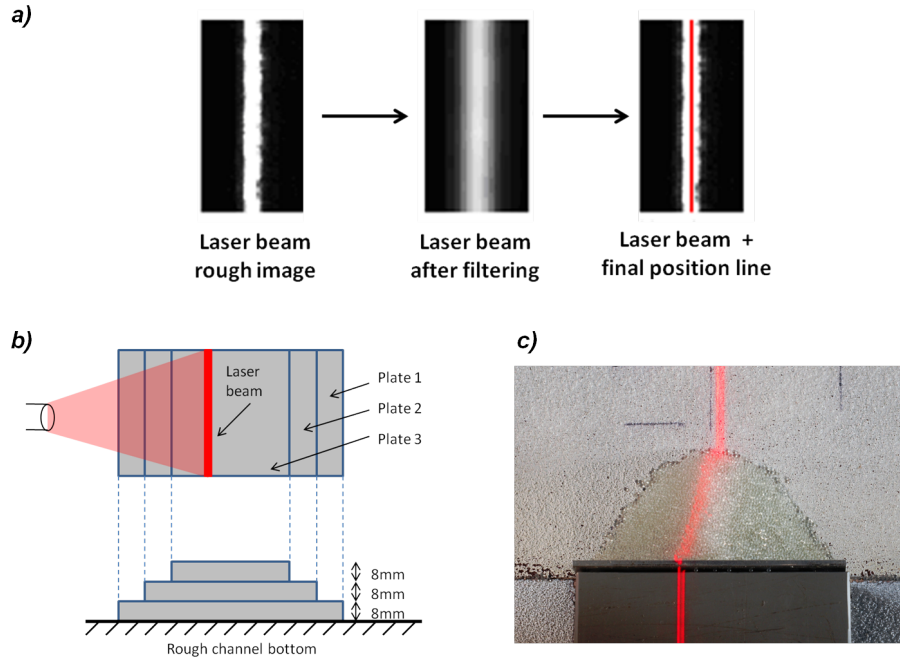


Figure 1.20: (a) The step-by-step process for the treatment of images obtained from height measurements. (b) Sketch showing the calibration procedure. (c) Final deposit height measurement.

pixels. In the case of a resolution of approximately 9.5 pix mm^{-1} and a maximum beam width of 20 pix, the precision was in the order of 0.5 mm ($=0.5d_{beads}$).

Mean surface velocity measurements

Surface velocity was calculated using a PIV technique applied to granular flows. PIV stands for Particle Image Velocimetry and it is an optical method for flow visualisation used to collect instantaneous velocity measurements and related fluid properties. Classical PIV consists of seeding a fluid with tracers and lightening a section of the flow in order to make particles visible and track their motion (speed and direction). Even if the released flow is not a fluid, the principle of the PIV can still be used when modifying certain techniques' details.

The implemented technique is referred to as *granular PIV* and it consists of two main phases: (i) the surface of the flow is recorded at a chosen section, (ii) images are treated, and the motion of particles' aggregates is tracked.

The view area, as already mentioned, consisted of a $10 \times 10 \text{ cm}$ square whose center was located on the channel axis, at a distance of 1.25 m from the releasing gate ($1250d_{beads}$). All sources of shadow had to be reduced as much as possible and, as shown in Fig.1.21.a, constant lighting was needed in order to maintain exactly the same light intensity during the flow. Once the flow was recorded, image sequences were treated with a Matlab processing program.

This technique is based on the assumption that the granular material, during the flow, moves downwards as a whole, with the same velocity of the flow. The principle consists of dividing an image in multiple sub-windows as shown in Fig.1.21.b and tracking their position during the entire time sequence. The acquisition frequency is known, thus the velocity values of the flow surface can be calculated from the obtained displacement vectors. The dimension of sub-windows can be chosen as well as the overlapping criteria and the maximum window displacement. The program creates a matrix for each sub-window of $n \times m$ dimensions corresponding to the window size in pixels. Then it converts images in gray scale and assigns a value between 0 (black) and 1

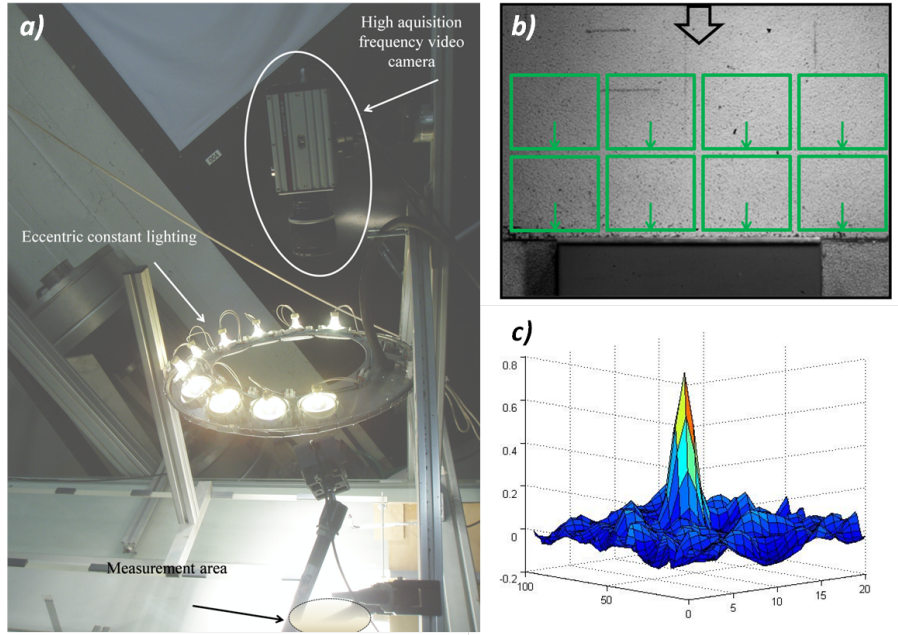


Figure 1.21: (a) PIV measurement set-up. (b) PIV technique principle. (c) Correlation index behaviour.

(white) to each matrix cell. Passing from one image to the next, each window moves around its original position within the maximum displacement allowed. For each new position the program re-calculates the color matrix and compares it with the original by finding the maximum cross-correlation between regions of the image (correlation index, see Fig.1.21.c). Lastly, it takes the position associated to the best correlation value, it defines the displacement vectors along the x and y -axis (see Fig.1.16.a for axis reference), and derives velocity vectors u_x and u_y . The maximum displacement selected for sub-windows depends on the flow velocity and must be chosen carefully. Values that are too high would mean long computing time but values that are too small would neglect the passage of the aggregates and distort results. The maximum allowed displacement along the x -axis was set at 80 pix for high slopes and at 20 pix for low slopes. The displacement on the y -axis was fixed at 20 pix for all of the tests. Each sub-window consisted of a 50-pixel-side square. The acquisition frequency of the video camera, the image sharpness and resolution, the number of sub-windows per image, their dimension, and other parameters play an important role in the estimation of this technique's precision. The precision obtained with the presented set-up was estimated at 0.01 m s^{-1} .

In order to validate results obtained with the *granular PIV* method, an additional technique was implemented and based on the presence of tracers into the flow. Tracers were made by patching two very tiny black-scotch pieces ($2 \times 2 \text{ mm}$) on one another with a glass bead in the middle. This solution allowed the tracer to have approximately the same density of a glass bead, to be visible and, due to its final shape, to float on the surface of the granular flow. The flow was recorded with a normal video camera at an acquisition frequency of 25 Hz and the image processing was done with Avistep, a free software programme. Avistep allows the viewing of a video through one image at a time, and the location of the position of an object in motion. A spatial and time calibration allows the derivation of the object's velocity. Even though this method was less accurate than the PIV, the results were consistent and fit together quantitatively.

The results obtained for flow velocity are presented in section 1.3.1. They only concern the flow velocity over time along the x -axis. Tests showed that, once the experimental set-up was adopted, the velocity component transversal to the main direction of the flow was negligible with respect to the longitudinal direction. This is probably due to the fact that the flow is canalised.

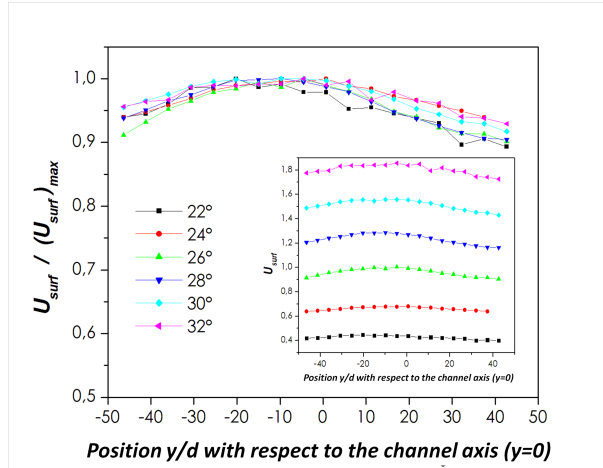


Figure 1.22: Cross-channel velocity profiles (y -axis direction). The velocity profiles are nearly uniform and thus the effect of the side walls is negligible. Note that the ten central centimetres of the channel correspond to the measurement area.

Under certain circumstances, the formation of eddies was previously observed [31]. We did not observe this type of phenomenon during the experiments.

A cross-channel velocity profile (y -axis direction) is additionally given in Fig.1.22 for some of the investigated slopes. The curves show that, in the ten central centimetres, the velocity profile is nearly uniform and therefore the effect of the side walls is negligible.

Force measurements

Force measurements were taken using two force sensors. Sensors were connected to the obstacle as they operated in parallel and measured forces along the x -axis. The granular avalanche flows down the channel and causes impact with the obstacle. Induced forces were recorded with an acquisition frequency of 1 kHz, which allowed very accurate measurements. Sensors measured a voltage value [V] which has to be converted in force data [N] using a conversion equation. This equation must be derived through a calibration process.

The calibration procedure was performed accurately. The principle consists of applying a well-known force and observing the sensor voltage output in order to derive the conversion equation. The calibration was done first for the *large* obstacle and, afterwards, for the *small* obstacle. First, the *large* obstacle was positioned horizontally and nine weights were loaded on top of one another and then taken down one at a time (see Fig.1.23.a). The loads consisted of steel cylinder masses of a 20 mm diameter and a height of 10 mm. Each cylinder has a mass of approximately 60 g (see Fig.1.23.b). This procedure was repeated at six positions along the uphill face of the obstacle. The load/unload cycle was tested in order to identify potential hysteresis effects. Figure 1.24 shows that these effects were negligible. The two force sensors worked in parallel. The position along the y_{obs} -axis of the gravity centre of the flow could not be precisely identified and, as a consequence, it was hard to assume that it corresponded to the center of the obstacle. Thus, the calibration was done at six different positions (five of which were spaced regularly along the obstacle length) in order to account for the effect of momentum potentially exerted on the obstacle.

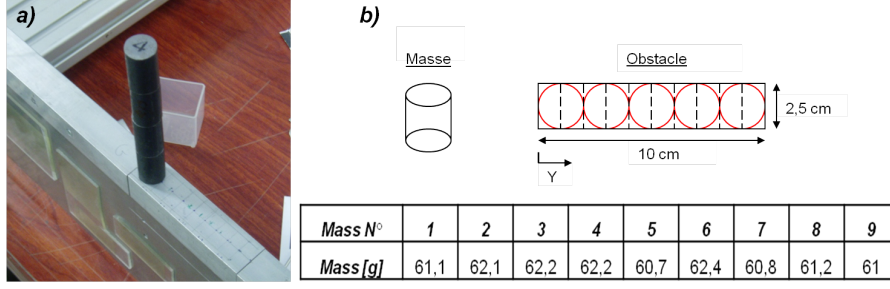


Figure 1.23: (a) Force sensor calibration procedure: weights are loaded on top of one another at different positions of the obstacle. (b) Calibration protocol. Six positions were chosen along the obstacle width and nine masses were used for the calibration.

Measurements, during both the calibration and real tests, were differential. The reference value of $F=0$ N corresponded to the average of the first 100 points recorded with no forces acting on the obstacle. For each sensor, $6 \times 9 = 54$ points of voltage measurements were obtained as a function of the force F and the position y_{obs} . For a constant y_{obs} , a relation $T(F)$ was found to be linear and equal to

$$T_r(F) = a_r F \quad (1.33)$$

$$T_l(F) = a_l F \quad (1.34)$$

where r and l denote the *right* and *left* sensor. a is the linear fit coefficient depending on the position y_{obs} . a_r and a_l vary linearly with y_{obs} , thus it was possible to write two other equations:

$$a_r = m_r y_{obs} + n_r \quad (1.35)$$

$$a_l = m_l y_{obs} + n_l \quad (1.36)$$

with m and n being the two linearity coefficients. The equations above lead to

$$T_r = F (m_r y_{obs} + n_r) \quad (1.37)$$

$$T_l = F (m_l y_{obs} + n_l) \quad (1.38)$$

The ratio between Eq.(1.37) and Eq.(1.38) gives an equation for the position of the gravity center of the incoming flow as function of the measured voltage and the four parameters previously obtained:

$$y_{gc} = \frac{T_l n_r - T_r n_l}{T_r m_l - T_l m_r} \quad (1.39)$$

and finally, using Eq.(1.39) in Eq.(1.37) or (1.38) allows the computation of the total force F acting on the obstacle

$$F = \frac{T_r m_l - T_l m_r}{m_l n_r - m_r n_l} \quad (1.40)$$

An ordinary least square fit was used to obtain the values of m and n from the ratios $\frac{T}{F}$, for the right and left sensors at different positions.

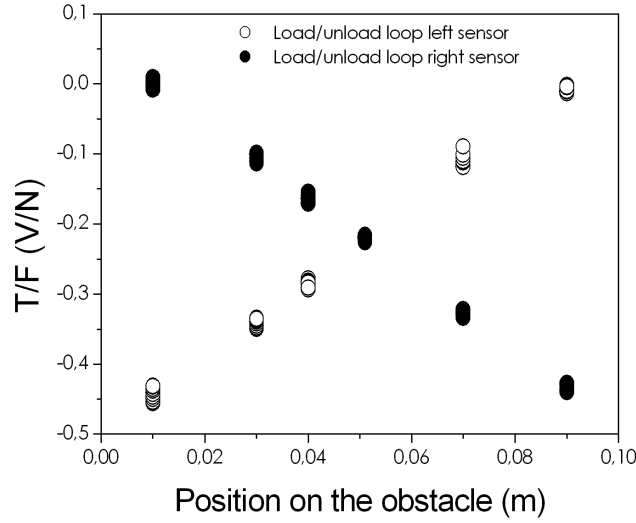


Figure 1.24: Voltage T over the force F versus the position on the obstacle. Load/unload cycles represent the calibration procedure for force sensors. No hysteresis effects were found.

Two different validation tests were executed in order to verify the reliability of the calibration procedure. A known force was applied and we checked whether the force value given by the system corresponded to the expected value. Both methods were based on this principle. For the first one, the obstacle was removed from the channel and repositioned horizontally (as for the calibration procedure). For the second one, the obstacle maintained the position corresponding to the avalanche experiments, and the weights were hooked onto it. With these two methods, the maximum gap between the measured and expected value, for a minimum calibration force of 0.65 N, was equal to 21 mN, corresponding to an error of 3%.

Measurements on the influence zone behaviour

The influence zone is here defined as the part of the flow uphill from the obstacle that is disturbed by the presence of the obstacle (see Fig.1.25). As it will be shown, this zone influences the flow dynamics and its interaction with the obstacle. Thus the flow behaviour uphill from the obstacle was analysed in detail in order to study this influence. The laser technique described above was used to investigate the behaviour of the free surface height upon impact with the obstacle. In tandem to this technique, an additional technique consisted of recording the flow-obstacle interaction with a high frequency video camera placed on the right side of the channel, normal to the main flow direction in order to treat recorded sequences.

A Matlab routine processed the images. First, the background and noises due to the light reflection on the beads were removed in order to obtain neat images of the flow (Fig.1.26.a). The flow surface was then extracted (Fig.1.26.b) and its free surface line were defined (Fig.1.26.c). From data regarding the free surface position at each image, it was possible to study its evolution along the time and its behaviour during the flow. The influence zone free surface slope α_{iz} , its length L_{iz} and its surface S_{iz} are the three parameters which were investigated. The acquisition frequency of the video camera allowed the calculation of the three parameters every $t = 1/350$ s. The derivative $\frac{\partial \alpha_{iz}}{\partial x}$ was calculated for the incoming flow images. When the α_{iz} value starts increasing regularly, that is the where the influence zone originates. Experimental tests allowed

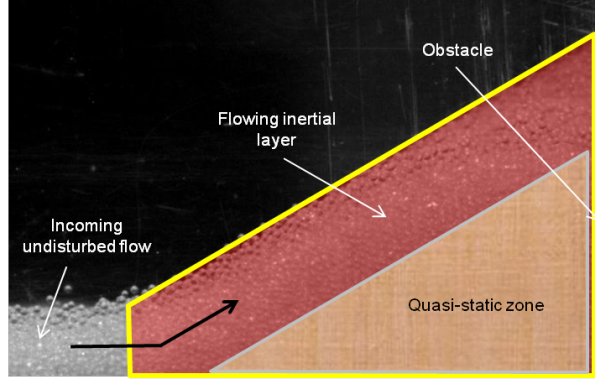


Figure 1.25: Influence zone definition. In this chapter, the influence zone is defined as the part of the flow uphill from the obstacle which is disturbed by the presence of the obstacle (yellow polygon). The grey line delimits the dead zone. The dead zone consists of the quasi-static part of the flow that is stuck uphill from the obstacle. An inertial layer flows on top of it.

the definition of an empirical threshold. The pixel identified by this threshold, with coordinates $(x_{ref}; z_{ref})$, acted as a reference for the calculation of L_{iz} and S_{iz} . As the downhill extent of the image was cropped at the uphill face of the obstacle, the influence zone length was calculated as:

$$L_{iz} = x_{max} - x_{ref} \quad (1.41)$$

and the surface S_{iz} and the free surface angle α_{iz} were calculated by assuming a trapezoidal shape, therefore:

$$S_{iz} = \frac{1}{2} [z_{ref} + z(x_{max})] L_{iz} \quad (1.42)$$

$$\alpha_{iz} = \arctan \left[\frac{z(x_{max}) - z_{ref}}{L_{iz}} \right] \quad (1.43)$$

where x_{max} is the total length of the image, and $z(x_{max})$ the height of the free surface at its downhill extent. The treatment was validated. A cross-comparison with data obtained from flow height measurements (laser techniques with and without obstacles) showed consistent results. The precision of this method depends, as for the case of flow depth, on the dilution rate of the flow. The arrival and the first phase of the flow are characterised by a very diluted state wherein image treatment cannot be very reliable. For the rest of the flow, the estimated error of the free surface detection is less than $2d_{beads}$, which corresponds to an error of less than 2% for the final deposit mean length.

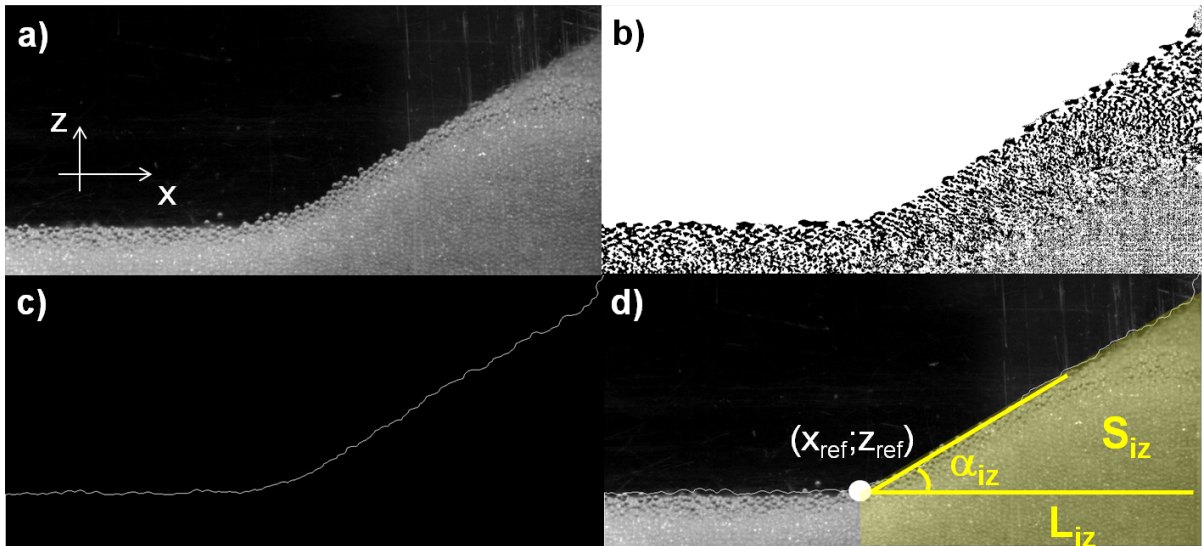


Figure 1.26: Step-by-step processing of the influence zone (yellow polygon in (d)) in order to calculate the parameters α_{iz} , L_{iz} and S_{iz} . An appropriate Matlab routine was developed.

1.3 The inclined granular plane: results

The repetition of the same test, in the same conditions, should theoretically give the same output. However, due to uncontrolled experimental conditions (air temperature, humidity, etc.), a random error constantly affects the results. To minimize this error, each test was repeated five to ten times at constant parameters and the averaged value was retained and ultimately used for data treatment. This approach is reliable if the distribution of the data's standard deviation is Gaussian. Preliminary tests proved that the distribution was Gaussian. Consequently, the values presented represent the average of five to ten tests performed in the same experimental conditions. However, particular attention was needed on the residual force measurement corresponding to the moment at which the flow stopped because it was noted that this configuration was particularly sensitive to uncontrolled experimental conditions.

Within the framework of Chanut's PhD thesis (2010) [36], similar tests were conducted for reference flow conditions and in the presence of a large obstacle. The presented data integrate these results where specified.

This section presents the results that were obtained. Tests on granular avalanches flowing down the channel without any obstacle were performed first (section 1.3.1). The measurements on this type of flow are called *reference measurements*. The evolution of flow depth and velocity over time was studied to characterise the avalanche dynamics. Then, the obstacles were mounted and force measurements were taken (section 1.3.2 and 1.3.3). Lastly, the influence zone forming uphill from the obstacle was analysed in detail (section 1.3.4).

1.3.1 The avalanche dynamics

Flow depth

Figure 1.27.a shows the flow height h versus time t . A moving average on 30 points was calculated in order to round the signal. In general, this type of signal displayed three main phases: (i) a rapid increase in height corresponding to the arrival of the avalanche front, (ii) a maximum value and finally (iii) a relatively slow decrease corresponding to the avalanche tail.

The influence of the slope is clearly visible: the higher the slope was, the maximum measured flow height was lower (see insert in Fig. 1.27.a). Moreover, when θ increased, the increasing phase profile and the decreasing profile, became steeper, the avalanche arrival time shortened and the flow duration decreased. For $\theta=21^\circ$, the trend was peculiar because the angle approached θ_{min} (20°): the friction forces at the bottom of the channel (and the effects of the side walls) became significant, which decreased the flow rate when moving away from the reservoir gate (the material was stored uphill). This jamming transition explains the drop in maximum height when approaching θ_{min} and is analysed in detail in section 1.3.2.

Figure 1.27.b shows the flow depth normalised by the maximum value h/h_{max} versus $t/t_{h=h_{max}}$, where $t_{h=h_{max}}$ is the time corresponding to the maximum height. The curves (particularly the decreasing phase) separated into two main groups highlight the transition between two regimes occurring around θ_{max} (28°). This transition is discussed in detail in section 1.3.2.

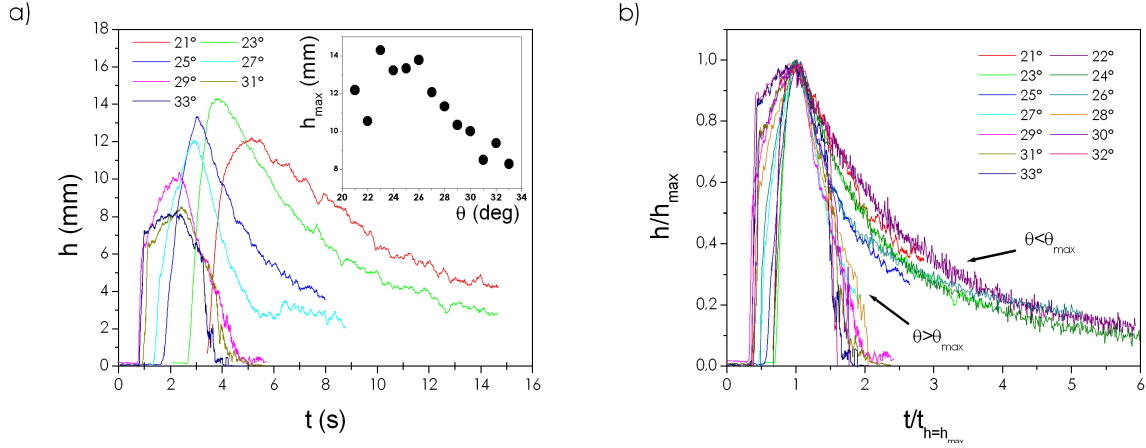


Figure 1.27: (a) Reference measurements: flow height h versus time t . The insert shows the maximum values of h versus the slope angle θ . (b) Flow depth normalised by the maximum value h/h_{max} versus $t/t_{h=h_{max}}$. $t_{h=h_{max}}$ is the time corresponding to the maximum height (values for even slope inclines are extracted from Chanut (2010) [36]).

Velocity

Figure 1.28.a shows the surface velocity u versus time t . As for flow depth results, a moving average of 30 points was done on raw data. $u(t)$ signals present three phases (increasing, maximum and decreasing) as the $h(t)$ signals. However, a plateau is observed above a critical slope close to θ_{max} .

The maximum velocity increases rather linearly with the slope as shown in the insert in Fig.1.28.a. Unlike the curve $h_{max}(\theta)$, the jamming transition is not visible here.

Figure 1.28.b shows the flow velocity normalised by the maximum value u/u_{max} versus $t/t_{u=u_{max}}$, where $t_{u=u_{max}}$ is the time corresponding to the maximum velocity. As for flow depth results, two groups of curves are clearly identified for $\theta < \theta_{max}$ and $\theta > \theta_{max}$.

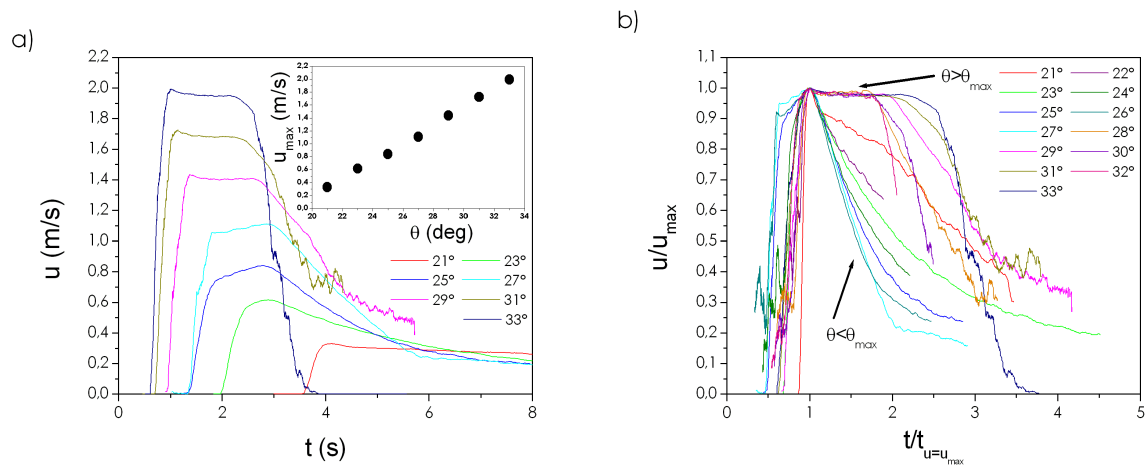


Figure 1.28: (a) Reference measurements: surface flow velocity u versus time t . The insert shows the maximum values of u versus the slope angle θ . (b) Surface flow velocity normalised by the maximum value u/u_{max} versus $t/t_{u=u_{max}}$. $t_{u=u_{max}}$ is the time corresponding to the maximum height (values for even slope inclines are extracted from Chanut (2010) [36]).

Flow depth and velocity data interpretation

The avalanche flows that were investigated are unsteady and non-uniform flows. However, a scaling law giving the depth-averaged velocity \bar{u} as a function of the flow depth h in steady and uniform flow conditions was previously proven for dense flows [63, 119]:

$$\bar{u} \propto h^{3/2} (\tan \theta - \tan \theta_{min}) \quad (1.44)$$

In non-steady experimental conditions (finite-sized granular avalanches), particular attention is required for the maximum values of \bar{u} and h which might correspond to a quasi-steady state. Equation (1.44) was validated with results obtained from reference tests. Unlike the steady regime, and because of the time dependency, the maximum value of h does not correspond to the maximum value of u . Thus, it was chosen for considering the maximum value of flow depth h_{max} and the velocity value corresponding to $t(h_{max})$. Figure 1.29 shows $u(h_{max})$ versus $h_{max}^{3/2}(\tan \theta - \tan \theta_{min})$. The scaling law is clearly verified for slope inclines between θ_{min} and θ_{max} . Above θ_{max} , the regime changes completely and cannot be reproduced by the scaling law. In the insert of Fig.1.29, the Froude number Fr is drawn versus h_{max}/h_{stop} . As found for the steady and uniform regime [119], Fr and h_{stop} are linearly correlated. However, the linear fit does not match the data very accurately. This discrepancy can be attributed to the unsteady flow state and the high Froude number values (with respect to the data in [119]).

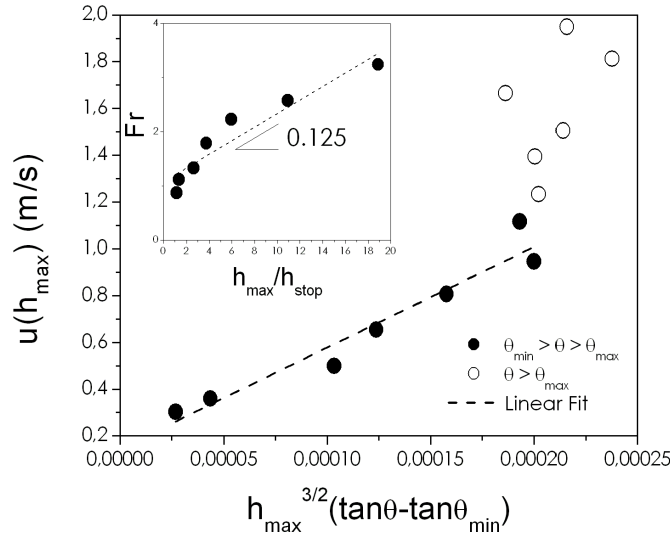


Figure 1.29: A scaling law representation showing the maximum velocity $u(h_{max})$ versus $h_{max}^{3/2}(\tan \theta - \tan \theta_{min})$ for all of the investigated slopes. The insert shows the Froude number Fr versus the maximum flow depth h_{max} normalised by the corresponding h_{stop} value in the range $[\theta_{min}; \theta_{max}]$. Note that the slope of the best-fit line is equal to 0.125, a value which is close to the value given in [119].

The relationship between flow depth and velocity data was analysed in greater detail by studying the behaviour of the $u(h)$ equation for each slope tested by hiding the time component t . A power-law equation $u = Ch^\beta$ was considered to fit the flow velocity u as a function of its height h plotted in Fig.1.30.a (example for 23°). A hysteresis phenomenon can be clearly observed between the front and the tail.

Figure 1.27-1.28 and Fig.1.30.a show how an avalanche parameter (flow depth or velocity) evolves over time at a given position (Eulerian approach). These graphs show changes in behaviour corresponding to the horizontal structure of the avalanche flow: the front, body and tail. In

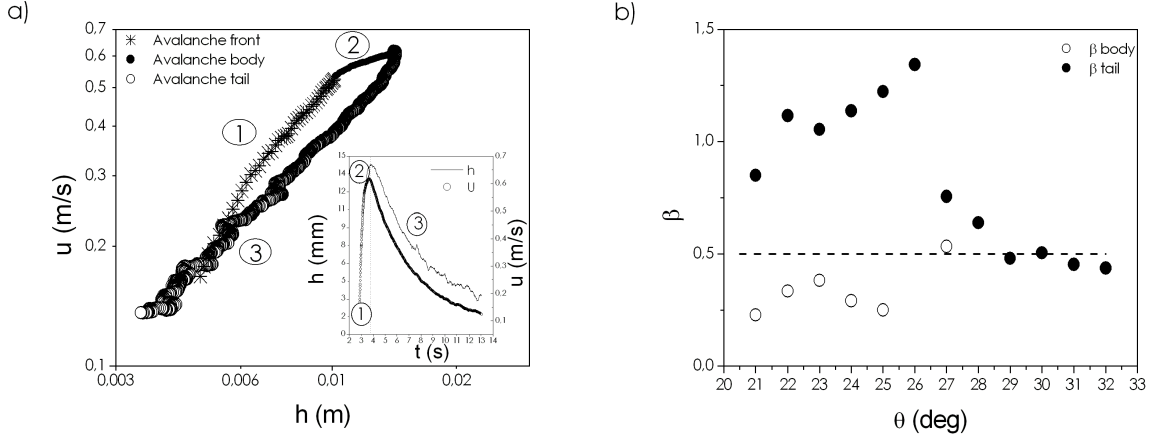


Figure 1.30: (a) Mean flow velocity u versus the flow depth h . An example for $\theta=23^\circ$. The insert reports u and h evolution values versus time t . (b) β values from the power relation $u=Ch^\beta$ for the avalanche body (\circ) and tail (\bullet) versus the slope angle θ . Note that for $\theta=33^\circ$, the value of β for the avalanche tail was found to be equal to 2.7 (large value not shown here) which might indicate a transition to a diluted gaseous regime.

the following section, the word *phase* systematically defines each of the three components of the avalanche. These phases are clearly represented in Fig.1.30.a. As the avalanche front (phase 1) is very diluted, only the body (phase 2) and the tail (phase 3) were considered.

For each slope tested, the β coefficient was systematically estimated. Figure 1.30.b shows β versus the slope angle. Data from the avalanche body reached values close to $1/2$ for slopes lower than θ_{max} but, beyond this critical angle, the body became too diluted for the measurements to remain reliable. Data from the avalanche tail highlight a transition occurring around θ_{max} : for lower angles, β varies between 1 and 1.5, while it stabilises around $\beta=1/2$ when θ exceeds θ_{max} . Even though the avalanche regime is unsteady and non-uniform, the β values obtained are reminiscent of well-known steady flow regimes. On the one hand, a rapid diluted regime can be characterised by a constant Froude number implying $u \propto h^{1/2}$ which corresponds to the scaling found for the avalanche tail at high slopes and for the avalanche body. On the other hand, a dense frictional regime can be described by a constant inertial number $I \propto Fr \frac{d}{h}$ implying $u \propto h^{3/2}$ as approximately found for the avalanche tail at low slopes. It should be noted that, near the bottom of the flow, above θ_{max} , the behaviour of a dense granular flow on a rough incline can resemble a flow on a flat base ($u \propto h^{1/2}$) [99]. However, if the latter case is associated with actual slipping, one may expect the diluted flow on a rough bottom (above θ_{max}) to fluidise, leading to an apparent sliding velocity.

All of these results highlight a transition from a dense frictional regime to a more diluted one. A transition can also be observed when considering the inertial number I introduced in section 1.1.2. This number is defined as the ratio:

$$I = \frac{5u_{surf}d}{2h^{3/2}\sqrt{\phi}g \cos \theta} \quad (1.45)$$

where u_{surf} is the mean surface velocity calculated with the PIV method introduced in section 1.2.2 and ϕ is the volume fraction coefficient. As it is difficult to estimate ϕ for experimental granular flows, attention is focussed on $I\sqrt{\phi}$. Figure 1.31.a shows the behaviour of $I\sqrt{\phi}$ as a function of the time t for the slopes investigated (from 21° to 33° each two degrees). As highlighted in [36], after the front phase, trends decrease in values (the flow depth increases), reach a minimum, and then start increasing again (the flow depth decreases). The minimum value

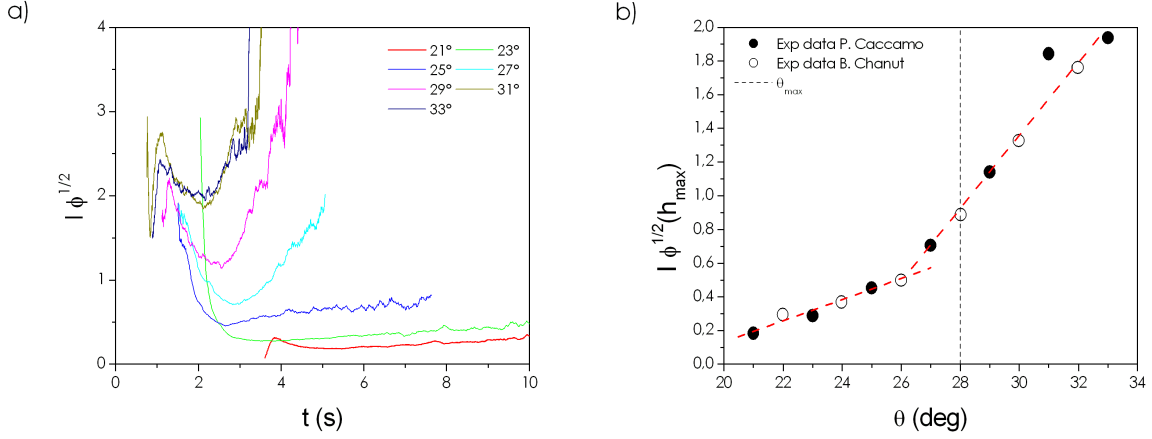


Figure 1.31: (a) $I\phi^{1/2}$ values over time t for some of the slopes investigated. (b) $I\phi^{1/2}$ values taken at $t = t_{h_{max}}$ and represented as a function of the slope angle θ . Experimental results show a change in the trend behaviour occurring around $\theta = \theta_{max}$.

of $I\sqrt{\phi}$ corresponds to the maximum value of h . The decreasing-increasing sequence becomes less dramatic when decreasing the slope angle. Figure 1.31.b shows values of $I\sqrt{\phi}(h_{max})$ as a function of the slope angle. Results were compared with those obtained in Chanut (2010) [36], and they correspond very well. Both sets of data highlight a change in the trend slope occurring around the θ_{max} angle.

This transition has already been observed, yet its theoretical description remains a serious challenge ([60] and references therein).

1.3.2 Force on a large obstacle spanning the channel

The force exerted by the incoming flow on a structure was measured. As previously mentioned, the first structure that was tested consisted of an obstacle spanning the entire width of the channel (catching dam type). The flow reached the obstacle upon impact and overcame it. Results are presented in the following.

Raw data: force over time

Figure 1.32.a shows the force F versus time t . A moving average on 100 points was done on data, which means that, at an acquisition frequency of 1 kHz, data were rounded to 0.1 s. Force signals present three main phases (increasing, maximum value and decreasing) as the $h(t)$ and $u(t)$ signals seen in the previous section. The increasing and decreasing phase becomes steeper when the slope angle is increased. The spread of the granular volume along the channel reduces and the body and tail parts of the avalanche tend to become one mixed entity. The force signal never ends with a zero value, but a residual force F_{res} , caused by the presence of the final deposit stored uphill from the obstacle, is observed for all of the slope inclines. This force F_{res} is the

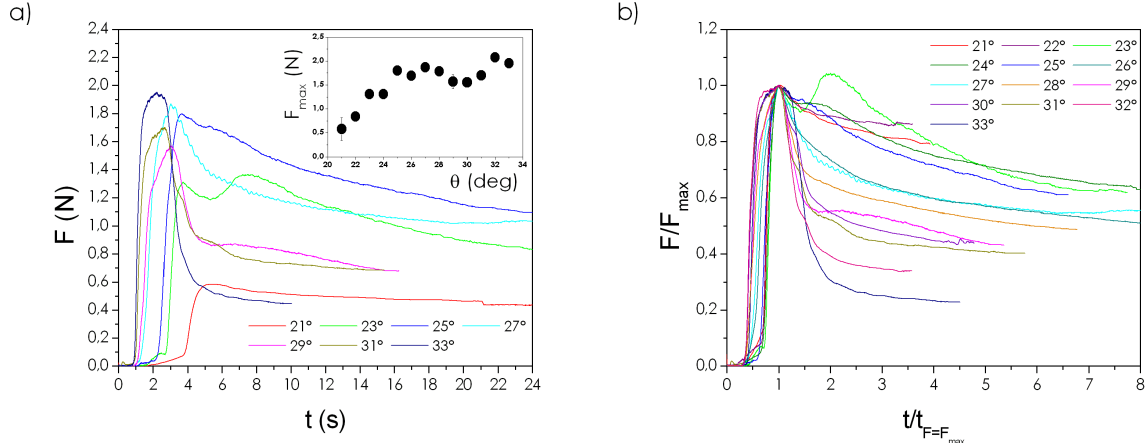


Figure 1.32: (a) Mean force F versus t . The insert shows maximum F values versus θ . Measurements were taken at a distance $x=1300d$ from the releasing gate. (b) Mean force normalised by the maximum value F/F_{max} versus $t/t_{h=h_{max}}$. $t_{h=h_{max}}$ is the time corresponding to the maximum height. Both graphs refer to the large obstacle.

result of a complex competition between the material weight w (which tends to increase F_{res} when w increases) and the friction force F_f mobilised at the base (which tends to decrease F_{res} when F_f increases). Data show that the residual force displays a maximum for intermediate slopes: this is an effect of the jamming transition as detailed in the following section.

The insert in Fig.1.32.a shows the maximum force F_{max} versus the slope angle θ . The maximum force drops sharply when approaching θ_{min} .

Figure 1.32.b, shows the force results normalised by the maximum value F/F_{max} versus dimensionless time $t/t_{F=F_{max}}$, where $t_{F=F_{max}}$ is the time corresponding to the maximum force. From these curves it is interesting to extract the values of F/F_{max} after the maximum point. Figure 1.33.a shows F/F_{max} at $t/t_{max} = 2$ and at $t/t_{max} = 3$. Both curves behave similarly and show that low slopes can still mobilise huge forces even after the maximum force peak. However, the force decreases sharply at higher slopes. An interpretation of the force data is given in the following.

Maximum force: dense to diluted transition

Reference tests showed a transition existing between two different flow regimes. Beyond the θ_{max} angle, the dense regime characterising the flow becomes a more diluted regime. These two regimes can be described by combining the following typical forces:

$$F_{hyd} = \frac{1}{2}\phi(t)\rho_p g h^2(t) \cos \theta l_{obs} \quad (1.46)$$

$$F_{kin} = \frac{1}{2}\phi(t)\rho_p u^2(t) h(t) l_{obs} \quad (1.47)$$

where $\phi(t)\rho_p$ corresponds to the density, l_{obs} is the obstacle length and all the time-dependent parameters were considered at $t=t_{h=h_{max}}$. Equation (1.46) corresponds to the gravity force, relevant in the dense frictional regime for which the force is likely to be driven by the flow weight related to its depth h . On the other hand, Eq.(1.47) corresponds to the kinetic force which is relevant in flow regimes for which the force is likely to be driven by the kinetic energy related to the velocity squared u^2 . This is the case for the diluted flows and also for dense flows at high Froude numbers.

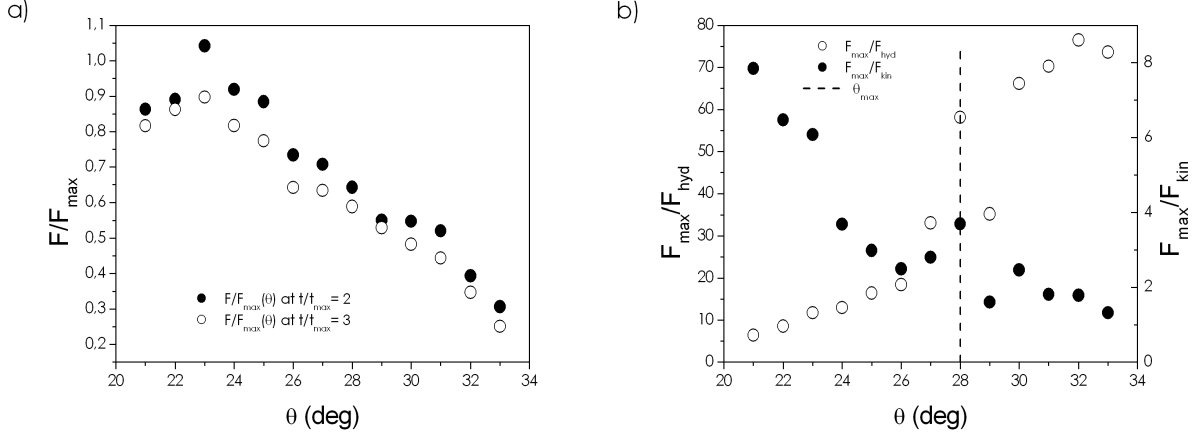


Figure 1.33: (a) The F/F_{max} signal versus the slope angle θ at different values of $t/t_{h=h_{max}}$. (b) F_{max}/F_{kin} and F_{max}/F_{hyd} ratios versus θ . Both graphs refer to the large obstacle.

In order to derive these two typical forces, it is necessary to estimate the volume fraction ϕ (not measured in our experiments). The scaling law giving ϕ versus I [60, 63] for stationary regimes was used as an initial approximation:

$$\phi(I) = \phi_{max} + (\phi_{min} - \phi_{max}) I \sqrt{\phi} \quad (1.48)$$

The depth-averaged volume fraction $\bar{\phi}$ was calculated by solving the above implicit equation considering the typical values $\phi_{min} = 0.4$ and $\phi_{max} = 0.6$ (see the result in Fig.1.34.a), on the basis of the depth-averaged inertial number \bar{I} :

$$\bar{I} = \frac{5}{2\sqrt{\bar{\phi}}} Fr \frac{d}{h} = \frac{5\bar{u}d}{2h\sqrt{gh\bar{\phi}\cos\theta}} \quad (1.49)$$

Figure 1.33.b shows the two normalised forces F_{max}/F_{kin} and F_{max}/F_{hyd} . Both curves indicate the dense to diluted transition occurring around θ_{max} . The ratio F_{max}/F_{kin} decreases when increasing the slope and it tends to 1 at high slopes, meaning that the maximum force is purely kinetic: $F_{max} \simeq \frac{1}{2}\phi\rho Pu^2h$. However, the ratio F_{max}/F_{hyd} increases with the slope angle and, when approaching θ_{min} , it remains much greater than 1. At $\theta = 21^\circ$, the force is roughly five to six times the typical hydrostatic force of the incoming flow. Another contribution plays a dominant role in the total force, and we assume that this contribution is due to the presence of the influence zone uphill from the obstacle.

Additionally, these results qualitatively match those obtained in previous studies [38, 51] based on 2D discrete numerical simulations (see Fig.7 in [38]).

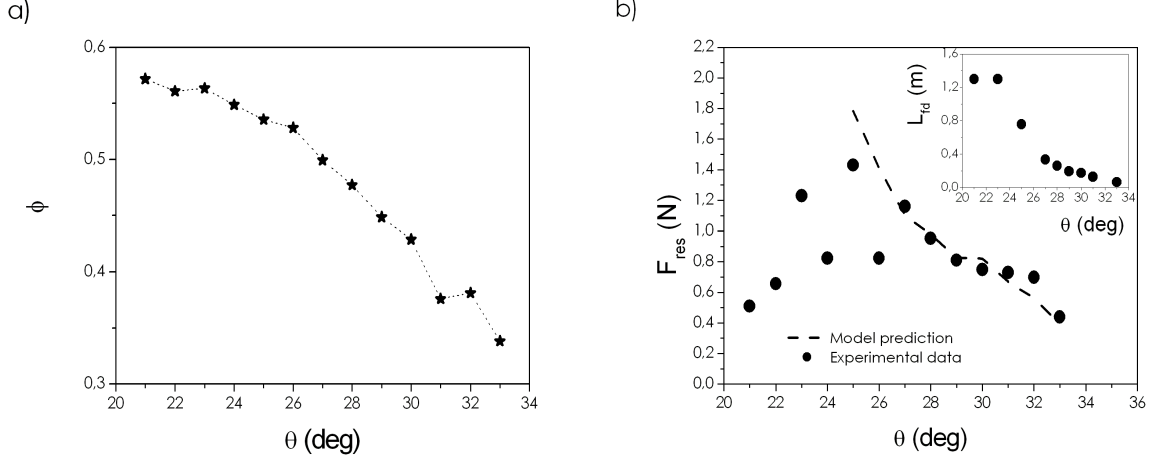


Figure 1.34: (a) Depth-averaged volume fraction $\bar{\phi}$ versus the slope angle θ . Data were calculated by solving Eq.(1.48). (b) Residual force F_{res} (values at $t=10$ s) induced on the large obstacle, versus the slope angle θ . Black data points represent experimental results while the dashed line connects data obtained from Eq.(1.50) with $\mu=\tan\theta_{min}$ ($\mu \simeq 0.36$). Note that the measurement of F_{res} (average value of 5–10 tests) is delicate because it is very sensitive to uncontrolled experimental conditions (day and operator) for angles below θ_{max} . The inset shows the measured values of the final deposit length L_{fd} versus the slope angle θ .

Residual force: jamming transition

In this section, residual forces will be discussed. The total signal duration strongly depends on the slope incline. The lowest recorded value is about 10 s for the highest slope (see Fig.1.32.a) and the maximum flowing time reaches more than 20 s. Thus, the residual force was arbitrarily assumed as the force at $t = 10$ s. Figure 1.34.b shows the measured residual force F_{res} versus the slope angle θ . F_{res} increases when decreasing the slope and it drops when approaching θ_{min} . A first qualitative explication arises from the experimental observation. At low slope inclines, the final deposit spreads across the channel up to the reservoir. Friction plays an important role in reducing the deposit weight exerted on the obstacle. On the other hand, for high slopes, most of the beads' volume goes past the structure, the final deposit is small and the force that it can exert decreases when increasing the slope. As a consequence, intermediate slopes exhibit a maximum of residual force. A simple model based on the equilibrium between the weight $w = c\phi\rho_p g L_{fd} H_{obs} \sin\theta$ and the basal friction $F_f = \mu c\phi\rho_p g L_{fd} H_{obs} \cos\theta$ describes the decrease of the residual force with the slope angle beyond θ_{min} :

$$F_{res} = c\phi\rho_p g L_{fd} H_{obs} (\sin\theta - \mu \cos\theta), \quad (1.50)$$

where c represents a shape coefficient, L_{fd} the dead zone length experimentally measured, H_{obs} the obstacle height and μ the basal friction coefficient. The volume fraction for the deposit was assumed to be equal to $\phi_{max}=0.6$.

The value of the shape coefficient c was derived from an accurate analysis of the influence zone behaviour at a fixed slope of 31° [34]. This analysis showed that the final deposit shape is trapezoidal. Consequently, the shape coefficient should equal 0.66. The basal friction coefficient μ was considered equal to $\tan(\theta_{min}) \simeq 0.36$, which typically characterizes a standstill condition (quasi-static deformation). This simple model accurately predicts the residual force for high slopes but it fails close to θ_{min} . At angles close to θ_{min} , we observed a deposit along the entire channel up to the reservoir, and almost no material overflowed the obstacle. The length of this deposit, and the resulting residual force, appear to be very sensitive to certain uncontrolled experimental conditions. The velocity at which the gate is opened, the ambient humidity rate and the state of roughness along the bottom (due to its degradation) are some of the parameters

influencing the residual force. Thus, the assumption is to attribute it to unstable states when approaching θ_{min} . As Eq.(1.50) is supposed to work in the case of geometrical catching because of the obstacle, it cannot take into account the additional friction effect related to h_{stop} , within the range $[\theta_{min};\theta_{max}]$. The gap between the model prediction and experimental data shows that this effect becomes dominant at the jamming transition.

The final deposit length L_{fd} was measured after each test and the mean values obtained are reported in the inset of Fig.1.34.b as a function of the slope angle θ . More considerations are provided in section 1.3.3 when these results are compared to those obtained in the presence of the small obstacle.

A similar analysis is undertaken in the next section. The obstacle geometry changes, and a smaller wall-like obstacle is considered. Force measurements are performed, maximum and residual forces are accurately investigated and both analyses are compared to the large-obstacle results presented above.

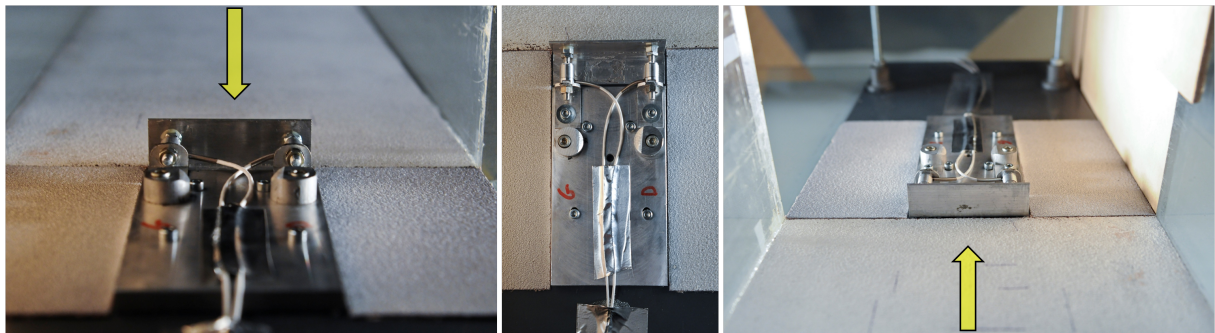


Figure 1.35: Overview of the small obstacle mounted at the end of the channel. The yellow arrows indicate the direction of the incoming flow.

1.3.3 Force on a small obstacle allowing lateral flows

Once the tests with the large obstacle were completed, the obstacle was replaced by a smaller structure (breaking-mound type) in order to investigate how the geometry of the structure can influence the flow dynamics and the induced forces. This new obstacle is visible in Fig.1.35 and has the same shape (wall-like obstacle) of the previous one (see Section 1.2.1 for more details) and the same height H_{obs} , but a length of 8 cm. This value represents a compromised solution for different requirements. Force sensors need a minimum beam width for their assembly set-up (see Fig.1.16.c) of about 3.5 cm each. However, enough space must be left between the side walls and the obstacle so that the lateral flow is not stuck by side walls that are too close. And lastly, a larger obstacle means smaller measurement errors and more calibration points. Additionally, Fig.1.22 shows that the walls' effects on the surface velocity are negligible at the obstacle edges. With respect to this graph, 4 cm on the left and on the right of the channel axis, the measured surface velocity corresponds to the 95% of the maximum surface velocity obtained along the axis. This value is considered acceptable for the tests performed.

Tests were carried out following the same experimental protocol defined for the large obstacle.

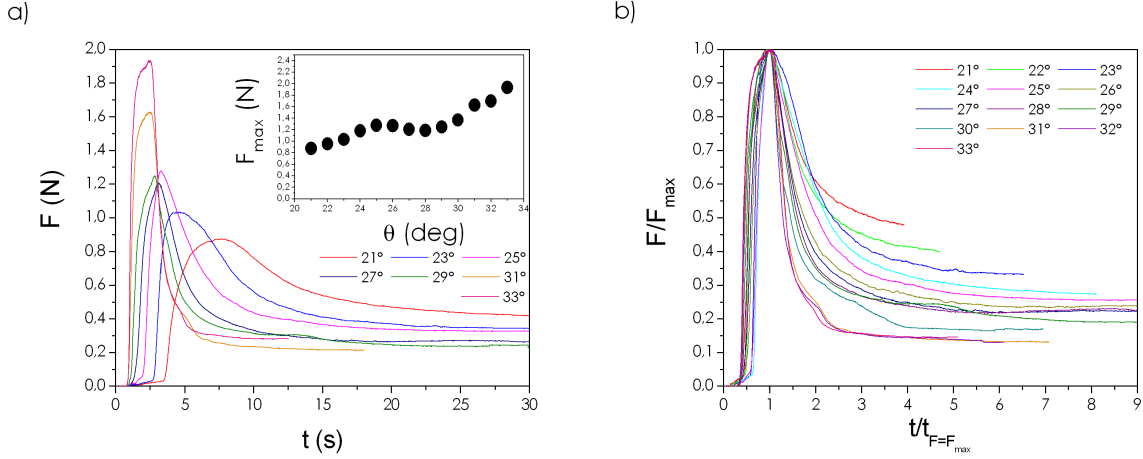


Figure 1.36: (a) Mean force F versus t . The insert shows maximum F values versus θ . Measurements were taken at a distance $x=1300d$ from the releasing gate. (b) Mean force normalised by the maximum value F/F_{max} versus $t/t_{h=h_{max}}$. $t_{h=h_{max}}$ is the time corresponding to the maximum height. Both graphs refer to the small obstacle.

Slopes ranging from 21° to 33° were investigated and five to ten tests were repeated in the same conditions for each slope. The average of these multiple tests is presented as the final result.

Raw data: force over time

Figure 1.36 *a* and *b* shows the obtained results. Data were reported on 100 points (0.1 s). Profiles show a regular evolution varying with the slope angle. The three main phases identified for previous measurements can still be observed. The gradient of the increasing and decreasing phases raises when increasing the slope, and gentle and rounded profiles at low slopes become steeper and sharper. The maximum force value mostly increases with the incline angle, except close to the θ_{max} angle where it slightly decreases before increasing again afterwards. The beads' volume at low incline angles moves slowly and spreads along the channel while the avalanche is more compact at higher slopes and it flows down as a whole. This implies that at high inclines, maximum induced forces are higher yet isolated (*peak* profile), while low slopes are characterised by maximum forces which are less important but can be mobilised for a longer period of time (*dome* profile). This result was found with the large obstacle as well (see section 1.3.2).

Maximum force: data interpretation

The data from force measurements on the small obstacle were treated like those for the large obstacle. For each slope that was investigated, the maximum force value was considered and compared to two force contributions, the hydrostatic and the kinetic components (see section 1.3.2 for details). Figure 1.37.a shows these ratios versus the slope angle.

Force values were normalised by the obstacle length in order to be compared. Thus, in the following section, we talk about forces for the sake of simplicity, but it is important to note that we are referring to forces over the obstacle length $\frac{F}{l_{obs}}$. Both profiles, as was the case for the large obstacle, present a bi-shaped behaviour and the

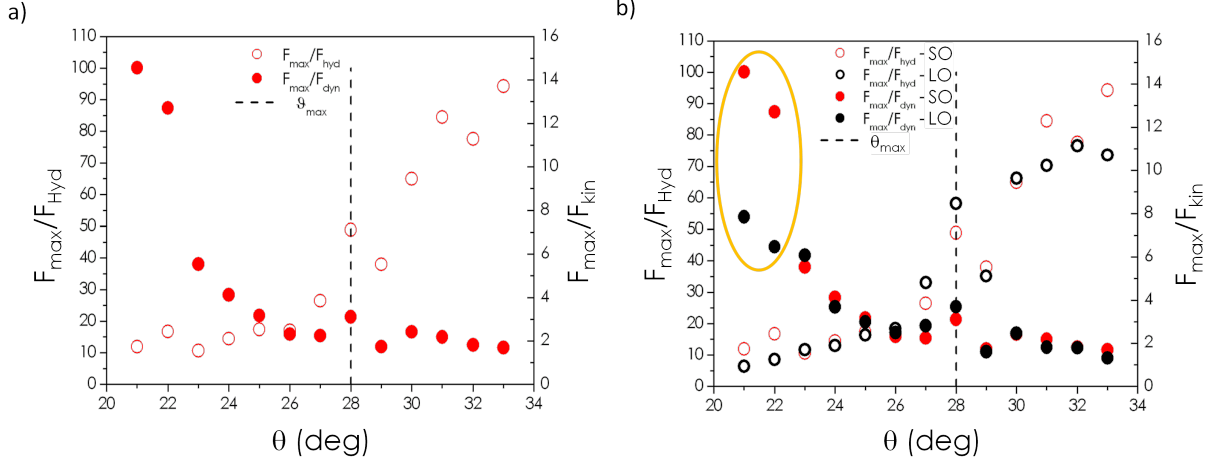


Figure 1.37: (a) F_{max}/F_{kin} and F_{max}/F_{hyd} ratios versus θ . Values refer to the small obstacle. (b) Comparison between $\frac{F_{max}}{F_i}$ obtained from the large and small obstacles versus the slope angle. Results differ at low slopes.

change occurs for both of them at approximately $\theta=28^\circ$ which corresponds to the θ_{max} angle. As for the large obstacle results, the ratio F_{max}/F_{kin} decreases when increasing the slope and it reaches a value close to 1 at very high slopes. The maximum force at high incline angles can be considered as purely kinetic in the presence of the small obstacle as well. The ratio between the maximum force and the hydrostatic contribution, on the other hand, decreases when decreasing the slope until a value of approximately 10 – 12, slightly higher than for the large obstacle. Figure 1.37.b shows the comparison between the results obtained with both the large and small obstacles. Trends are rather similar except at low slopes. This is evidence of the obstacle shape's influence on the dynamics of the flow. Figure 1.38 confirms this gap. Three representative slopes were considered. For a low slope (22°), a mean (26°) and a high slope (32°), the force profiles were presented for the large and the small obstacle as a function of time t . The three graphs show how the maximum force values overlap at high and intermediate incline angles, while at low slopes, the small obstacle is subjected to a maximum force two times greater than the maximum force exerted on the large obstacle. We suppose that this difference is due to a network of forces acting along the y -axis and reducing the force exerted on the structure (the Janssen effect). This network would appear at low slopes in the presence of the large obstacle. The walls' presence, the weak flow velocity and the significant influence of the basal friction contribute to the formation of such a phenomenon. A dimensionless number G was set to highlight the influence of the obstacle shape that rises when approaching the θ_{min} angle. This number is defined as:

$$G = \frac{F_{max}^{SO} - F_{max}^{LO}}{F_{max}^{LO}} \quad (1.51)$$

and it corresponds to the difference between the two maximum forces over the maximum force exerted on the small obstacle. *LO* and *SO* stand for *large* and *small* obstacles. Figure 1.38.d shows the behaviour of G for all of the investigated slopes. This coefficient is rather constant and close to zero for all of the inclinations with the exceptions of 21° and 22° , where it suddenly increases.

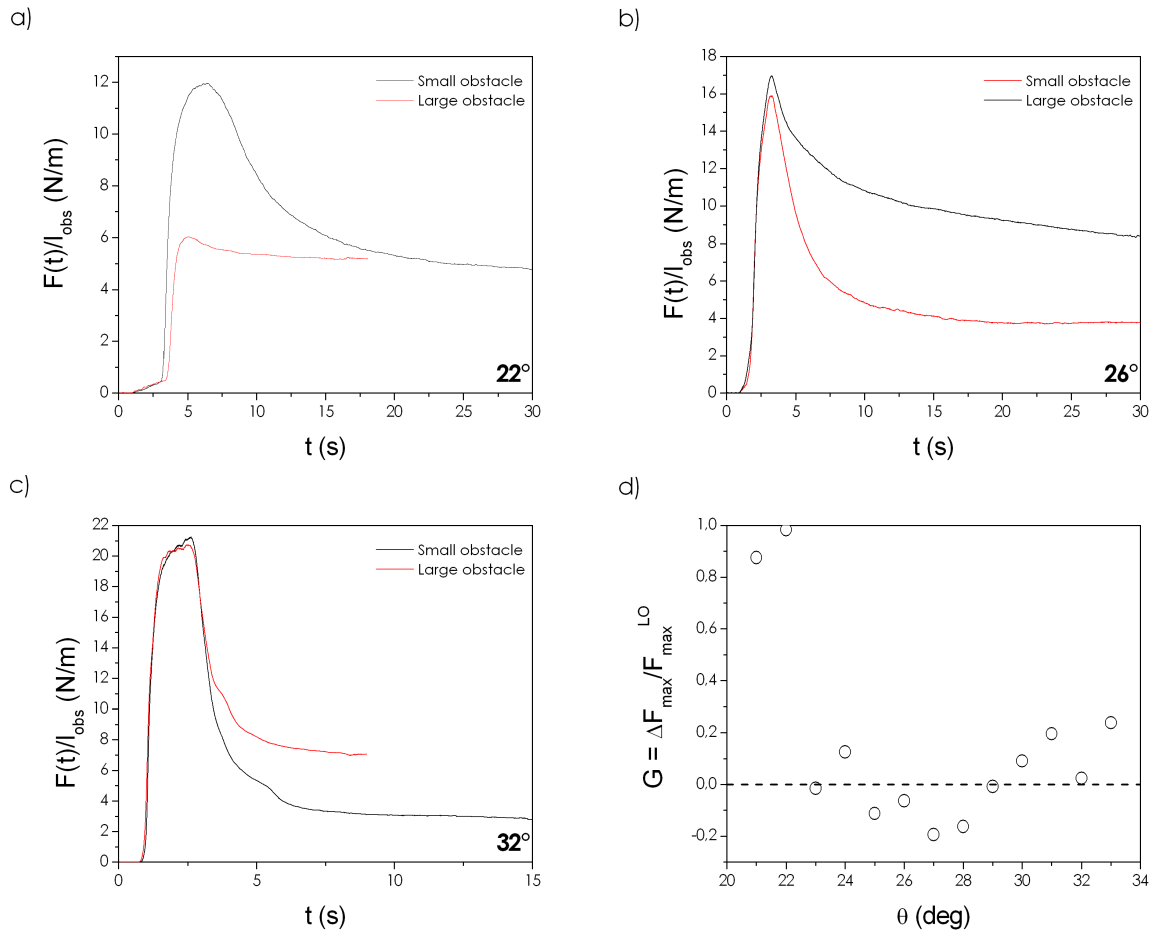


Figure 1.38: Graphs presenting the force per unit length measured from the large and small obstacles versus time t at (a) 22° , (b) 26° and (c) 32° . (d) Dimensionless number G versus the slope angle. The results confirm that the influence of the obstacle shape becomes significant at low slopes approaching θ_{\min} .

Final deposit and residual forces

Experimental results on the residual force were compared to the model prediction described in Eq.(1.50) and based on the equilibrium between the weight w of the final deposit and the basal friction F_f . Due to lateral flows, the flow duration is longer for all of the slope angles. In this case, the residual force was therefore considered as the force value at $t=15$ s. Due to the new high frequency video camera (see section 1.2.1 for details), it was possible to use a high acquisition frequency without any restriction on the acquisition time for this set of experiments, as was the case for previous measurements. Results were normalised by the obstacle length in order to be compared with other data. The residual force, as explained in section 1.3.2, is due to the presence of a deposit uphill from the obstacle that continues pushing on it once the flow has finished. This final static contribution is found to be much lower when lateral flows can occur. This set-up lets a larger part of the avalanche volume pass through the obstacle section and thus the amount of beads blocked by the structure decreases, and the induced force thus becomes lower.

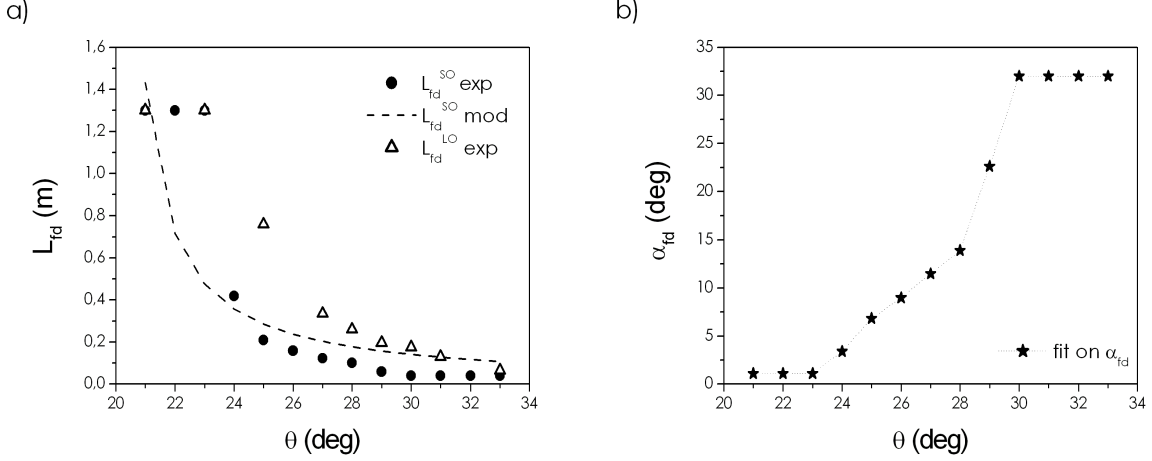


Figure 1.39: Length of the final deposit versus the slope angle. Data come from experimental measurements from both the large and small obstacles and from the analytical model prediction. (b) Values of the fitted α_{fd} versus the slope angle.

The model parameters did not change (see section 1.3.2 for details). The volume fraction ϕ is assumed equal to $\phi_{max}=0.6$, the effective friction coefficient μ is considered equal to $\tan(\theta_{min}) \simeq 0.36$ and the shape coefficient is $c=0.66$. L_{fd} corresponds to the observed final deposit length which is represented in Fig.1.39.a. Even with the lateral flow allowed, at low slopes ($\theta < 23^\circ$) the final deposit can be observed along the entire length of the channel, up to the reservoir. L_{fd}^{SO} saturates at a value of 1.3 m. Beyond $\theta=23^\circ$ the value of L_{fd} decreases, causing the inclination angle to increase up to approximately $\theta=30^\circ$ where it reaches a state of equilibrium. A comparison with values concerning the large obstacle shows that the final deposit length is the same for both cases at very high slopes (and consequently for the residual force as well). However, profiles rapidly diverge as the slope decreases and values become lower than those obtained in the case of the large obstacle. This is clearly due to, as for residual forces, the loss of a significant part of the beads' volume passing around the obstacle and leaving the measurement area.

An analytical model [36, 38, 51] is presented in section 1.4. This model, applied to steady regimes, requires a closure equation to calculate the length L_{fd} as $L_{fd}=H_{obs}/(\tan \alpha_{fd})$. Results show a qualitative agreement between experimental data and the analytical prediction. α_{fd} is generally assumed to be equal to $(\theta - \theta_{min})$. A fit was made for the α_{fd} value in order to minimise the gap between experimental results and the analytical prediction. Figure 1.39.b shows the results. In agreement with the measured values of L_{fd} , for a fixed H_{obs} (0.025 m), the minimum value of α_{fd} corresponds to the maximum value of L_{fd} for low slopes. These data are not very representative because L_{fd} becomes saturated. Beyond $\theta = 23^\circ$, α_{fd} increases with the slope. The length of the final deposit becomes shorter and the slope becomes steeper. For $\theta > \theta_{max}$, both values for L_{fd} and α_{fd} remain constant. These results confirm the influence that the characteristic angle θ_{max} has on the flow dynamics.

Residual forces are represented in Fig.1.40.a versus the slope angle. F_{res} increases gradually when the slope decreases and, unlike the large obstacle profile, values do not drop as the θ_{min} angle is approached.

Figure 1.40.b shows a comparison between residual forces obtained for both the obstacles and their corresponding analytical predictions. If the two profiles present a qualitatively similar trend, the difference in values is quantitatively relevant. Fig.1.40.c displays the ratio $\frac{F_{res}^{SO}}{F_{res}^{LO}}$ versus

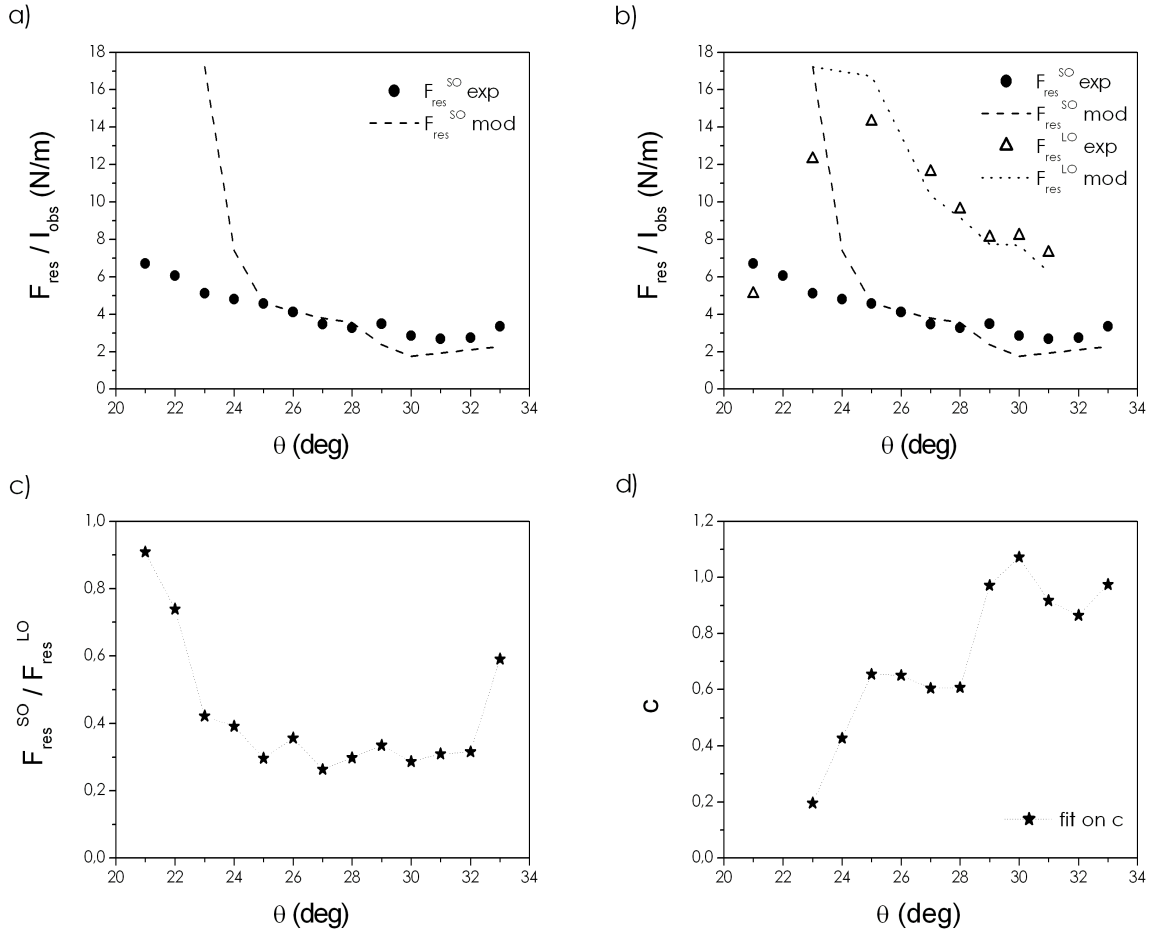


Figure 1.40: (a) Residual forces acting on the small obstacle versus the slope angle θ . Black dots represent the experimental results and the dashed line represents the model prediction. (b) Cross-comparison of analytical and experimental data obtained from the large (LO) and the small (SO) obstacle. (c) Residual force ratio versus the slope angle. (d) Values obtained from the fit of c versus the slope angle.

the slope angle θ . This ratio is close to 1 for very low slopes and it then decreases to stabilise at a rather constant value of approximately 0.3. Lastly, Fig.1.40.d presents the results obtained from a fit which was made on the shape coefficient c . $c = 0.66$ is a good value for a trapezoidal shape of the final deposit, which is the case for an obstacle spanning the channel.

However, when the lateral flow is allowed, the deposit shape becomes a tetrahedral and this value is most likely no longer as effective. By changing c , the gap between experimental data and the model can be improved. c was fitted in order to minimise this gap. Results are provided for $\theta > 23^\circ$ because the deposit length reaches saturation below this slope. After a rapid increase, the shape coefficient reaches a rather constant value close to $0.6 - 0.66$. However, c suddenly changes when passing the θ_{max} threshold and becomes very close to the unit for $\theta > \theta_{max}$. This behaviour suggests that the value assumed for c is well-adapted for slope angles below θ_{max} , even if the deposit shape changes. Beyond this slope, in the presence of an accelerating regime, the shape coefficient no longer plays a role in the computation of the residual force.

An additional study was conducted on the final deposit found at the end of the flow uphill from the small obstacle. The aim was to relate the final force value to the volume of the deposit. This volume was measured by developing a specific laser technique. The principle utilised is the same as that introduced in section 1.2.2: a laser line is projected along the channel and its

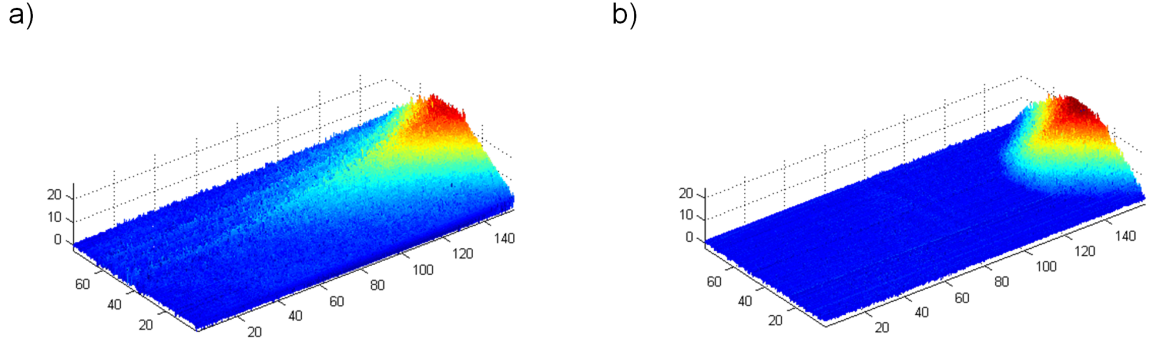


Figure 1.41: 3D representation of the final deposit obtained through a developed laser technique for (a) $\theta = 27^\circ$ and (b) $\theta = 33^\circ$.

position is deviated in the presence of an object. This new technique is operated in static conditions (and not during the flow). Once the flow stopped, the deposit was thoroughly scanned by using a moving laser beam. The same VLL laser from section 1.2.1 was used but mounted on a moving dolly in order to scan the whole deposit area. The measurements were differentials, and a calibration procedure calculated the deviation Δ of the laser line between the bottom of the channel and multiple standard plates, of known thickness, for all of the image's pixels. This method, applied to the final deposit, provided a 3D representation of the deposit volume. An example is given in Fig. 1.41.(a) for an intermediate (27°) and high (33°) slope. At low slopes below 25° , the deposit length became too long to be entirely included in the measurement area. Thus, for $\theta > 26^\circ$, the volume was calculated from the 3D model ($Vol.m$) and two types of validation were carried out. The first method consisted of recuperating all of the beads of the deposit in a cylinder and deriving the bead volume ($VolCyl$) with respect to the established cylinder volume. The second method consisted of weighing the bead volume recuperated and deriving the value of the volume ($VolMass$) from the particle density ($\rho_p = 2450 \text{ kg m}^{-3}$) and assuming a volume fraction $\phi = 0.6$.

Figure 1.42.a shows the results. The volume values are presented versus the slope angle and cross-compared with the measured residual forces. Even if both validation methods were approximative, they provided clearly consistent data. This confirms the conclusion that a volume fraction of $\phi = 0.6$ for beads at the standstill state is a reasonable value. On the other hand, values obtained from Matlab processing are systematically lower than the other two sets of data. The excellent agreement of these two sets leads us to think that the program developed underestimated real values. The precision of the laser technique (in the order of $1d_{beads}$) is probably not perfectly adapted for this type of precise measurement.

The volume data show a behaviour that is qualitatively similar to that of residual forces. Figure 1.42.b suggests a rather linear relation between the two parameters. However, at the current state, it is difficult to reach a exhaustive conclusion.

Although this new laser technique turned out to be promising, it still requires improvement. Time schedules did not allow a more detailed investigation of these features. It will be interesting to consider it for future work planning.

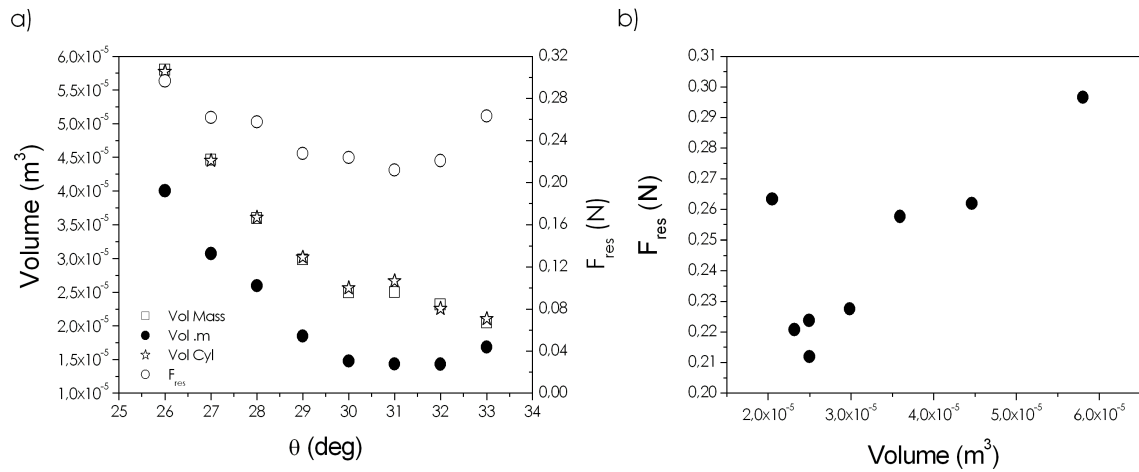


Figure 1.42: (a) Volume values (left y -axis) versus the slope angle θ compared to measured residual forces F_{res} (right y -axis). Volume measurements were taken with three different techniques: a laser technique ($Vol.m$), a volume method ($VolCyl$) and a mass method ($VolMass$). (b) Residual forces versus the volume values obtained with the mass method.

The results presented in this chapter indicate the presence of a zone, upstream from the obstacle, where the incoming flow is disturbed by the presence of the wall-like structure (see Fig.1.25 for details). This zone was called the influence zone and its relevant role to the flow dynamics ultimately led our attention to a special analysis of the behaviour of this influence zone. The next section presents this analysis in detail.

1.3.4 The influence zone uphill from the obstacle

The previous sections highlight the important role that the influence zone has in the dynamics of a dry granular flow and in the definition of the involved forces. Interest in this influence led to an accurate analysis of the influence zone behaviour. Attention was focussed on the evolution of its free surface over time. Two different methods were used to handle this study. The laser technique was employed to investigate the height evolution of the free surface upon impact with the obstacle, and a high frequency video camera recorded tests from the channel side and allowed a special image treatment process. Initially, the PIV technique was supposed to be used to investigate the behaviour of the surface flow velocity upon impact with the obstacle. Nevertheless, this type of measurement was not found to be effective. As mentioned in section 1.2.2, this method is based on the assumption that the granular material, during the flow, moves downward as a whole, with the same velocity as the flow. However, upon impact with the obstacle, this assumption is no longer valid and thus this technique is no longer reliable. Results are presented in this section. An initial rough analysis of the obtained videos (side-view) gives the impression that a transition occurs in the dead zone regime. This is confirmed by both measurements.

Free surface height measurements

The laser technique allows us to draw the free surface profile of the influence zone at different times. Figure 1.43.a shows the flow height h normalised over the beads' diameter d , along the x -axis uphill from the obstacle. At $0 < t < 1.335$ s the avalanche front arrives, it hits the obstacle and a jet occurs. Near $t=2$ s a dead zone regime is reached. A quasi-static triangular zone forms uphill from the obstacle and the inertial flow starts overflowing (Fig.1.43.b). This inertial layer becomes thicker ($t=2.29$ s) and then thinner again before the transition starts. At $3.15 < t < 4.72$ s the influence zone switches from a dead zone to a granular jump regime (Fig.1.43.c). Curves show a change in the influence zone shape. The triangular quasi-static zone develops into more of a trapezoidal surface, increasing in volume and progressing uphill in the opposite direction of the flow until the motion stops. This new regime is characterised by a discontinuity in flow depth and surface velocity. Figure 1.43.d is equivalent to a view from above the channel axis where it is possible to visualise the obstacle and the position of the influence zone front (y -axis) throughout the flow duration (x -axis). Height values, the position along the x -axis, and the times all match well with values in Fig.1.43.a.

A problem occurs when using the laser technology to measure the height of the free surface flow upon impact with the obstacle. As explained in section 1.2.2, the laser technique was calibrated with a range of heights, from 0 to 24 mm. However, the interaction between the flow and the obstacle brings to height values up to 40 mm. Nevertheless, cross-comparison with results obtained from other techniques show consistent results even if they are beyond the calibration range.

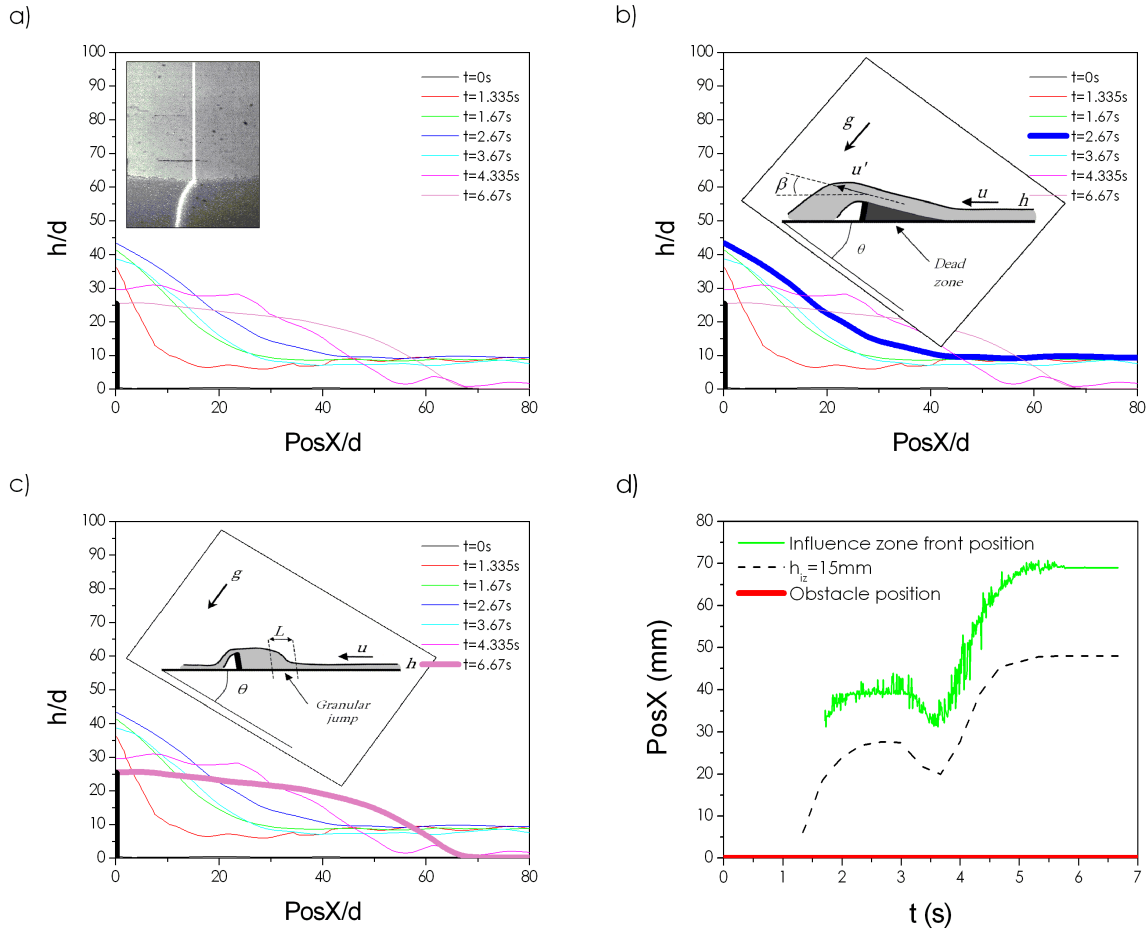


Figure 1.43: (a) Flow height versus the position uphill from the obstacle. Data are obtained with the laser technique and taken at different points t of the flow. (b) Comparison between experimental results and the theoretical profile characterising a dead zone regime and (c) a granular jump regime. (d) Position of the influence zone border line along the x -axis over time t .

Free surface evolution by video measurements

Figure 1.44 *a*, *b* and *c* show results obtained from the accurate treatment of side-view images that were introduced in the last section. As previously mentioned, three parameters were chosen to describe the evolution of the influence zone (see Fig.1.26.d): its mean slope α_{iz} , its length L_{iz} and its surface S_{iz} . Figures show α_{iz} , L_{iz} and S_{iz} versus time t . The flow phases that were found with laser measurements can here be re-identified with greater precision. Near $t=1$ s the front arrives at the obstacle (phase 1). The α_{iz} angle reaches very high values (jet effect) and the raw data of L_{iz} and S_{iz} fluctuate. At $1 < t < 2$ s the influence zone generates (phase 2), the uphill deposit assumes a triangular shape, α_{iz} decreases, and L_{iz} and S_{iz} start increasing. The dead zone reaches a stationary regime around $2 < t < 3.5$ s : α_{iz} and L_{iz} stabilise at a rather constant value ($d/dt=0$, phase 3). S_{iz} experiences an increasing-decreasing phase due to the thickening-thinning process of the inertial layer flowing above the dead zone, as shown by flow depth measurements. After $t \simeq 3.5$ s the transition starts (phase 4). The granular jump leads to the dead zone regime. The transition implies a decrease of α_{iz} and an increase of L_{iz} until the flow stops. As the influence zone progresses upward, S_{iz} increases. A short decreasing of the surface value follows just before the end of the motion due to the fact that the last portion of the avalanche volume flows down the channel eroding a part of the final volume. After $t \simeq 5.2$ s the avalanche flow comes to a standstill. The final deposit, stored uphill from the obstacle, is then

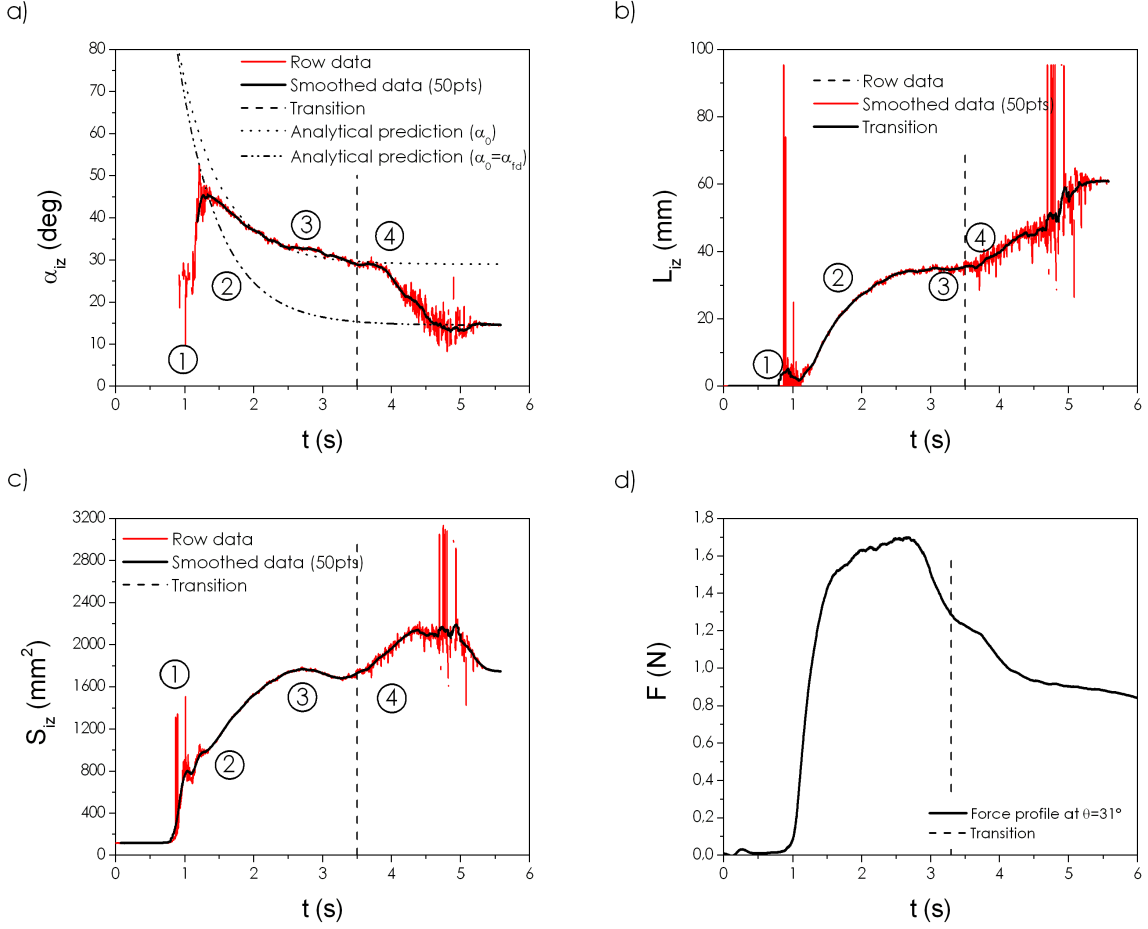


Figure 1.44: Results obtained from side-view measurements, at $\theta=31^\circ$, concerning: (a) the influence zone mean angle α_{iz} versus time t , (b) the length L_{iz} versus t and (c) the surface S_{iz} versus t . The dashed line indicates the transition time derived from experimental data analysis. (d) Mean force value F versus the time t at $\theta=31^\circ$. The dashed line corresponds to the time t^* theoretically obtained.

characterised by constant values of the three parameters corresponding to static conditions. The final value of L_{iz} is in a few millimetres of agreement with the value obtained from the laser technique. This difference is due to the fact that the two measurements are not from the same test. Laser measurements must be done in the dark while side videos do require light. The transition presented here provides new insight into understanding influence zone behaviour. In the previously cited analytical model, applied to unsteady regimes (see section 1.4.2), the influence zone parameters L_{iz} and α_{iz} are defined as follows.

An empirical exponential law defines the angle α_{iz} as:

$$\alpha_{iz}(t) = \alpha_0 + \left(\frac{\pi}{2} - \alpha_0\right) e^{-\frac{T_i - t}{\tau_{iz}}} \quad (1.52)$$

and the length L_{iz} :

$$L_{iz}(t) = \frac{H_{obs}}{\tan(\alpha_{iz}(t))} = \frac{H_{obs}}{\tan\left(\alpha_0 + \left(\frac{\pi}{2} - \alpha_0\right) e^{-\frac{T_i - t}{\tau_{iz}}}\right)} \quad (1.53)$$

(see for further detail [36]). α_0 is the value of α_{iz} reached for the stationary regime which, in this case, corresponds to the value reached during the constant uniform phase. T_i the time of impact of the flow on the structure and τ_{iz} is the characteristic time for the formation of the influence zone.

For the analytical model presented in section 1.4, τ_{iz} is fixed at 0.4 s on the basis of the DEM simulation reported in [38]. For each slope incline, the τ_{iz} coefficient was chosen in order to obtain the best value for the final deposit length L_{fd} with respect to the values experimentally measured. This value was found to be rather constant and equal to 0.4 s.

Note that the DEM simulations considered a ratio $H_{obs}/h = 1$, which was not the case for experimental tests. In our case this ratio varies and it never reaches the unit value. Furthermore, $L_{iz}(t)$ and $\alpha_{iz}(t)$ are measured during the entire flow duration. Measurements on the influence zone length can be considered very precise. $\alpha_{iz}(t)$ is calculated as described in section 1.2.2, assuming that the influence zone is a trapezoid with a basis of z_{ref} and $z(x_{max})$ (with respect to the notation in Fig.1.26.d) and height L_{iz} . This assumption is well-verified for a dead zone regime, but it becomes less realistic when a granular jump occurs. Figure 1.44.a compares the experimental data with the model prediction setting $\alpha_0=29^\circ$, $T_i=0.8$ s and $\tau_{iz}=0.6$ s. The analytical model aptly represents the behaviour of $\alpha_{iz}(t)$ during the formation of the influence zone until the stationary phase, but it cannot reproduce the transition. If the model is forced in order to stabilise α_{iz} at a value corresponding to the angle α of the final deposit ($\alpha_0 = \alpha_{fd} = 14.5^\circ$), the law is no longer reliable except for the final slope value.

This result proved that the analytical model can aptly describe the behaviour of the influence zone in a dead zone regime, but it fails when a transition to a granular jump regime occurs. Implementing this new contribution into the analytical model is beyond the scope of the present work, but this finding highlights the interest as well as the diverse perspectives of this type of study.

Experiments have proven that the transition occurs at a time t^* close to 3.5 s. Figure 1.44.d shows the time-dependent force signal obtained from force measurements at $\theta=31^\circ$. The curve is characterised by an increase in values until reaching a maximum, preceding a decreasing phase. A change in the decreasing trend can be observed near $t=t^*$. Previous interpretations of this type of data did not confer any peculiarity to the trend, but when it is viewed with the awareness of such a transition, at a time $t^* \simeq 3.5$ s the force profile reveals a temporary change in its behaviour. This is probably due to the effect of the transition on the force acting on the obstacle.

The dead zone to granular jump transition was analysed in greater detail. According to the classic analysis of the bi-dimensional hydraulic jump, the mass and momentum fluxes are conserved across the jump while the mechanical energy dissipates [75]. Equation (1.54) is obtained by writing the mass and momentum conservation across a stationary jump in order to calculate the critical obstacle height H_c that can generate a jump:

$$\frac{H_c}{h} = \frac{1}{2} \left(\sqrt{1 + 8Fr^2} - 1 \right) - Fr^{2/3} \quad (1.54)$$

Four main assumptions can be made: the density ρ is constant, the incoming regime is stationary, friction dissipations and gravity forces are not considered (see for further detail: section 1.1.4). This equation was compared to the ratio $H_{obs}/h(t)$, where H_{obs} is the obstacle height ($H_{obs}=0.025$ m) and h corresponds to the experimental data obtained for the reference flow depth at $\theta=31^\circ$. Figure 1.45.a shows the ratios $H_{obs}/h(t)$ and H_c/h plotted versus time t . The two curves cross at time $t=3.3$ s, which roughly corresponds to the time t^* at which the dead zone to granular jump transition occurred in the laboratory analysis of the side-view videos. This analytical result represents an initial validation of the obtained experimental data. Equation (1.54) only depends on the flow Froude number, meaning its height and its velocity.

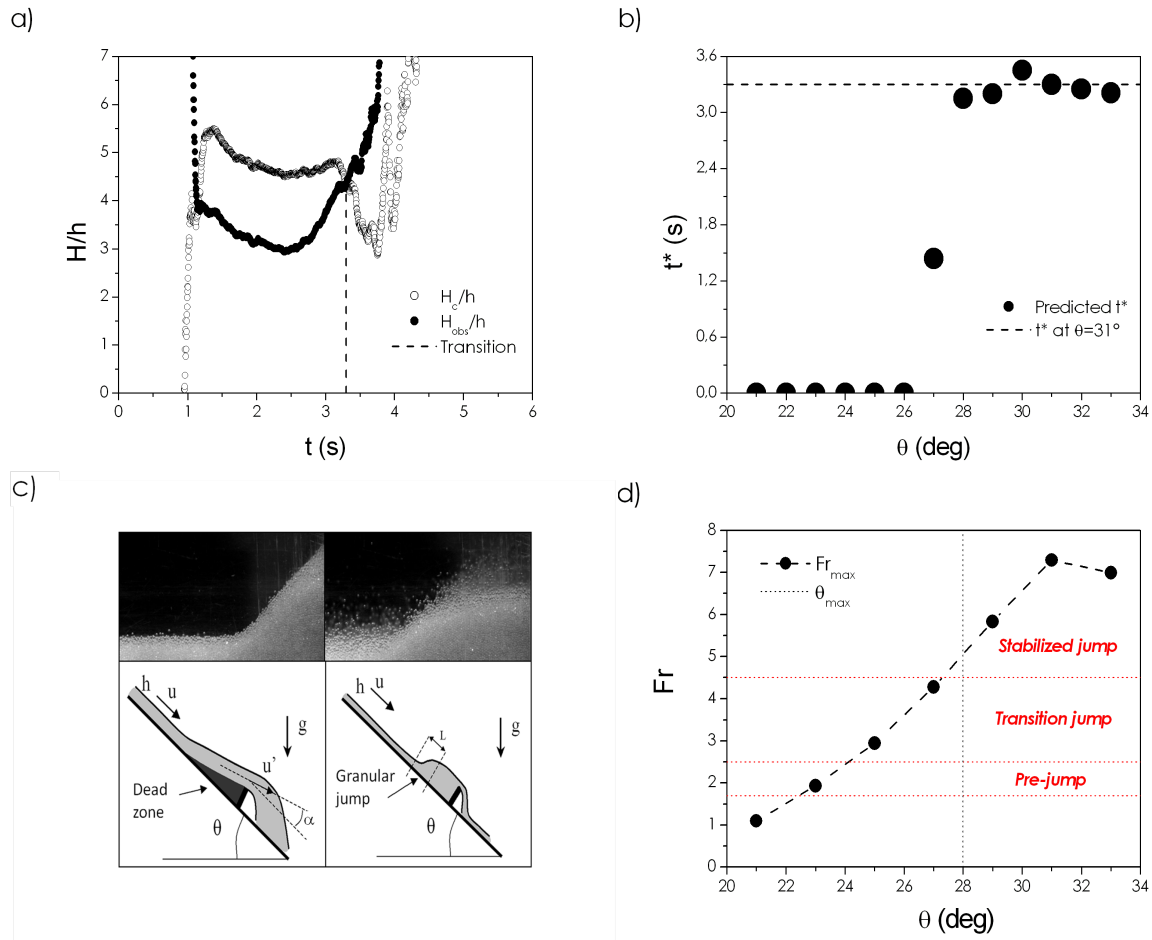


Figure 1.45: (a) Comparison between the theoretical ratio H_c/h and the experimental ratio H_{obs}/h versus time t . The intersection between the two curves indicates the time at which the transition should occur. (b) Transition time versus the slope angle. Values represent a prediction based on reference measurement data. (c) Sketches representing the dead zone and granular jump regimes with respective images corresponding to the two phases that occur during the flow. (d) Maximum Froude number versus the slope angle. The vertical dashed line corresponds to $\theta = \theta_{max}$ whereas the horizontal dotted lines represent the Hager [71] classification thresholds.

Thus, even if this detailed analysis was done for only 31° , using experimental data coming from reference tests ($\theta=21^\circ - 33^\circ$), it was possible to theoretically estimate the time t^* for all of the inclines. Figure 1.45.b shows the estimated t^* versus the slope angle θ . The results represent an analytical prediction that must still be validated by laboratory tests. According to these results, the transition from dead zone to granular jump regime would not occur for $\theta < \theta_{max}$. Beyond the θ_{max} angle, however, transitions generate at a rather constant time t and equal $3.2 - 3.3$ s. Another possibility could be reading this transition as an effect of the unsteady nature of the flow. Since the volume of glass beads is limited, this could be interpreted not as a transition, but rather as simple consequence of the beads' depletion coming to standstill. The cross-comparison between experimental and analytical results makes us lean towards the transition assumption. However, the finite volume should somehow influence this phenomenon.

Within the framework of hydraulics, Hager (1992) [71] classified granular jumps depending on the Froude number magnitude of the incoming flow:

- *Pre-jump* if $1.7 < Fr < 2.5$. The water surface is quite smooth and the velocity distribution is fairly uniform. The efficiency of the jump is low.

- *Transition jump* if $2.5 < Fr < 4.5$.
- *Stabilized jump* if $4.5 < Fr < 9$. These jumps have relatively high energy dissipation and they present a compact and stable appearance.
- *Choppy jump* for $Fr > 9$.

Figure 1.45.d shows the Froude values of the incoming flow Fr as a function of the slope θ . Coupling these data with the aforementioned classification could bring an additional contribution to the "transition theory." The granular flow would only be affected by the *stabilized jump*. The slope (θ_{max}) and the Froude ($Fr=4.5$) thresholds correspond to the obtained results. However, the same classification applied to granular flows would be necessary to validate this finding. A similar work has already been done by Brennen et al. (1983) [27], but further experiments should be carried out to confirm the results that we obtained.

This last outcome represents a curious result coming from small-scale physical modelling which should be validated by new experiments or by different approaches. As acknowledged throughout the entire dissertation, the study of a complex phenomenon such as snow avalanches requires a strategy based on different approaches in order to corroborate the results. From this perspective, an analytical model was developed in parallel with the PhD experimental work, in order to predict the force acting on a wall-like obstacle during granular flows. Experimental results provided a fundamental contribution to this research as they were able to validate the analytical predictions.

The next sections present this model, from its first draft intended for steady flows, to its improvements for unsteady conditions, up to model validation through numerical and experimental results.

1.4 The analytical force model

The force exerted by a granular flow on an obstacle is an important matter concerning a large number of processes [45, 54, 84, 148, 151, 156]. Previous chapters have proven that when a granular flow hits an obstacle, a nearly triangular dead zone forms uphill from the obstacle. The length of this zone depends on the slope incline and it is constant in steady flow regimes, while it varies with time when dealing with non-steady flows. The dead zone significantly influences the force exerted on the obstacle. This influence has already been proven with discrete numerical simulations [51] as confirmed by the experimental results shown in section 1.3.

For granular flows down an incline in stationary regimes, a depth-averaged hydrodynamic analytical model was proposed to calculate the normal force acting on a wall-like obstacle [51] and is described in the following sections. Section 1.4.1 presents the first version, simplified for steady flows. Afterwards, the model was adapted to time-varying phenomenon occurring in non-steady regimes [38]. These improvements are detailed in section 1.4.2. The model predictions were compared with results obtained from discrete numerical simulations (see [37] for details) and, within the framework of this PhD work, to the experimental results presented in section 1.3. The cross-comparison results are shown in section 1.4.3 (numerical data) and section 1.4.4 (experimental data).

1.4.1 Model's equations for steady flows

Figure 1.46 shows a sketch of the granular flow interacting with a wall. A cohesionless dry granular material flows down a rough incline with a constant slope θ and hits a wall-like obstacle of height H_{obs} . A dead zone of length L_{dz} forms uphill from the obstacle while an inertial layer starts flowing above and a jet occurs downhill from the wall. For the sake of simplicity, we assumed here that the dead-zone length corresponds to the influence zone length ($L_{dz} = L_{iz}$). By applying the momentum conservation to the control volume (hatched zone in Fig.1.46), the model calculates the normal force acting on the wall (x -axis) as:

$$F_n = F_{kin} + F_{hyd} + F_w - F_f \quad (1.55)$$

Note that, as mentioned in section 1.3.3, we refer to force for the sake of simplicity, but these are forces per unit length ($\frac{F}{l_{obs}}$).

This force represents the sum of four main contributions: a kinetic force F_k , a hydrostatic force F_h , the force resulting from the control volume weight F_w and the basal friction force F_f .

These forces were defined as:

$$F_{kin} = \beta_u \bar{\rho} \bar{u}^2 h \left[1 - (1 - \kappa \alpha_{jet}^0) \cos \alpha_{jet}^0 \right] \quad (1.56)$$

$$F_{hyd} = \frac{1}{2} k \bar{\rho} g h^2 \cos \theta \quad (1.57)$$

$$F_w - F_f = \left[\bar{\rho} \left(V_0 - \frac{1}{2} L_{dz} H_{obs} \right) + \frac{1}{2} \rho_{dz} L_{dz} H_{obs} \right] g (\sin \theta - \mu_{dz} \cos \theta) \quad (1.58)$$

where β_u represents the Boussinesq coefficient equal to $\frac{\bar{u}^2}{u^2}$. κ is a velocity reduction factor equal to $(1 - e)/(\pi/2)$, and e is the restitution coefficient [51]. k is the earth pressure coefficient

[121, 136] representing the ratio between the two normal stresses σ_{xx} and σ_{zz} . $\bar{\rho}$ corresponds to the mean density of the overall control volume and ρ_{dz} is relative to the dead zone ($\bar{\rho} < \rho_{dz}$). Details on how to derive these equations can be found in Faug et al. (2009) [51]. Some additional equations were needed in order to close the model. They concern (i) the jet deflecting angle α_{jet}^0 , (ii) the dead zone angle α_{dz}^0 , (iii) the free surface angle α_{iz}^0 , (iv) the control volume V_0 , (v) the length L_{dz} of the influence zone and (vi) the basal friction coefficient μ_{dz} , respectively:

$$\alpha_{jet}^0 = \frac{\alpha_{dz}^0 + \alpha_{iz}^0}{2} \quad (1.59)$$

$$\alpha_{dz}^0 = \theta - \theta_{min} \quad (1.60)$$

$$\alpha_{iz}^0 (\theta < \theta_{max}) = \frac{\theta_{min}}{\theta_{max} - \theta_{min}} (\theta - \theta_{min}) \quad (1.61)$$

$$\alpha_{iz}^0 (\theta > \theta_{max}) = \frac{\pi}{2} - \left(\frac{\theta_{min} - \frac{\pi}{2}}{\theta_{max} - \frac{\pi}{2}} \right) \left(\frac{\pi}{2} - \theta \right) \quad (1.62)$$

$$V_0 = \frac{1}{2} h L_{obs} \left[2 + \tan \left(2\alpha_{jet}^0 - \arctan \frac{H_{obs}}{L_{dz}} \right) \left(\frac{L_{dz}}{h} - \delta_h \sin \alpha_{jet}^0 \right) + \frac{\delta_h}{L_{dz}} (H_{obs} - h) \sin \alpha_{jet}^0 \right] \quad (1.63)$$

$$L_{dz} = \frac{H_{obs}}{\tan(\theta - \theta_{min})} \quad (1.64)$$

$$\mu_{dz} = \tan \theta_{min} \quad (1.65)$$

With respect to Fig.1.46, u is the velocity of the incoming undisturbed flow (section A) and h is its height, while u^* and h^* are the flow parameters at section A^* . δ_u represents the velocity ratio $\frac{u^*}{u}$ ($\delta_u = 1 - \kappa\alpha$) and, similarly, $\delta_h = \frac{h^*}{h} = (1 - \kappa\alpha)^{-1} = \frac{1}{\delta_u}$ (assuming $\rho \simeq \rho^*$).

The entire set of calculations required to obtain these equations can be found in [51]. These equations are valid for steady regimes. For unsteady conditions, an additional time-dependent contribution must be considered. The next section discusses the assumptions and improvements needed for the model in order to become operational in non-steady regimes.

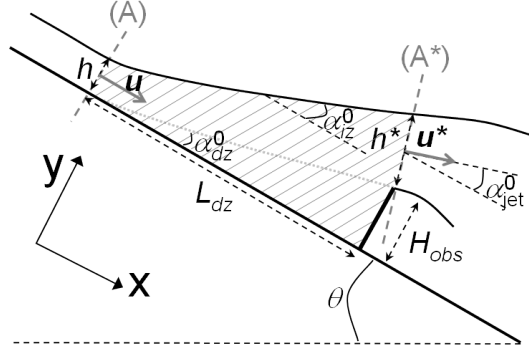


Figure 1.46: Sketch of the control volume V_0 considered in the mass and momentum balance. The section (A) is normal to the channel bottom and represents the uphill border of the influence zone. h and u are the parameters of the incoming and undisturbed flow at section (A). Section (A*) is normal to the main direction of the flow leaving the influence zone and h^* and u^* are the flow parameters at section (A*). L_{dz} is the length of the dead zone and H_{obs} the obstacle height. α_{dz}^0 , α_{iz}^0 and α_{jet}^0 are the dead zone angle, the free surface angle and the jet angle, respectively. The three angles are evaluated with respect to the bottom of the channel. The sketch is taken from [38]

1.4.2 Model's equations for unsteady flows

Working with finite volume granular avalanches means that time dependency must be taken into account. The analytical model introduced in the previous section needs to be adjusted by considering an additional term $\frac{d}{dt}(\int \int_V \rho u dV)$ in the momentum balance. The time-varying flow depth $h(t)$, the depth-averaged velocity $\bar{u}(t)$ and the depth-averaged density $\rho(t)$ are also needed.

Assuming that $t=0$ s corresponds to the avalanche release and that the averaged velocity inside the dead zone is equal to zero:

$$\frac{d}{dt} \left(\int \int_V \rho u dV \right) = \frac{d}{dt} \left(\int \int_{V_0 - \frac{1}{2}H_{obs}L_{dz}} \rho u dV \right) \quad (1.66)$$

and thus the following approximation was introduced:

$$\frac{dM}{dt} = \frac{d}{dt} \left(\int \int_V \rho u dV \right) \cdot x \simeq \frac{d}{dt} \left[\rho_V u_V \left(V_0 - \frac{1}{2}H_{obs}L_{dz} \right) \right] \quad (1.67)$$

where u_V and ρ_V represent the mean velocity and density relative to the volume $V_0 - \frac{1}{2}H_{obs}L_{dz}$. The time dependency of the two angles α_{dz} and α_{iz} is introduced by assuming an exponential increase of their value before they reach an asymptotic value α_{dz}^0 and α_{iz}^0 .

$$\alpha_{dz}(t) = \alpha_{dz}^0 + \left(\frac{\pi}{2} - \alpha_{dz}^0 \right) e^{-\frac{(T_i-t)}{\tau_{iz}}} \quad (1.68)$$

$$\alpha_{iz}(t) = \alpha_{iz}^0 + \left(\frac{\pi}{2} - \alpha_{iz}^0\right) e^{-\frac{(T_i-t)}{\tau_{iz}}} \quad (1.69)$$

α_{dz}^0 and α_{iz}^0 correspond to the steady state values. τ_{iz} is a characteristic time for the influence zone formation and T_i corresponds to the time of impact. Equation (1.68) and Eq.(1.69) are valid for $t \geq T_i$ whereas, for $t < T_i$, α_{dz} and α_{iz} are equal to $\frac{\pi}{2}$. The comparison with numerical data showed that results are clearly represented by the model when setting the value of τ_{iz} at 0.4 s. The time-varying length of the influence zone then becomes:

$$L_{dz}(t) = \frac{H_{obs}}{\tan[\alpha_{dz}(t)]} \quad (1.70)$$

and the control volume is converted to a time-dependent variable by providing the time-varying values of $L_{dz}(t)$ and $\alpha_{dz}(t)$ (see Eq.(1.63) for the definition of V_0). Lastly, the same relationship is maintained for the computation of the basal friction coefficient μ_{dz} , but the time-dependency is introduced through the dead zone angle α_{dz} :

$$\mu_{dz}(t) = \tan[\theta - \alpha_{dz}(t)] \quad (1.71)$$

This is how the analytical model was adapted to non-stationary regimes. It is efficient to predict the normal force exerted on a wall-like obstacle by a finite-sized granular avalanche. To validate the model, the predictions were compared to results from numerical modelling and experimental simulations.

1.4.3 Model's predictions compared to previous discrete numerical simulations

Numerical results were obtained from discrete simulations using the molecular-dynamics model [44, 46, 50, 143]. Rigid spheres interact with one another. The normal force is modelled by a damped linear spring, and a linear spring, restricted to a threshold value (according to friction between grains described by a Coulomb condition), represents the tangential force. More details on this method can be found in [37, 51] and references therein.

Discrete numerical simulations reproduce 2D spheres ($d=1$ mm with a small poly-dispersity: $\pm 10\%$ in size) flowing down a rough incline. The particle density is $\rho_p = 2450$ kg m⁻³ (glass material) and the investigated slopes range from 16° to 32°. The time-dependent force exerted by the granular flow on an obstacle of height H_{obs} is measured at a distance $\frac{x}{d} = 500$ from the releasing gate. The obstacle height is set to equal the maximum height of the incoming and undisturbed flow at $x = 500d$.

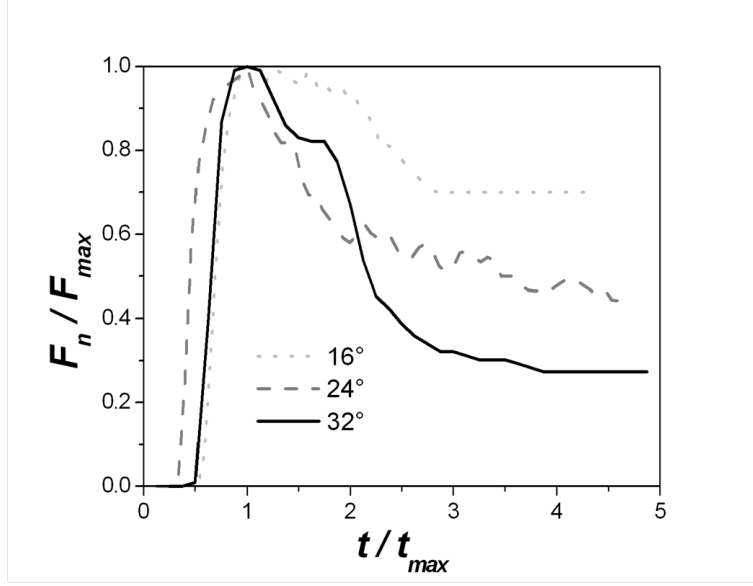


Figure 1.47: Normal force, scaled by its maximum value, versus a dimensionless time (moving average of 0.2 s). The curves represent the analytical prediction of the normal force for three representative slope angles.

Figure 1.47 shows the time-varying forces for three representative slopes (16° , 24° and 32°). As already mentioned in section 1.3.2 for experimental data, force profiles typically present (i) an initial phase of value increase, (ii) a peak and (iii) a decreasing phase. Obtained numerical results were cross-compared with the model predictions and the model sensitivity was analysed with respect to the basal friction coefficient μ_{dz} , the time-derivative term in the momentum balance, and the model's set of parameters κ , k and β_u .

Figure 1.48 resumes all of the obtained results. A time-dependent basal friction coefficient (instead of a constant coefficient) provides profiles which are consistent with the numerical data when considering the increasing and maximum value phases (Fig.1.48 a, b, and c). However, discrepancies persist in the decreasing phase. The temporal variation of the momentum balance is defined in Eq.(1.67) and it did not prove to be very helpful for improving the model prediction. Figure 1.48 d, e and f show this influence. At any rate, a small contribution is made within the force increasing phase where consideration of the $\frac{dM}{dt}$ factor yields a better fit between numerical and analytical data.

The influence of three model parameters was also analysed. Different values of the earth pressure coefficient k , the velocity reduction factor κ and the Bousinesq coefficient β_u were tested. Results are shown in Fig.1.48 g, h and i. Varying these parameters leads to a slight improvement of the model prediction for the increasing and maximum phase of the force profile. Moreover, this small positive influence exists only for high slopes whereas the model sensitivity to these parameters is insignificant at low slopes for the three phases.

Thus, adjusting the model by fitting all of the aforementioned parameters shows how significant improvements can contribute to analytical prediction. Yet these improvements mainly concern the increase and maximum phase of a typical force signal. To reduce the gap between the analytical and numerical results, an additional fit was achieved through the basal friction coefficient. Assuming that:

$$\mu_{dz}(t)^* = c_\mu \tan[\theta - \alpha_{dz}(t)] \quad (1.72)$$

the basal friction coefficient is equal to the one defined in Eq.(1.71) times a calibration parameter c_μ . Figure 1.48 j, k and l show the results. The values of c_μ were derived in order to minimise the difference between numerical and analytical profiles (least square method). Figure 1.49 shows

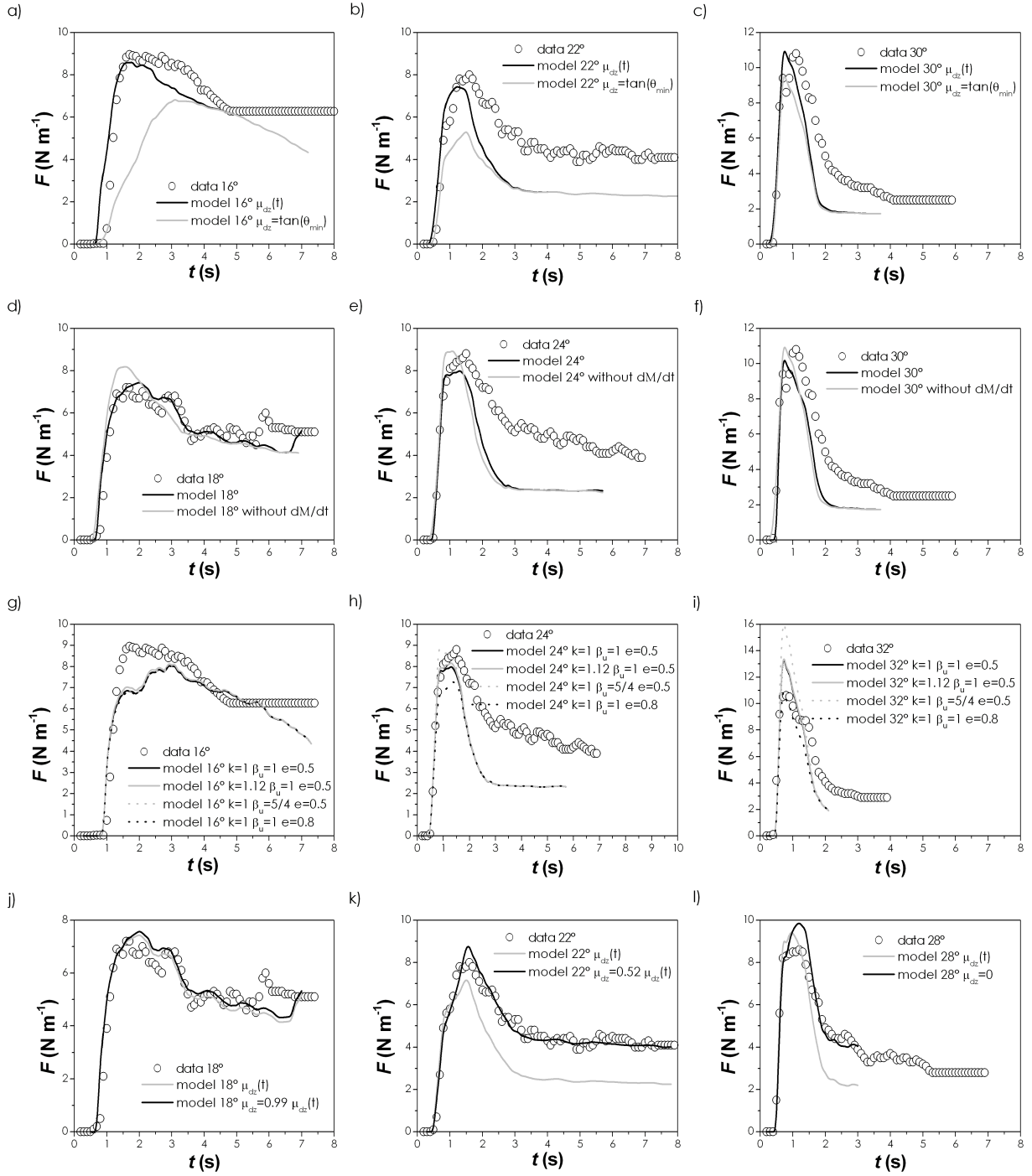


Figure 1.48: The time-averaged force versus time. Comparison between the numerical data (\circ) and the analytical model prediction: (a), (b) and (c), using $\mu_{dz}(t) = \tan[\theta - \alpha_{dz}(t)]$ (black line), or $\mu_{dz} = \text{const} = \tan\theta_{min}$ (gray line). The following values were considered: $\theta_{min}=14^\circ$, $\theta_{max}=24^\circ$, $k = 1$, $\kappa = 0.32(e=0.5)$, $\beta_u = 1$ and $\phi_{max} = 0.64$. Three examples are given for $\theta=16^\circ$, 22° and 30° . (d), (e) and (f), considering the time-derivative term in the momentum balance (black line), or not (gray line). The following values were considered: $\theta_{min}=14^\circ$, $\theta_{max}=24^\circ$, $k = 1$, $\kappa = 0.32(e=0.5)$, $\beta_u = 1$ and $\phi_{max} = 0.64$. The friction coefficient was considered as $\mu_{dz}(t) = \tan[\theta - \alpha_{dz}(t)]$. Three examples are given for $\theta=18^\circ$, 24° and 30° . (g), (h) and (i), testing different sets of parameters (i) $k = 1$, $\kappa = 0.32(e=0.5)$, $\beta_u = 1$ (solid black line), (ii) $k = 1.12$, $\kappa = 0.32(e=0.5)$, $\beta_u = 1$ (solid gray line), (iii) $k = 1$, $\kappa = 0.32(e=0.5)$, $\beta_u = 5/4$ (dashed gray line) and (iv) $k = 1$, $\kappa = 0.13(e=0.8)$, $\beta_u = 1$ (dashed black line). The friction coefficient was considered as $\mu_{dz}(t) = \tan[\theta - \alpha_{dz}(t)]$, $\theta_{min}=14^\circ$ and $\theta_{max}=24^\circ$. Three examples are given for $\theta=16^\circ$, 24° and 32° . (j), (k) and (l), using $\mu_{dz}(t) = \tan[\theta - \alpha_{dz}(t)]$ (black line), or $\mu_{dz} = c_u \tan[\theta - \alpha_{dz}(t)]$ (gray line). The following values were considered: $\theta_{min}=14^\circ$, $\theta_{max}=24^\circ$, $k = 1$, $\kappa = 0.32(e=0.5)$, $\beta_u = 1$ and $\phi_{max} = 0.64$. Three examples are given for $\theta=18^\circ$, 22° and 28° .

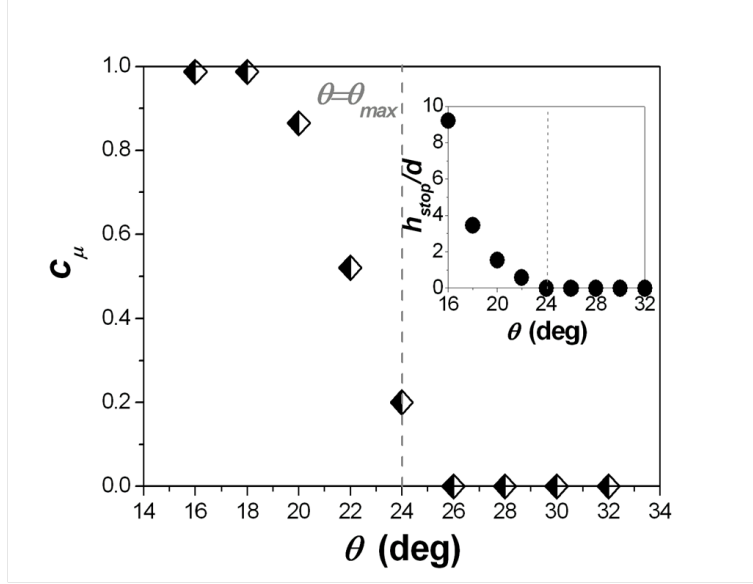


Figure 1.49: Obtained best-fit values for the calibration coefficient c_μ versus the slope θ . The inset shows the $h_{stop}(\theta)$ behaviour of the granular material modelled in numerical simulations.

the chosen values of the calibration parameter as a function of the slope angle. The θ_{max} angle (see section 1.1.2) for treated discrete numerical simulations is 24° . Results show a clear change in behaviour occurring around θ_{max} . It is difficult to explain the observed trend. Its behaviour is probably related to the function $h_{stop}(\theta)$ represented in the insert in Fig.1.49. In the absence of an obstacle, referring to the experimental findings of section 1.3, it is reasonable to assume that for $\theta > \theta_{max}$, we deal with a diluted regime where the granular flow is constantly accelerated and thus the effective basal friction equals zero. However, for $\theta < \theta_{max}$, a deposit remains on the bottom and the deposit thickness increases as the slope angle increases, suggesting that the basal friction also increases.

In the presence of an obstacle, due to lack of better knowledge of the frictional processes involved at the base of the dead zone (no friction measurements were taken), we can only suggest a potential relationship between the $h_{stop}(\theta)$ function and the obtained results. The interpretation of such behaviour was beyond the scope of this work and remains an open question. One of the advantages of analytical model prediction is that the different components of the normal force F_n (see Eq.(1.55)) can be considered separately and their contribution can be observed over time. Figure 1.50 *a*, *b* and *c* show all of these contributions for a low (16°), intermediate (24°) and high slope (32°). Possible observations go back to the considerations made in section 1.3.2. The graphs show that the most relevant contribution is given by the kinetic force at high slopes. The maximum force is purely kinetic. Nevertheless, at low slopes, the difference between the control volume weight and the basal friction predominates. Lastly, a final comment must be done regarding the decreasing phase of the force profiles. For all slope angles, the total normal force acting on the obstacle is mainly influenced by the difference $F_w - F_f$.

When a finite-sized granular avalanche reaches a wall-like obstacle, a dead zone forms uphill and highly influences the normal force acting on the wall. This total force is clearly predicted by the presented analytical model. The cross-comparison with data obtained from discrete numerical simulations allows the calibration of the model.

The following section presents further improvements that were made by comparing the model prediction with the experimental results presented in section 1.3.

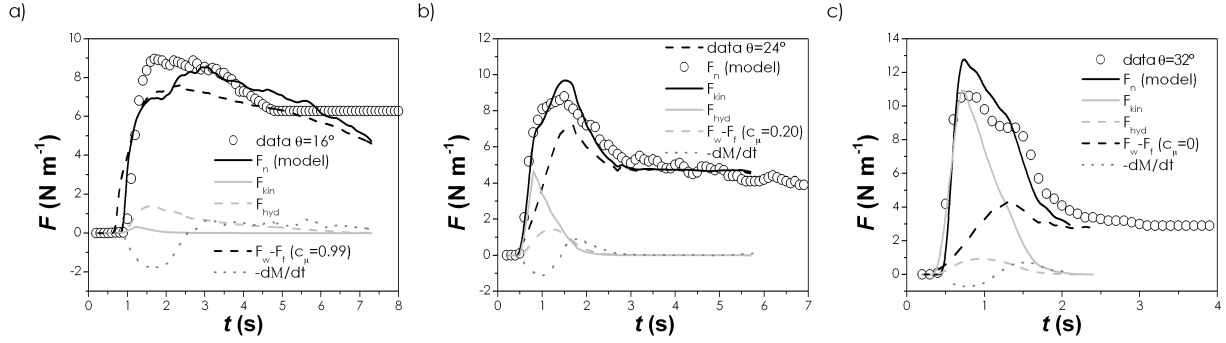


Figure 1.50: Normal force acting on the obstacle versus time t (black line). The model allows the separation of three contributions of Eq.(1.55) as well as their independent display: the kinetic force (grey line), the pressure force (grey dashed line) and the $F_w - F_f$ contribution. The influence of the time-derivative term in the momentum balance is also given. Three examples are shown for 16° , 24° and 32° .

1.4.4 Model's predictions compared to experimental results

The model's prediction quantitatively matches the experimental data. Even if the results are consistent, two different fit procedures can be applied in order to enhance this agreement. The volume fraction $\bar{\phi}(t)$ corresponds to $\theta > \theta_{max}$ and the τ_{iz} coefficient, on the other hand, was adapted for slope angles close to θ_{min} ($\theta < 25^\circ$). Figure 1.51 shows the final results. Particular attention is required for the volume fraction coefficient. Despite the lack of experimental measurements of $\bar{\phi}(t)$, this was calculated as a function of the inertial number $I(t)$ as given in Eq.(1.48) and its maximum value ϕ_M was considered. However, preliminary tests showed that setting $\phi_M = \phi_{min}$ ($=0.4$) provides better results for $\theta < \theta_{max}$. Beyond the θ_{max} angle, the gap between the analytical prediction and experimental profiles can be even further decreased by fitting the value of ϕ_M independently for all of the slope angles. The values obtained in this manner are shown in Fig.1.52.a. Results are presented in the form of a difference $\phi_{fit} - \phi_M$. We assumed that, for $\theta < \theta_{max}$, $\phi_{fit} = \phi_M = \phi_{min}$. Above θ_{max} this difference increases with the slope. This behaviour can be seen, consistent with the experimental findings detailed in section 1.3.2, as a further expression of the presence of the dense to diluted transition. Otherwise, results shown in Fig.1.52.a could also be related to an artefact on the fitting procedure of ϕ . Taking into account all of the experimental evidence indicating the effect of the dense to diluted transition, we lean towards this first assumption. However, future research will have to further investigate these results. The value of ϕ_M and ϕ_{fit} were also compared to those obtained experimentally in [30]. Figure 1.52.b presents the values of $\bar{\phi}/\phi_{max}$ as a function of $\tan\theta/\tan\theta_{min}$. For slope angles below θ_{max} , $\phi_{fit} = \phi_M$ and their behaviour is consistent with the compared tests. Beyond θ_{max} , data show that the matched values are compatible with other experimental results whereas values obtained from the $\bar{\phi}(\bar{I})$ equation are systematically lower when $\theta \geq 27^\circ$. This result confirms that the $\bar{\phi}(\bar{I})$ relationship is valid for $\theta_{min} < \theta < \theta_{max}$, as mentioned in section 1.3.2.

The second fit procedure concerns the τ_{iz} coefficient. This value was previously set to 0.4 [38]. Nevertheless, tests showed that, even if the model prediction fails when approaching the θ_{min} angle ($\theta \leq 24^\circ$), using τ_{iz} as a fitting parameter can reduce the gap between the analytical prediction and the experimental data. Figure 1.52.c shows the values of τ_{iz} that were chosen as a function of $\frac{\tan\theta}{\tan\theta_{min}}$. Figure 1.51 shows that the model very accurately predicts the normal force acting on the wall for high and intermediate slopes. At low slopes however, even after fitting the ϕ and τ_{iz} parameters, the model fails by overestimating the force.

Note that this analytical prediction does not take into account any possible side-wall effects. However, side-walls are suspected of facilitating the formation of force networks acting on the

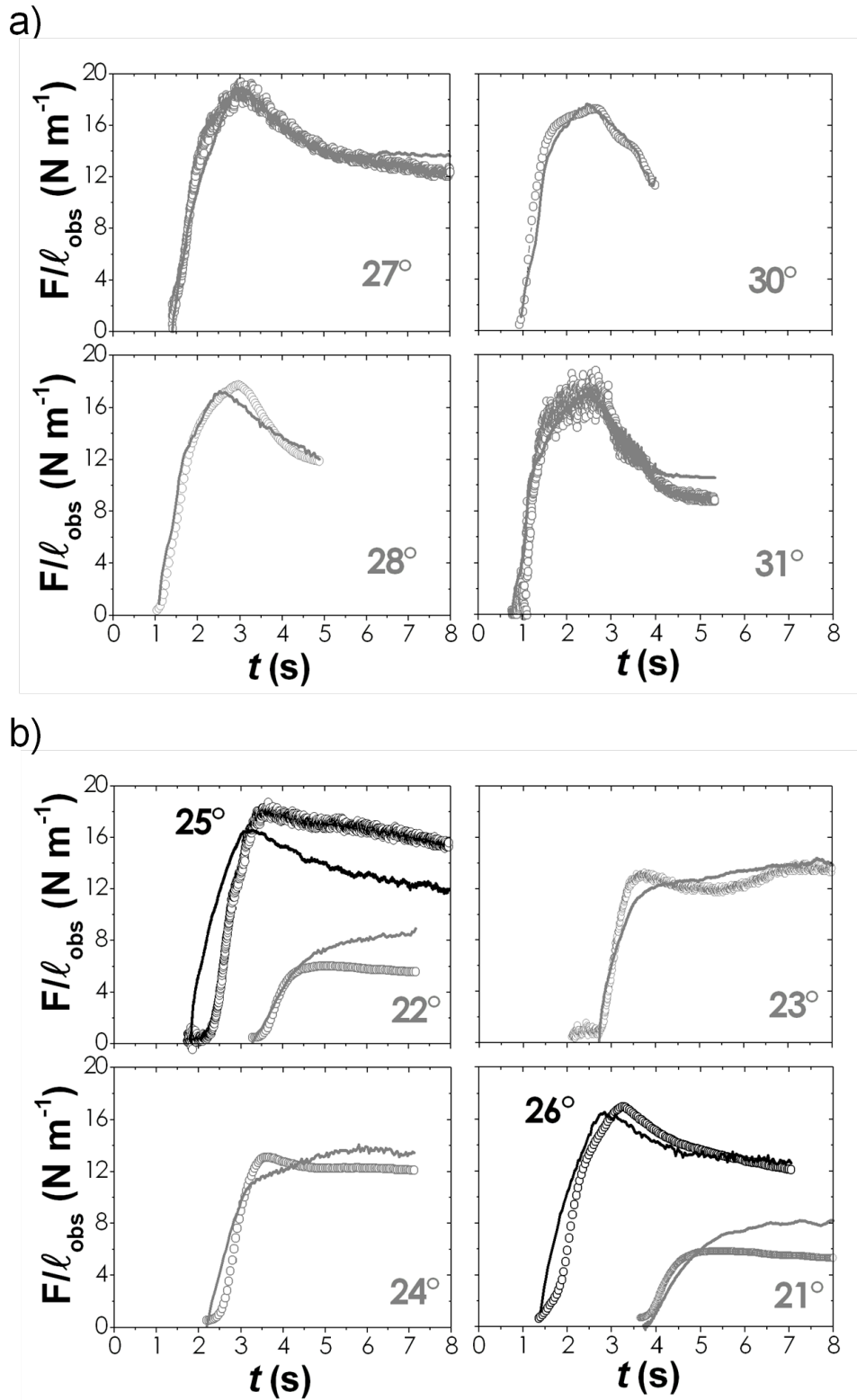


Figure 1.51: Normal force per unit width versus time t . Graphs show a cross-comparison between the model prediction (—) and the experimental results (\circ). In (a), the model prediction considers $\bar{\phi} = \phi_{fit}$, whereas in (b) a matched value of τ_{iz} is used for $\theta \leq 24^\circ$.

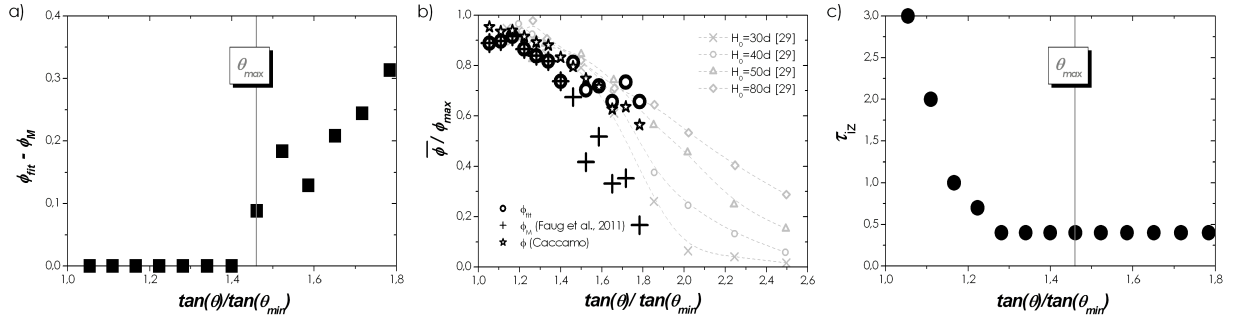


Figure 1.52: (a) $\phi_{fit} - \phi_M$ versus the slope angle ($\tan \theta / \tan \theta_{min}$). No fitting procedure was done for $\theta < \theta_{max}$ ($\phi_{fit} = \phi_M$). (b) Normalised volume fraction $\bar{\phi}/\phi_{max}$ versus the slope angle ($\tan \theta / \tan \theta_{min}$). A comparison is made between data from [30], the maximum values ϕ_M (derived from \bar{I}) and the fitted values ϕ_{fit} . The black empty stars represent the data displayed in Fig.1.34. a. (c) Best fit values of the characteristic time τ_{iz} versus the slope angle ($\tan \theta / \tan \theta_{min}$).

y -axis and reducing the force exerted on the obstacle (see also section 1.1.2 and section 1.3.2). Additional effects of the jamming transition are not taken into consideration. In laboratory tests the granular flow reaches the obstacle after covering a distance of $x=1300d$ ($x=500d$ for 2D DEM simulations in [38]). Such a long distance leads to the fact that, at low slopes, the avalanche comes to a standstill before reaching the wall with no, or very slight, overflow. These two contributions aide in reducing the normal force acting on the wall, and they were not taken into account for the model. The implementation of these two contributions into the model represents a future challenge.

In tandem with considerations made in section 1.3.2, an analytical prediction of the maximum forces exerted at each slope is given. Figure 1.53 shows these results. Note that the graphs in section 1.3.2 dealt with maximum force data while results presented in the following deal with maximum pressures. This is due to the fact that scaling must be done when comparing the experimental, numerical and analytical results (numerical simulations were considered to have a constant ratio of $h/H_{obs} = 1$, which is not the case for experimental tests). Thus, to get rid of this dependency, pressure values were obtained by scaling the maximum forces with the obstacle surface ($l_{obs}H_{obs}$). Afterwards, for each investigated slope, these maximum values were divided by two typical pressure contributions:

$$P_h^0 = \frac{1}{2} \bar{\rho}_p g H_{obs} \cos \theta \quad (1.73)$$

$$P_u^0 = \frac{1}{2} \bar{\rho}_p u^2(t_{F_{max}}) \quad (1.74)$$

where $u(t_{F_{max}})$ is the flow velocity at $t = t_{F_{max}}$. P_h^0 is the hydrostatic pressure contribution and P_u^0 is the kinetic pressure contribution.

Comments on the behaviour of these two ratios were already made in section 1.3.2. It is worth noting in Fig.1.53 that the analytical prediction for maximum values of pressure, is fully compatible with experimental and numerical results.

Even if the behaviour of a gravity-driven granular flow must still be further investigated, the outcome presented validated the robustness of the model.

It would be interesting to discover reasonable assumptions for adapting this analytical model to the geometry of the small obstacle (with lateral flows allowed). In this case, the different shape and behaviour of the influence zone greatly complicate the task and present a complex challenge for future developments.

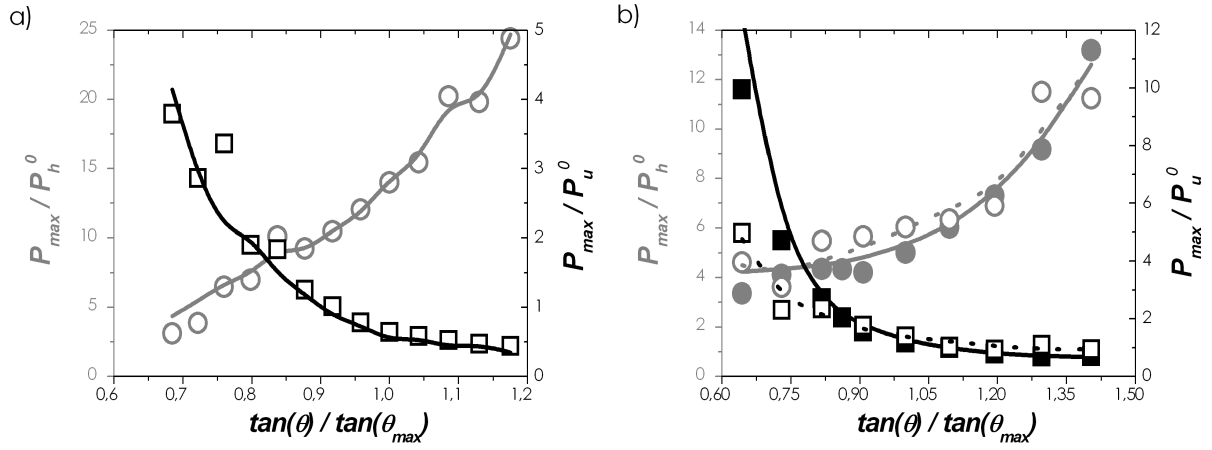


Figure 1.53: P_{max}/P_i^0 ratios versus the slope angle ($\tan\theta/\tan\theta_{min}$). The maximum pressure values P_{max} were scaled by the kinetic (P_u^0) and the hydrostatic (P_h^0) pressure contributions. The model predictions (lines) were compared to the same ratios (symbols) obtained from (a) experimental data and (b) discrete numerical simulations. Further details can be found in [52].

1.5 Conclusions and outlook

This chapter described the experimental work that was conducted to investigate dense-snow avalanches by using a small-scale model wherein snow was simulated by a granular material. The initial sections explained why glass beads were adopted to carry out the laboratory tests. Beyond the visual aspect, rheology and dynamics similarities justified the use of a granular material for the planned research.

An experimental device was set up. It consisted mainly of an inclined channel with a width and length which were fixed at a variable slope. Tests were performed in a range of slopes, from 21° to 33° . Measurements were taken of the flow velocity (PIV method), its height (laser technique) and on the mean force exerted on a wall-like obstacle (force sensors). Reference tests were performed first, in order to characterise the flow dynamics without an obstacle, and force measurements were then carried out. Two different types of obstacles were tested: a large obstacle spanning the entire width of the channel and a smaller obstacle allowing lateral flows. The obtained results were analysed, validated by means of already-existing scaling laws, and cross-compared. Results from previous numerical simulations also provided sets of data that proved useful for the comparison and validation of the experimental work.

Main results of chapter 1

1. The two characteristic angles of granular material, θ_{min} (associated with quasi-static conditions) and θ_{max} (associated with the transition towards collisional regimes) were found to equal 20° and 28° respectively. These two angles largely influence the flow dynamics and its interaction with obstacles.
2. For reference flows (the granular avalanche flows down without impacting any obstacle):
 - (a) the maximum flow depth decreases when the slope increases, but it drops when approaching θ_{min} ;
 - (b) the maximum surface velocity increases with the slope angle;
 - (c) the $h(t)$ and $u(t)$ profiles form two groups for slope angles θ below or above θ_{max} ;
 - (d) finite-sized granular avalanches exhibit maximum flow depth and corresponding velocities that follow the flow scaling evidenced for steady and uniform flows in the range $[\theta_{min}; \theta_{max}]$.

These results were published in Granular Matter [33].

7. Force measurements on a large obstacle (catching dam type) showed that:

- (a) the maximum force is rather constant for $\theta_{min} < \theta < \theta_{max}$. It drops when approaching θ_{min} and it increases for $\theta > \theta_{max}$;
- (b) for high slopes, the maximum force is purely kinetic;
- (c) for low slopes, the hydrostatic contribution becomes important but the apparent weight of the dead zone also plays an important role;
- (d) residual forces F_{res} are related to the avalanche final deposit and tend to decrease with the slope, except when approaching the θ_{min} angle where the values of F_{res} decrease. At low slopes, friction plays an important role in reducing the deposit weight acting on the obstacle. A simple model based on the equilibrium between the deposit weight w and the basal friction F_f aptly describes the residual force behaviour, except close to the θ_{min} angle.

These results were published in *Granular Matter* [33].

8. Force measurements on a small obstacle (breaking mound type) showed that:

- (a) maximum forces increase with the slope angle;
 - (b) for high slopes, the small obstacle (*SO*) is subjected to the same maximum force ($\frac{F_{max}}{l_{obs}}$) than the large obstacle (*LO*) whereas for low slopes; $\frac{F_{max}^{SO}}{l_{SO}} = 2\frac{F_{max}^{LO}}{l_{LO}}$. This is probably due to a network of forces acting along the y -axis and reducing the force exerted on the structure (Janssen effect) in the presence of the large obstacle;
 - (c) residual force values decrease with the slope angle.
9. Upon impact with an obstacle, a quasi-static zone forms directly uphill from it and an inertial layer starts flowing above and overflows the obstacle. These two parts compose the influence zone which plays an important role in the flow dynamics. A detailed analysis of the evolution of this zone was carried out for a fixed slope of 31° and showed that:
- (a) the shape of the influence zone and its regime evolve during the flow. A transition was observed from a dead zone regime to a granular jump regime;
 - (b) an analytical prediction shows that for $\theta < \theta_{max}$ the transition does not occur, while it does beyond θ_{max} and the time t^* at which the transition happens is rather constant.

These results were published in the proceeding of the international symposium *Fluid and Structure Interaction*, Orlando, May 2011 [34].

10. A depth-averaged hydrodynamic analytical model was developed to calculate the normal force acting on a wall-like obstacle. The model's predictions were compared to the experimental results and the data correspond well.

These results were published in *Physical Review E* [52].

Perspectives from chapter 1

1. The dead zone to granular jump transition was experimentally found for a fixed slope of 31° . Some analytical predictions were made for the other slopes, but it would be of great interest to investigate this transition for a larger range of slopes in order to verify the reliability of the analytical predictions. Additionally, two wall-like obstacles of different sizes were used, a first structure representing a classical catching dam case and a second structure modelling a potential breaking mound. In reality, these two protection solutions are frequently coupled together. It would indeed be interesting to combine different types of structures in laboratory tests in order to analyse their interaction with the incoming flow.
2. The analytical model, developed in conjunction with this PhD work, was tested with the force data obtained through the large obstacle spanning the entire flow width. This model should be adapted to predict the force acting on a breaking-mound-like obstacle, in order to compare the analytical prediction to the obtained experimental results. The new shape of the influence zone must be carefully calculated. A laser technique was developed providing the *3D* reconstruction of the granular avalanche deposit uphill from the obstacle. Although some discrepancies with experimental data affected the results, this new method appeared to have great potential and should be improved in order to be made operational.
3. A cohesionless and mono-disperse material was used to simulate the dense snow avalanche. A more realistic modelling of snow flows should account for cohesion and poly-dispersity.
4. The dead zone contribution and the dead zone to granular jump transition were investigated for granular flows and results evidenced their important role in the flow behaviour and the total force exerted. These two phenomena should be studied on full-scale avalanches.
5. Although the most recent European design guidelines for avalanche protection structures (Barbolini et al., 2009 [13]) are based on a consistent dynamic representation of the flow behaviour, the role of the dead zone and the dead zone to granular jump transition are not taken into consideration. Future updating should take them into account.

Chapter 2

A small-scale water tank to model powder snow avalanches

Contents

2.1	Present understanding	89
2.1.1	Physical modelling	89
2.1.2	Analytical and numerical models	94
2.1.3	Focus on the bed-erosion process	96
2.1.4	Focus on density	96
2.1.5	Avalanche-obstacle interaction	97
2.2	The water tank: method	100
2.2.1	Froude-scale modelling	100
2.2.2	Experimental device	101
2.2.3	Measurement techniques	106
2.3	The water tank: results	115
2.3.1	Some qualitative considerations	115
2.3.2	Maximum height	116
2.3.3	Front velocity	117
2.3.4	Core velocity	119
2.4	Conclusions and outlook	129

An aerosol avalanche is a turbulent flow resulting from the suspension of snow particles in the air. It appears to be a big snow cloud travelling at a very high velocity [20] ($20 - 100 \text{ m s}^{-1}$ [115]). The wind, or breath, of the avalanche usually anticipates the actual aerosol avalanche. This consists of an airflow that travels several meters in front of the aerosol avalanche ($10 - 100 \text{ m}$; Nishimura et al. (1989) [114] found a value of 17.3 m) without snow-crystal entrainment. The wind pressure is weak, being approximately 5 kN m^{-2} , but enough to generate damage (trees, roofing, etc.). An aerosol avalanche usually originates from a dense avalanche. For powder snow, the majority of researchers suggest that, in the presence of cold dry snow with a low cohesion rate, the avalanche must reach a velocity of 10 m s^{-1} before the air forms a snow cloud [20, 79]. More cohesive types of snow can also generate an aerosol, but the velocity necessary for forming the cloud would be higher.

An aerosol avalanche is composed of a turbulent-eddy structure moving rapidly and increasing its volume until it exceeds a height of several dozen metres. The snow density for an aerosol avalanche greatly varies ($\rho = 1 - 10 \text{ kg m}^{-3}$).

In the domain of avalanche protection design, as previously mentioned in the introduction, defence structures are built mainly to stop the dense part of an avalanche. The aerosol part does not follow the terrain morphology and generally overtakes the obstacle. This study intends to quantify the positive effect of a catching-dam-like obstacle and to estimate the residual risk that the powder avalanche still represents downhill from the protection structure.

A small-scale model was set up for laboratory experiments. An inclined channel with a fixed slope of 13° was immersed in a water tank. A reservoir stores the material used to model the aerosol avalanche. This consists of a dyed salt solution that, analogous to density currents, represents the heavy fluid ($\rho = 1200 \text{ kg m}^{-3}$) flowing into a lighter ambient fluid ($\rho_{ref} = 1000 \text{ kg m}^{-3}$).

Section 2.1 gives a general overview of the present knowledge of powder-snow avalanche modelling, and section 2.2 focusses on the experimental set-up and the techniques used for density, front and core velocity, and flow height measurements. The data obtained describe the flow dynamics in reference conditions (with no obstacle) and in the presence of two different obstacles. Results are presented in section 2.3. Lastly, section 2.4 concludes the chapter.

2.1 Present understanding

Modelling a powder snow avalanche is a delicate research domain. As previously mentioned for the dense part of the avalanche (see chapter 1), a through approach for investigating such a complex phenomenon consists of carrying out real-scale experiments in tandem, small-scale physical simulations, and numerical modelling. Aerosol avalanches are complex phenomena that involve non-uniform, non-steady, non-linear, free-boundary flows and are driven by non-conservative density differences and a combination of body and pressure forces [94]. The number of variables exceeds the number of governing equations (closure problem) and simplifying assumptions are needed in order to solve the equation system. Mathematical and numerical models allow accurate study of the structure of density currents. Regardless, reliable sets of data coming from field measurements or physical simulations are necessary to better define these assumptions and to validate the models. Aerosol avalanche field experiments are very complex and, at the moment, not widely developed. However, new technologies and measurement techniques have been developed. Through the years, pulsed Doppler radar, laser scan, high frequency pressure sensors and capacitance sensors were introduced to real-scale experimental sites (Col du Lautaret in France, Vallée de La Sionne in Switzerland, Ryggfonn in Norway, Kurobe Canyon in Japan and M. Pizzac in Italy) to study the behaviour of dense snow avalanches more than their aerosol counterparts. Recently, through an ongoing collaboration between Irstea of Grenoble (France) and the University of Nagoya (Japan), several new sensors were installed at the Col du Lautaret avalanche site. They consist of snow drift sensors that were previously tested in Antarctica, which aim to investigate powder-snow avalanches by measuring the snow drift related to their transit. Unfortunately, this winter season (2011 – 2012) did not provide any opportunities to release artificial avalanches. However, test sites provide real data on the dynamic processes occurring through snow avalanches and, in some rare cases, specifically through aerosol flows. There remains very limited understanding of the interaction between a powder-snow avalanche and an obstacle. Thus, small-scale tests and numerical simulations greatly enhance the general understanding of powder avalanches.

Aerosols are gravity finite-volume currents as they are driven by the effect of gravity acting on their mass. In the following sections, this type of flow is called a *density current* when it is modelled by single-phase flows and a *turbidity current* when the flow is composed of a suspension of particles. The *finite-volume supply* expresses the non-steady nature of this phenomenon. The word *cloud* can also be used to define its finite size.

This section will provide an overview of the existing knowledge of the modelling of powder-snow avalanches in terms of small-scale physical simulations as well as analytical and numerical models.

2.1.1 Physical modelling

Small-scale tests date back to the 1970s and have developed over three main axes using different principles: *(i)* a heavy fluid flowing in a lighter fluid, *(ii)* bi-phase simulations with water and *(iii)* bi-phase simulations with air.

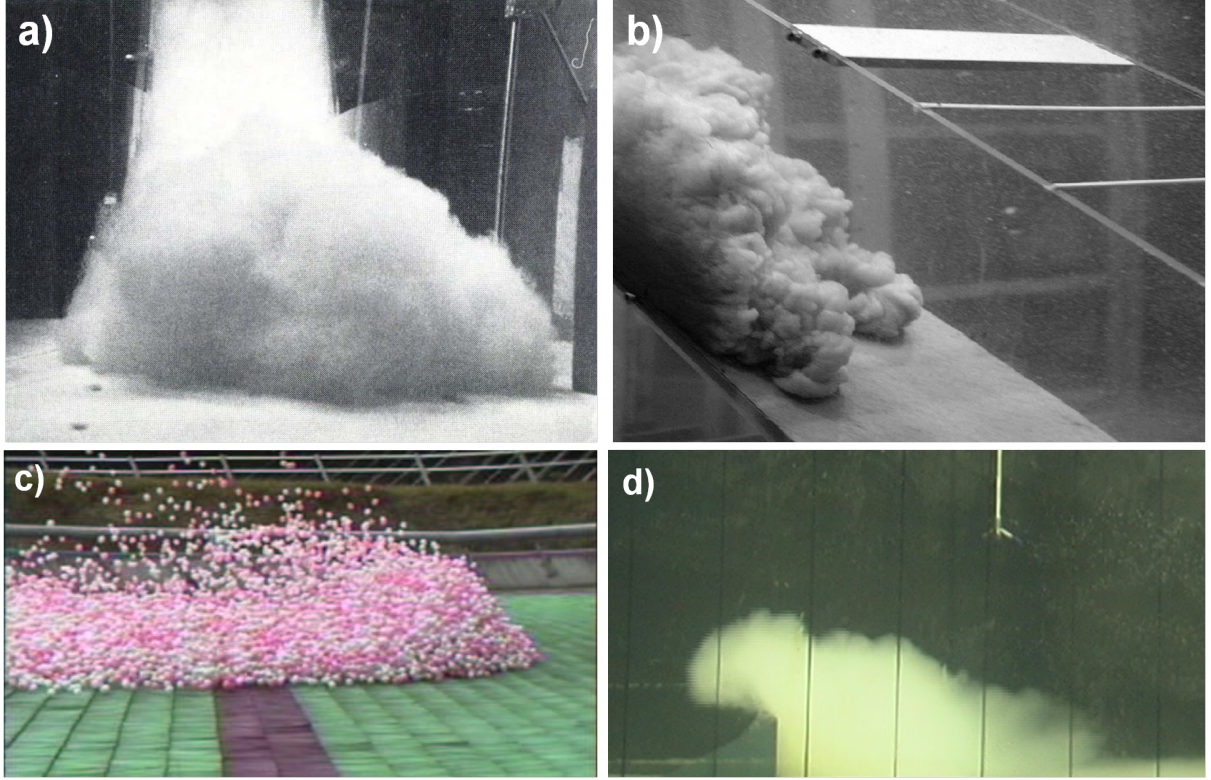


Figure 2.1: Different physical modelling principles: (a) polystyrene beads in water [73], (b) sawdust suspension in water [127], (c) ping-pong balls in the air [111] and (d) dyed salt water in water (photo P. Caccamo)

i) Heavy fluid flowing in a lighter fluid

The work presented in this chapter is based on this type of modelling. We therefore detail this part in particular as well as provide equations supporting modelling principles in the following section.

The pioneering research was conducted by Hopfinger and Tochon-Danguy (1977) [80] and Beghin (1978) [16]. A salt solution represents the heavy fluid that flows in a lighter fluid (water). These flows are gravity-driven flows because the solution moves only due to the effect of gravity, and the flows are assumed to be mono-phase fluids with variable density and, depending on the supply, they consist of either density *clouds* (finite volume supply) or density *currents* (continuous supply). Flows are supposed to be highly inertial.

In 1967, Soo [145] showed that the mass conservation equation for the fluid phase of a suspension can be written as:

$$\frac{d\rho_{ref}}{dt} + \frac{\partial\rho_{ref}u_i}{\partial x_i} = \frac{\rho_{ref}}{1-\phi} \left[u_i \frac{\partial\phi}{\partial x_i} - \frac{\partial\phi u_{pi}}{\partial x_i} \right] \quad (2.1)$$

where ρ_{ref} is the reference ambient fluid density, u is the flow velocity, x its position, ϕ is the suspension volume fraction, and u_{pi} represents the velocity of the solid particles. i stands for the investigated axis (x , y or z). If the ambient fluid is incompressible, Eq.(2.1) becomes:

$$\rho_{ref} \frac{\partial u_i}{\partial x_i} = \frac{\rho_{ref}}{1-\phi} \left[u_i \frac{\partial\phi}{\partial x_i} - \frac{\partial\phi u_{pi}}{\partial x_i} \right] \quad (2.2)$$

However, if the falling velocity of solid particles is weak with respect to the turbulent velocity of the suspension ($u'_i \approx u'_{pi}$), $\partial u_i / \partial x_i = 0$. Suspension currents behave as homogeneous and incompressible fluids with a density $\rho = \rho_p \phi + \rho_{ref}(1 - \phi)$ (ρ_p is the particle density).

For an aerosol avalanche, the particles' diameter is approximately $100 \mu\text{m}$ and is characterised by a falling velocity ranging from 20 cm s^{-1} to 50 cm s^{-1} [126]. As the entrainment mechanism is mainly affected by the eddy structures, it is reasonable to assume that the entrainment velocity is approximately the characteristic velocity u of the eddy structures (turbulent velocity), and thus $\frac{dh}{dt} = u$. For defining x_{fr} the front position and u_{fr} the front velocity,

$$\frac{dh}{dt} = \frac{dh}{dx_{fr}} u_{fr} \approx u \quad (2.3)$$

Consequently, considering $\frac{dh}{dx_{fr}} \approx 3.5 \times 10^{-4} \theta + 0.004$ [16] (θ is the slope angle for 2D flow) and a front velocity of 50 m s^{-1} , a turbulent velocity of about 2 m s^{-1} is obtained (for $\theta = 10^\circ$). The avalanche can be assumed as a homogeneous fluid, but this assumption is no longer justified for lower slopes or front velocities.

In 1979, Beghin [16] showed that, if the shear forces induced by the air and the bottom are neglected, the momentum equation can be written as follows:

$$\rho \frac{d\vec{u}}{dt} = -\vec{\nabla} P + \rho \vec{g} \quad (2.4)$$

Considering reference conditions for hydrostatic equilibrium ($\vec{\nabla} P_{ref} = \rho_{ref} \vec{g}$) and defining $\rho = \rho_{ref} + \Delta\rho$ and $P = P_{ref} + P'$, the above equation becomes:

$$\left(1 + \frac{\Delta\rho}{\rho_{ref}}\right) \frac{d\vec{u}}{dt} = -\frac{\vec{\nabla} P'}{\rho_{ref}} + \frac{\Delta\rho}{\rho_{ref}} \vec{g} \quad (2.5)$$

At this point, the Boussinesq approximation must be presented. This assumption states that for certain buoyancy-driven flows, density differences are small enough to be neglected, except where they appear in terms multiplied by g , the gravity acceleration. The essence of the Boussinesq approximation is that the difference in inertia is negligible, but that gravity is strong enough to make the specific weight appreciably different between the two fluids. If $\frac{\Delta\rho}{\rho_{ref}} \ll 1$, the Boussinesq approximation can be applied. In this case, Eq.(2.5) becomes:

$$\rho_{ref} \frac{d\vec{u}}{dt} = -\vec{\nabla} P' + \Delta\rho \vec{g} \quad (2.6)$$

Gravity-driven flows can therefore be distinguished in flows characterised by a low density (with respect to the ambient fluid), for which the Boussinesq approximation is valid and flows with a high density ratio for which this approximation is no longer reliable.

Beghin and Olagne (1991) [20] conducted laboratory experiments showing that, for Boussinesq flows, the growing height, length, and width rates of an avalanche depend linearly on the slope angle (for slopes higher than $5^\circ - 10^\circ$).

A dimension analysis details the relevant physical quantities. By defining:

$$\rho^* = \frac{\rho}{\rho_{ref}} \quad g^* = \frac{g}{g_0} \quad x^* = \frac{x}{h} \quad t^* = \frac{tu}{h} \quad P^* = \frac{P}{\rho_{ref} u^2} \quad (2.7)$$

where h and u are the characteristic dimensions of the flow fixed by the boundary conditions, Eq.(2.6) becomes:

$$(1 + \Delta\rho^*) \frac{du^*}{dt^*} = -\vec{\nabla} P'^* + \Delta\rho^* \frac{h}{u^2} \vec{g} \quad (2.8)$$

Equation (2.8) shows that only two parameters must be respected: the densimetric Froude number $Fr_d = \frac{u}{\sqrt{\frac{\Delta\rho}{\rho_{ref}} gh}}$ and the density ratio $\frac{\Delta\rho}{\rho_{ref}}$. Once the Boussinesq approximation is validated,

the only parameter to observe is the densimetric Froude number. In the case of avalanches, where density variations are significant, both parameters should be taken into account. However, in the past, the Boussinesq approximation was generally applied to the physical modelling of powder snow avalanches. Today, we maintain that the two dimensionless parameters (Fr_d and $\frac{\Delta\rho}{\rho_{ref}}$) must be observed to use small-scale results for real-scale applications.

ii) Bi-phase simulations in water

Herman and Hutter (1991) [73] reproduced a turbulent flow, made by a suspension of polystyrene beads flowing into the water. In this case, the falling velocity of particles cannot be neglected, and an additional dimensionless number was therefore considered. The velocity ratio $\frac{u}{u_{fall}}$ was taken into account in addition to the densimetric Froude number and the density ratio. This type of modelling still does not fulfil the density similarity.

Rastello (2002) [127] generated turbidity currents of sawdust flowing in water. The particles' falling velocity was taken into account ($u_{fall} \simeq 8 \text{ mm s}^{-1}$) and the erosion/entrainment phenomenon was investigated.

iii) Bi-phase simulations in the air

Bozhinskiy and Sukhanov (1998) [26] simulated powder snow avalanches by using dry-powder materials. The flow started as a dense avalanche and the aerosol part developed on top of it. This solution was not found to be very promising.

Nishimura et al. (1998) [111] conducted experiments with ping-pong ball avalanches at the Miyanomori ski jump in Sapporo, Japan. Up to 550000 ping pong balls were released, the flow developed a 3D structure with a distinct head and tail. Air pressure tubes provided sets of data which were used to investigate the structure of the airflow around the avalanche.

Turnbull and McElwaine (2008, 2010) [153, 154] developed a futuristic experimental model for powder snow avalanches which makes use of fine dry snow to form suspension currents in the air. The density ratio similitude requirement is finally achieved due to the high density difference $\Delta\rho = \rho - \rho_{ref}$ so that the currents are non-Boussinesq. The Reynolds number is relaxed, which means that it is assumed that, for $Re > 2000$, the flow is fully turbulent and thus the viscosity effects can be neglected. The Richardson number Ri is defined as:

$$Ri = \frac{g\Delta\rho h \cos\theta}{\rho_{ref}u^2} \tag{2.9}$$

where ρ is the flow density, h the mean flow depth, u the mean flow velocity, and θ the slope angle. In order to satisfy the requirement for the Richardson number ($Ri \leq 1$ for an unstable surface), very high slopes are required. The slope ranged between 40° and 90° for the experimental tests, values which are significantly higher than in nature. The avalanche starts as a dense current and becomes a suspension current during the flow. The shape and position of the current were tracked by using two video cameras, and a high frequency pressure sensor recorded the air flow. Results were shown to be consistent with the in-situ observation of natural powder-snow avalanches observed in Russia, Japan and Switzerland and with numerical simulations (with the exception of the height and aspect ratio).

In summary, Table 2.1 gives an overview of the experimental studies conducted throughout the past 40 years to simulate powder-snow avalanches. The adopted modelling principle, the types of measurements, the techniques, and the key points of each study are provided.

Table 2.1: Summary of physical modelling applied to powder snow avalanches (Re^* indicates that the Reynolds number is high enough to consider the flow as fully turbulent and $\frac{\Delta\rho}{\rho_{ref}}$ means that the requirement is unmatched).

<i>Authors (year)</i>	<i>Simulation principle</i>	<i>Similitude requirements</i>	<i>Velocity measurement</i>	<i>Density measurement</i>	<i>Various</i>
Hopfinger and Tochon-Danguy (1977) [80]	Dyed salt water in water	Re^* , $\frac{\Delta\rho}{\rho_{ref}}$, Fr_d	Image processing	Conductivity sensors	Pioneer work
Beghin (1979) [16]	Dyed salt water in water	Re^* , $\frac{\Delta\rho}{\rho_{ref}}$, Fr_d	Image processing	No	
Beghin and Closet (1990) [18]	Dyed salt water in water	Re^* , $\frac{\Delta\rho}{\rho_{ref}}$, Fr_d	Image processing	No	Flow/obstacle interaction
Herman and Hutter (1991) [73]	Polystyrene beads in water	$\frac{u}{u_{fall}}$, Fr_d	Acoustic based measurements	Qualitative observation	Kink zone and run-out zone investigation
Bozhinskiy and Sukhanov (1998) [26]	Dry particle material in air	Fr	Image processing	No	Dense flow developing an aerosol layer on top
Nishimura et al. (1998) [111]	Ping-pong balls in air	$\frac{u}{gL}$	Image processing + tubes for the airflow	No	Pressure measurements
Naaïm-Bouvet et al. (2002) [107]	Dyed salt water in water	Re^* , $\frac{\Delta\rho}{\rho_{ref}}$, Fr_d	Image processing and velocimetry	No	Flow-obstacle interaction and internal velocity measurements
Rastello (2002) [127]	Dyed salt water and sawdust suspension in water	Re^* , $\frac{\Delta\rho}{\rho_{ref}}$, Fr_d	Image processing and conductivity sensors	No	Bed-erosion measurements
Sampl et al. (2004) [135]	Dyed salt water in water	Re^* , $\frac{\Delta\rho}{\rho_{ref}}$, Fr_d	Image processing and Doppler velocimetry	No	Flow-obstacle interaction in 2D and 3D configurations
Caccamo (2008) [32]	Dyed salt water in water	Re^* , $\frac{\Delta\rho}{\rho_{ref}}$, Fr_d	Image processing and Doppler velocimetry	No	Influence of the dam's height on the flow behaviour
Turnbull and McElwaine (2008) [153]	Polystyrene beads in air and cold dry snow in air	Re^* , $\frac{\Delta\rho}{\rho_{ref}}$, Ri , St (Stokes number)	Image processing	No	Cold dry snow in air satisfy the density ratio requirement!
Brossard (2010) [29]	Dyed salt water in water	Re^* , $\frac{\Delta\rho}{\rho_{ref}}$, Fr_d	Image processing and Doppler velocimetry	No	Bed-erosion measurements

2.1.2 Analytical and numerical models

Mathematical modelling of gravity currents ranges from simple hydraulics equations and box models to complex turbulence models.

KSB model and further development

The first analytical model was initially proposed by Kulikovskiy and Sveshnikova [95] and successively modified by Beghin [16, 17, 19, 20] and it is known as the KSB-model. The avalanche cloud is considered as having a finite volume, a deformable block with a semi-elliptic shape, driven by the force of gravity. The incorporation of ambient fluid is taken into account as well as the friction with the bottom and with the ambient fluid and its motion caused by the avalanche. This simple analytical model is based on the resolution of the mass and momentum equations (all detailed equations can be found in the references cited in this section). An avalanche couloir is divided into sections and, for each section, the equations are solved by using the experimental laboratory results obtained for the growing flow rates by Beghin and Olagne (1991) [20].

In France, the KSB-model was implemented in AVAER, a computer tool for practitioners, wherein the most interesting parameter is the impact pressure. The kinetic pressure is typically calculated as $P_{kin} = \frac{1}{2}\rho u^2$, where ρ is the flow density and u stands for the flow front velocity. Beghin and Closet (1990) [18] proposed to correct this equation by adding a safety coefficient $k(z)$. This coefficient takes into account the vertical profiles of horizontal velocity and density evolving during the flow. Thus,

$$P_{kin} = k(z)\frac{1}{2}\rho u^2 \quad (2.10)$$

This equation was based on laboratory experiments carried out by Hopfinger and Tochon-Danguy (1977) [80]. They found that the maximum velocity inside the cloud is higher than the front velocity ($u_{max} = 1.5 - 2.5u_{fr}$), and that the density of the lower part of the avalanche is higher than the mean value ($\rho_{low} \simeq 2 - 4\rho_{mean}$). In 1995, Rapin proposed a different function of $k(z)$ [123]. Figure 2.2.a shows the different values of the $k(z)$ coefficient versus the flow thickness.

In 2004, small-scale experiments carried out by Rastello and Hopfinger [125] improved the model. Physical simulations were conducted in a water tank. The closure coefficients of the model, regarding the evolution of the cloud shape and the air entrainment rate, were obtained through laboratory experiments. These coefficients are valid within the Boussinesq limit whereas a correction of inertial effects, which must be taken into account when applied to large density difference clouds (such as avalanches), was proposed.

Later, Ancey (2004) [6] showed how the growing rate of the height and velocity of the buoyant cloud (semi-elliptic-shaped) also depended on the Richardson number, and he proposed an alternative expression for these rates which led to more appropriate values. This modelling presents the possibility of taking the bed entrainment into account, but it is not effective with high concentrations of particles. An additional improvement was achieved by Turnbull, McElwaine and Ancey (2007) [155], who proposed an adjustment account for the entrained-snow volume in the model. The snow entrainment rate can play a significant role in the dynamics of powder-snow avalanches. More details on this topic are given in section 2.1.3.

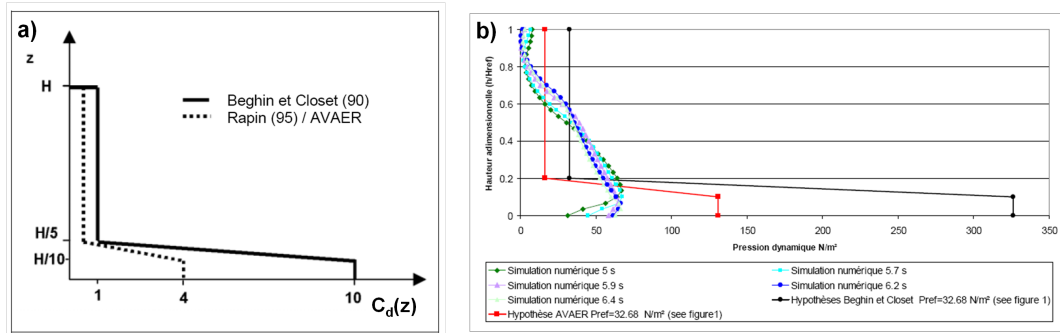


Figure 2.2: (a) Behaviour of the $C_d(z)$ coefficient over the height z . The black line represents values proposed by Beghin and Closet (1990) [18], and the dotted line corresponds to values obtained by Rapin (1995) [123] as used in the AVAER software. (Naaim-Bouvet et al. (2003) [109], Fig.1). (b) Pressure values obtained with analytical and numerical models. (Naaim-Bouvet et al. (2003) [109], Fig.11)

CFD models

At the end of the last century, important advances were made in the numerical modelling applied to powder-snow avalanches [109, 135] which was achieved alongside small-scale studies. CFD (Computation of Fluid Dynamics) models such as FLUENT [109] or FIRE [135] (although others may be used) represent these advances. They consist of numerical models based on mass and momentum equations. Two mass equations are considered, for the salt solution as well as for the ambient fluid, whereas only a momentum equation is taken into account assuming that both components move at the same velocity. The system is finally closed with a turbulence model ($k - \varepsilon$ type).

One advantage of a numerical model of this nature is the access it grants to the pressure profile inside of the avalanche cloud. Figure 2.2.b shows a comparison between pressure values obtained by analytical and numerical models. The maximum pressures were found at approximately $z = 0.1h$ with both models, but the values obtained through FLUENT are significantly lower than those from AVAER.

The numerical model allowed the simulation of powder-snow avalanches with a more appropriate density ratio than that obtained for small-scale experiments. Results showed that the incorporation rate of ambient fluid considered at the laboratory is too high [135]. Nevertheless, neither the numerical model nor physical simulations evaluated the bed erosion and re-suspension, phenomena which, providing additional volume to the cloud, significantly influence its front velocity. In the absence of bed erosion, the avalanche is characterised by an acceleration phase followed by a deceleration, whereas, when considering the erosion supply, the cloud constantly accelerates. Moreover, when comparing the model prediction to the experimental results, as previously done by Naaim-Bouvet et al. (2003) [109], two additional limits appeared. As a matter of fact, the model was not able to reproduce the vertical velocity as obtained through physical simulations and an effect due to numerical diffusion was also observed. The gap between numerical and experimental results widened with the increase of the x and y position ($x = 0$ corresponded to the releasing gate and $y = 0$ to the channel bottom). A better spatial resolution could compensate for this discrepancy, but it would require much longer processing time.

There are other, more complex models (see, for example, Fukushima and Parker (1990) [61]) that can be used to model powder-snow avalanches, but their description is beyond the scope of this thesis.

2.1.3 Focus on the bed-erosion process

Surveys of spontaneous avalanches have long indicated that the deposit mass may exceed the release mass of an avalanche by a significant factor, but precise values were not available [82]. Gruber and Bartelt (2000) [69] and Sovilla (2004) [146] evaluated the dense part of several spontaneous avalanches through mass balance, and they proved that the final deposit mass can be up to four times the initial released mass. Snow particle entrainment is also an important process to be considered when investigating powder avalanche dynamics. It increases the flow mass and compensates for the density decrease due to the incorporation of ambient air.

However, while the erosion rate for the dense part of an actual avalanche can be experimentally measured at different sections of the avalanche path by using different devices (switches, pressure sensors, photo-electrical sensors, buried radars) [137, 150], in-situ measurements on the aerosol part are very complex and have not yielded any consistent results.

This phenomenon was initially integrated into numerical models by Hopfinger and Tochon-Danguy (1977) [80]. Fukushima and Parker (1990) [61] took it into account in their complex model, and, as previously mentioned, Rastello and Hopfinger (2004) [125], Ancey (2003, 2004) [5, 8] and Turnbull et al. (2007) [155] updated the KSB model in order to consider the erosion rate. According to Rastello and Hopfinger, the sediment incorporation rate only depends on the slope angle, while Ancey assumes that it depends on the Richardson number (Eq.(2.9)).

Small-scale experiments on bed erosion were carried out by Rastello (2002) [127] and Brossard (2010) [29]. Rastello conducted tests in a water tank using salt water as a heavy fluid (density clouds) that can erode a bed composed of glass beads, or a sawdust suspension flow (turbidity clouds) that can erode a sawdust bottom. Brossard continued this type of investigation modelling density clouds (salt water flowing downward in a water tank) eroding a bed composed of PMMA particles. His model was based on the KSB type, and it took into account the flow/bed interaction and the particle exchange. Finally, in 2011, Louge et al. [100] presented a model, which was not directly related to avalanche dynamics, but which underscored the role of porous snow cover in the erosion process. Through back analysis and estimation of the snow cover pressure gradients in the Vallée de La Sionne site, the model predicts which cover would produce a powder snow avalanche and which cover would not.

Significant progress was achieved through numerical and laboratory modelling of the bed erosion process due to a powder-snow avalanche, but in-situ measurements are still missing and should be included in future research.

2.1.4 Focus on density

It is very difficult to measure the density of powder-snow avalanches, yet this parameter is very important for calculating pressures that can be exerted by the flow. Consequently, density often represents significant assumptions.

In small-scale experiments, depending on the material adopted, it is possible to determine the density of the particles forming the aerosol cloud (ping-pong balls, fine dry snow) or the initial density of the flow (salt water, sawdust suspension). However, the density of the multi-phase flow (particles + water or air + eroded particles) remains a complex issue. Due to the involve-

ment of the ambient fluid in the erosion and entrainment of bed particles, the density varies throughout the entire flow duration.

For the dense part of an avalanche, several real-scale avalanche sites were equipped with sensors in order to measure the density evolution. In the Revolving Door [48] and Vallée de La Sionne sites, capacitance sensors were installed and provided good results. For the aerosol part of the avalanche, full-scale density measurements are difficult to collect and consistent results have not yet been established. Laboratory experiments allow the reproduction of powder-snow avalanches. In the ETH experiments, carried out by Keller and Issler (1996) [90], the particle concentration was measured. However, only numerical simulations are able to investigate accurately the spatial and temporal evolution of the density parameter. Thus, physical modelling and in-situ measurements allow the calibration of numerical models using the front flow velocity, its maximum velocity and the flow height. Numerical models then investigate the density parameter which is difficult to obtain otherwise.

2.1.5 Avalanche-obstacle interaction

Little research has investigated the interaction between the flow and the obstacle on small-scale laboratory models. Different slopes were chosen but they generally represented the typical slope values for the run-out zones. The pioneering studies belong to Hopfinger and Tochon-Danguy (1977) [80]. For slopes equal to or greater than 10° , first Beghin and Closet (1990) [18] and then Augé (1995) [11] performed experimental tests with unsteady flows striking deviation and catching dams in 2D and 3D configurations. Keller and Issler (1996) [90] also investigated the influence of obstacles on the dynamics of an aerosol avalanche, and they evaluated the effectiveness of retarding and deviating dams.

These research works (except for Keller and Issler) mainly concerned measurements of the front velocity of the avalanche cloud. Innovative studies were done by Naaïm-Bouvet et al. (2002) [107] who used ultrasonic Doppler velocimetry to measure the avalanche velocity in the cloud. In the following section, we provide more details about two of the above cited works: the study of Beghin and Closet (1990) [18] and the study of Naaïm-Bouvet et al. (2002) [107]. These two works provided the main inspiration for the experimental measurements collected within the framework of this PhD.

i) The study of Beghin and Closet, (1990) [18]

This study concerned the effects of a dam on a powder-snow avalanche and it aimed to compare the effectiveness of catching and deflecting dams. The buoyant cloud was simulated by a dyed salt solution flowing on a plane (3D flow) immersed in a water tank. Figure 2.3.a shows the configuration set-up. The simulated avalanche consisted of a purely aerosol avalanche (without a dense part), the bed entrainment was not taken into account and only the front velocity of the avalanche was measured.

Results proved that, for a catching dam, 50% of the flow kinetic energy (calculated using the front velocity) can be dissipated with a dam height rising to 15% of the aerosol height. The most effective dam height is approximately $\frac{h}{10} - \frac{h}{5}$, where h represents the height of the avalanche.

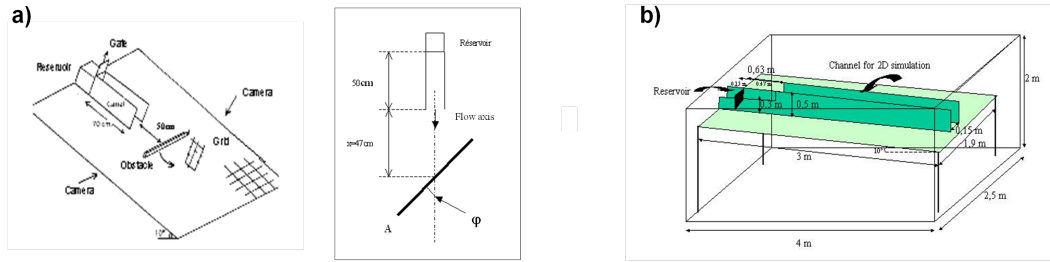


Figure 2.3: Experimental configurations implemented in (a) the work of Beghin and Closet (1990) [18] and (b), the work of Naaim-Bouvet et al. (2002). Fig.3 in [107].

Higher values for the dam's height would not be much more effective, but they would imply much more expensive structures. However, a deflecting dam was found to be most effective when centred on the flow axis. A deflecting angle $\varphi=45^\circ$, with respect to the flow axis, showed a higher deviating power than an angle of 30° . The knowledge of the internal structure and disturbances induced on the flow by the obstacle still had to be improved.

ii) The study of Naaim-Bouvet et al., (2002) [107]

The interaction between powder avalanches and defence structures was investigated for quasi-2D and 3D configurations. The avalanche cloud was simulated by salt water mixed with kaolin flowing into pure water inside of a water tank. Figure 2.3.b shows the set-up. Measurements were primarily taken on the cloud velocity. The Doppler ultrasonic velocimeter was able to provide a new relevant contribution. This new technology measures the component of the particles' velocity vector in the direction of the transducers and can provide velocity measurements inside of the avalanche. The front velocity was found to be weakly dependent on the initial slope, volume and density ratio conditions. It was characterised by an initial acceleration phase, right after releasing the gate, followed by a deceleration phase which was more significant in the 3D configuration, probably because of the lateral growth of the avalanche. In the 2D and 3D configurations, the velocity inside the avalanche presented higher values than the front velocity. In the 2D simulations, the maximum velocity was approximately 1.5 times greater than the front velocity, in accordance with Hopfinger's results. In Hopfinger (1983) [79], laboratory experiments showed that the velocity inside the cloud could be 1.5 – 2.5 times greater than the front velocity, and that the density was significantly larger than the average density close to the ground (by a factor 2 to 4). Therefore, the measured peak pressure can be larger than the pressure calculated from the front velocity and the mean density by a factor of 10.

The reduction of the front velocity was observed to be an increasing function of the dam height; furthermore, the larger that the distance downstream from the dam was, the reduction was smaller. And lastly, the dam's efficiency was found to be less significant in a canalised avalanche configuration where the loss of kinetic energy is approximately 10% less than for 3D flows. Dams are therefore more efficient on an open-slope configuration.

This work provided a significant contribution to the general knowledge of powder-snow avalanche dynamics and on the interaction with obstacles. However, certain limitations must be acknowledged. The Doppler velocimeter allowed the measurement of the flow velocity in only one direction; this means that the study of horizontal and vertical velocities was not carried out on the same test, which leads to a loss of precision. Tests were released manually, without the aid of any synchronisation device, which means high uncertainties for t_0 . Thus, to process and compare results, velocity profiles were shifted in order to synchronise all of the horizontal (parallel to the slope) velocity peaks. Only the lower part of the cloud, where velocities were found to be at their maximum, was investigated because the cloud concentration decreases when the

measure height is increased, and the Doppler velocimeter did not work well. Lastly, the density ratio requirement was not satisfied.

As a result of the outcome discussed in this section, we decided to conduct small-scale experiments using a heavy fluid flowing in a lighter fluid. Thus, powder-snow avalanches were modelled as density clouds obtained through a finite-size volume of dyed salt solution flowing into water (more details are given in section 2.2.2). Tests were performed in different set-up configurations and aimed to investigate the dynamics of a buoyant cloud and its behaviour upon interaction with an obstacle. Attention was focussed on the influence of two catching dams on the dynamics of a quasi-2D aerosol flow. Measurements made use of image processing and Doppler velocimetry. An innovative contribution was provided by the use of a new 3D Doppler velocimeter. With respect to the instrument used in Naaim-Bouvet et al. (2002) [107], Sampl et al. (2004) [135] and Caccamo (2008) [32], this new tool presents several advantages. All of the performed tests were perfectly synchronised by the use of a switch which automatically started the signal-recording when the release gate was opened. 3D velocity measurements mean that horizontal and vertical velocities were measured exactly at the same time and on the same test. The acquisition frequency was much higher ($f_{ac} = 200$ Hz) than the previous one ($f_{ac} = 25$ Hz), and thus a higher frequency not only provided more data, but also greatly increased the chances of measuring the real velocity peak. And lastly, the velocimeter was also equipped with an acoustic sensor indicating the distance between the sensor and the channel bottom (positioning facility). Section 2.2.3 explains how to obtain density values through back analysis of distance data, which represents a very promising possibility for density measurements.

The following sections describe the experimental set-up and the measurement techniques used for small-scale experiments.

2.2 The water tank: method

Small-scale models greatly facilitate the study of complex phenomena such as powder avalanches. As previously mentioned, the purpose of these experiments was to investigate the dynamic behaviour of the flow upon impact with an obstacle. A small-scale model representing a simplified powder-snow avalanche flowing down a slope incline was used to study how the flow dynamic parameters were influenced by the presence of a dam.

Physical modelling, to be consistent with reality, must satisfy similarity requirements which, for the type of flows presented in this chapter, are associated to dynamical and geometrical similarities. Some notions about dynamic similarity were provided in section 2.1.1 and are reiterated in section 2.2.1.

Section 2.2.2 describes the experimental set-up consisting of an inclined channel ($\theta = 13^\circ$) immersed in a water tank where, through analogy with density currents, a dyed salt solution ($\rho = 1200 \text{ kg m}^{-3}$) flows into a lighter fluid (water, $\rho = 1000 \text{ kg m}^{-3}$). The main measurement techniques are illustrated in section 2.2.3. Using image processing and the ultrasound Doppler velocimetry, measurements were taken of the flow density, height, front velocity, and core velocity. The results obtained in reference conditions (without any obstacle) and in the presence of two different dam-like structures are presented in section 2.3. Section 2.4 ends the chapter with conclusions and outlooks.

2.2.1 Froude-scale modelling

Small-scale modelling must meet similarity requirements to provide results that can be used for the study of the real-scale phenomenon. The Froude-scale modelling is based on a similarity approach in which the current is fully characterised by a series of dimensionless variables [94]. The dimensional analysis identifies the number of dimensionless parameters representing all of the variables controlling the system (see section 2.1.1). In small-scale powder avalanche modelling, these parameters are:

1. The Reynolds number, $Re = \frac{\rho u L}{\eta_d}$, which represents the contribution of inertial on viscous forces (where ρ is the flow density, u is its mean velocity, L is a characteristic dimension and η_d is the fluid dynamic viscosity);
2. The densimetric Froude number, $Fr_d = \frac{u}{\sqrt{\frac{\Delta\rho}{\rho_{ref}} gh}}$, which reflects the ratio of inertial to gravitational forces acting on the flow (u is the mean velocity and h the flow height);
3. The density ratio, $\frac{\Delta\rho}{\rho} = \frac{\rho - \rho_{ref}}{\rho_{ref}}$, representing the density difference between the two fluids adopted (ρ is the aerosol density and ρ_{ref} the ambient fluid density)

Currents that share the same value of Reynolds and Froude numbers are considered to be dynamically similar. In the case of Froude-scale modelling, the Froude number of the small-scale phenomenon must be the same of the real phenomenon. However, Re is relaxed, which means that we assume for $Re > 2000$, that the flow is fully turbulent and thus the viscosity effects can be neglected.

Table 2.2: Dimensionless numbers

	Reality	Small-scale model
Re	10^8	10^4
Fr_d	0.5	0.5
$\frac{\Delta\rho}{\rho_{ref}}$	4 – 10	0.2

Table 2.2 gives the values of these three dimensionless parameters for real powder-snow avalanches and small-scale tests presented in this section. The Reynolds number is very high for both cases, which means fully turbulent flows and thus the Re requirement is relaxed. The densimetric Froude number is respected but the density ratio is not conserved. A very high velocity is necessary in order to achieve both requirements in laboratory tests, which means that an experimental device of huge dimensions is required. It is difficult to satisfy the density ratio similarity because this dimensionless number differs by orders of magnitude between the processes that unfold in nature and those reproduced in the laboratory.

In the 1980s [18, 20, 139], at the beginning of physical modelling, this was not considered a serious deficiency because density is always combined with gravity, which is accounted for in the densimetric Froude number. However, the relative difference in density might have a reducing effect on the entrainment rate of the ambient fluid [80]. In the 2000s, due to the improvement of technical instrumentation (in both laboratory and in-situ measurements), the numerical modelling of physical simulations was carried out, allowing the numerical simulation of the flow behaviour for higher density ratios (2, 5 and 10). Previous studies carried out by Naaim-Bouvet et al. (2004) [108] showed that the ratio between the entrainment effects (drag and ambient-fluid incorporation) and the gravity force strongly depends on the densimetric Froude number. It was found to be up to 40% for powder avalanches and 60% for gravity-current flows. The density ratio actually considered in the water tank experiments (see section 2.2.2) is lower than the real one. However, as already mentioned in section 2.1.1, recent experimental devices [153] allowed the density ratio requirement to be respected.

2.2.2 Experimental device

The adopted experimental set-up was mainly composed of an inclined channel immersed in a water tank and the necessary measurement tools. All of these components are described in this section and their technical features are described.

The water tank

The experiments were carried out in a 4 m × 2.5 m × 2 m water tank with glass walls (see Fig.2.4.a). An inclined channel of 2.6 m long and 0.3 m wide has been installed inside of the water tank. The channel slope has a constant incline of 13°, representing the average slope of the study area. As discussed in the introduction, this small-scale model aims to reproduce the real

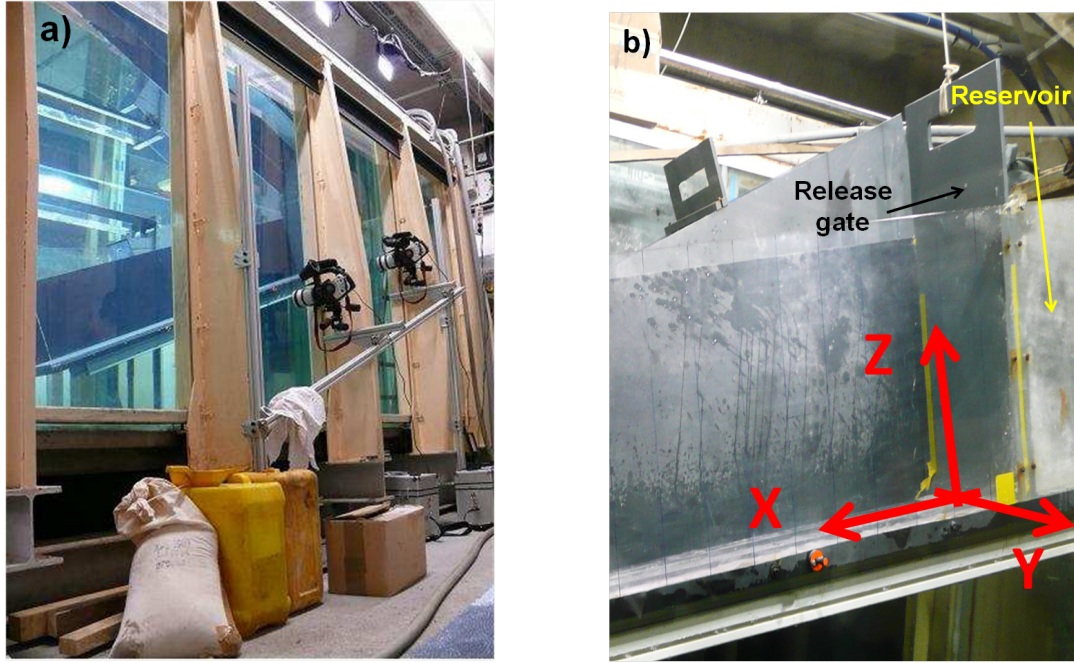


Figure 2.4: (a) A water-tank overview and (b) the reference system that is used throughout this chapter. The x -axis corresponds to the channel axis, and $x = 0$ is set at the release gate. The z -axis is normal to the channel bottom and to the flow direction, $z = 0$ corresponds to the channel bottom. The y -axis, consequently, is defined normal to the x and z -axis.

avalanche site of Taconnaz (more details of this site can be found in chapter 3). Looking down the channel in the flow direction, the left lateral wall corresponds to the side on which video cameras were installed and the wall was made of Plexiglas in order to allow video recording. In the following sections, this will be called the *front-wall*. The right lateral wall (which will be called the *back-wall*) was made of black PVC in order to provide a dark background contrast against the white colour of the density cloud. A mesh of $10 \text{ cm} \times 10 \text{ cm}$ was drawn on the front-wall to have a dimension reference.

The first 20 cm of the channel are separated from the rest by a release gate (see Fig.2.4.b) in order to create the reservoir where the heavy fluid simulating the avalanche is stored. By opening the gate, 4 litres of fluid are released and start flowing along the channel. A reference system is set here and is used throughout the entire chapter. As shown in Fig.2.4.b, the x -axis corresponds to the channel axis, and $x = 0$ is set at the release gate. The z -axis is normal to the channel bottom and to the flow direction, and $z = 0$ corresponds to the channel bottom. The y -axis, consequently, is defined normal to the x and z -axis. Powder-snow avalanches are simulated by a heavy fluid dispersing in a lighter fluid. The heavy fluid consists of dyed salt water: salt water in saturated conditions has a density of 1185 kg m^{-3} , which rises a value of $\rho = 1200 \text{ kg m}^{-3}$ when the kaolin is added. This white powder makes the gravity current visible from outside the water tank and, most importantly, it provides the particle suspension required by the ultrasonic Doppler velocimeter. A finite volume of fluid is released quasi-instantaneously from the immersed reservoir generating an unsteady density cloud.

Contrary to what occurs in nature, the laboratory-simulated avalanche starts as a pure powder avalanche, and the bed entrainment of particles is not taken into account. A real-scale reference phenomenon must be considered and its dimensions must be extrapolated in order to calculate the reference densimetric Froude number of the reference avalanche. This obtained value of Fr_d defines the characteristic dimensions (height and velocity) of the small-scale flow necessary to

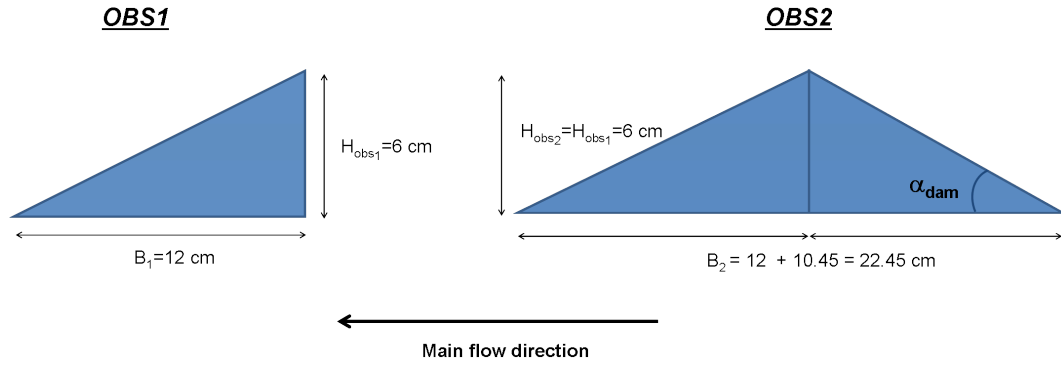


Figure 2.5: Dams' cross-sections

fulfil the dynamic similarity requirement. No real data were available concerning powder-snow avalanches on the Tacconnaz site, and empirical considerations therefore evaluated the estimation of a reference avalanche characterised by a maximum height of 50 m, a maximum front velocity of 30 m s^{-1} and a density ratio of 4, as in Naaïm et al. (2010) [106]. Initially, different fluid volumes were tested and a fluid volume of 4 l was finally chosen because this value best fulfilled the densimetric-Froude similarity requirement. Additionally, a scale factor of 1 : 415 was found to match the geometrical similarity between the real site dimensions and those available for the small-scale laboratory model. See Caccamo (2008) [32] for more details.

The obstacles

A catching-dam-like obstacle was installed at a distance of 1 m from the releasing gate. This obstacle was mounted on the channel bottom, placed with the uphill vertical wall perpendicular to the channel axis and to the flow main direction in order to span the entire width of the channel. The dam has a triangular cross-section with a height $H_{obs1} = 6 \text{ cm}$ and a base $B_1 = 12 \text{ cm}$ representing the shape and the dimension ratios of a classic earth-filled protection structure. This configuration is indicated in the following sections as *OBS1*. Along with the scale factor (1:415), these dimensions reach a real-scale height of 25 m (and a base of 50 m), which is the height of the final catching dam that composes the Tacconnaz protection system.

In the second step, different dam geometry was considered and a new structure was designed. This second configuration is indicated in the following sections as *OBS2* and aims to reproduce a dam with an uphill mill pond already filled with snow, even a different structural solution where the uphill wall is not vertical but inclined at an angle α_{dam} with respect to the ground. Thus, a quasi-symmetric structure was added to *OBS1* with a height $H_{obs2} = H_{obs1}$ and an angle $\alpha_{dam} = 32.10^\circ$ which gave a total base $B_2 = 22.45 \text{ cm}$. Figure 2.5 shows the two structure's sections.

The video cameras

As shown in Fig.2.4.a, outside of the water tank, close to the lateral glass wall, two video cameras were installed to record the flow experiments. They are two Canon *XL1* video cameras with a recording frequency of 25 fps. They were placed on the side with their longitudinal axis perpendicular to the channel and the transversal axis parallel to the flow direction in order to see the avalanche flowing horizontally. The height of the cloud, its length, and its shape were measured, and the flow front velocity was derived through image treatment. The two video cameras were placed with their fields of view overlapping in order to ensure continuity between measurements obtained from the uphill and downhill cameras.

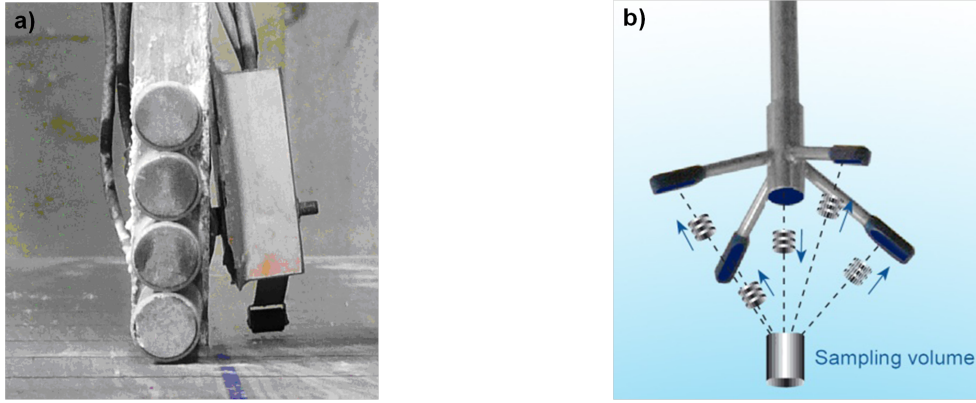


Figure 2.6: (a) The four beams of the ultrasound Doppler velocimeter, on top of one another and adjacent to the flow path and (b) the Vectrino velocimeter operating principle. A pulse is transmitted from the central transducer, and the Doppler shift introduced by the reflection from particles suspended in the water is picked up by the four receivers.

The ultrasound Doppler velocimeter

Previous experiments from Naaim-Bouvet et al. (2002) [107], Sampl et al. (2004) [135] and Caccamo (2008) [32] made use of an ultrasound Doppler Velocimeter. This type of technology measures the component of the particle velocity vector in the direction of the transducer. The principle of this sensor is based on the change in frequency of an acoustic wave resulting from the movement of particles in suspension. In pulsed Doppler ultrasound, instead of emitting continuous ultrasonic waves, an emitter periodically sends a short ultrasonic burst, and a receiver continuously collects echoes issued from targets that may be present in the path of the ultrasonic beam. The acoustic near field is cylindrical from the head of the transducer up to a distance of 16.7 mm. Afterwards it diverges at an angle of 5.2° . The size of the sampling volume can therefore be easily calculated.

An array of four transducers coupled with the expanded ultrasonic unit was used for the experiments. The four beams were placed horizontally, on top of one another (see Fig.2.6.a) and connected by a mechanical arm to a moving structure that allowed the measurement position to be varied along the channel axis. In order to optimise the acquisition times, it was decided to use only two transducers at once instead of four [32, 107].

The Vectrino

The Vectrino is a high-resolution acoustic velocimeter used to measure turbulence and $3D$ water velocity in a wide variety of applications from the laboratory to the ocean. The basic measurement technology is coherent Doppler processing, which is characterised by accurate data and no significant offset. The Vectrino uses the Doppler effect to measure current velocity by transmitting a short pulse of sound, listening to its echo, and measuring the change in pitch or frequency of the echo. In contrast to standard Doppler profilers (Ultrasound Doppler Velocimeter) and current meters, the Vectrino is a bi-static sonar. This means that it uses separate beams for transmission and reception. It transmits through a central beam and receives through four beams displaced off to the side (see Fig.2.6.b). The sampling volume is located 5 cm away from the sensor to provide undisturbed measurements. It consists of a cylinder with a diameter of 6 mm and a height of 3 mm. When the pulse travels through the focal point of the receiver beams, the echo is recorded in each of the acoustic receiver elements. The echo is then processed in order to find the Doppler shift, the scaling is adjusted with the measured speed of sound in the liquid,

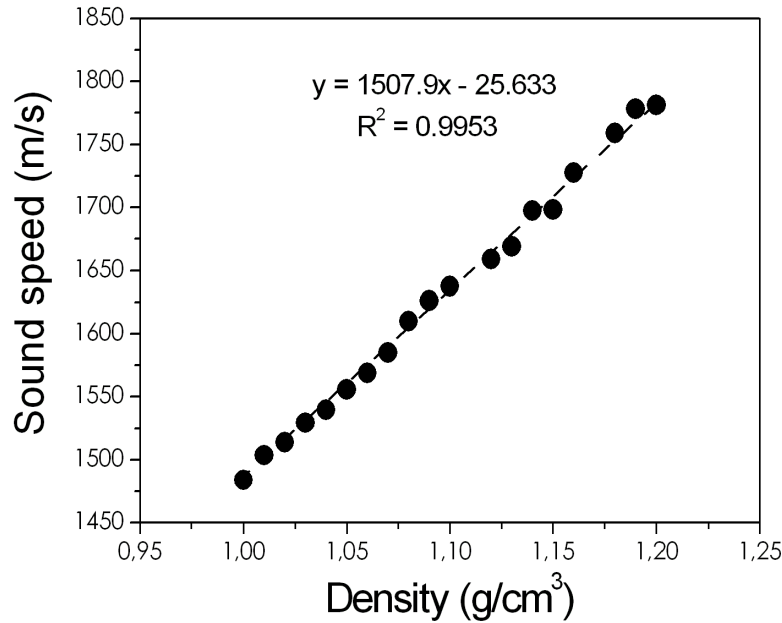


Figure 2.7: Sound speed variation versus the flow density. Data extracted from Sampl et al. (2004) [135].

and the velocity vector is recorded or transmitted to a computer at a rapid rate. The Vectrino Lab Probe is used in a variety of laboratory applications, such as in hydraulic laboratories to measure turbulence, 3D velocities in flumes, and physical models. We used it to measure the 3D velocity profile of a density cloud flowing down a channel. As for the ultrasound Doppler velocimeter, the instrument is connected to an adjustable structure allowing the variation of the measurement position along the channel axis (x , y and z adjustment). The x and y setting is made according to a grid which was drawn on the channel bottom and an acoustic sensor indicating the distance between the sensor and the channel bottom allows a precise positioning along the z -axis.

The drawings with dimensions of the Vectrino and the technical specifications are available in Annexe 1.

Measurements from both the ultrasonic Doppler velocimeter and the Vectrino are sensitive to the flow salinity which defines the sound speed. Based on the relationship reported in Sampl et al. (2004) [135] and displayed in Fig.2.7, a fixed mean flow density of 1100 kg m^{-3} was assumed and thus the speed of sound was set at 1633 m s^{-1} and maintained constant for all of the tests.

The switch

A waterproof switch was installed adjacent to the reservoir gate (see Fig.2.8.a). Its function is fundamental as it allows the perfect synchronisation of each test regarding maximum velocity measurements (Vectrino velocimeter), front velocity, and maximum height measurements (image processing). Upon opening the gate, the switch sends an input pulse which releases the velocimeter recording and, at the same time, turns on an LED (light-emitting diode). This LED is placed in order to remain in the field-of-view of both video cameras (see Fig.2.8.b). When treating image sequences, the time t_0 corresponds to the first image with the LED on. Thus,

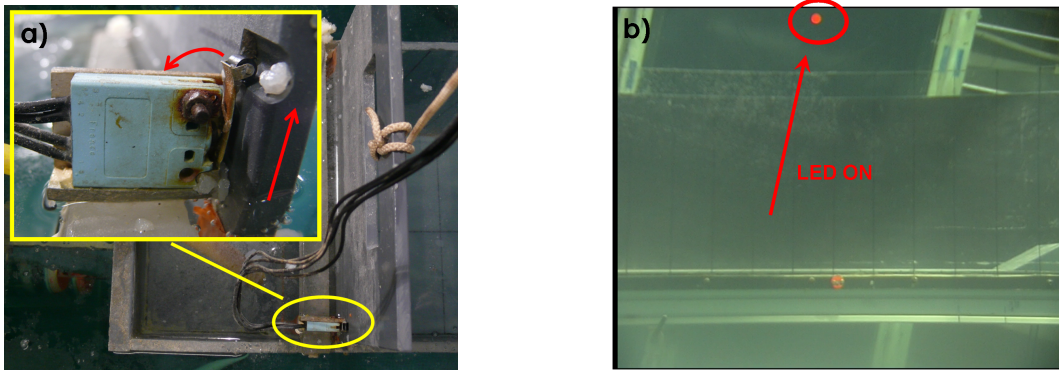


Figure 2.8: (a) Overview and detail of the switch. When the release gate is opened, it activates and sends the t_0 signal to the acquisition devices. (b) Image showing the LED on (top center). For image processing, the time associated with this image corresponds to t_0 .

the switch ensures a perfect synchronisation of all collected measurements and removes a source of potential error.

2.2.3 Measurement techniques

Mean density measurement

Density measurements represented an unexpected potential of the Vectrino. As discussed at the end of section 2.1.5, an acoustic sensor indicates the distance from the Vectrino probe to the channel bottom. The sensor works as an emitter and as a receiver. It emits a pulse which is reflected by the bottom and re-collected by the receiver. The acquisition frequency of the sensor is $f_{ac} = 10$ Hz. The distance is calculated by measuring the pulse travel-time t_{pulse} , which depends on the speed of sound c_s and, in turn, depends on the fluid density when the density difference is due to a difference in the fluid salinity. Thus, with respect to Fig.2.9. a, fixing the sound speed in the Vectrino input parameters as $c_s = c_{s0}$ (c_{s0} being the sound speed for pure water), the reference distance is:

$$d_0 = \frac{c_{s0}}{t^0} \quad (2.11)$$

where t^0 is the pulse travel-time in reference conditions (the sensor is immersed in pure water). When the flow crosses the measurements' section, the sensor records a variation of the bottom distance. This is due to the fact that a higher salinity causes a higher density (ρ_1), which implies a higher sound speed (c_{s1}) and thus a shorter travel-time (t^1) for the acoustic pulse.

$$d_1 = \frac{c_{s0}}{t^1} \quad (2.12)$$

$$c_{s1} = d_0 t^1 = d_0 \frac{c_{s0}}{d_1} \quad (2.13)$$

The sensor interprets it as a distance variation (see Fig.2.9. b) that can be easily related to the effective density variation when knowing the $c_s(\rho)$ relation. Measurements were based on the $c_s(\rho)$ relation found in Sampl et al. (2004) [135] and displayed in Fig.2.7.

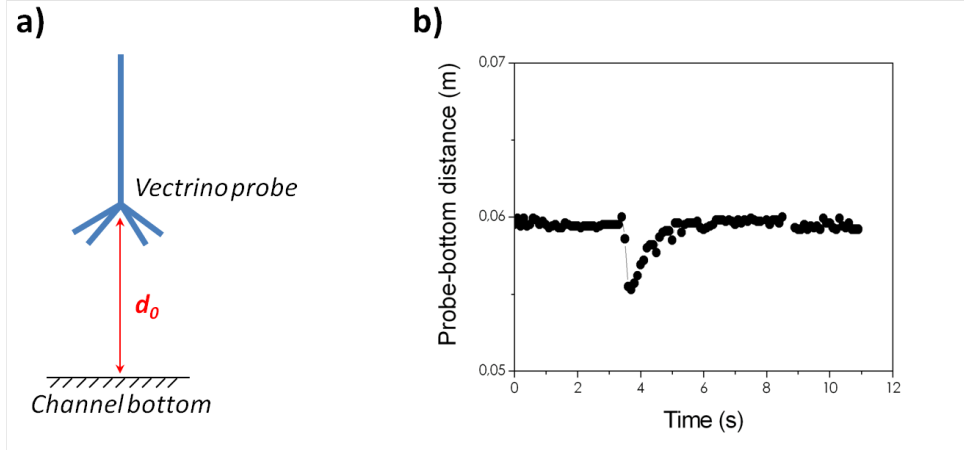


Figure 2.9: (a) Sketch showing the density measurement principle. (b) Typical distance profile obtained with the Vectrino. The Vectrino probe is fixed at a distance $d_0 = 0.06$ m from the channel bottom. This distance variation is related to a density variation.

Some preliminary results are presented here and the problems that were encountered explain our decision to not continue with this type of measurement.

Figure 2.10.a shows three typical density profiles and their mean values, obtained at $x = 1$ m and $z = 0.06$ m. Initial values are very close to $\rho = 1000$ kg m⁻³ (pure water conditions), but at the passage of the cloud, they rapidly increase up to a peak value, after which they decrease immediately. The passage of the cloud lasts around 2 s, which is in excellent agreement with image sequence analysis. The maximum value rises to $\rho = 1085$ kg m⁻³ for these tests, but this was found to vary significantly (1060 – 1110) as it is highly influenced by the time that the salt solution takes to enter the reservoir (in contact with pure water). For $t > 6$ s, the final value is not equal to 1 because a wake still transits in the channel (this phenomenon is visible in Fig.2.16 for the three pictures at $x = 1.12$ m). Results seem to confirm the expectations. Naaim-Bouvet et al. (2002) [107] and Caccamo (2008) [32] assumed a mean density of 1100 kg m⁻³, and all of the velocity measurements collected through the ultrasound Doppler and the Vectrino velocimeters were set, as already mentioned in section 2.2.2, on a mean sound speed $c_s = 1633$ m s⁻¹ corresponding to $\rho = 1100$ kg m⁻³. Data also confirm that the maximum density is localised and most likely at the front of the avalanche.

However, we were confronted with certain problems. Due to the fact that the Vectrino distance measurements are supposed to be used to set the sensor position before the velocity measurement, two technical details limited our type of utilisation. The acquisition frequency was fixed at $f_{ac} = 10$ Hz and not user-adjustable providing few measure points with respect to the dynamics of the phenomenon. However, no synchronisation devices were possible and thus the precise time t_0 was unknown and the synchronisation between different tests was made by shifting the entire profile in order to set the density maximum at the same time $t_{\rho_{max}}$. Additionally, the values obtained represented the depth-averaged density of 6 cm. Because of the Vectrino features, the sensor cannot be placed below $z = 0.05$ m, otherwise the control volume would be below the channel bottom (see section 2.2.2 for details). As mentioned in Kneller and Buckee (2000) [94], this kind of flow presents a stratified density structure which is not accounted for by the depth-averaged information. Measurements were taken at different z -positions in order to derive vertical profiles for the flow density, but inconsistent values were found (typically $\rho < 1000$ kg m⁻³). This is probably due to the fact that the sensor might not be entirely immersed in the cloud during the entire transit duration if the z -position is increased. This case-scenario would mean that, at certain times, t the acoustic pulse passes through pure water

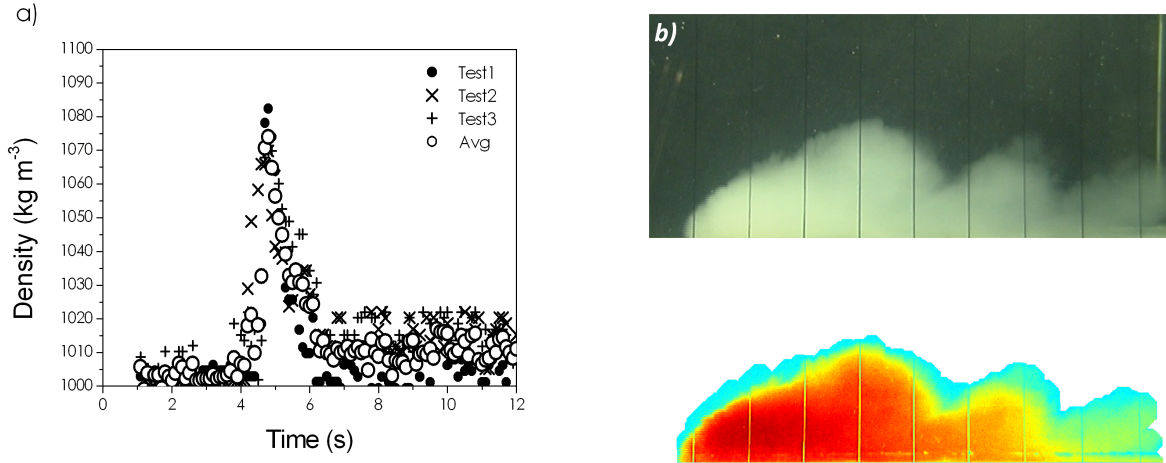


Figure 2.10: (a) Measured density values over time. Three tests were conducted in *REF* conditions at $x = 1$ m and $z = 0.01$ m, and the blank circles represent their mean trend. (b) Density measurement trial technique. A colour analysis was attempted but results were found to be very qualitative.

with a speed c_0 , and at other times t , its speed varies with flow salinity and everything is finally averaged, providing distorted values. One last aspect consists of the initial density values which are generally very close to 1000 kg m^{-3} but not exactly 1000 kg m^{-3} . We attributed this to the accuracy level of the distance sensor and of the temperature sensor (which provides the temperature for the computation of the distance made by the VECTRINO software). Thought to be used as a positioning facility, this sensor does not satisfy the precision criteria needed to ensure precise and reliable results concerning the density variations that occur inside a buoyant cloud. Although this method was found to be very compelling, the needed improvements would have required too much time from the given schedule. Thus, we decided to not pursue the improvement of this technique, which remains a good challenge for future research. Lastly, a final trial was conducted in order to better understand the density distribution inside the cloud from a qualitative point of view. As previously done by Turnbull and McElwaine (2008) [153], we inverted the gray scheme of image sequences in order to more clearly see the flow structure, and we then turned them back into a colour-mash for better visualisation. Based on the principle that denser regions of flow reflect more light than less dense regions, the density scale ranges from dark-red to azure colour in the treated images. Thus, a colour analysis of Fig.2.10.b shows a higher density inside the cloud, defining its front and body components, which clearly decreases all around the core and forms the tail of the avalanche. However, this method only allowed very qualitative considerations that were not very reliable, and we decided to abandon this technique that can scarcely be improved.

Maximum height measurement

This type of measurement was taken by means of the two video cameras. Clear water conditions were needed in order to have neat images for post-processing, thus, maximum height (and front velocity) measurements were done first. At the beginning of both sets of experiments, with and without obstacles, the water tank was emptied, cleaned, and refilled with fresh water. The aerosol cloud flowing down the channel was recorded and images were treated. Two different methods were used.

The first technique was the less accurate of the two, but still allowed the estimation of general trends. Looking through the sequence image by image, when the avalanche front reached a reference mesh line, the maximum height was calculated by manually taking the z -coordinate,

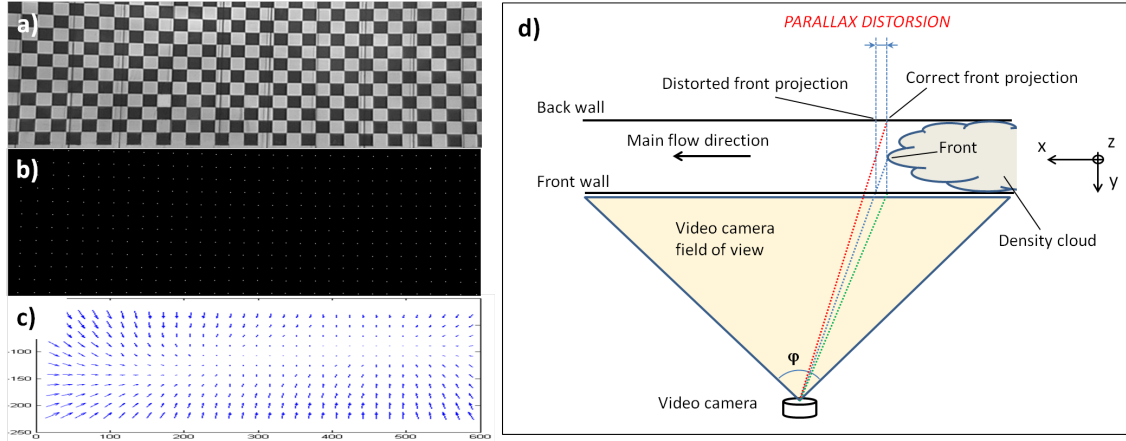


Figure 2.11: Calibration steps: (a) the checker-pattern is recorded and changed to a gray-scale image, (b) intersection points are detected and (c) the deformation rate is given for all intersection points. (d) Sketch showing the origin of the parallax distortion.

in pixels. This value was then transformed in mm using the pix/mm ratio previously estimated. The obtained value was then related to the front x -position. This method did not take into account the error introduced by the lens deformation.

The second technique was developed within the framework of this thesis, and it did take into account this type of error and thus represents a more accurate method for collecting maximum height (and front velocity) measurements. The principle consists of processing the image sequence in order to re-create an artificial mask that reproduces the density cloud. This mask then provides easy access to the more interesting parameters of the cloud, such as its front position and its maximum height. This technique corrects the error from the lens deformation. An accurate calibration is needed as first step. A checker-pattern is printed on a large plastic surface, fixed on the two lateral walls (one at the time), and recorded by the video camera (Fig.2.11.a). The calibration program is based on the principle that, due to the image deformation, the checker-pattern cells do not have the same dimension in recorded images (whether they do in reality). The procedure follows these steps:

- we assumed that the deformation is zero for the central pixels of the image and that it increases when increasing the distance from the center;
- the program detects all intersection points of the checkerboard (Fig.2.11.b);
- it searches the two central points and calculates the distance in pixels (for horizontal deformation, it searches the two central points on the same line and, for the vertical deformation, it searches the two central points on the same column);
- this value is used as a reference to calculate the deformation rate cell by cell;
- a deformation value is assigned to each intersection point (Fig.2.11.c) and values are then designated to measure the deformation for each pixel of the image.

This procedure was carried out four times for both the uphill and downhill cameras, and the left and right lateral walls were used. The video cameras were installed at the beginning of the tests and they did not move until the end in order to maintain the same field of view and image dimension. Raw images were cropped in order to focus on the avalanche path (see Fig.2.12.a), and crop dimensions were constant for all tests recorded. The calibration output consisted of two matrices of $n \times m$ dimensions corresponding to the dimensions, in pixels, of the cropped images. Each matrix cell corresponds to a pixel of the image and it contains the real corrected

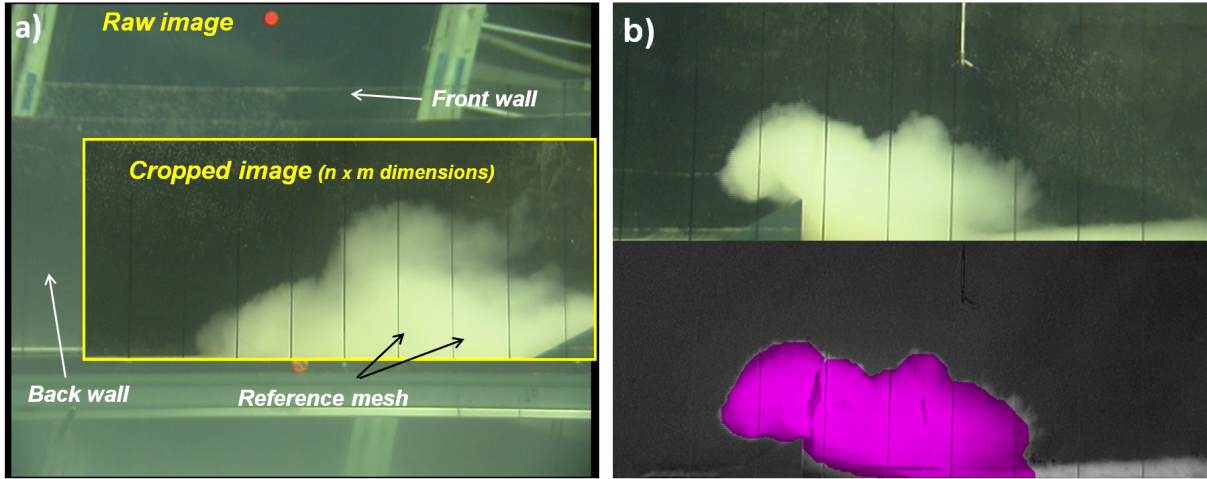


Figure 2.12: (a) Raw image obtained from the downhill video camera and the size of the crop made through the treatment and (b) visual restitution of the generated avalanche mask.

x -position (the first matrix) and z -position (the second matrix) in mm . A pix/mm ratio is calculated by knowing the dimension of a checker-pattern cell (3 cm) and the respective number of pixels of the reference value.

As a second step, after the calibration procedure, data processing was conducted. A home-made program was developed in order to treat the image sequences. The treatment proceeds step by step:

- it opens the image and gray-scales it;
- the background is removed and the avalanche contour is corrected by using a gray-level threshold;
- the cloud surface is detected and a mask is created (the mask consists of a matrix of 0-value for the background and 1-value for the avalanche, see Fig.2.12.b);
- the mask matrix is multiplied by the two position matrices (X and Z) obtained from the calibration. The results consists of two new matrices with 0-values for the background and the corrected position (X and Y) for each pixel of the image forming the density cloud;
- in the mask Y -matrix, the maximum value represents the maximum height (and the minimum non-zero value in the X -matrix corresponds to the x -position of the front).

The data processing used the outcomes of the calibration procedure. The treatment was applied separately to the uphill and downhill cameras. Image sequences obtained from each test were treated two times, with the first treatment using the front-wall calibration and the second treatment using the back-wall calibration. This yielded two sets of data whose average was considered as a final result. This detail allowed us to minimise the parallax error affecting our measurements. The detected front position corresponds to the projection of the avalanche front on the front-wall, which, as shown in Fig.2.11.d, is not perpendicular to the x -axis, but rather depends on the field of view angle and on the front position along the x -axis. The processing program was developed in Matlab; in section 2.3, the results obtained with this program are reported in the graphs as $\langle resultname \rangle.m$ (see, for example, Fig.2.17.a-b). Note that presented results always show the maximum flow height versus the flow front position, and not the position at which the maximum is measured. To display h_{max} as a function of the maximum height position would be less representative of the flow dynamics.

This processing program was found to provide very accurate values. Raw data concerned the

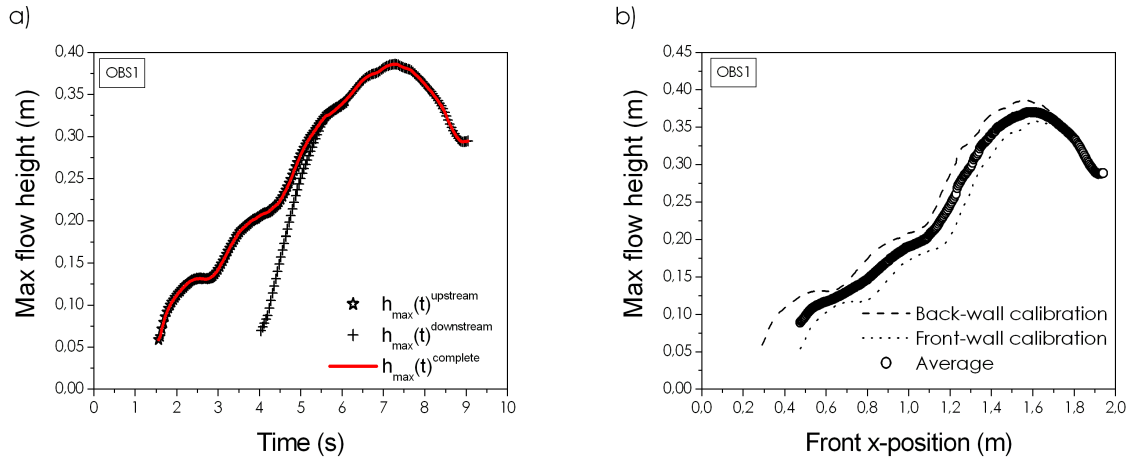


Figure 2.13: (a) Maximum flow heights versus time for the uphill and downhill video cameras (single test result in the *OBS1* configuration). Data on the overlap zone correspond perfectly. The red-line represents the complete profile. (b) Maximum height values obtained from a single test in the *OBS1* configuration using the front and back-wall calibration. Blank circles represent the average between the two profiles.

maximum height of the cloud as a function of time. Image processing was conducted for images coming from the uphill and downhill video cameras. The excellent consistency between uphill and downhill data provided the first validation of the program's quality. Data were approximated over ten points (0.4 s) and then combined in order to obtain a single set of data for the entire length of the channel. Note that the beginning of the downhill signal is distorted because the first images do not capture the entire cloud, which arrives image by image. Data correspond well together when the entire cloud is visible in both uphill and downhill images, as shown in Fig.2.13.a. As mentioned before, the treatment was applied using the calibration previously executed for the front and back lateral walls of the channel. Two similar profiles for the maximum height were obtained (see Fig.2.13.b), and the average values were considered as the final result. One problem arose during the series of experiments. The two video cameras were removed by another team (cameras are shared) from their fixed position after the second set of experiments (*OBS1* configuration). As the entire calibration procedure on which the image processing was based (and which lent the program its innovative quality) was valid as long as all of the tests were recorded from exactly the same camera positions, the last set of experiments could not be treated using the same program. Results obtained in the *REF* conditions and in the presence of *OBS1* are represented by the dashed profiles in Fig.2.17.a (*REF.m* and *OBS1.m*).

Thus, the first technique aforementioned was used. The maximum flow height was recalculated for *REF* and *OBS1* and calculated for *OBS2* in order to yield results that can be compared due to their mutual processing technique.

Front velocity measurement

The front flow velocity (u_{fr}) was measured by recording the flow and treating the image sequences. As was the case for height measurements, the image treatment requires an accurate calibration because images are affected by a potentially significant deformation of the lens of the video camera (see Caccamo (2008) [32] for more details).

Two different techniques were used to measure the front velocity. The first technique consists in watching the sequence image-by-image and counting the number of images the avalanche requires in order to cover a distance of 10 cm corresponding to the grid unit drawn on the front Plexiglas wall. A mean velocity value is derived and assigned to the x -coordinate corresponding

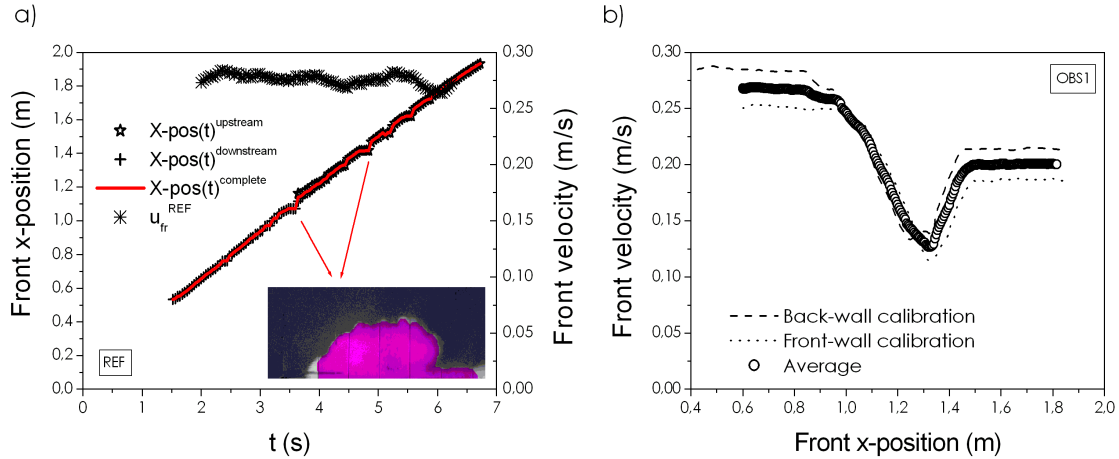


Figure 2.14: (a) Avalanche front position versus time for the uphill and downhill video cameras (single-test results, in the *REF* configuration). Measurements on the overlap zone correspond perfectly. The red line is the complete profile and the starred trend represents the obtained front velocity. The inset shows a malfunctioning of the processing program. The cloud mask sometimes blocks at the crossing of the mesh line and loses several images before regaining the right position. (b) Front velocity profiles with *OBS1* obtained using the front and back-wall calibration (single-test case). Circles represent the average between the two profiles.

to the central point of the grid cell. This method was also used in Naaim-Bouvet et al. (2002) [107] and Sampl et al. (2004) [135] and has the advantage of not being sensitive to the lens deformation problem because it is based on known distances. Measurements were collected separately for the uphill and downhill video cameras, and the values obtained in the overlap zone were averaged.

The second technique was developed within the framework of this thesis and represent a much more accurate method for front velocity (and maximum height) measurements. Considerations similar to those previously made for the maximum flow height (see the previous section *Maximum height measurements* for details) can be done for front velocity results. Values were derived from the same Matlab program which provided maximum height data through automatic image processing. The Matlab procedure extracted the front position from the flow mask. For each image, this mask provided a value for the front position and maximum height. The obtained velocity values were corrected relative to the image deformation from the video camera lens, because a calibration procedure was at the base of the image processing program. Raw data relate to the front position of the cloud as a function of time. Image processing was utilised for the images coming from the uphill and downhill video cameras. As can be observed in Fig.2.14.a, the two profiles correspond very well. Both trends appear to be clearly linear for the reference case. Values were then combined in order to obtain a single set of data for each test. The average of the two profiles was taken relative to the overlap zone. The obtained complete profile was still found to be highly linear in the *REF* configuration. This was not the case in the presence of obstacles. From data on the front position, the front velocity was calculated as the local slope of the position profile ($\frac{dx_{fr}}{dt}$). A moving linear interpolation was made on 25 points and the slope coefficient was taken as u_{fr} . Values were finally plotted as a function of x_{fr} . As for the maximum height, the treatment was done using the back-wall and front-wall calibration in order to reduce errors due to the depth of field and parallax, and the final average profile was considered as representative (Fig.2.14.b). As for maximum height results, in section 2.3, the results reached through this program are reported in the graphs as $\langle resultname \rangle.m$ (see, for example, Fig.2.18.a-b).

This treatment was implemented only in *REF* and *OBS1* configurations because of the same

problem encountered with height measurements. After the *OBS1* test campaign, the two video cameras were removed. As a consequence, the first technique, as mentioned before, provided the front velocity measurements for the complete set of three configurations.

Core velocity measurement

Core velocity was found to be higher than the front velocity [80, 91, 107] and, due to turbulence eddies, the maximum velocity values were found inside of the cloud. To measure the core velocity, the Vectrino Doppler velocimeter was used. The instrument's operating principle was explained in section 2.2.2. Measurements were taken at different positions along the x -axis ($y = 0$). Table 2.3 gives an overview of the investigated position for the three configuration cases. Positions were calculated with respect to the releasing gate (x_0). The obstacle was placed at $x = 1$ m.

Table 2.3: Investigated channel positions

	0.5m	0.7m	0.9m	0.99m	1m	1.15m	1.30m	1.50m	1.70m	1.90m
REF	X	X			X		X	X	X	X
OBS1				X	X	X	X		X	
OBS2		X	X		X	X	X		X	

As shown in Tab.2.3, some additional positions were investigated with respect to the reference case. $x = 0.90$ m corresponds to the beginning of the uphill ramp of *OBS2*; $x = 0.99$ m is right before the obstacle ridge, and $x = 1.15$ m represents the end of the downhill ramp for *OBS1* and *OBS2*.

At a fixed x -position, vertical profiles of velocities ($u(z)$) were achieved by positioning the sensor at different heights with respect to the bottom of the channel. Typically, a height ranging from 0 to 20 cm (30 cm around the obstacle) was investigated through 9 to 13 distinct z -values. Mechanical constraints limited the investigation of the maximum height for $x = 0.5$ m and $x = 0.7$ m, where the Vectrino supporting structure could not reach z -values higher than $z = 0.1$ m because of the presence of the ceiling. For a fixed position ($x; z$), three to five tests were repeated and their results were averaged.

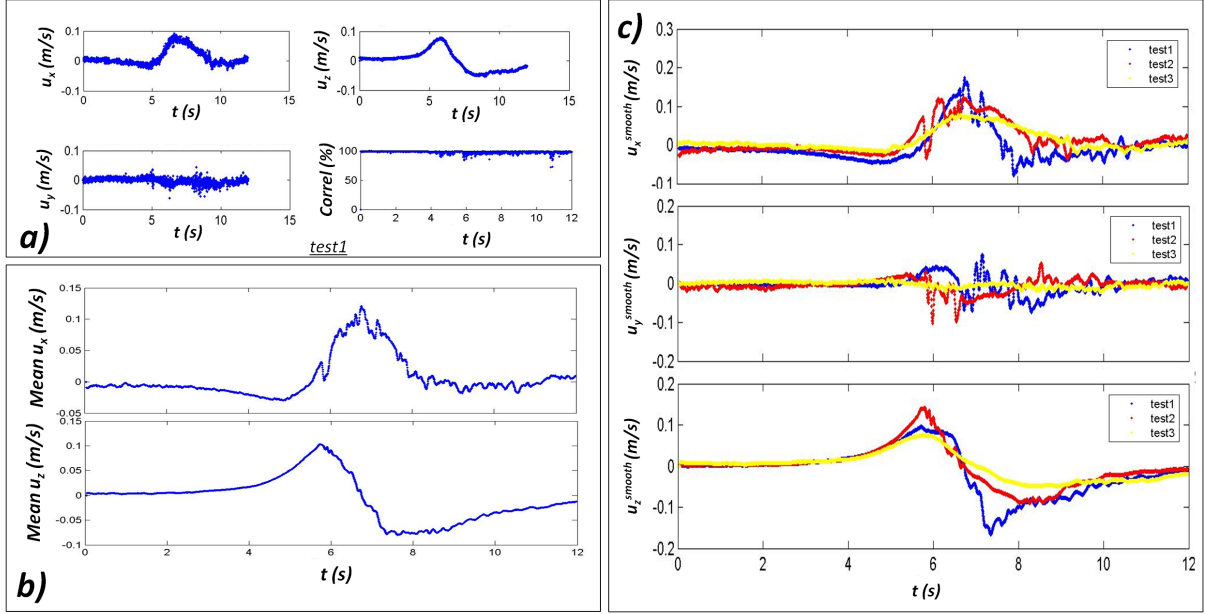


Figure 2.15: Typical output of Vectrino measurements. The example measurement was taken at $x = 1.30$ m and $z = 19$ cm in the OBS2 configuration. (a) Typical profiles obtained from a test (test1). Low-correlation and aberrant data were removed. (b) Final mean profiles for u_x and u_z . (c) Comparison of smoothed profiles.

The Vectrino gave an output for the time evolution of several parameters: the three velocity values (u_x , u_y and u_z), for which it furnishes the signal amplitude, its signal-to-noise ratio, and the correlation index (Fig.2.15.a). The correlation index can be considered as a reliable indicator of the quality of the measurements [132]. To ensure data quality, the correlation had to be higher than 70%. Thus, raw data obtained from the Vectrino were subjected to additional treatment. Velocity values corresponding to a correlation lower than 70% were removed as well as aberrant values. A velocity value was considered aberrant if it was higher than realistic limitations or when $u_t - u_{t-1}$ was higher than a fixed threshold. After that, the velocity signals were rounded (mean average on ten points), and the average was taken from the three similar tests (Fig.2.15.b-c). As shown in these figures, the time-dependent velocity profiles were generally similar, but occasionally the maximum velocity peaks were slightly shifted in time. Thus, in order to avoid smoothing maximum values, the average of the three maximum peaks was also considered. We believe that, although this choice introduces an error in the data synchronisation (data are presented versus the position along the channel axis and not versus the time), it provides more reliable results from an engineering point of view. Results are shown in section 2.3.

2.3 The water tank: results

2.3.1 Some qualitative considerations

A part of the measurements that were taken through aerosol avalanche modelling were based on image processing. Sequences of images were recorded for density currents in the three investigated configurations (*REF*, *OBS1* and *OBS2*). Some preliminary considerations can be made by watching videos and qualitatively observing the flow behaviour in the reference conditions and interacting with the obstacles. Figure 2.16 gives an overview of the flow behaviour for the three configurations at three different positions, uphill from the obstacle ($x_{fr} \simeq 0.85$ m), around the obstacle ($x_{fr} \simeq 1.2$ m) and downhill from the obstacle ($x_{fr} \simeq 1.8$ m).

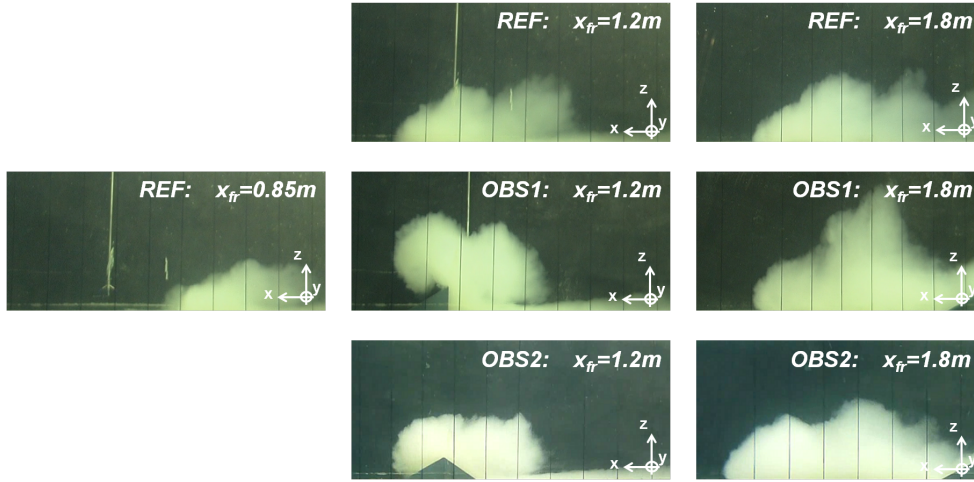


Figure 2.16: Visual overview of the flow behaviour at three different channel sections and for the three investigated configurations. The flow behaviour is supposed to be similar for all the configurations far uphill from the obstacle (section at $x_{fr} = 0.85$ m).

1. Reference flows flow down the channel with a velocity that appears to be rather constant. Their turbulent structure develops into a series of eddies rotating clockwise of different dimensions. Note that, from now on, the clockwise and counter-clockwise rotations are considered looking at the channel from the position of the video cameras and thus with respect to a cloud flowing down from the right to the left.
2. In the *OBS1* configuration, the incoming flow hits the vertical wall of the dam and bursts. The cloud height rapidly increases, the front of the flow separates into two main parts, an upper part rotating clockwise expanding upward and a second part generating new eddies turning counter-clockwise, as observed in Caccamo (2008) [32]. The impact with the obstacle makes the cloud incorporate the ambient fluid, its surface increases and thus its density, theoretically, decreases. The flow is subjected to a strong deflection with the formation of a vertical jet.
3. In the presence of the second dam configuration (*OBS2*), a different behaviour was observed. The flow does not hit the obstacle, but rather it passes smoothly over it, without any visible detachment from the surface. The obstacle seems to not be very efficient in terms of flow dynamic reduction.

These qualitative observations are confirmed by the results presented in the following sections.

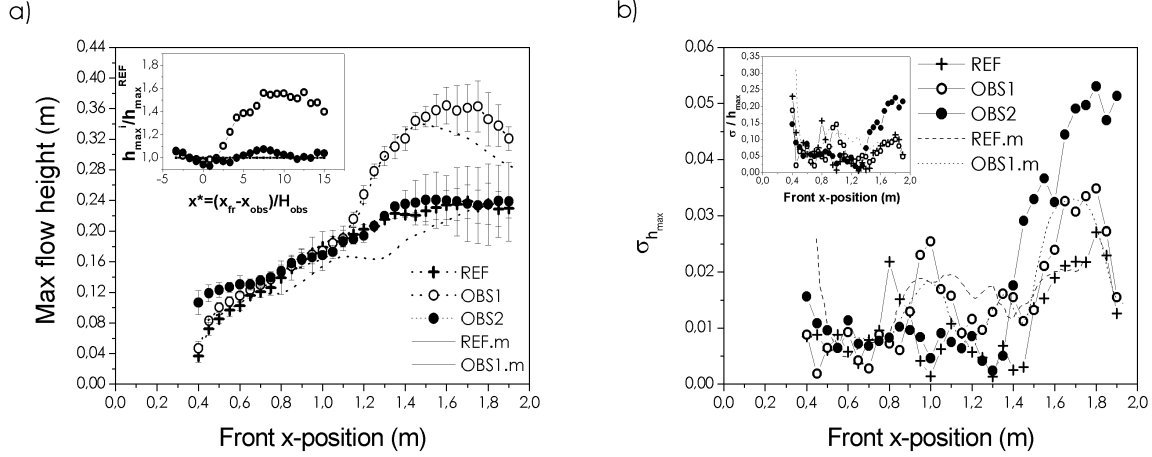


Figure 2.17: (a) Final maximum height values obtained with the two tested techniques, and the three investigated configurations. Maximum height is presented versus the front x-position. In the inset, the h_{max} values are shown in terms of $\frac{h_{max}^i}{h_{max}^{REF}}$ ($i = OBS1, OBS2$) versus the dimensionless distance $x^* = \frac{(x_{fr} - x_{obs})}{H_{obs}}$. (b) Standard deviation behaviour for maximum height results, obtained with the two different techniques, versus the front position. The inset shows the relative weight of $\sigma_{h_{max}}$ with respect to the height values h_{max} , versus the front position.

2.3.2 Maximum height

The maximum height results were obtained with the program presented in section 2.2.3. Final results are presented in Fig.2.17.a. In order to show the results obtained in dimensionless terms (as displayed, for example, in the inset of Fig.2.17.a), the front position is given with respect to

$$x^* = \frac{x_{fr} - x_{obs}}{H_{obs}} \quad (2.14)$$

x^* is also used in the following to interpret the data concerning the front and core velocity of the flow. Profiles obtained through the automatic technique qualitatively fit well with the others, which represents the first validation of the developed technique.

Results

In reference conditions, the maximum flow height increases rather linearly up to $x = 1.4$ m and then stabilises at a constant value of $h_{max}^{REF} \simeq 0.24$ m. In the presence of the obstacle (*OBS1*), the maximum height rapidly increases up to $h_{max}^{OBS1} = 0.36$ m ($x^* \simeq 6$) right after the impact. Thus, the presence of *OBS1* increases the maximum flow height of a factor 0.5 with respect to reference conditions (see the inset in Fig.2.17.a). *OBS2* has almost no influence on the height behaviour of the flow. Nevertheless, this result was to be expected when considering the qualitative considerations made in section 2.3.1. These results must nonetheless be handled with caution.

Error

When looking at Fig.2.17.b, the error relative to the standard deviation shows high values for $x > 1.4$ m, especially for the *OBS2*-configuration. This is mostly due to the turbulent cloud structure. The main eddies are supplied with the material forming the cloud's head and body and, rotating clockwise, they bring this material back to the tail. The tail of a finite-volume density current consists of the last part of the cloud, much more diffused and less dense than

the head and the body. Thus, in order to consider the most relevant values when measuring the maximum flow height, attention was focussed on the head and body part of the avalanche. However, it is not easy to define the borders of these three parts. The maximum height value typically increases with a growing eddy, but when this eddy goes back to the tail, the maximum value is once again attributed to a new growing eddy of the body. This leads to a maximum height profile that does not increase constantly but that, in correspondence to the change of reference eddy, slightly decreases, only to start increasing again until the next change. Such behaviour is more pronounced when the cloud and its turbulence are highly developed, meaning high values of x . Consequently, for high values of x , the curves obtained for maximum height are less possible to reproduce, which implies a higher standard deviation. The automatic treatment program defines the head and body part of the avalanche with respect to a fixed gray-scale threshold. This ensures a constant image treatment and removes all errors from the operator boundary choice. In Fig.2.17.b, the *REF.m* and *OBS1.m* profiles show error values which still increase with the front position but which are lower than the others by nearly a factor 2.

2.3.3 Front velocity

Results

Results obtained through the first automatic technique in the *REF* conditions and in the presence of *OBS1* are represented by the dashed profiles in Fig.2.18.a (*REF.m* and *OBS1.m*). The front velocity of the reference flow is constant and approximately equal to $0.27 - 0.28 \text{ m s}^{-1}$. Measurements for the *OBS1* configuration show a similar front velocity value before $x = 1 \text{ m}$ (the obstacle's position) which drops significantly after impact with the obstacle. The inset in Fig.2.18.a shows that the obstacle (*OBS1.m*) induces a front velocity loss which rises the 51% of the reference (*REF.m*) value directly downhill from the obstacle. Regardless, the flow re-accelerates and, at a distance which was found to be around $x^* = 8$, it rises to a rather constant final value that is still lower than the reference case ($u_{fr}^{OBS1.m} \simeq 0.78u_{fr}^{REF.m}$).

Because of the problem mentioned in the previous section (the removal of the video cameras), the flow front velocity was recalculated for *REF* and *OBS1* and calculated for *OBS2*. Results are all compared together in Fig.2.18.a. There are no significant differences between the two sets of data. In the presence of *OBS1*, the front velocity presents a drop of 48% (with respect to reference conditions) right after the obstacle ($x^* \simeq 4$), which increases again until stabilising around $x^* \simeq 9$ at a rather constant value $u_{fr}^{OBS1} = 0.8u_{fr}^{REF}$. The influence of *OBS2* on the front velocity is less significant. Immediately downhill from the obstacle ($x^* \simeq 2.5$), we measured a velocity loss of 30%, a value which decreases up to 90% at $x^* \simeq 5$ and then remains constant. Even if this method is less accurate, the *REF* and *OBS1* profiles are similar to previous results obtained using the automatic treatment (*REF.m* and *OBS1.m* in Fig.2.18.a).

Error

Figure 2.18.b presents the standard deviation values obtained with the two measurement techniques. Error values relative to the less accurate method are generally higher with respect to the *REF.m* profile. However, *OBS1.m* shows the highest values. This is due to the fact that the

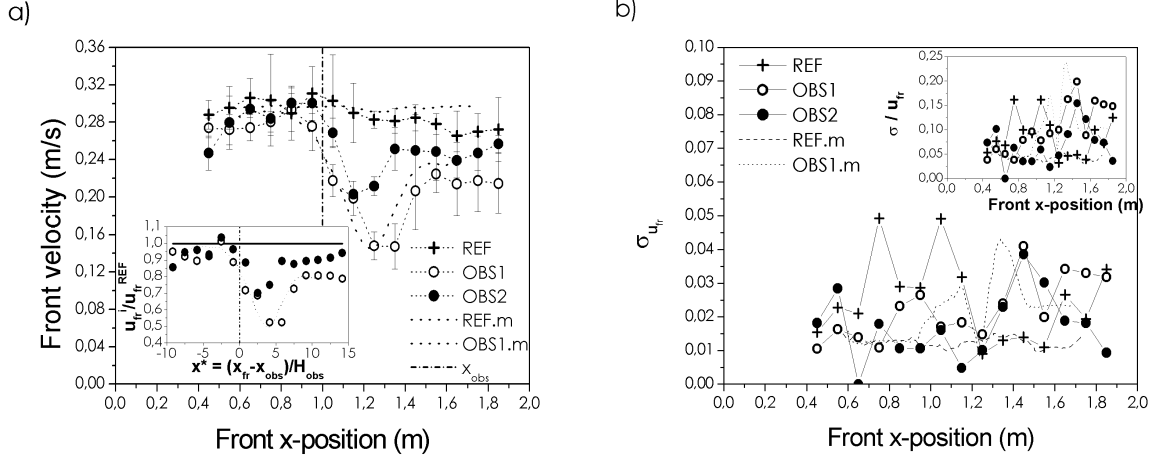


Figure 2.18: (a) Obtained front velocity results. The main figure shows the final profiles obtained through the two different methods by averaging all of the tests of the three configurations investigated (*REF*, *OBS1* and *OBS2*). Front velocity is represented versus the front x -position. In the inset, velocity values are represented in terms of the ratio $\frac{u_i^i}{u_{REF}^i}$ ($i = OBS1, OBS2$) versus a dimensionless distance $x^* = \frac{x_r - x_{obs}}{H_{obs}}$. (b) Standard deviation behaviour for front velocity results obtained through the two different techniques versus the front position. The inset shows the relative weight of σ with respect to the velocity values, versus the front position.

profiles obtained from each test in the *OBS1* configuration show a very similar behaviour with a peak of minimum velocity that always has the same y -value (u_{fr}), but never exactly the same x -value (x_{fr}). Thus, averaging all of the profiles increases the data standard deviation around the peak and provides it with a bi-maximum-shaped profile (see the dotted-line in Fig.2.18.b). The inset shows the standard deviation normalised by the front velocity values and plotted versus the front position. The highest error does not exceed 25% of the velocity value.

Another source of error, which comes from the automatic treatment of raw front position data, must be mentioned even if it is difficult to quantify. When looking carefully at the two profiles of Fig.2.14.a obtained from the uphill and downhill video cameras, it must be noted that sometimes, for a few tenths of a second, the front position remains constant with time. This behaviour is due to the fact that the cloud mask, obtained through image processing, is sometimes blocked when crossing the mesh line as showed in the inset in Fig.2.14.a and loses several images before regaining the right position. A correction was made: raw data were compared to the linear fit calculated on the complete curve and, when the difference $x_{fr}^{raw} - x_{fr}^{fit}$ was higher than a fixed threshold, the raw value were replaced by the assigned value.

These results validate those obtained through the new program that was developed. A comparison between the effects of the two different obstacle solutions was made and it confirmed the preliminary qualitative observations of section 2.3.1. An *OBS2*-type solution still has a reduction effect on the front flow velocity, but this contribution is clearly less significant than that obtained with *OBS1*.

2.3.4 Core velocity

The use of Vectrino for core velocity measurements provided a large amount of data concerning u_x , u_y and u_z . As previously mentioned, the core velocity is generally found to be higher than the front velocity. Front velocity values were identified by the symbol u_{fr} . The Vectrino collected 3D measurements on the core velocity and thus, for the sake of simplicity, these values are represented by the symbols u_x , u_y and u_z in the following sections, depending on the direction. However, the transversal component u_y is neglected. The results showed that the lateral velocities are insignificant in canalised-avalanche flows with respect to the horizontal and vertical contributions, and we mainly attributed this to a lateral momentum induced on the channel structure by the opening of the gate. Additionally, in the domain of protection structure design, the y -component of the core velocity does not represent the most effective parameter. Thus, attention is concentrated on the u_x and u_z components.

Note that, in the following, the core velocity values for a given x -position is expressed as:

a)

$$U_i^+(z) = \frac{1}{n} \sum_1^n u_i^{max}(z) \quad (2.15)$$

with

$$u_i^{max}(z) = \max [u_i(z, t)] \quad (2.16)$$

where $i = x, z$, depending on which core velocity contribution is considered, and n is the number of similar tests carried out for the same given (x, z) position ($n = 3 - 5$).

u_i can be positive or negative, thus, by analogy, it is possible to define

$$U_i^-(z) = \frac{1}{n} \sum_1^n u_i^{min}(z) \quad (2.17)$$

with

$$u_i^{min}(z) = \min [u_i(z, t)] \quad (2.18)$$

$U_i^+(z)$ and $U_i^-(z)$ are fictitious profiles of the flow velocity. They represent the profiles of maximum (and minimum) velocity.

b)

$$U_i^{max} = \max (U_i^+(z)) = \max \left[\frac{1}{n} \sum_1^n u_i^{max}(z) \right] \quad (2.19)$$

$$U_i^{min} = \min (U_i^-(z)) = \min \left[\frac{1}{n} \sum_1^n u_i^{min}(z) \right] \quad (2.20)$$

$$(2.21)$$

U_i^{min} is defined only if $\min [U_i^-(z)] < 0$.

c) At $t = t_{U_i^{max}}$:

$$V_i^+(z) = \frac{1}{n} \sum_1^n u_i(z)_{(t=t_{U_i^{max}})} \quad (2.22)$$

And at $t = t_{U_i^{min}}$:

$$V_i^-(z) = \frac{1}{n} \sum_1^n u_i(z)_{(t=t_{U_i^{min}})} \quad (2.23)$$

$V_i^+(z)$ and $V_i^-(z)$ are real profiles as they represent the velocity profile at the time where the maximum (and minimum) value is observed.

Horizontal core velocity ($V_x^+(z)$)

Figures 2.19-2.20 give a qualitative overview of the results that were obtained. The aim is to give an idea of how the flow core velocity behaves. Figures 2.19.a-c show the evolution of $V_x^+(z)$.

- In the reference case, maximum horizontal core velocities were constantly observed in the lowest part of the cloud ($z \simeq 0.01$ m). The velocity decreases, when increasing z , quite linearly up to $z \simeq 0.11 - 0.12$ m and then remains rather constant for $z > 0.11 - 0.12$ m. A cross-comparison with the results of the maximum height presented in Fig.2.17.a shows that this threshold z -value ($z \simeq 0.11 - 0.12$ m) approximately corresponds to half of the maximum cloud height. Reference profiles are very similar for all of the investigated sections.
- In the presence of *OBS1*, the behaviour far uphill from the obstacle is not supposed to vary. When the flow hits the obstacle, the horizontal core velocity is nearly divided in half. The values still decrease with the height but the trend is less pronounced. The flow bursts and directly downhill from the dam, a profile's inversion occurs: the maximum horizontal core velocity U_x^{max} is found for the highest z -values, while at the bottom $V_x^{+,OBS1} \simeq \frac{V_x^{+,REF}}{5}$. For $x = 1.3$ m ($x^* = 5$), the velocity profile is rather constant, and for $x = 1.7$ ($x^* \simeq 11.5$), a profile similar to the reference-case is observed again, but with lower maximum values.
- In the *OBS2* configuration, the flow behaviour is between the *REF* and *OBS1* scenarios. The horizontal core velocity is similar to that of the reference case when it crosses the obstacle section; immediately downhill ($x = 1.15$ m), the vertical profile of horizontal core velocities changes and the maximum was found for $z \simeq 0.1$ m. However, the maximum value remains constant. Downhill, the last two sections being investigated show profiles of a similar shape, unlike those obtained in the reference configuration, and slightly lower values.

Vertical core velocity ($V_z^+(z)$)

Similar considerations can be made for vertical core velocities (Fig.2.20.d-f).

- Reference vertical profiles of $V_z^+(z)$ were found to be rather constant across the channel and characterised by a semi-elliptical shape. The maximum values occur in the profile center ($z \simeq 0.08 - 0.10$ m) and the minimum values occur at the borders ($z \simeq 0.01$ m and $z \simeq 0.19$ m).
- Upon impact with the obstacle (*OBS1*), the maximum vertical core velocities $U_z^{max}(z)$ increase by a factor of 2 before decreasing again immediately downhill until the end, to values that are lower than the reference values. At $x = 1.15$ m and $x = 1.30$ m, profiles are constant over the height, and velocity regains the semi-elliptical profile as in reference conditions at the final section ($x = 1.7$ m).
- In the *OBS2* configuration, the flow behaviour is between the *REF* and *OBS1* scenarios.

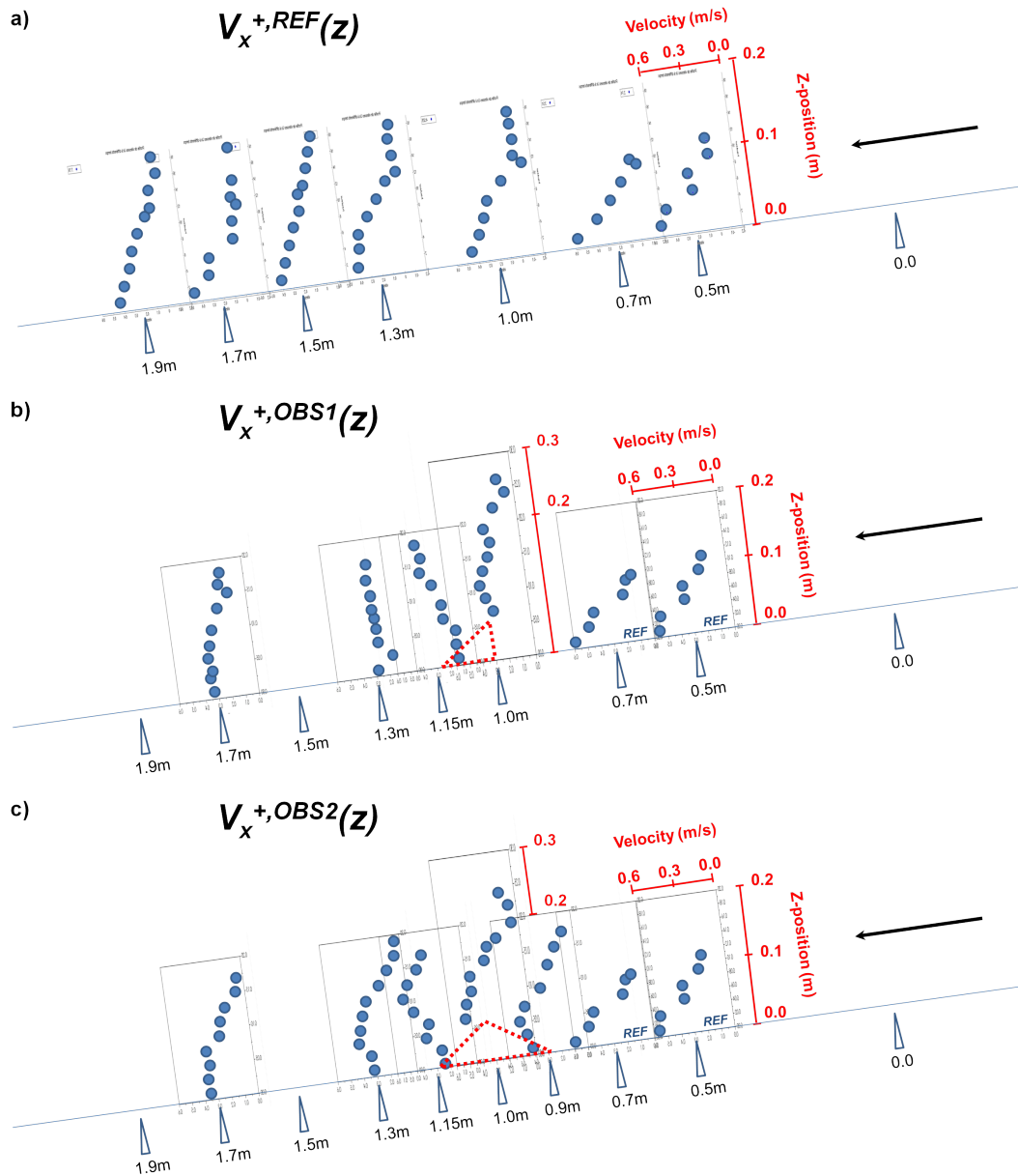


Figure 2.19: General overview of the core velocity profiles $V_x^+(z)$ obtained. The results are shown in order to give an idea of the qualitative behaviour of the density cloud velocity in the three configurations being investigated. The black arrow indicates the direction of the incoming flow. Values of $V_x^+(z)$ presented here consist of core velocities in the flow direction ($V_x < 0$ moves up the channel). More detailed graphs, including error bars, are provided in the following. Profiles represent: (a) $V_x^{+,REF}(z)$, (b) $V_x^{+,OBS1}(z)$ and (c) $V_x^{+,OBS2}(z)$. The z -axis ranges from 0 to 0.2 m (except for measurements collected at $x = 1$ m in the presence of the obstacle where $0 < z < 0.3$ m) while the x -axis ranges from 0 to 0.6 m s^{-1} .

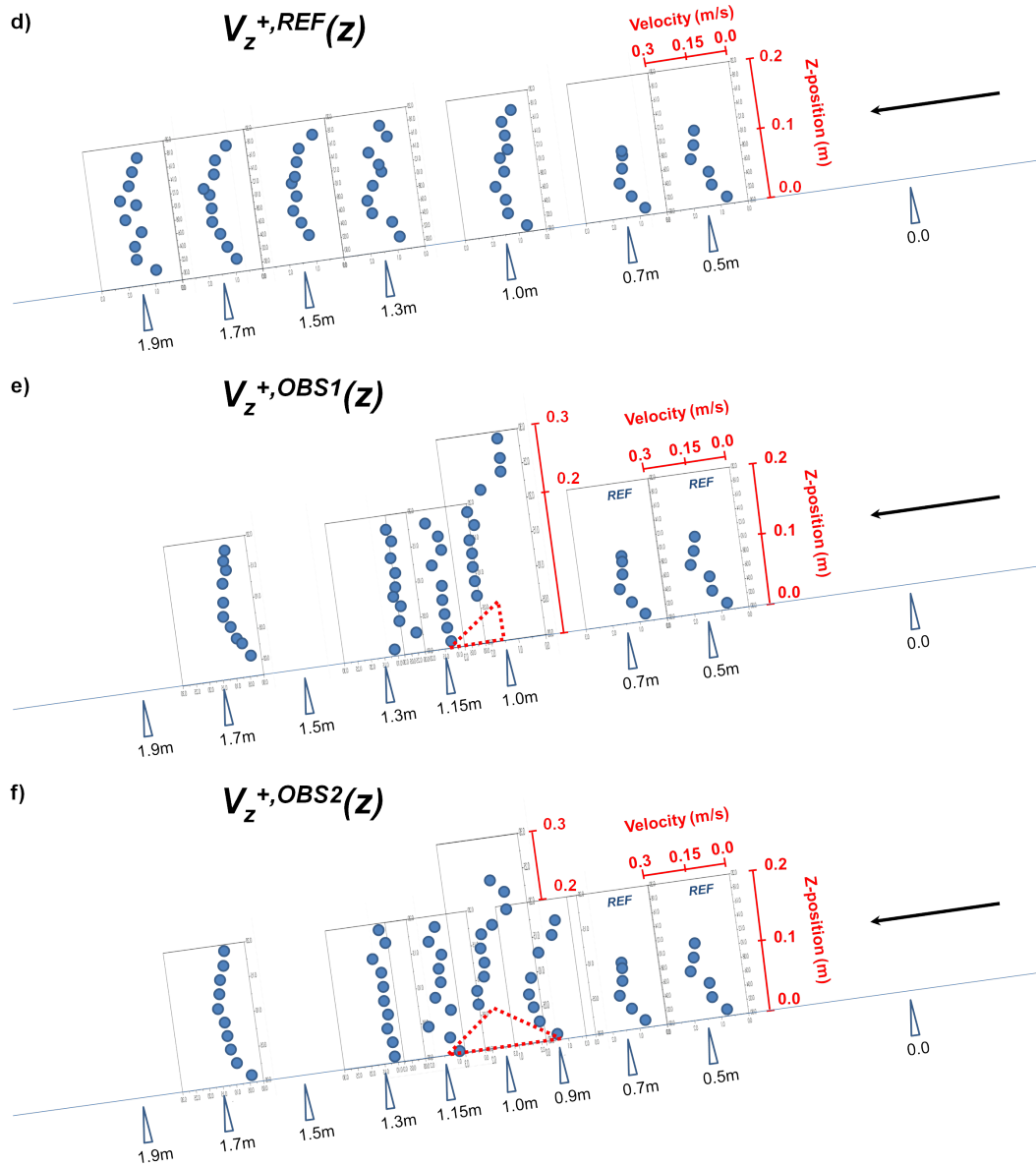


Figure 2.20: General overview of the core velocity profiles $V_z^+(z)$ obtained. The results are shown in order to give an idea of the qualitative behaviour of the density cloud velocity in the three configurations being investigated. The black arrow indicates the direction of the incoming flow. Values of $V_z^+(z)$ represent vertical velocity in the direction of the z -axis (see Fig.2.4.b for the remainder). More detailed graphs, including error bars, are provided in the following. Profiles represent: (d) $V_z^{+,REF}(z)$, (e) $V_z^{+,OBS1}(z)$ and (f) $V_z^{+,OBS2}(z)$. The z -axis ranges from 0 to 0.2 m (except for measurements collected at $x = 1$ m in the presence of the obstacle where $0 < z < 0.3$ m) while the x -axis ranges from 0 to 0.3 m s^{-1} .

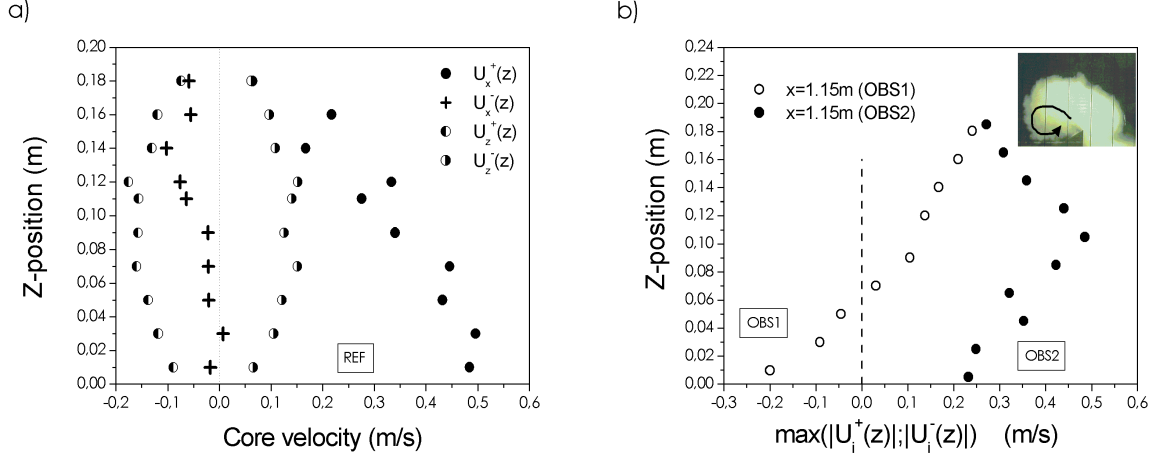


Figure 2.21: (a) Typical profiles of $U_x^+(z)$, $U_x^-(z)$, $U_z^+(z)$ and $U_z^-(z)$ (values obtained for $x = 1.7$ m in the reference conditions). U_z^+ and U_z^- show symmetrical profiles. (b) Profile obtained at $x = 1.15$ m in the presence of *OBS1* and *OBS2* by representing, for each z -position, $\max(|U_i^+(z)|; |U_i^-(z)|)$.

Upward and downward core velocity (U^+ , U^-)

In general, vertical core velocities ($U_z(z)$) were found to have positive (U_z^+) and negative (U_z^-) values on the same order of magnitude. The resulting $U_z(z)$ profiles are thus symmetric, as shown in Fig.2.21.a. A cross-comparison with maximum height results displayed in Fig.2.17.a demonstrates that the maximum values of the core vertical velocity are recorded at approximately $z = \frac{h_{max}}{2}$, whereas minimum values correspond to $z = 0$ and to $z = h_{max}$. But when looking at the horizontal core velocities ($U_x(z)$), the prevailing contribution is positive (U_x^+), which reflects a density cloud flowing mainly downwards. However, in some cases, the upward component ($U_x^-(z)$) was found to be significant. Several reference measurements showed, for a given z -value, $|U_x^-(z)| \simeq |U_x^+(z)|$ or barely higher for high values of z . This is due to the fact that the horizontal positive velocity $U_x^+(z)$ decreases with the flow height while the negative velocity $U_x^-(z)$ increases (eddy structures rotating clockwise).

In the *OBS1* configuration, upon impact with the obstacle, the horizontal positive velocity $U_x^+(z)$ decreases in values while $U_x^-(z)$ increases and $|U_x^{max}| \simeq |U_x^{min}|$. The only investigated position which provided $|U_x^{min}| \simeq 2|U_x^{max}|$ was at $x = 1.15$ m and $z = 0.01$ m in the presence of *OBS1* (see Fig.2.21.b). As mentioned in section 2.3.1, the front of the flow separates into two main parts when it strikes the obstacle, an upper part that continues rotating clockwise and a second part that generates new eddies turning counter-clockwise (see the inset in Fig.2.21.b).

The flow in the *OBS2* configuration shows a behaviour similar to the reference flow (no visible flow detachment from the surface). Upward horizontal core velocities become significant only for a few positions at high z -values and, right after the obstacle, values of $U_x^-(z)$ were still recorded, but $|U_x^-(z)| < |U_x^+(z)|$. Apart from these exceptions, the maximum downward horizontal velocity was generally found to be approximately five times greater than the maximum upward horizontal component ($|U_x^{max}| \simeq 5|U_x^{min}|$).

Comparison maximum horizontal core velocity (U_x^{max}) - front velocity (u_{fr})

In order to compare with front velocity data, the U_x^{max} were taken for each x -position that was analysed. Results are shown in Fig.2.22.a. The core velocity behaviours differ slightly from those obtained for front velocities (see Fig.2.18.a). Reference values decrease until $x = 1$ m to reach a rather constant velocity around $0.45 - 0.5$ m s⁻¹. However, upon impact with *OBS1*, the flow core velocity drops to a value representing 69% of the reference value and then remains

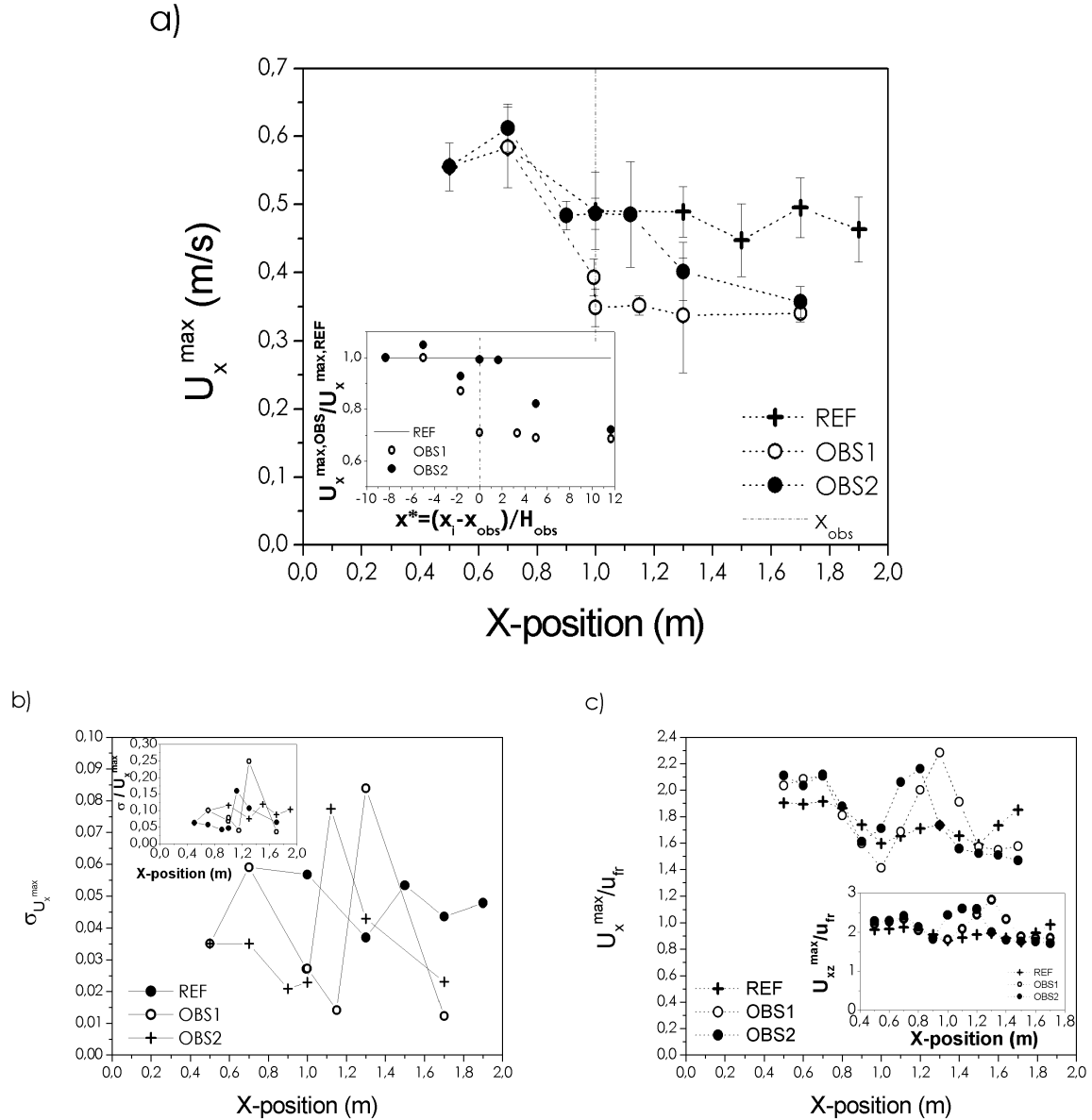


Figure 2.22: (a) Maximum horizontal core velocity U_x^{max} versus the channel x -position for the three tested configurations (*REF*, *OBS1* and *OBS2*). The vertical dot-dashed line represents the obstacle position. The inset shows the velocity ratios versus an x -axis position x^* which has its origin at the obstacle position and is expressed in terms of obstacle heights. (b) Standard deviation obtained for the maximum core velocity results versus the x -position. The inset shows the relative weight of σ with respect to the maximum horizontal core velocity values U_x^{max} . (c) $\frac{U_x^{max}}{u_{fr}}$ ratios versus the channel x -position.

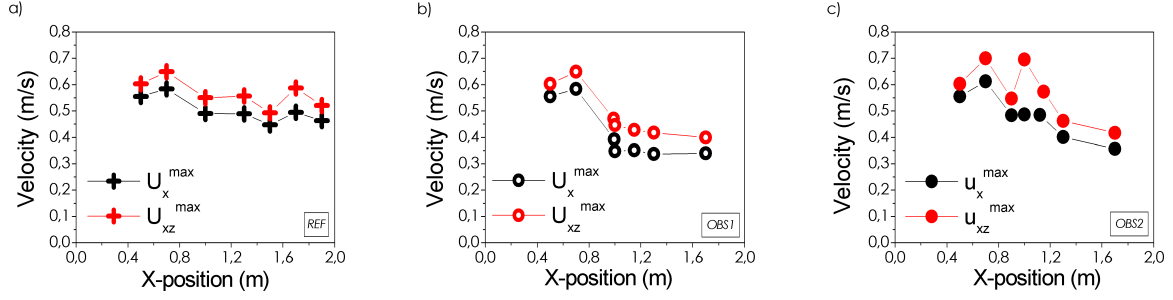


Figure 2.23: Comparison between maximum horizontal core velocities U_x^{max} and the maximum norm values U_{xz}^{max} , versus the x -position along the channel. Graphs are presented for (a) the *REF*, (b) the *OBS1* and (c) the *OBS2* configuration.

constant, as shown in the inset of Fig.2.22.a. Compared to the front velocity, immediately downhill from the obstacle, the *OBS1* profile is subjected to a minor velocity loss (30% instead of 50% for u_{fr}), but this value is conserved ahead, while the front velocity, at a distance $x = 1.35$ m ($x^* \simeq 6$), starts to increase until it reaches a final constant value of $u_{fr}^{OBS1} \simeq 0.8u_{fr}^{REF}$. The maximum horizontal core velocity in the *OBS2* configuration behaves as in reference conditions until $x = 1.15$ m ($x^* \simeq 2.5$) and then starts decreasing until the end of the channel, where a velocity $U_x^{max,OBS1} \simeq U_x^{max,OBS2} \simeq 0.7U_x^{max,REF}$ was recorded. Figure 2.22.b shows the error related to the standard deviation of the VECTRINO results. Values are of the same order of those obtained for the front velocity.

Velocity values obtained for the maximum horizontal core velocity are higher than those recorded in the front. According to Naaim-Bouvet et al. (2002) [107], the velocity just behind the nose of the head was greater than the front velocity. In the 2D simulation, the velocity maximum was about 1.5 times the front velocity, which was in accordance with Hopfinger's results. The slope was 10° in both cases, but Hopfinger and Tochon-Danguy (1977) suggested a slope-angle dependence. Keller's measurements (1995) in a 3D configuration with slope angles ranging from 30° to 45° did not reveal any slope dependence of this ratio. They obtained values at approximately 1.5 – 1.6 which remained constant even on a horizontal run-out [90]. Figure 2.22.c shows the values we obtained for the $\frac{U_x^{max}}{u_{fr}}$ ratio. With a fixed slope angle of 13° , this value ranges within 1.6 and 1.9 for reference flows while, for obstacle configurations, this range increases: 1.4 – 2.3 with *OBS1* and 1.4 – 2.1 with *OBS2*.

Core velocity norm (U_{xz})

Up until now, horizontal and vertical velocities were considered separately in order to compare maximum and front velocities. As the VECTRINO provided the 3D components of the flow velocity, we calculated the velocity norm, and then we compared the maximum horizontal core velocities U_x^{max} to the maximum norm values U_{xz}^{max} . This allows us to verify whether the maximum values of U_x and U_z occur at the same time, what their norm is, as well as the norm direction.

Note that the norm velocity was calculated according to

$$u_{xz}(z, t) = \sqrt{u_x(z, t)^2 + u_z(z, t)^2} \quad (2.24)$$

$$u_{xz}^{max}(z) = \max [u_{xz}(z, t)] \quad (2.25)$$

$$U_{xz}(z) = \frac{1}{n} \sum_1^n u_{xz}^{max}(z) \quad (2.26)$$

$$U_{xz}^{max} = \max [U_{xz}(z)] \quad (2.27)$$

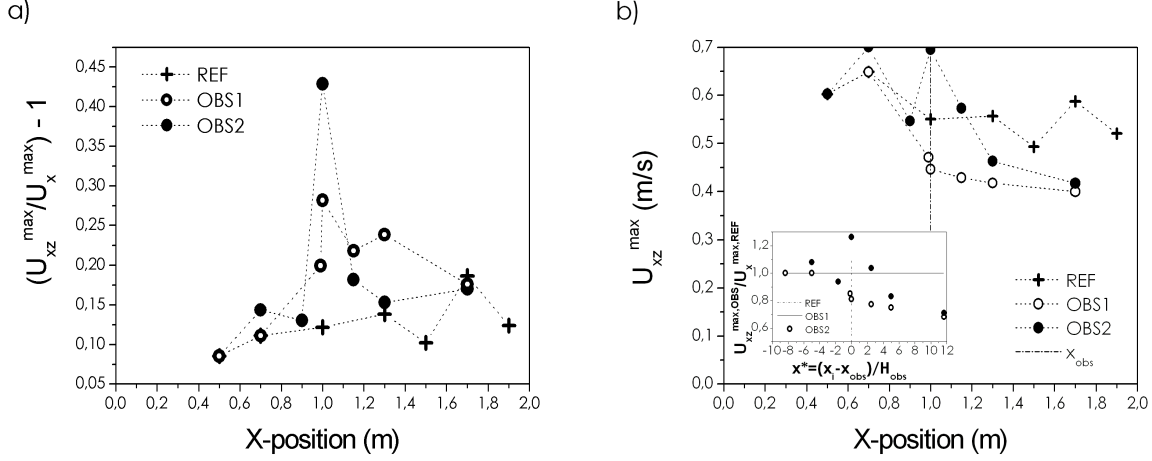


Figure 2.24: (a) Ratios between U_{xz}^{max} and U_x^{max} versus the x -position for the three investigated configurations (*REF*, *OBS1* and *OBS2*). (b) In tandem with Fig.2.22.a, the maximum norm velocity U_{xz}^{max} is plotted versus the channel x -position for the three tested configurations (*REF*, *OBS1* and *OBS2*). The vertical dot-dashed line represents the obstacle's position. The inset shows the velocity ratios versus an x -axis position x^* which has its origin at the obstacle's position and is expressed in terms of obstacle height.

Figures 2.23.a-c show the comparison between maximum horizontal core velocities U_x^{max} and the maximum norm values U_{xz}^{max} versus the x -position along the channel. For each investigated x -position, a vertical profile of $U_x^+(z)$ and $U_{xz}(z)$ was obtained. The maximum values U_x^{max} and U_{xz}^{max} were extracted and plotted as a function of the x -position. Graphs show that the behaviours are qualitatively similar, but the norm profiles generally present higher values. The ratios between U_{xz}^{max} and U_x^{max} are shown in Fig.2.24.a versus the x -position. For the reference configuration, the norm is approximately 10 – 18% higher than the simple horizontal contribution. Data indicate that, the consideration of U_{xz}^{max} instead of the maximum norm value U_x^{max} leads to an underestimation of the incoming velocity of up to 18%. This is remarkable when considering that, for the estimation of impact pressures, $P_{kin} \propto u^2$.

The ratio $\frac{U_{xz}^{max}}{U_x^{max}}$ increases in the presence of *OBS1*, upon impact with the obstacle. The norm reaches a value 28% higher than the horizontal contribution at $x = 1$ m and then decreases constantly until $U_{xz}^{max} = 1.17U_x^{max}$ at $x = 1.7$ m ($x^* \simeq 11.5$)

The behaviour in the *OBS2* configuration is between the *REF* and *OBS2* scenarios, with the exception of one value. At $x = 1$ m, directly above the obstacle ridge, the maximum norm rises a value of 43% higher than the maximum horizontal velocity. This value shows the effect of the uphill ramp of *OBS2* which induces a significant contribution to the vertical maximum velocity U_{xz}^{max} . Figure 2.24.b presents the maximum norm U_{xz}^{max} versus the position along the channel. In tandem with Fig.2.22.a and by analogy to considerations previously discussed, the trends for the maximum velocity norms, in the three configurations, behave similarly from a qualitative point of view, but values remain higher. These results highlight the importance of the vertical velocity contribution in the computation of the total incoming velocity.

The inset of Fig.2.22.c shows the ratio between $\frac{U_{xz}^{max}}{u_{fr}}$, analogous to the main graph ($\frac{U_{xz}^{max}}{U_x^{max}}$). Trends have the same qualitative behaviour, but values are higher. This ratio ranges between 1.75 and 2.2 for reference flows and between 1.7 and 2.8 in the presence of the obstacles.

Figure 2.25.a presents the values of z at which the maximum norm was registered versus the position along the x -axis. Data confirm previous results. In reference conditions, the maximum norm value U_{xz}^{max} is controlled by the horizontal contribution $U_x^+(z)$ which is maximum close to the channel bottom. Upon impact with *OBS1*, this behaviour changes. The maximum norm occurs at increasing values of z , up to $x = 1.2$ m ($x^* \simeq 3$) where, due to the burst of the density

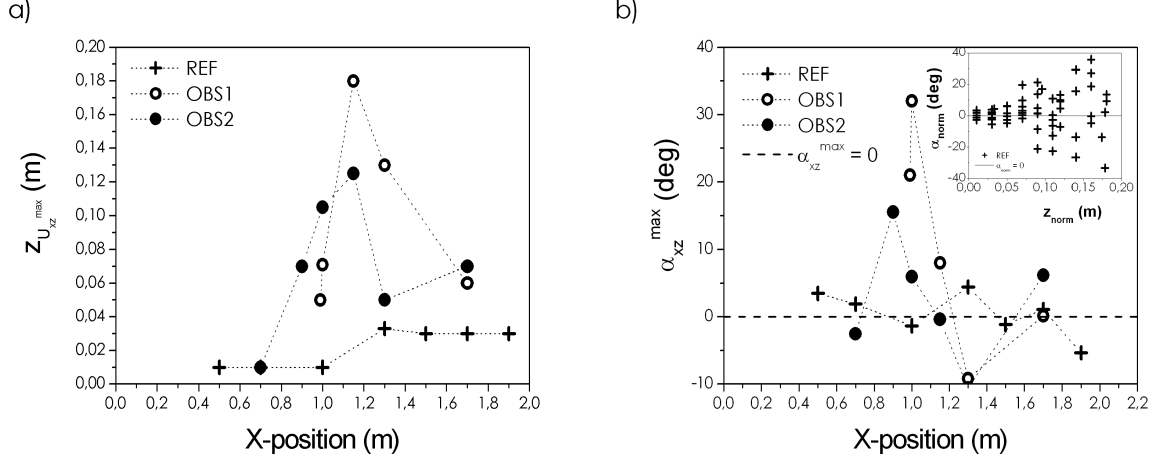


Figure 2.25: (a) Z -position at which the maximum norm value is recorded, versus the x -position for the three investigated configurations (*REF*, *OBS1* and *OBS2*). (b) Norm angle α_{xz}^{max} associated to the maximum norm value, versus the x -position for the three investigated configurations (*REF*, *OBS1* and *OBS2*). The dashed horizontal line represents $\alpha_{xz}^{max} = 0^\circ$. The inset shows values of α_{xz}^{max} versus the z -position at which the maximum norm is found. The dashed horizontal line represents $\alpha_{xz}^{max} = 0^\circ$.

cloud, $z_{norm} = 0.18$ m. This value then decreases to $z = 0.06$ m for $x = 1.7$ m ($x^* \simeq 11.5$). The data obtained for *OBS2* fall between those from the *REF* and *OBS1* configurations.

Maximum norm direction (α_{xz}^{max})

Lastly, when considering the norm, the direction of this velocity vector is also significant. Figure 2.25.b shows the angle α_{xz}^{max} associated to the maximum norm U_{xz}^{max} . Note that α_{xz} is calculated with respect to a plane parallel to the channel bottom (for $\alpha_{xz}^{max} = 0^\circ$, $U_{xz}^{max} \equiv U_x^{max}$ and for $\alpha_{xz}^{max} = 90^\circ$, $U_{xz}^{max} \equiv U_z^{max}$), and, for a given x -position, the velocity norm is calculated from the time-dependent profiles of $u_x(z, t)$ and $u_z(z, t)$ according to:

$$\alpha_{xz}^*(z, t) = \arctan \left[\frac{u_z(z, t)}{u_x(z, t)} \right] \quad (2.28)$$

and, afterwards, this angle is always associated to the norm velocity value:

$$\alpha_{xz}^{*,max}(z) = \alpha_{xz} [u_{xz}^{max}(z)] \quad (2.29)$$

$$\alpha_{xz}(z) = \alpha_{xz} [U_{xz}(z)] \quad (2.30)$$

$$\alpha_{xz}^{max} = \alpha_{xz} [U_{xz}^{max}] \quad (2.31)$$

In reference conditions, the angle related to the maximum norm is rather low, $-5^\circ < \alpha_{xz}^{max} < 5^\circ$. The horizontal contribution is dominant. The inset of Fig.2.25.b supports these considerations. For all of the (x, z) positions analysed in the *REF* configuration, the horizontal ($U_x(z)$) and vertical ($U_z(z)$) contributions provided a norm ($U_{xz}(z)$) and an angle $\alpha_{xz}(z)$ associated to it. All of the obtained values of α_{xz} are plotted together versus their z -position. This graph shows that the values of this angle are low, close to the bottom, because $U_x(z)$ is dominant, whereas increasing z , $U_x(z)$ decreases and thus α_{xz} increases.

In the presence of *OBS1*, upon impact with the structure, the vertical contribution becomes significant and then the angle associated to the maximum norm increases up to values of $\alpha_{xz}^{max} \simeq 35^\circ$ right above the obstacle ridge ($x = 1$ m). Downhill from it, this value decreases rapidly to reach

a value close to zero for $x = 1.7$ m ($x^* \simeq 11.5$).

In the *OBS2* configuration, α_{xz}^{max} ranges between approximately -10° and 10° . Note that the higher value, observed at $x = 0.9$ m, must be corrected with respect to the ramp slope ($\alpha_{dam} = 32^\circ$).

A high value of the α_{xz}^{max} angle means that the maximum velocity norm vector, upon impact with a potential obstacle, is not normal to the structure's uphill face (we assume an uphill vertical face with respect to the local slope), which is effective in terms of structure solicitation. However, when designing a protection structure, reference results must be considered because they represent the dynamic behaviour of the incoming, undisturbed flow. Since the worst-case scenario should be taken into account, results showed the importance of considering the incoming velocity norm, rather than the simple horizontal contribution.

2.4 Conclusions and outlook

This chapter investigated the influence of an obstacle on the dynamics of a finite-volume density current modelling a powder-snow avalanche.

A constant volume (4 l) of a dyed salt solution reproduced the small-scale aerosol flowing down an inclined channel ($\theta = 13^\circ$) immersed in a water tank. Reference tests, in the absence of the obstacle, characterised the dynamic parameters of the flow and then the influence of two different types of obstacles on these parameters was investigated. Both of the obstacles represent a catching dam. *OBS1* has a vertical uphill face ($\alpha_{dam} = 90^\circ$) while *OBS2* has an inclined uphill face ($\alpha_{dam} = 32^\circ$). Measurements were taken for the maximum flow height and on the front and core velocity by using image processing and the ultrasound Doppler velocimetry.

Small-scale laboratory experiments are supposed to fulfil three similitude requirements corresponding to three dimensionless numbers: (i) the densimetric Froude number Fr_d , (ii) the Reynolds number Re and (iii) the density ratio $\frac{\Delta\rho}{\rho_{ref}}$. Although the Reynolds and the densimetric Froude numbers are respected, the density ratio remains unmatched. Thus, small-scale results are subjected to a density distortion.

Main results of chapter 2

1. Results showed that the *OBS2* (inclined upstream face solution) has a lower influence on the flow dynamical behaviour with respect to a catching dam with a vertical uphill face (*OBS1*). The density cloud flows up and down the dam ramps, without any visible detachment from the surface.
2. The maximum flow height increases rapidly after the impact with *OBS1*. $h_{max}^{OBS1} \simeq 1.5h_{max}^{REF}$ at a distance $x = 7H_{obs}$ downhill from the obstacle and it remains rather constant. $h_{max}^{OBS2} \simeq h_{max}^{REF}$ all across the channel.
3. The front velocity u_{fr} drops upon impact with the dam. Immediately downhill from it, $u_{fr}^{OBS1} \simeq 0.5u_{fr}^{REF}$ and $u_{fr}^{OBS2} \simeq 0.7u_{fr}^{REF}$. Then the flow re-accelerates to stabilise at a rather constant value for $x > 7H_{obs}$ ($x = 0$ is set at the upstream vertical face of the obstacle): $u_{fr}^{OBS1} \simeq 0.78u_{fr}^{REF}$ and $u_{fr}^{OBS2} \simeq 0.9u_{fr}^{REF}$.

4. The core velocity represents the maximum velocity measured in the density cloud. 3D measurements were taken using an acoustic Doppler velocimeter. The horizontal (u_x) and vertical (u_z) contributions were investigated simultaneously (details on the notation are provided in section 2.3.4):
 - (a) the horizontal core velocity loss induced by the obstacle is lower than that obtained for the front velocity;
 - (b) with *OBS1*, immediately downhill from the obstacle, the maximum horizontal core velocity drops. $U_x^{max,OBS1} \simeq 0.7U_x^{max,REF}$ and it remains constant downwards;
 - (c) with *OBS2*, after the impact, $U_x^{max,OBS2}$ starts decreasing constantly up to $x \simeq 12H_{obs}$ where $U_x^{max,OBS2} \simeq U_x^{max,OBS1} \simeq 0.7U_x^{max,REF}$;
 - (d) the ratio $\frac{U_x^{max}}{u_{fr}}$ varies between 1.6 and 1.9 for reference conditions and between 1.4 and 2.3 for the obstacle scenarios. The values are consistent with previous studies;
 - (e) in *REF* conditions, the typical horizontal core velocity profile $V_x^+(z)$ is characterised by maximum velocities for low values of z (close to the bottom). Velocity then decreases, increasing z . However, the typical $V_z^+(z)$ profile has a semi-elliptical shape with its maximum corresponding to $z \simeq \frac{h_{max}}{2}$ and the minimum values for $z = 0$ and $z = h_{max}$;
 - (f) upon impact with an obstacle (*OBS1*-type), vertical core velocities increase and certain upward horizontal core velocities appear (up to $|U_x^{min}| \simeq 2|U_x^{max}|$) directly downhill from the obstacle.

5. When dealing with the flow dynamic characteristics, the maximum core velocity norm U_{xz}^{max} is a more precise parameter to take into account, rather than U_x^{max} :
 - (a) results showed that, in reference conditions, the maximum norm can be up to 18% greater than the maximum horizontal contribution. This is remarkable when considering that, for the estimation of impact pressures, $P_{kin} \propto u^2$;
 - (b) Upon impact with an obstacle, the difference between the maximum norm and the maximum horizontal core velocity increases up to $U_{xz}^{max} \simeq 1.3U_x^{max,i}$ ($i = OBS1, OBS2$);
 - (c) the ratio $\frac{U_{xz}^{max}}{u_{fr}}$ varies between 1.75 and 2.2 for reference conditions and between 1.7 and 2.8 for the obstacles situations. Values are higher than those obtained for the ratio $\frac{U_x^{max}}{u_{fr}}$;
 - (d) in reference conditions, $U_{xz}^{max,REF}$ is controlled by $U_x^{max,REF}$ and thus $U_{xz}^{max,REF}$ is registered at low values of z . However, upon the impact with *OBS1*, $U_{xz}^{max,OBS1}$ occurs at increasing values of z , up to $x = 2.5H_{obs}$ where, due to the burst of the density cloud, $z_{norm} = 0.18$ m. This value then decreases down to $z = 0.06$ m for $x \simeq 11.5$. The data obtained for *OBS2* are between those from the *REF* and *OBS1* configurations.

6. An angle α_{xz}^{max} (relative to a plane parallel to the channel bottom) is associated to the maximum velocity norm and indicates its direction:
 - (a) in reference conditions, this angle is rather low, $-5^\circ < \alpha_{xz}^{max} < 5^\circ$. The horizontal contribution U_x^{max} is dominant;
 - (b) upon impact with *OBS1*, the norm angle increases rapidly up to $\alpha_{xz}^{max} \simeq 35^\circ$, and decrease afterwards;
 - (c) in the *OBS2* configuration, the α_{xz}^{max} behaviour is between that obtained in the *REF* and *OBS1* configurations.

Perspectives from chapter 2

1. In terms of protection effectiveness, laboratory tests showed that a catching dam with the upstream face vertical to the slope (*OBS1* configuration) is more efficient than a dam with an inclined upstream face (*OBS2*). In fact, as mentioned in section 2.3.1, in presence of *OBS2* the flow does not hit the obstacle but it rather passes smoothly over it, without any visible detachment from the surface. The ramp effect is remarkable and the avalanche reaches faster (in terms of time) a given point downstream from the obstacle. On the contrary, in the *OBS1* configuration, the incoming flow hits the vertical wall and bursts. The cloud maximum height rapidly increases, the front of the flow separates in two main parts, an upper part rotating clockwise (for a cloud flowing down from the right to the left) expanding upward and a second part generating new eddies turning counter-clockwise. The flow is subjected to a strong deflection with the formation of a vertical jet. In the future, it would be interesting to investigate the threshold angle α_{dam}^{thr} of the uphill ramp above which the flow starts behaving as it would in the presence of a wall-like obstacle. Attention should be focused on the influence of the upstream face angle, of the local terrain slope and of the incoming flow velocity and density. Note that the water tank experiments can not fulfil the density requirement and thus they are affected by a density distortion. Numerical modelling should be used to study the density parameter.
2. Two catching-dam-type obstacles of different shapes were used and their influence on the flow dynamic behaviour was studied. In tandem with small-scale experiments on granular flows described in chapter 1, new laboratory tests should be conducted to investigate the influence of an obstacle causing lateral flows (breaking-mound-type) on the density cloud behaviour.
3. A mean-value approach was chosen for the study presented. Considering the turbulent nature of this type of flow, it could be of great interest to conduct a different analysis focusing on the fluctuations of height and velocity signals, in order to better understand the effects of turbulence on the flow dynamics.

Chapter 3

The experimental site of Taconnaz

Contents

3.1	Context and description of the site	135
3.2	The study led to improve the protection system	138
3.2.1	Historical data analysis	138
3.2.2	Physical, analytical and numerical modelling	139
3.2.3	Residual risk analysis	141
3.3	Monitoring of the avalanche path	143
3.3.1	The site equipment	143
3.3.2	Preliminary results	145
3.4	Conclusions	154

Previous chapters emphasised on the need of a multi-scale approach in order to achieve an exhausting work providing consistent data. This need becomes even more important when dealing with a matter as complicate as the pressures that an avalanche exerts on a structure upon impact.

With this being considered, chapter 1 and chapter 2 treated the physical small-scale approach while this chapter presents the real-scale experimental site of Taconnaz. This site was equipped through the INTERREG European project named "DynaVal" by configuring the existing avalanche protection system with velocity and pressure sensors. Several real-scale experimental sites already existed (and were mentioned in the previous chapters): Ryggfonn in Norway [62], Vallée de La Sionne in Switzerland [148, 149], Col du Lautaret in France [22, 152]. For years, these sites have allowed the collection of data on the dynamics of full-scale artificially released avalanches

which greatly enhanced the general knowledge of avalanche dynamics. One of the aims of the Dynaval project was to investigate, through an experimental approach, pressures that can be exerted on structures located in the run-out zone of an avalanche path and the influence of an obstacle on the flow behaviour. The recently developed sites of Taconnaz (France) and of Punta Seehore (Italy), along with the already existing site of Col du Lautaret, represent three sites covering the entire range of velocities and pressures expected for real-scale avalanches. The equipment of the two new sites (Taconnaz and Punta Seehore) and the improvement of the Lautaret site were funded by the Dynaval project.

Only the site of Taconnaz is described in this chapter because it is directly related to the scope of this dissertation. Regardless, table 3.1 gives an overview of the complementarity of these three sites in terms of velocity, pressure and volumes. More details on the other two sites can be found in Thibert et al. (2008) [152] for the Col du Lautaret, and in Segor et al.(2011) [141] for Punta Seehore.

Table 3.1: Complementarity of the experimental sites in term of velocity, pressure and volume of mobilised snow. Table extracted from Bellot et al. (2012) [21].

	<i>Punta Seehore (Italy)</i>	<i>Lautaret (France)</i>	<i>Taconnaz (France)</i>
Scale	Small	Intermediate	Large
Type of release	Artificial	Artificial	Natural
Run-out distance	400 – 500 m	500 – 800 m	up to 7500 m
Mean slope	38°	36°	25°
Volume	200 – 400 m ³	500 – 10000 m ³	1600000 m ³
Pressure	0.5 ton m ⁻²	3 – 5 ton m ⁻²	up to 100 ton m ⁻²
Velocity		up to 30 – 40 m s ⁻¹	up to 70 m s ⁻¹

Section 3.1 provides a description of the site of Taconnaz. Section 3.2 summarises the assessment and the technical evaluation led by Irstea on the Taconnaz site in order to improve the existing defence system. An overview is necessary to introduce the work of this dissertation. This overview is provided in section 3.3 with a description of the experimental site's construction, the instrumentation that was adopted, and the preliminary results that were obtained. Lastly, section 3.4 concludes the chapter.

3.1 Context and description of the site

The content of this section is mainly based on references [105] and [106]. The Tacconnaz avalanche path is situated between the municipalities of Chamonix and Les Houches (Haute Savoie, France), on the left side of the Arve river, just below the Dome du Goûter. An image of the site is provided in Fig. 3.1.a. The morphological characteristics of the site such as its surface, length, and height difference, along with the presence of the Tacconnaz glacier directly above, make it an exceptional couloir. During the last century, several avalanches (dense and mixed avalanches) of huge dimensions occurred and threatened inhabited areas. In 1991 an avalanche protection system was constructed to preserve the village of Tacconnaz, the national road that passes below and all related structures. This defence structure, through the years, was affected by significant avalanches that overflowed and damaged it (February 1999 and April 2006), revealing the limits of the system set up in 1991. Afterwards, local municipalities decided to improve this system. Irstea (Cemagref at the time) was asked to predetermine the dense avalanche hazard at the entry of the run-out zone, to design the best combination of defence structures capable of spreading the flow, dissipating the energy and retaining the dense reference avalanche, and to analyse the residual risk of the powder part of the avalanche.

This section deals with the characteristics of this extraordinary avalanche path as well as the history of the defence system from its construction in 1991 until today.

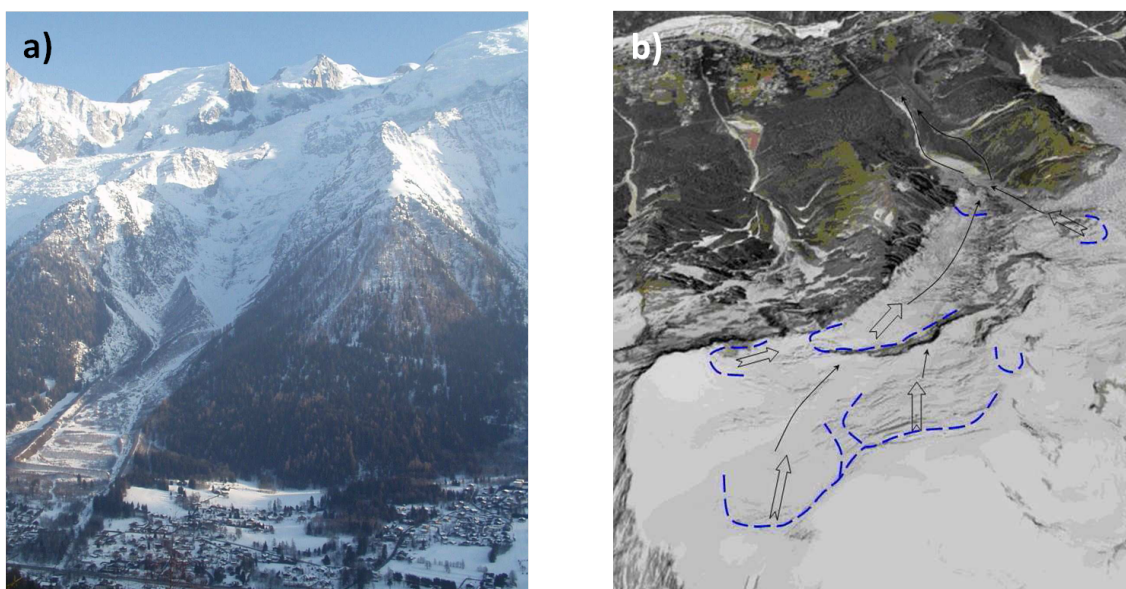


Figure 3.1: (a) Global overview of the Tacconnaz avalanche path (source RTM). (b) Image taken from www.geoportail.fr, showing the potential release area of the couloir.

As previously mentioned, the starting zone surface of the avalanche path, its length and the altitude drop are all exceptional features of this avalanche site. However, the immensity of the starting zone is the principle characteristic of the path (see Fig.3.1.b). Three main starting zones can be identified.

Between the altitude of 4000 m and 3300 m a.s.l., a wide glacier area represents the first important morphological aspect. This first release area has a very irregular topography, a surface of approximately $2 \times 10^6 \text{ m}^2$ and a mean slope of 30° . Its orientation ranges from north-east to north-west, and the area is thus subject to the dominant winds that generates potential accumulation problems. The upper part of the area is delimited by a slope-braking-line generating

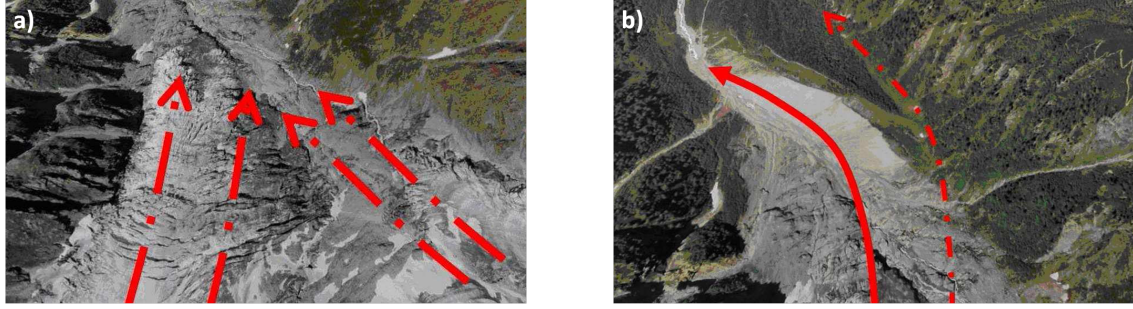


Figure 3.2: (a) Image taken from www.geoportail.fr showing the junction between the two glacier's branches occurring at approximately 2150 m a.s.l. and (b) aerial view of the moraine that deviates most of the avalanches flowing through the path (source RTM).

seracs that can potentially trigger an avalanche. Considering that in this sector the cumulated height of precipitation of three days, for a return period of one-hundred years, is two meters, this single area has already the potential to generate catastrophic avalanches in terms of volume. This area alone can generate a snow volume of more than four million cubic meters considering the typical (100 years return period) snow height of $\simeq 2$ m.

Downhill, the avalanche basin continues and a second departure area is identified between the altitudes of 3300 m and 2800 m a.s.l.. A second long seracs line constitutes another trigger zone for avalanches. This area supplies a flowing and erosion zone characterised by a mean slope of 31° , a width of 400 m and a length of approximately 1800 m. An avalanche generated from this sector can reach, for the centennial precipitation case-scenario (cumulated on three days), a volume of 1.6×10^6 m³.

Further downhill, on the right side, at an altitude between 2600 m and 2000 m a.s.l., a third release area is 800 m long, 300 m wide, and with a mean slope of 25° . This area alone, for the centennial precipitations conditions of three days, can generate an avalanche with a volume greater than 0.5×10^6 m³.

The two branches come together at an altitude of approximately 2150 m a.s.l. (see Fig.3.2.a). The couloir continues downhill at a mean slope of 30° , a length of 900 m and a mean width of 300 m. The snow volume that an avalanche can entrain in this sector, for the case-scenario conditions of centennial precipitations cumulated on three days, is more than 0.7×10^6 m³. At 1700 m a.s.l. of altitude, the avalanche encounters a moraine of approximately 80 m of height that, in most cases, deflects the flow to the left (see Fig.3.2.b). Regardless, fast avalanches can overflow this natural obstacle on the right side and surround it. Such a phenomenon is even more likely if the avalanche has an aerosol component because the powder avalanche contribution does not follow the topography. From this altitude, the couloir slope decreases uniformly until entering the run-out zone where the current defence structures are placed. The run-out zone has a mean slope of 13° . Historical records show that the difference between the maximum and minimum avalanche run-out distances is $\Delta_{r_o} > 1000$ m.

This is an exceptional couloir: it has a total length higher than 7500 m, a mean slope of approximately 25° and a width that varies with the altitude, generally around 300 – 400 m. Above 1700 m a.s.l. of altitude, this avalanche basin is covered by ice. Avalanches can entrain a part of the glacier, as observed in the deposit of the avalanche that occurred in February 1999. The ice volume of this deposit was estimated to be more than 0.2×10^6 m³. The density, measured in the deposit few days after the event of April 2006, was higher than 600 kg m⁻³. Ice blocks of several cubic meters struck the protection structures and damaged them. Such events must to be taken into account and, when designing protection structures in this area, it is very important to consider a significant increase of the flow density. Punctual impacts of ice

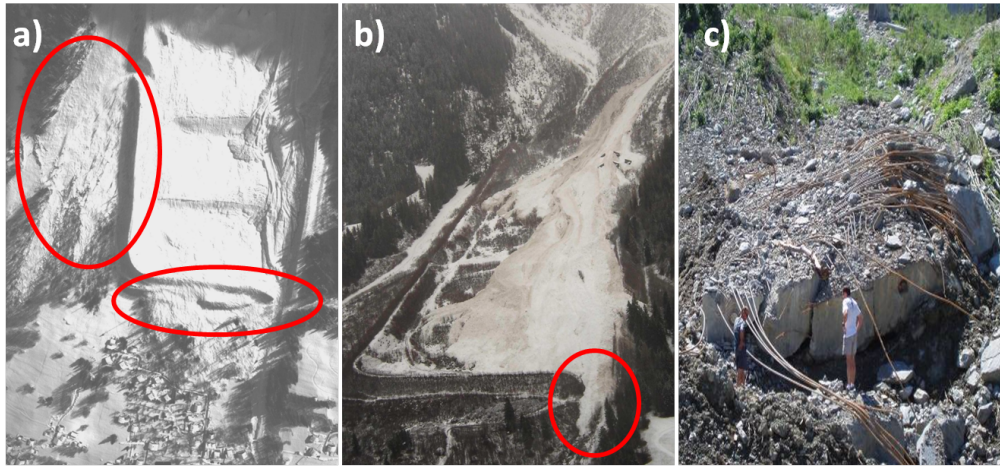


Figure 3.3: (a) Avalanche deposit from the event of February 1999. The avalanche overflowed the system both on the right as well as the downhill frontal sides, as indicated by the red circles. (b) Wet snow avalanche deposit of April 2006 (source RTM). (c) Damage of a deflecting wall destroyed by the event of April 2006 (source Irstea).

blocks transported by the avalanche can generate pressures ten times the pressure generated by a normal avalanche [105].

Seventy five avalanches were recorded on the Taconnaz site between 1900 and 2000. As reported in Rapin (2001) [124], 21% of these episodes were released by serac calving, 61% stopped at an altitude lower than 1130 m a.s.l., and for 22% of them, the arresting altitude was even lower than 1080 m a.s.l.. Consequently, if we do not take into account the protection system, an avalanche reaches the village of Taconnaz once every five years, according to statistics. Data also show that in 1937 and 1984, four avalanches descended lower than 1100 m a.s.l during the same winter.

As serac calving is a very important factor that must be taken into account when dealing with the avalanche path of Taconnaz, a terrestrial photogrammetry survey was implemented in order to monitor this process through the INTERREG European project GlariskAlp, independent from yet complementary to this PhD work. By using low-cost, broad consumer, non-metric cameras (Canon 5DMKII), the digital elevation model (*DEM*) of the serac fall area is obtained and, in case of serac calving, the released volumes can be calculated. More detailed information is available in Harter et al. (2012) [72].

In 1991, a passive protection system was built in the run-out zone of the avalanche path. This system was designed to contain wet snow avalanches with a volume up to $0.8 \times 10^6 \text{ m}^3$. The system included: (i) deflecting walls made of reinforced concrete to deviate the flow, dissipate its energy and spread it around the system, (ii) an intermediate area where the flow should slow down as it passes through breaking mounds made of reinforced earth and (iii) a downstream deposit zone composed of a front and lateral braking dam to stop and store the avalanche. Two main episodes demonstrated the limits of this system: in February 1999 (Fig.3.3.a) a very fast dry snow avalanche with a low friction rate significantly overflowed the final front and lateral dams. The powder part alone was estimated to have a volume of $0.75 \times 10^6 \text{ m}^3$. Later, in April 2006, a wet snow avalanche overflowed the system again (Fig.3.3.b). Even if the deposit volume was significantly lower than the design capacity, half of the deflecting walls were destroyed and some breaking mounds were damaged (Fig.3.3.c). The local municipalities thus decided that the system needed to be improved.

3.2 The study led to improve the protection system

As was the case for section 3.1, the content of this section is also based on references [105] and [106]. Irstea was asked to carry out a technical evaluation of the avalanche protection system. The goal was to predetermine the dense avalanche hazard in the run-out zone, to design the best combination of defence structures in order to enhance the existing protection system, and to analyse the residual risk of to the powder part of the avalanche which, in any case, overflows the obstacles.

This section provides a summary of the study led by Irstea.

First, a morphological analysis of the site was conducted and historical data were analysed (see section 3.2.1). Each recorded event was back-calculated using a numerical model of dense flow avalanches. A statistical analysis of the parameters at the entry of the run-out zone allowed the evaluation of the 100-year return period event. Then, physical and numerical models of dense avalanches interacting with defence structures were combined in order to design the most effective passive structure combination capable of containing the reference scenarios (section 3.2.2). Finally, physical and numerical modelling of the interaction between the powder avalanche and the designed defence structure were conducted to show that the proposed improvements did not increase the residual risk of the powder part downhill from the defence structures (section 3.2.3).

3.2.1 Historical data analysis

A morphological analysis of the avalanche path and its release area was already presented in section 3.1. A cross-comparison of the meteorological data recorded daily in Chamonix (1042 m a.s.l.), Vallorcine (1300 m a.s.l.) and Les Houches (1008 m a.s.l.), combined with a vertical gradient of 3.81 mm m^{-1} for a mean annual cumulative precipitation of 8.85 m (according to Durand et al. (2009) [49]) provided a 3-day cumulative precipitation at the starting zone of the Tacconnaz avalanche path (3300 m a.s.l.) of 1.6 – 2.3 m, with a mean value of 2 m.

Afterwards, historical data available from the Permanent Avalanche Survey (EPA) were analysed. The EPA database contains qualitative and quantitative information about all of the avalanches recorded since the beginning of the 20th century. The data concerning the deposits' dimensions were used to estimate the volume of the final deposit of each recorded event. Figure 3.4.a shows the obtained results in terms of run-out distance and altitude versus the final deposit volume.

The back analysis of the EPA data was conducted by using a 2D numerical model for avalanche dynamics (more details can be found in Naaim et al. (2010) [106]). The height and velocity variations were recorded and analysed for each avalanche. The Froude number Fr , defined as the square root of the ratio between the kinetic and potential energy, was then calculated for each event. The obtained values are reported in Fig.3.4.b in relation to the friction coefficient μ_0 (friction coefficient of the avalanche close to a standstill state). A correlation appeared between the two parameters.

The numerical simulations combined with statistical analysis provided as final results the volume V and the Froude number Fr of the reference event. Several pairs (Fr, V) were considered but the one which remained, for a return period of 100 years, yield the Froude number $Fr^{100} = 4.29$ and the reference volume $V^{100} = 1.6 \times 10^6 \text{ m}^3$.

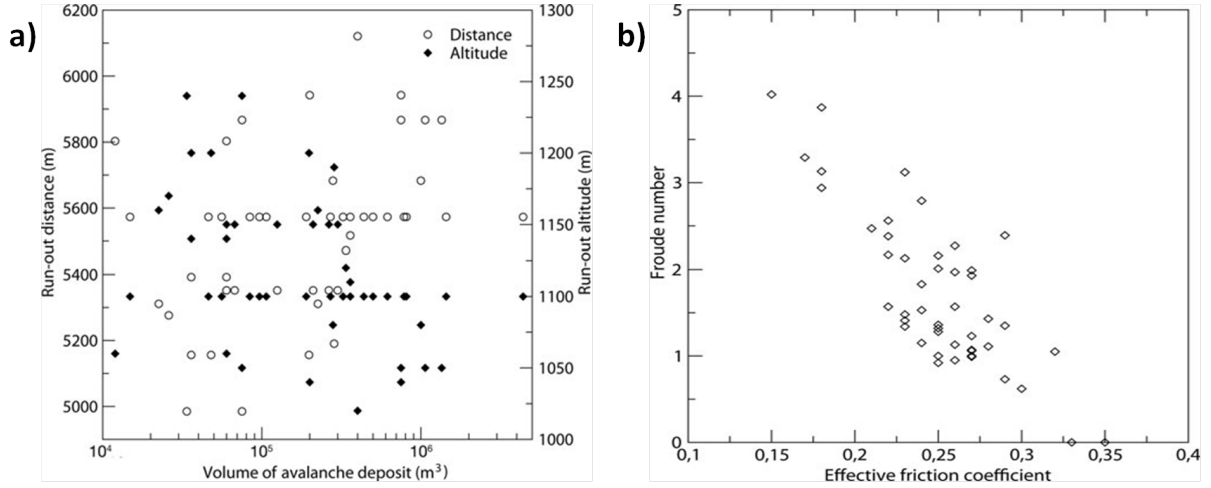


Figure 3.4: (a) Run-out distance and altitude in relation to the volume of the avalanche deposit. No direct correlation is evidenced between these two parameters. (b) Froude number of the incoming flow versus the effective friction coefficient. Here a correlation appears between the two parameters. (Both graphs were extracted from Naaim et al. (2010) [106]).

Thus, different solutions were considered in order to improve the system. To compare the effectiveness of various configurations, physical modelling was widely implemented due to its previous success.

3.2.2 Physical, analytical and numerical modelling

A simplified small-scale model was built to simulate the run-out zone of the Taconnaz avalanche path. It mainly consisted of an upstream channel with a variable slope leading to an inclined plane, with a fixed slope of 13° representing the mean slope of the run-out zone. A picture of the model, which represents the final solution, is visible in Fig.3.5.a.

Three dimensionless numbers were determined from the dimension analysis of the Saint Venant depth-averaged equations which were already introduced in chapter 1 (see Naaim et al. (2010) [106] for details) and consisted of (i) the geometric scale, (ii) the Froude number and (iii) the difference between the slope and the friction angle ($\tan \theta - \mu$). These numbers represented three similitude requirements that had to be respected to validate the physical modelling. The small-scale model has a geometrical scale of 1 : 500 and the slope of the run-out zone is 13° both in reality and on the small-scale plane. The slope of the upstream channel can be adjusted in order to define the incoming flow velocity and thickness that provides specific Froude numbers for the flows in question. Avalanches are modelled by granular materials which are stored in the upstream reservoir. PVC beads with a diameter $d = 0.1$ mm were mixed with glass beads with a diameter $d = 1$ mm. Different proportions for the two materials were tested and the one providing a run-out distance equal to the real maximum run-out observed historically was selected. Thus, a proportion of 10% PVC beads and 90% glass beads allowed to reproduce, at near standstill, the real value of ($\tan \theta - \mu$). To minimize errors due to the experimental nature of the modelling, every test was repeated five times and the mean value as well as its standard

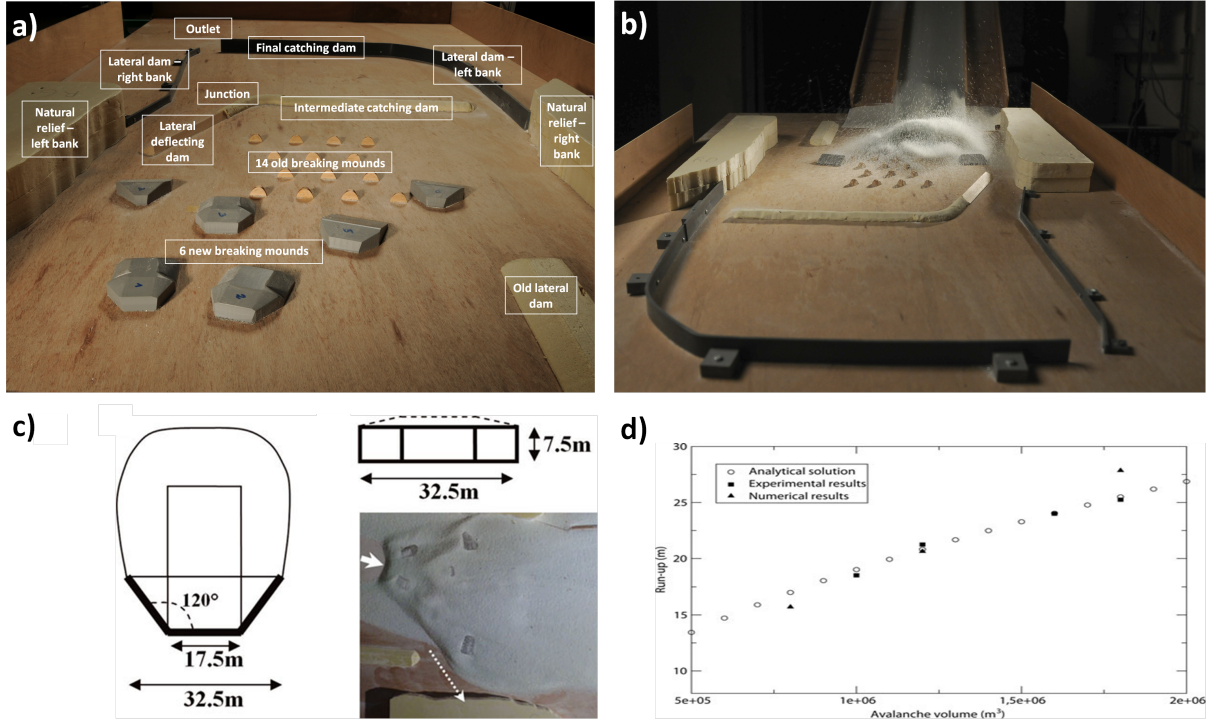


Figure 3.5: (a) Run-out zone represented in the small-scale model. The model shows the final chosen configuration (photo Irstea). (b) View of the experimental device with a granular avalanche impacting the breaking mounds (photo Irstea). (c) Mound sections and, bottom-right, a picture showing the spreading effect of the three rows of mounds for the incoming flow. (d) Run-up height versus the avalanche volume, comparison of results coming from analytical, physical and numerical modelling (graph extracted from [106]).

deviation were compared.

The solution under consideration was based on the use of breaking mounds at the entry of the run-out zone in order to slow down the flow and dissipate part of its energy. The physical model effectively allowed us to study the optimal shape and placement of the breaking mounds through the protection system. The best results were found with two mounds with a height of 7.5 m, approximately in the same row, separated by a distance of 30 m. The uphill vertical wall has a rectangular shape with a base of 17.5 m and is normal to the ground and to the main flow direction. Figure 3.5.b shows the details of the mound section. A second row of mounds of the same shape was added downhill and, to improve the spreading capacity of the system, a fifth and sixth mound were placed on the lateral sides, 80 m downhill from the second row. This configuration decreased the run-out distance by 25% with respect to the existing conditions.

Physical modelling was implemented mainly to study the performance of the protection system. Additionally, an analytical model was used to validate the laboratory tests and to estimate the necessary height for the intermediate and final catching dams in order to contain the volume estimated for the centennial event. The classical dam design principles from Salm (1982) [133], based on the energy conservation, were initially used:

$$\frac{1}{2}\rho u^2 + \rho gh = \rho gh_r + \frac{1}{2}\rho u^2 \gamma \quad (3.1)$$

where ρ , u and h are the incoming mean flow density, velocity and height, respectively. h_r stands for the run-out height and γ is the energy dissipation coefficient (with respect to the coefficient λ presented in the introduction, $\frac{1}{\lambda} = 1 - \gamma$). The sum of the kinetic and potential energy is

conserved by replacing the flow height with the run-up height h_r upon impact and by taking into account the energy dissipation γ . Equation (3.1) leads to a run-up height:

$$h_r = h \left[1 + Fr^2 \frac{(1 - \gamma)}{2} \right] \quad (3.2)$$

According to the Voellmy friction law, the Froude number depends mainly on the slope and the frictions parameters which were considered similar for the reference avalanche and that of 1999 and, in addition, we may assume that $\lambda^{1999} = \lambda^{100}$. Thus, $h_r = f(h)$ and $\frac{h_r}{h_r^{1999}} = \frac{h}{h^{1999}}$. In Chambon and Naaim (2009) [35] a simple linear relationship between the flow height at a given location and the avalanche deposit was found leading to:

$$\frac{h_r}{h_r^{1999}} = \frac{h}{h^{1999}} = \sqrt{\frac{V}{V^{1999}}} \quad (3.3)$$

This final relationship yields to a run-up height of 24 m when considering a centennial avalanche volume $V^{100} = 1.6 \times 10^6 \text{ m}^3$ and a Froude number $Fr^{100} = 4.29$, equal to that of the avalanche of 1999.

Numerical simulation, combined with the small-scale model, proved to be an effective tool to validate the technical solutions designed for the entire protection system. The topography of the run-out zone was modified in order to take into account the presence of protection structures. Friction parameters and the hydrograph set as the boundary condition at the top of the run-out zone corresponded to the reference values. For the final catching dam, it was finally decided to increase its height from 14 m to 25 m, as a combined result of physical, analytical and numerical simulations (see Fig.3.5.d).

To compensate for the potential overflow of the final catching dam found through both numerical and physical simulations, the system was enhanced by an additional catching dam, placed in the middle of the storage basin, downhill from the former breaking mounds. The dam has a length of 120 m and a height of 7 m.

It is important to note that the protection system was designed with respect to the dense part of an avalanche. It is essentially impossible to stop the aerosol part which, due to its dimensions and characteristics, generally overflows the obstacle. The final commitment was to verify that the proposed protection system enhancements did not increase the residual aerosol risk downhill from the obstacle.

3.2.3 Residual risk analysis

To conduct this type of analysis, a reference avalanche must first be defined. It is important to note that the definition of the powder snow reference (centennial event) avalanche is much harder than for the dense case. For the dense part, the *EPA* provides information on the release and deposit volumes, run-out distances, release altitudes, which allow the estimation of the incoming flow height and velocity by inverse analysis. However, for the aerosol part, such data are not available and eye-witnesses are very scarce. Thus the choice of the aerosol reference avalanche

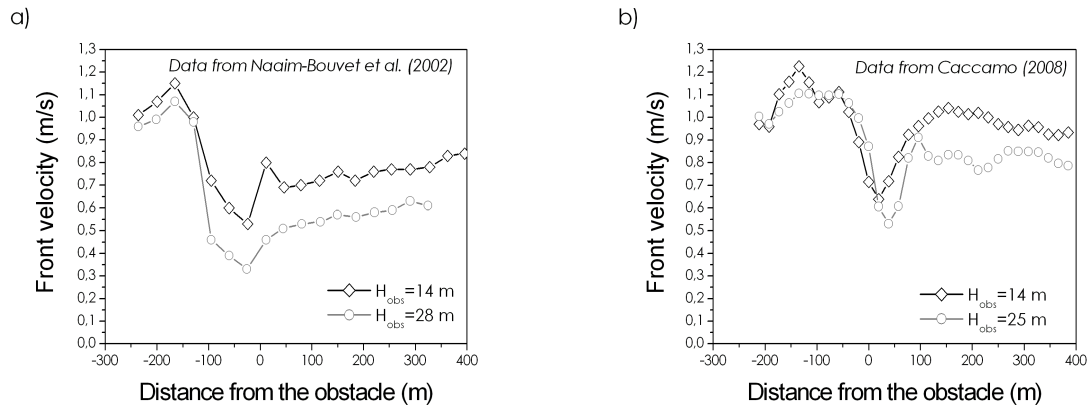


Figure 3.6: Results from the first (a) and second (b) series of experiments. Both graphs show a significant gain in terms of risk reduction related to the aerosol velocity downhill from the dam.

is made by the the expert and depends upon his experience.

A real reference avalanche with a maximum height of 50 m and a maximum velocity of 30 m s^{-1} was considered. The powder avalanche investigation was conducted by means of physical simulations. The same experimental device described in section 2.2.2 was used. Dyed salt water was used to reproduce the aerosol avalanche. A first set of data was taken from Naaim-Bouvet et al. (2002) [107]. These experiments made use of an immersed channel, 2.85 m long and 0.15 m wide with a fixed slope of 10° . A constant volume of 4 l was used and the geometrical scale was set at 1 : 350. Consequently, a dam height of 0.04 m reproduced the existing dam ($H_{obs} = 14 \text{ m}$) while a second dam height of 0.08 m reproduced a dam of 28 m. Afterwards, a second series of tests was carried out [32]. The test were based on a rather similar set-up, but the channel length was fixed at 2.4 m, its width at 0.3 m and a slope of 13° represented the mean slope of the Taconnaz's run-out zone. The geometrical scale of 1 : 350 was maintained, thus the existing dam still had a small-scale height of 0.04 m while the new tested dam had a height of 0.0714 m representing the designed dam's real height (see section 3.2.2). Results are shown in Fig.3.6. Both graphs show that the increased height of the existing dam still does not retain the aerosol avalanche. This was to be expected, and the important result was that the velocity drop induced on the flow was more significant in presence of the designed higher dam. Thus, the safety condition for goods or structures potentially placed downhill from the dam would not worsen.

As mentioned in the previous chapter, this type of physical modelling did not match the density ratio requirement (see section 2.2.1). To compensate for this discrepancy, numerical simulations were run in parallel. Numerical models were then compared with the results of physical modelling and therefore allowed the investigation of the dynamic behaviour of the flow in good density-ratio conditions. Results found that the increase of the dam's height yields to a general decrease of pressures downhill from the dam. Indeed, at a distance reaching the inhabited area, pressures were decreased by a factor 2 with respect to those estimated in presence of the existing dam. This represented a significant gain in terms of risk reduction [106, 135].

3.3 Monitoring of the avalanche path

The detailed study led to improve the effectiveness of the avalanche protection system ended with a final solution proposing the construction of six new breaking mounds with a height of 7.5 m, an intermediate catching dam with a height of 7 m and the raising of the downhill dam up to a height of 25 m. This configuration was supposed to contain avalanches up to the centennial event characterised by a Froude number of 4.29 and a volume of $1.6 \times 10^6 \text{ m}^3$. Today, five out of six breaking mounds are completed and operational and the height of the final catching dam has been raised although it has not yet reached 25 m.

After this study, a new challenge was determined through the framework of this thesis that consists of trying to monitor the avalanche path by measuring the velocity and pressure of the avalanches entering the protection system. A first trial had been run several years prior when one of the deflecting wall was equipped with two force sensors. Unfortunately, the catastrophic avalanche of 2006 destroyed the equipped wall and the two sensors were found in the storage basin once the snow had melted. In fall 2009, new velocity and pressure sensors were installed on three of the new retarding mounds.

Section 3.3 describes the contribution provided by this PhD project to the full-scale experimental site of Tacconnaz, which represented an integral part of the Dynaval project.

Section 3.3.1 describes the instrumentation process. Winter 2009/2010 did not provide any consistent data because of technical problems. However, on December 29, 2010, the first avalanche was properly recorded and obtained signals that are presented in section 3.3.2. Preliminary results show a significant increase of the drag coefficient C_d for low Froude numbers. Lastly, section 3.4 provides the conclusions drawn from the work presented.

3.3.1 The site equipment

Sensors employed in the Tacconnaz site had to withstand site temperatures that can easily range between -30°C and 30°C , resist pressures of up to 100 ton m^{-2} , and be able to measure a velocity of 60 m s^{-1} (values correspond to those of the centennial event plus a security margin). The choice of the sensors had therefore to be extremely accurate. The three retarding mounds of Fig.3.7.a were equipped. Two pressure sensors and two velocity sensors were installed on the edge each mound between the front and the lateral wall. For each mound, a pair of pressure and velocity sensors was placed at two different heights (approximately $\frac{1}{3}H_{obs}$ and $\frac{2}{3}H_{obs}$) in order to obtain the pressure measurements from the front wall, normal to the main flow direction, and velocity measurements on the lateral wall. On the chosen side of each mound, a reinforced-concrete coating was added (Fig.3.7.b) in order to support the sensor installation, as shown in Fig.3.7.c. Special pre-cast plates (see the upper inset in Fig.3.7.c) host the sensors. The set-up configuration of a mound is visible in Fig.3.8.a. Transducers based on the principle of extensometry gauges were chosen for pressure measurements as they preserve low frequencies and allow temperature compensation.



Figure 3.7: (a) Site overview and sketch of the three mounds that were equipped. (b) Installation of the reinforced concrete coating on the edge of the mound. (c) View of a breaking mound. The coating support the special pre-cast plates (upper inset) hosting the sensors. The lower inset shows the protective chamber buried at the bottom of each mound where the acquisition units are placed. Photo source Irstea.

An example is given in Fig.3.8.b. The upper circular plate ($d_{plate} = 0.2$ m) transfers the exerted pressure to the sensor. To fulfil the $100\text{-ton}\cdot\text{m}^{-2}$ requirement, a measuring range of up to 30 kN was required. Technical requirements led to the selection of *PNC710* sensors produced by *TCE*. The optimal sampling frequency ($f_{ac} = 1.2$ kHz) was calculated by determining the stiffness coefficient ($k_s = 7.5 \times 10^8$ N m⁻²) for the sensors and sizing the bandwidth of the expected signals.

A rather well-known technology was then selected for velocity measurements, an infra-red reflection sensor composed by an emitter and a receiver working on the infra-red wave-length. The signal captured by the receiver is a function of the reflecting capacity of the object passing in front of the sensor, in the main direction of the flow. Two sensors are placed close to each other (see sketch in Fig.3.8.c) and they provide similar signals but shifted in time. The time shift between the two signals coupled with the fixed distance between the two sensors provide the flow velocity. This type of technology is implemented in the *OPB608A* sensors made by Opteck, and was has previously been used for avalanche velocity measurements [24, 48].

The signal acquisition is made by a specific unit placed in a water-proof box buried at the bottom of the mound (see the lower inset of Fig.3.7.c). It consists of CompactRIO chassis equipped with a controller and *NI9239* and *NI9215* analog input modulus. The three mounds' boxes are connected by an Ethernet network and, as the run-out zone is not accessible during the winter due to security reasons, they all communicate with a remote central control station. This station was installed in an underground protective chamber, approximately 300 m far from the avalanche basin where it is permanently accessible. A *GSM* router allows the consultation of the station from the distance, thereby downloading the recorded data.

The system must be operative at any time because avalanches are naturally released and thus the acquisition units record continuously in circular memory. When an acquisition unit detects an event, it sends a signal to the unit of mound $n^{\circ}5$ (see the numbering of Fig.3.7.a) which releases the recording of all the other mounds and provides their time synchronisation. When an avalanche occurs, the system records the 120 s following t_0 and stores them in a specific memory space, together with the 60 s preceding the t_0 signal.

The installation of the entire monitoring device was completed at the beginning of winter 2009/2010. During the first winter, an avalanche reached the defence system but technical problems occurred. The acquisition system had memory saturation problems and National Instrument notified it later. The event was therefore not registered. These problems were fixed during the following summer and the first event was finally recorded on December 29, 2010 (during winter 2011 – 2012 two avalanches occurred, but both stopped one meter uphill from mound $n^{\circ}1$). The next section presents the preliminary results obtained.

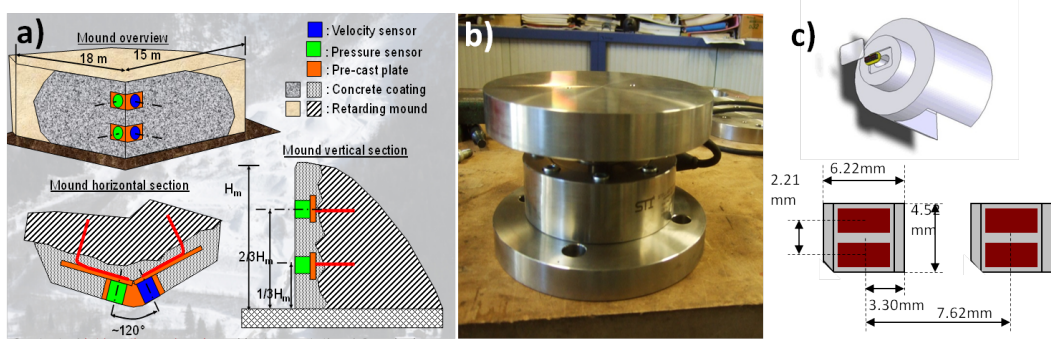


Figure 3.8: (a) Typical set-up configuration of the equipped breaking mounds. (b) Pressure sensors. The upper circular plate transfers the exerted pressure to the sensor (Photo H. Bellot). (c) Sketches and dimensions of the infra-red velocity sensors.

3.3.2 Preliminary results

The first recorded avalanche occurred on December 29, 2010. It consisted of a rather dry snow avalanche with ice blocks breaking off from the glacier, which reached the storage basin and the final catching dam. The avalanche occurred during the night and thus no eye-witness testimonies were available. As the event was not as powerful as other historical avalanches of the site, we decided not to carry out a *DTM* of the final deposit and to wait for the next avalanche, hopefully much bigger (only one scan was allowed by the project budget). A picture of the deposit is shown in Fig.3.9. Part of the sensors worked properly. Table 3.2 summarises the sensor which functioned properly (*X*) and those that did not (empty cell). Only the mounds *M1* and *M3* were affected by the avalanche, and *M5* was not reached by the flow. *P* and *u* stand for pressure and velocity sensor, respectively, and *high* and *low* define the two different heights at which sensors were installed on each mound (see Fig.3.8.a). *n.a.* stands for "not attained". The obtained results are presented in the following.

Table 3.2: Overview of the sensors functioning during the avalanche of 29 December 2010.

<i>M1</i>	<i>high</i>	<i>low</i>	<i>M3</i>	<i>high</i>	<i>low</i>	<i>M5</i>	<i>high</i>	<i>low</i>
<i>u</i>	X	X	<i>u</i>		X	<i>u</i>	n.a.	n.a.
<i>P</i>			<i>P</i>	X		<i>P</i>	n.a.	n.a.



Figure 3.9: Avalanche deposit of the event that occurred on December 29, 2010. The yellow circle indicates the presence of a person on the top of a breaking mound in order to give a dimensional reference. The inset shows the granular nature of the deposit (photo H. Bellot).

Pressure sensors: calibration and first results

Pressure sensors provided voltage values $T(t)$ that were treated in order to remove the offset value T_{offset} which can affect measurements when using this type of sensor. The offset was calculated as the mean value of $T(t)$ out of 100 points preceding the arrival of the avalanche, and pressure values were calculated using the calibration coefficients a and b previously obtained from the sensor calibration procedure. The a and b parameters were provided by the sensor constructor and they were obtained from a charge/discharge cycle on 13 calibration points. Thus, the pressure was calculated as:

$$P = a(T(t) - T_{offset}) + b \quad (3.4)$$

An error estimation (Υ) was calculated in order to account for the error due to:

- the signal discretization related to the offset calculation $\Upsilon(T_{offset})$,
- the linear fit providing the a and b coefficients ($\Upsilon(a)$ and $\Upsilon(b)$), which could be affected by hysteresis and non-linearity issues,
- the signal discretization for obtaining each single measurement point $\Upsilon(T(t))$,

and provide the equation for the error propagation:

$$\Upsilon(P)^2 = a^2 \times \Upsilon(T(t))^2 + a^2 \times \Upsilon(T_{offset})^2 + (T(t) - T_{offset})^2 \times \Upsilon(a)^2 + \Upsilon(b)^2 \quad (3.5)$$

This model is based on the error precognition of the *GUM* (1998) [3] and allows each measurement to be associated to the relative error. The relative error obtained for each single contribution above cited was less than 1% of the pressure value, which is a very good result.

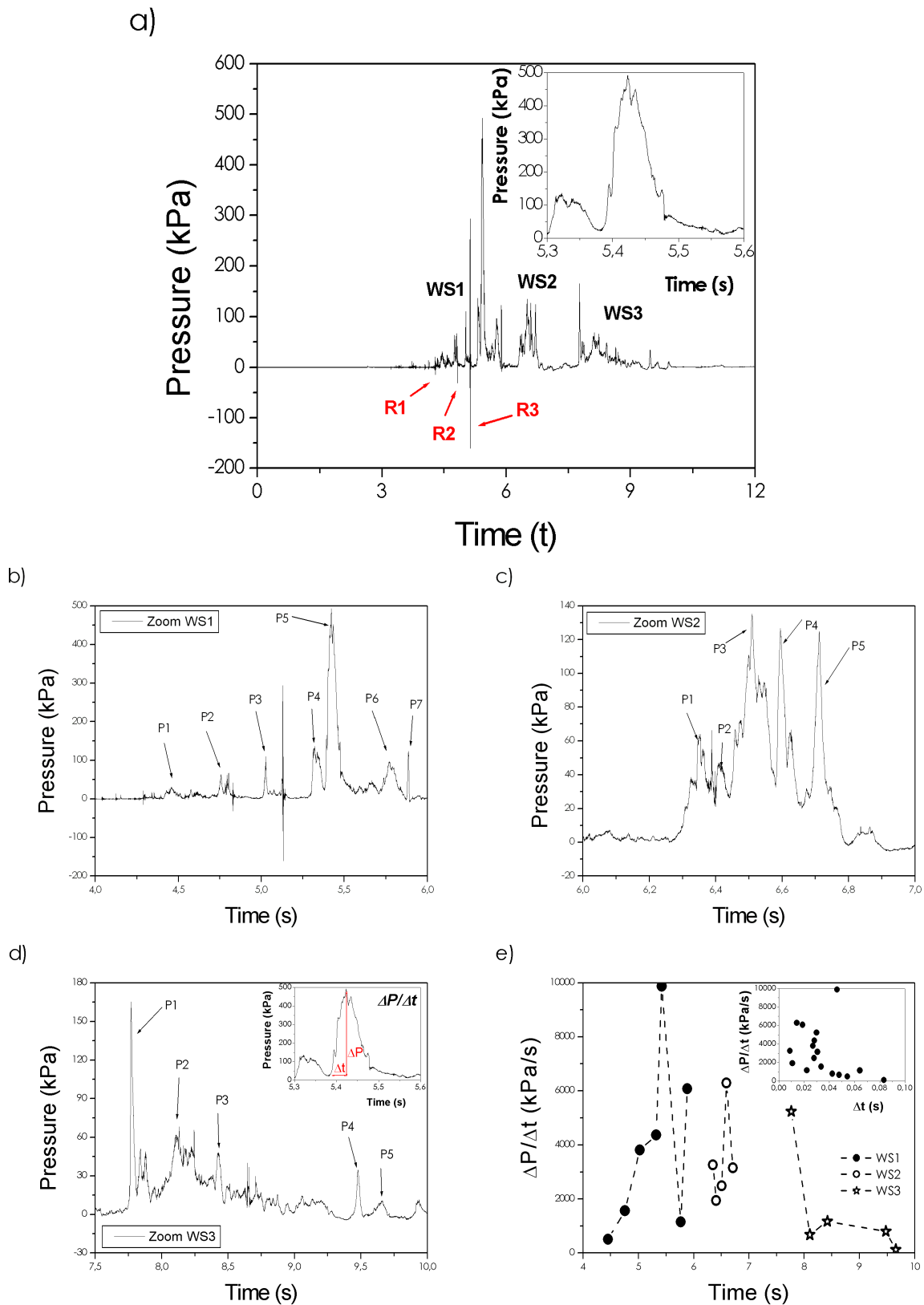


Figure 3.10: (a) Pressure values versus time. The maximum peak pressure reaches a value of almost 500 kPa. The inset shows that this peak is continuous, and not a single localised value. Three wave surges (*WS1*, *WS2* and *WS3*) are identified in the main pressure signal and zoomed in (b), (c) and (d). Arrows indicate the pressure peaks considered in order to calculate the pressure gradients (e): $\frac{\Delta P}{\Delta t}$ over time t . Gradients are calculated as shown in the inset.

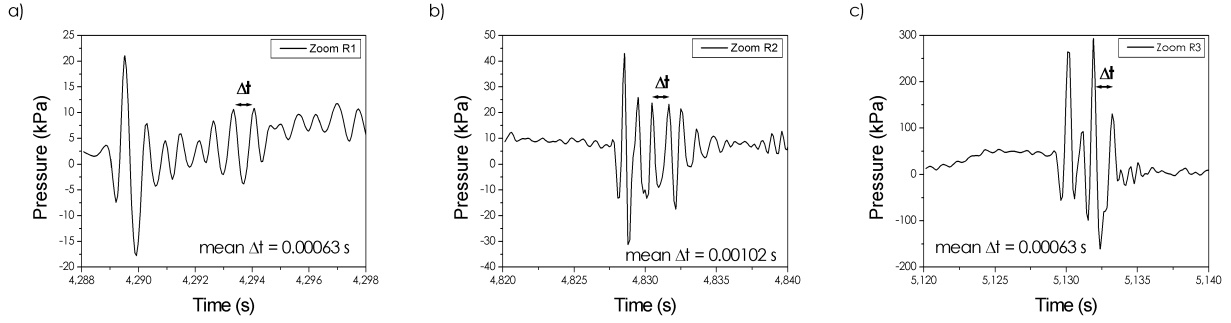


Figure 3.11: Single blocks impacted the sensor and generated resonance effects as evidenced in the main pressure signal. Three main events were analysed: (a) *R1*, (b) *R2* and (c) *R3*.

Preliminary results are shown in Fig.3.10.a. Data were recorded from mound $n^{\circ}3$. Because of certain sensors malfunctions (see Tab.3.2), the data presented below were provided by the low velocity sensor and the high pressure sensor.

The maximum peak pressure reaches a value of almost 500 kPa and, as shown in the inset of Fig.3.10.a, the maximum value consists of a continuous peak, not a single localised value. It must be noted that the measured pressure peak corresponds to half of the maximum design pressure mentioned in section 3.3.1.

Upon observing the pressure signal of Fig.3.10.a, it is possible to identify three main wave surges (*WS1*, *WS2* and *WS3*) which impacted the sensors at approximately $t \simeq 4.4$ s, $t \simeq 6.3$ s and $t \simeq 7.7$ s. These three surges are zoomed in on Fig.3.10.b-d. As it can be observed, the first wave (*WS1*) is characterised by several isolated pressure peaks. Some resonance effects are evident from the presence of negative pressure peaks, and they are discussed later in this section. The zoom in on the second surge (*WS2*) shows a compact pressure signal with relevant pressure peaks and finally *WS3* is characterised by an important localised peak followed by an increase of pressure and a long, rather constant, decreasing phase. We analysed some of the pressure peaks of the three wave surges (*P1*, *P2*...*Pi* in the figures) in order to estimate the pressure gradient $\frac{\Delta P}{\Delta t}$ (see the inset in Fig.3.10.d) that the avalanche is capable of inducing on an obstacle. The results are shown in Fig.3.10.e. The maximum pressure gradients are recorded during the first wave. Values reach $\frac{\Delta P}{\Delta t} = 10000$ kPa s $^{-1}$, which is an extremely high value for structure solicitations. The gradient tends then to decrease throughout the surges, and the *WS3* values are much lower and rather constant around $\frac{\Delta P}{\Delta t} \simeq 1000$ kPa s $^{-1}$ (ten times lower than the maximum peak). The inset of Fig.3.10.e shows the $\frac{\Delta P}{\Delta t}$ versus Δt . An underlying trend can be identified: the highest pressure gradients occur within the shortest time-lapses. Although this analysis does not remain very accurate, it highlights the very significant pressures and pressure gradients that can be exerted by an avalanche. Additionally, the continuum nature of pressure peaks rules out the possibility that maximum peaks are associated with the impact of single rocks or ice blocks.

Regardless, block impacts can probably make the sensors resonate. We suppose that the negative values of pressure indicated in Fig.3.10.a are related to the resonance of the sensor due to the impact of single blocks. We used three different approaches to investigate these resonance issues.

1. The first method aimed to identify roughly the natural frequencies of the system. The three main resonance events (*R1*, *R2* and *R3*) were analysed. Figure 3.11.a-c shows a zoomed image of the pressure signal. The mean value of Δt was calculated by averaging the time lapse between all the vibration peaks, in order to obtain the mean resonance frequency f_n of the sensor ($f_n = \frac{1}{\Delta t}$). Table 3.3 summarises the preliminary results. Both *R1* and *R3*

provide a similar resonance frequency approximately $f_n \simeq 1600$ Hz whereas *R2* shows a lower frequency of $f_n \simeq 1000$ Hz.

Table 3.3: Calculated values of Δt , f_n and σ_{f_n} for the three resonance cases *R1*, *R2* and *R3*.

	<i>R1</i>	<i>R2</i>	<i>R3</i>
<i>mean</i> Δt (s)	6.34×10^{-4}	1.02×10^{-3}	6.34×10^{-4}
<i>mean</i> f_n (Hz)	1637	1016	1617
σ_{f_n}	345	203	281

- Tests were also conducted with the impact hammer. The sensor was hit by the hammer and we observed the output pressure signal and its Fourier transform. A representative example is given in Fig.3.12. The pressure signal is shown in the inset whereas the main graph presents the associated Fourier transform. The results display a main natural frequency at approximately $f_n = 700$ Hz. This value was not found in preliminary results, but secondary peaks can also be observed around $f_n = 1000$ Hz and $f_n = 1700$ Hz which are very similar to those that were previously obtained.

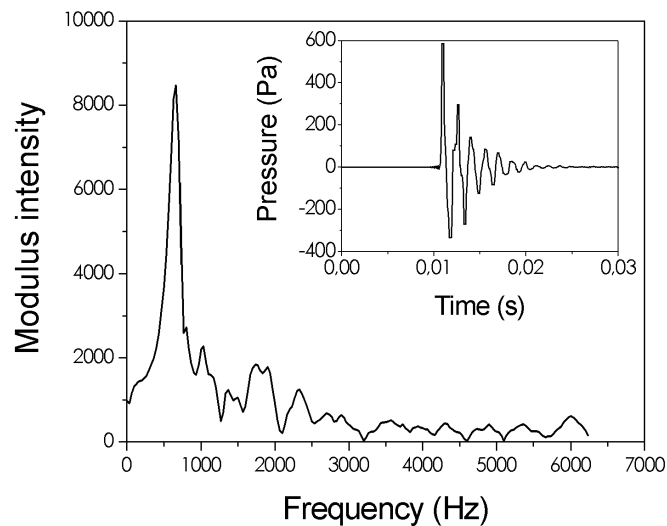


Figure 3.12: Impact hammer results for a single example case. In the inset: pressure signal versus time. In the main graph: Fourier transform of the signal.

- Finally, a frequency analysis of the entire pressure signal was conducted. The obtained Fourier transform is presented in Fig.3.13.a and confirms the previous results. Three peaks can be observed very clearly at $f_n = 600$ Hz, $f_n = 1000$ Hz and $f_n = 1600$ Hz. We filtered the pressure signal by means of a Butterworth-type filter (red line in Fig.3.13.a) in order to remove the contribution of the resonance effects from the signal. Figure 3.13.b shows the pressure signal before and after the filtering. No significant differences are evident, except in correspondence to the resonance events. Thus, the three main vibrating modes that were identified most likely depend on the application point of the impact with respect to the sensor center, while they only have a local effect on the pressure signal.

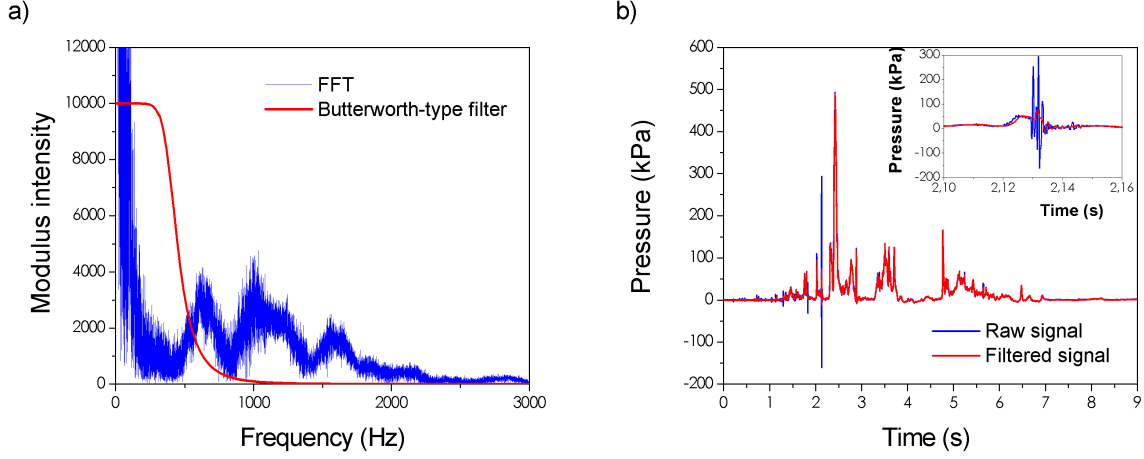


Figure 3.13: (a) Fourier transform of the entire pressure signal (blue line) and Butterworth-type filter representation (red line). (b) Pressure signal before (blue line) and after (red line) the filtering process. The inset shows a detail of the signal in correspondence to a resonance effect.

The Fourier transform was further integrated in order to investigate the influence of the blocks' impact in terms of avalanche power PW and energy E_{av} . We define the relative power and the energy, respectively, as:

$$PW = \frac{\sum_{i=1}^{f_n^{max}} MI_i^2}{PW^{tot}} \quad (3.6)$$

$$E_{av} = \frac{\sum_{i=1}^{f_n^{max}} MI_i^2 f_n^i}{E_{av}^{tot}} \quad (3.7)$$

where MI stands for the modulus intensity and PW^{tot} , E_{av}^{tot} for the total power and energy, respectively. Figure 3.14 displays the results. 45% of the energy ($\sim 65\%$ of the power) is released by the avalanche flow whereas 65% ($\sim 45\%$) of the total energy (power) comes from isolated impacts due to single blocks. This result underscores the role played by the presence of rocks or ice blocks on the impact energy of an avalanche.

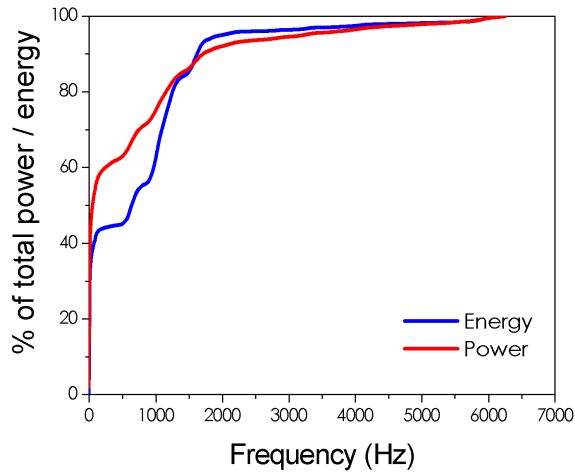


Figure 3.14: Relative power (red line) and energy (blue line) versus the frequency f .

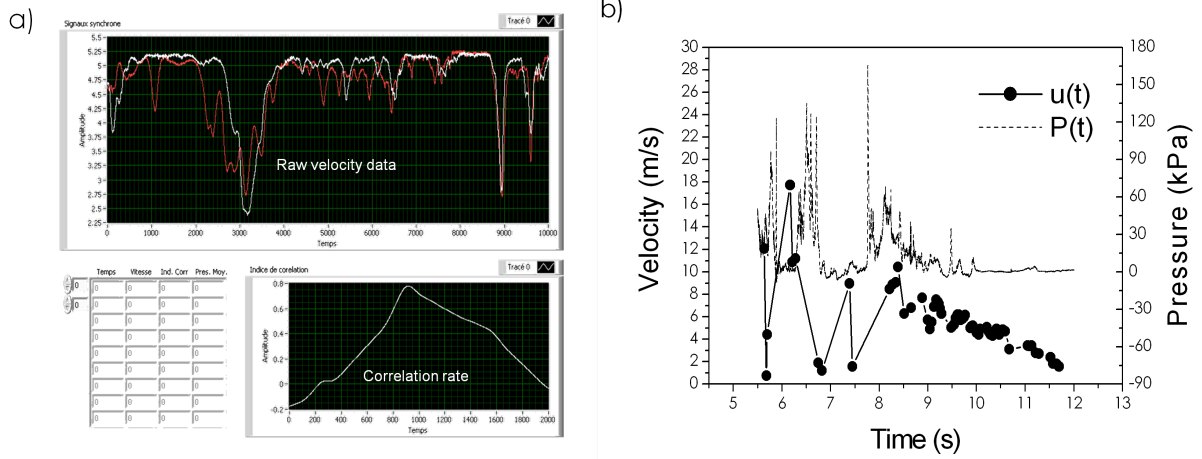


Figure 3.15: (a) Raw signal provided by velocity sensors and the correlation rate behaviour. (b) Velocity (left axis) and pressure (right axis) values versus time. Velocity data were obtained by processing the raw signals.

Velocity sensors: raw data

Figure 3.15.a shows the typical signal provided by the velocity sensors. The two signals present a similar behaviour but shifted in time. The analysis of this local time-shift uses a correlation rate C given by Bouchet et al. (2003) [24] that is equal to:

$$C = \frac{\Sigma(x_i - \bar{x})(y_{i+j} - \bar{y})}{\sqrt{\Sigma(x_i - \bar{x})^2} \sqrt{\Sigma(y_{i+j} - \bar{y})^2}} \quad (3.8)$$

where x , in this case, corresponds to the time t and y to the signal amplitude. This correlation index is calculated for different time-shifts and the value providing the highest correlation is retained and used for the velocity computation. An example of the behaviour of this parameter is also given in Fig.3.15.a. C also represents an indicator for measurement quality. High values of the correlation rate mean accurate and consistent data.

Figure 3.15.b displays the velocity data obtained from the correlation technique. Note that the signal starts around $t = 5$ s. Unfortunately, the treatment of $t < 5$ s provided correlation rates too low to be used. However, for $t > 5$ s, after some dispersed values, a decelerating continuum phase can be clearly observed. It is interesting to note that the decelerating phase, for $t > 8$ s, corresponds to the third final wave surge evidenced by the pressure signal $P(t)$ and zoomed in Fig.3.10.d. Thus, the following graphs do not concern the front of the avalanche, but rather its body and tail.

The next section presents a preliminary analysis and interpretation of the raw pressure and velocity values presented above.

Data interpretation

The obtained set of data is not very representative at the moment. As the database of recorded avalanches increases, it will become possible to gather much more informations and many more statistics on the flow behaviour. Regardless, certain preliminary considerations and comparisons can already be construed. The signals of pressure and velocity that are presented were used to interpret the data.

Figure 3.16.a shows the ratio $\frac{P}{u^2}$ versus time t . The $\frac{P}{u^2}(t)$ profile remains rather constant until a specific time $t^\diamond = 10.5$ s, and then increases rapidly: for $t > t^\diamond$, even if the velocity continues to

decrease linearly, the ratio suddenly increases. This behaviour is also clear when looking at the ratio $\frac{P}{u^2}$ versus the flow velocity u as displayed in Fig.3.16.b. For velocity values approximately higher than $u^* = 5 \text{ m s}^{-1}$, the ratio $\frac{P}{u^2}$ is constant and it suddenly increases for $u < u^*$. Results indicate that for low flow velocities, a particular regime occurs where high pressures can still be exerted on a structure, despite the low velocity. This result is related to and in accordance with the results presented in section 1.3.2 for granular flows at the laboratory.

Two main parameters are still missing in order to optimize this type of measurements: (i) the height of the flow and (ii) its density. Thus, we did some significant assumptions in order to compare these results with those previously obtained from the Vallée de La Sionne and Col du Lautaret. It is important to state beforehand that we are aware that certain assumptions were made and consequently, the following results should be taken cautiously.

The Froude number Fr is frequently used to represent the flow characteristics while the measurements we took are very localised. The pressure plate surface is very small with respect to the avalanche front section and the same can be said for velocity sensors. We defined a local Froude number $Fr_{loc} = \frac{u}{\sqrt{gz_{sens}}}$ where u represents the measured local velocity and z_{sens} is the height

at which the sensors are placed ($z_{sens} = 6.6 \text{ m}$). A mean density of 500 kg m^{-3} was assumed. Such a high value is justified by the massive presence of ice blocks coming from the glacier and by the low slope typical of the run-out zone. Figure 3.16.c places our results with respect to those published in Sovilla et al (2008) [149] and to two avalanches recorded at Col du Lautaret in 2010 and 2011. The product ρC_d is derived from Eq.(2.10) ($\rho C_d = \frac{2P}{u^2}$) and represented as a function of the Froude number Fr . This type of representation removes the uncertainty of the density value. The data from Lautaret are calculated assuming a constant flow height $h = 1 \text{ m}$ (except for $n^\circ 10022010$ where $h = 0.5 \text{ m}$) and a constant mean density of $\rho = 300 \text{ kg m}^{-3}$. A general tendency is observed: the drag coefficient decreases when the Froude number increases. The data from Taconnaz have generally lower Fr , which is probably due to the fact that, in addition to the sites' differences, the measurements were carried out on a lower slope ($\theta = 13^\circ$ for Taconnaz, $\theta = 21^\circ$ for Vallée de La Sionne and $\theta = 36^\circ$ for Lautaret), and we assumed a constant height $h = z_{sens} = 6.6 \text{ m}$ while Sovilla et al. (2008) used the values $h(t)$ provided by flow-depth sensors.

Figure 3.16.d shows similar results. The drag coefficient is represented versus the Froude number. Data are displayed in a log-scale graph and appear to be rather linear. Thus, a power-fit can be used leading to a relation

$$C_d = KFr^{-n} \quad (3.9)$$

where K is a constant value and n is the fit slope.

Four sets of data were used for the comparison. Three of them were obtained from artificially-released avalanches at Col du Lautaret assuming $\rho = 300 \text{ kg m}^{-3}$ for the 10022010 and 18032011 avalanches [53] and $\rho = 120 \text{ kg m}^{-3}$ for the 15022007 event, as published in Thibert et al. (2008) [152]. The fourth set represents the avalanche of Taconnaz ($\rho = 500 \text{ kg m}^{-3}$). It is important to note that the advantage of this representation is that, if we assume a constant value for the flow height and density ($h(t) = h^*$ and $\rho(t) = \rho^*$), the parameter n is independent from h^* and ρ^* . Different values of flow height would shift the data along the x -axis while changing the flow density would vertically translate the data. These variations affect the value of the constant K but not n . However, for time varying values of $h(t)$ and $\rho(t)$, this consideration is no longer valid.

Results are consistent. The value of n ranges between 1.19 and 1.78. Differences are certainly influenced by the measurement errors and probably related to the natural variability of snow parameters and to the different snow conditions characterising different avalanche events. Similar values were already proposed by previous studies. Laboratory experiments on granular flows

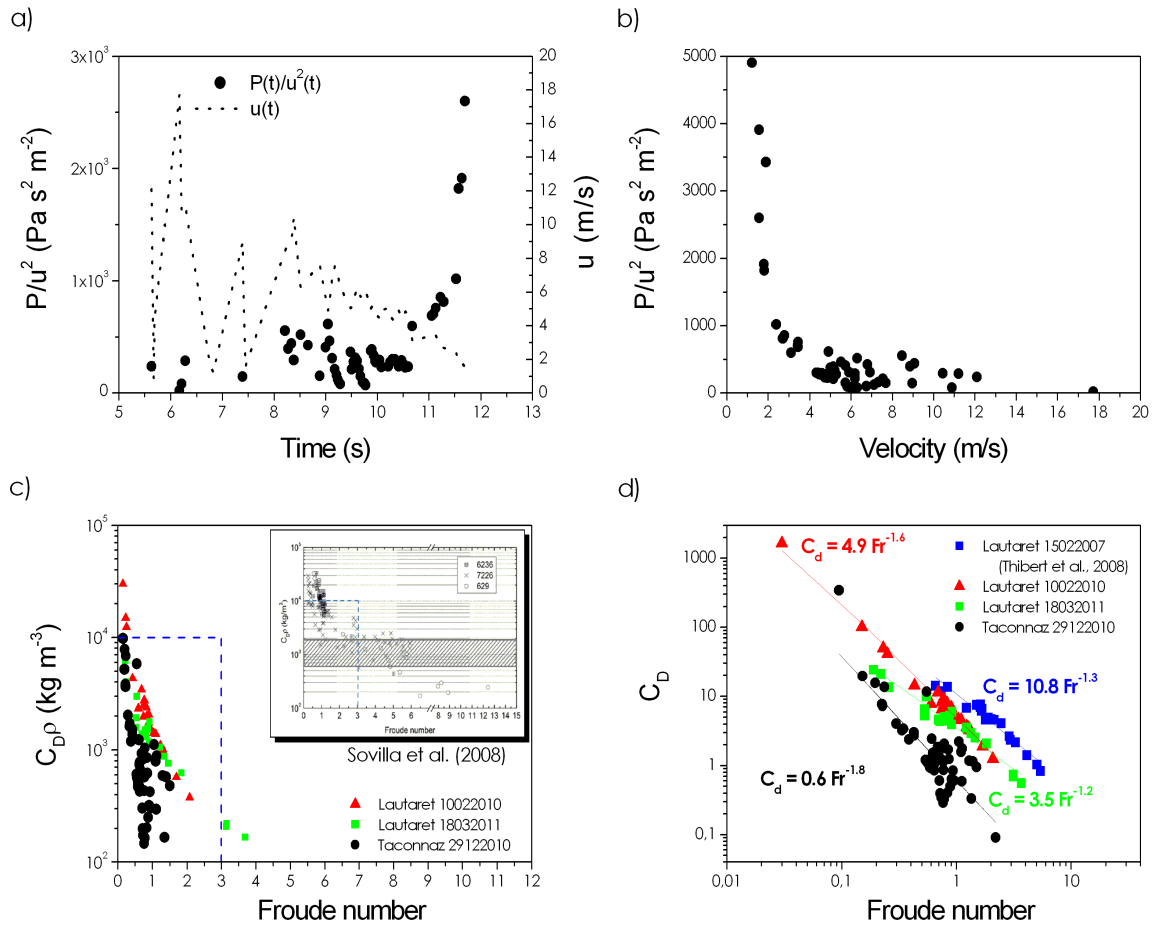


Figure 3.16: Preliminary analysis of the results obtained from the first event recorded on the Taconnaz site: (a) $\frac{P}{u^2}$ ratio (left axis) and velocity u (right axis) versus time t . (b) $\frac{P}{u^2}$ ratio versus the flow velocity u . (c) $C_{D\rho}$ versus the local Froude number. The inset shows the same graph but displays the data from Vallée de La Sionne published in Sovilla et al. (2008) [149]. (d) C_D versus the Froude number Fr . The obtained data are compared to those from Thibert et al. (2008) [152] and to two recent avalanches recorded at Col du Lautaret and published in Faug et al. (2012) [53] ($\rho_{15022007} = 120 \text{ kg m}^{-3}$, $\rho_{10022010} = \rho_{18032011} = 300 \text{ kg m}^{-3}$ and $\rho_{29122010} = 500 \text{ kg m}^{-3}$).

carried out by Wieghardt (1975) and Chehata et al. (2003) [161, 39] and field data from Sovilla et al. (2008) founded $n = 2$ suggesting that for $Fr < 1$ (subcritical flow) the velocity u and the drag pressure are independent whereas for $Fr > 1$ (supercritical flow) these two parameters are dependent and linked by the classical kinetic pressure formulation of Eq.(2.10). $n = 2$ was also found in Pazwash and Robertson (1975) [118] for Bingham fluids, and for viscoplastic yield-stress fluids Tiberghien (2007) obtained $n = 1.7$.

Figure 3.16.d, regardless of height and density assumptions, demonstrates that the drag coefficient decreases with the Froude number and that, for low values of Fr , high impact pressures can still be measured. Even if the data remain scarce, this result confirms the considerations previously made in Gauer et al. (2007) [62] and in Sovilla et al. (2008) [149].

3.4 Conclusions

The avalanche path of Taconnaz represents an extraordinary site of abnormal dimensions. The risk represented by a potential avalanche is very high due to the threatened issues, their vulnerability and the uncontrolled nature of the hazard (natural release and serac calving influence). Several improvements were made after the construction of the original protection system built in 1991.

Today, the existing configuration is the result of an exhaustive study combining in-situ measurements with numerical and physical modelling. This configuration is designed and optimised to contain an event with a return period characterised by a Froude number $Fr^{100} = 4.29$ and a volume $V^{100} = 1.6 \times 10^6 \text{ m}^3$.

In 2009, three breaking mounds were equipped with pressure and velocity sensors. The installation campaign represented a huge investment in terms of labour and money that only started yielding results two years later. To better understand the behaviour of extreme snow avalanches and to further interpret the data, more events still need to be recorded.

Even though the main efforts were probably centred around the start-up of the site activity, the maintenance of such a structure will be expensive and time-consuming. Regardless, the preliminary results seem to be interesting and they demonstrate that the entire system works effectively despite its complexity.

Main results of chapter 3

1. The first avalanche was recorded on December 29, 2010. The entire system that was installed worked effectively.
2. In this particular case: velocity measurements yielded good results for $t > 5 \text{ s}$, but before $t = 5 \text{ s}$ the correlation rate was found too low to be reliable.
3. A complete pressure signal was recorded and:
 - (a) the maximum pressure reaches $P = 500 \text{ kPa}$;
 - (b) very high pressure gradients were exerted by the avalanche (up to 10000 kPa s^{-1});
 - (c) resonance effects, due to the impact of single blocks, are visible in the pressure signal. Three main vibrating modes were found ($f_n \simeq 600 \text{ Hz}$, $f_n \simeq 1000 \text{ Hz}$ and $f_n \simeq 1600 \text{ Hz}$), probably depending on the impact application point with respect to the sensor center. If these isolated impacts only affect the time-dependent pressure signal locally, their contribution to the total energy released by the avalanche is very significant ($\sim 65\%$).
4. For $t > 5 \text{ s}$, where we had both velocity and pressure measurements, the data interpretation showed that:
 - (a) at low velocity regimes, high pressures can still be exerted;
 - (b) the drag coefficient C_d seems to increase when the Froude number Fr decreases (it confirms the observed behaviour from small-scale tests with grains as well as from full-scale tests at Col du Lautaret and Vallée de La Sionne).

Conclusion

Contents

Context	155
Method	155
Granular avalanches past a wall	157
Density currents past an obstacle	159
The full-scale experimental site of Taconnaz	163
Future perspectives	164

Context

Since man began to inhabit mountainous areas, natural phenomena became natural risks. Mountainous areas, during the last century, were subjected to a significant urbanisation process. The development of alpine tourism, in particular, implied the construction of infrastructures, roads, and railways to host and ensure human activity. A growing need for space arose. At first the safest areas were occupied but, today, urbanisation increasingly concerns areas that are threatened by natural hazards, and snow avalanches in particular. The development boom came to require a more scientific approach for protection design, based on progress in the domains of mechanics and geosciences. However, scientific studies must be carried out in order to improve existing knowledge.

Within the field of snow avalanche protection, a quantification of the physical vulnerability of structures subjected to avalanche impacts depends on a thorough understanding of the flow dynamics and an enhanced comprehension of the flow-obstacle interaction.

Method

This PhD research was conducted in order to improve the existing knowledge of flow dynamics and the flow-obstacle interaction. The approach was mainly experimental. The first part concerned laboratory tests on a small-scale model:

- dry dense snow avalanches were modelled on a small-scale by analogy to granular flows. An experimental device was used, consisting of an inclined channel with a variable slope. The investigated slopes range between 21° and 33° . A constant volume (4 l) of dry, cohesionless and mono-dispersed glass beads was stored in a reservoir, and when the gate was released, it starts flowing downwards, until reaching impact with an obstacle at $x = 1.3$ m ($= 1300d_{beads}$), at which point force, velocity, and flow depth measurements were taken;
- aerosol avalanches were reproduced by analogy to density currents. The experimental device consisted of an inclined channel with a fixed slope ($\theta = 13^\circ$), immersed in a water tank ($\rho = 1000$ kg m $^{-3}$). A constant volume of a dyed salt solution ($\rho = 1200$ kg m $^{-3}$) was released from the reservoir. It starts flowing downwards and, 1 m downstream from the opening gate, it impacts a dam-like obstacle. Measurements on the flow height, front, and core velocity were taken.

For both dense and powder laboratory avalanches, reference tests were first conducted. The simulated avalanche flows down the channel without reaching impact with any obstacle. This allowed the characterisation of the dynamic properties of the flow. Afterwards, the obstacle was mounted and the flow-obstacle interaction was studied. Both experimental devices investigated the flow behaviour in the presence of two different types of obstacles. On the granular channel, a catching-dam-like obstacle was used first and then replaced by a breaking-mound-like obstacle. On the other hand, experiments in the water tank made use of a catching dam protection with the upstream face both vertical ($\alpha_{dam} = 90^\circ$ with respect to the terrain slope) and inclined ($\alpha_{dam} = 32^\circ$).

The second part consisted of full-scale measurements. A full-scale experimental site was set on the already existing avalanche protection system of Tacconnaz (Chamonix, France). Three breaking mounds were equipped with pressure and velocity sensors in order to measure the characteristic parameters of real-scale avalanches. Field data aim to yield additional results to validate the physical modelling carried out in the laboratory and, in general, theoretical and numerical simulations.

Even if the slopes investigated for the dense ($\theta = 21^\circ - 33^\circ$) and powder ($\theta = 13^\circ$) laboratory avalanches and that of in-situ measurements ($\theta = 13^\circ$) are not the same, the Froude scaling ensures the dynamic similarity of these three different approaches.

Granular avalanches past a wall

The dynamic properties of dense-snow avalanches provide the designing parameters for the construction of protection structures like catching or deflecting dams and breaking mounds. Thus, the aim was to quantify the force that such a flow can induce on an obstacle and to investigate the influence of the obstacle on the flow behaviour.

Dense snow avalanches were simulated on small-scale models by using dry cohesionless and mono-dispersed granular material. This type of material is characterised by two classic angles, θ_{min} and θ_{max} , referring to the effective friction related to quasi-static deformations and rapid collisional regimes, respectively. Below θ_{min} , the flow slows down and stops, whereas above θ_{max} , the granular avalanche accelerates. In-between, for $\theta_{min} < \theta < \theta_{max}$, uniform flow conditions can be reached even for non-steady flows. These two angles were experimentally found equal to 20° and 28° , and they largely influence the flow dynamics.

Unsteady granular flows are typically characterised by three main phases: (i) a diluted front, (ii) a dense body and (iii) a tail.

Reference flows

Height profiles typically show a rapid increase in values (front), a peak (body) and a decreasing phase (tail). The θ_{max} angle defines the behaviour of two groups of curves that differ on the decreasing phase slope. The trend for maximum flow depth values is peculiar approaching θ_{min} because the friction forces (and side-walls effects) become significant, a jamming transition occurs and the maximum flow height drops. For $\theta_{min} < \theta < \theta_{max}$, maximum values are rather constant and they decrease linearly beyond θ_{max} .

The profiles of the flow surface velocity also exhibit two different behaviours: increasing phase - peak - decreasing phase for $\theta < \theta_{max}$ whereas for $\theta > \theta_{max}$, the peak becomes a plateau of velocity values which remain constant for several seconds before decreasing. Maximum values increase linearly with the slope angle.

The results obtained for the flow depth and the surface velocity were applied to an already existing scaling law, giving the depth-averaged velocity \bar{u} as a function of the flow depth h in steady and uniform flow conditions:

$$\bar{u} \propto h^{3/2} (\tan \theta - \tan \theta_{min}) \quad (3.10)$$

Results confirmed that even with finite-sized granular avalanches in non-steady conditions, for $\theta_{min} < \theta < \theta_{max}$, the scaling law is clearly verified and thus the uniform flow can be reached.

Force measurements on a large obstacle (LO)

A large obstacle spanning the entire width of the flow (catching-dam-type) was mounted and force measurements were taken.

The obtained force profiles are characterised by a rapid increase in values, a peak, and a decreasing phase which becomes steeper when increasing the slope. Maximum force values are at their minimum closer to the θ_{min} angle (basal friction and lateral walls effect), rather constant at approximately $\theta_{min} < \theta < \theta_{max}$, and they increase again above θ_{max} .

When comparing the maximum force values $F_{max}^{LO}(\theta)$ with the hydrostatic ($F \propto \rho gh$) and kinetic ($F \propto \rho u^2$) contributions, we found that, for high slopes, the maximum force is purely kinetic ($\frac{F_{max}^{LO}}{F_{kin}^{LO}} \simeq 1$) while, for low slopes, the hydrostatic contribution becomes significant but a third

contribution influences the total force. We assume that this influence is due to the presence of the influence zone uphill from the obstacle. More details on the influence zone are given in the following. The time-dependent force profiles do not end at a zero value. Because of the final deposit trapped by the dam and that continues to be pushed even after the motion stops, a constant residual force remains at the end. This force is related to the final deposit and tends to increase when decreasing the slope, except approaching the θ_{min} angle, where the values of F_{res}^{LO} drop. At low slopes, friction plays an important role in reducing the deposit weight acting on the obstacle. A simple model based on the equilibrium between the deposit weight w and the basal friction F_f aptly describes the residual force behaviour, except close to the θ_{min} angle.

Force measurements on a narrow obstacle (SO)

The large obstacle spanning the entire width of the flow was replaced by a narrow obstacle, allowing lateral flows (breaking-mound-type), and the same measurements were repeated.

Note that, in order to compare the forces observed with the two obstacles, values were divided by the obstacle length l_{obs} . Thus, in the following, we talk about forces for the sake of simplicity, but it is important to remember that these are forces per unit length ($\frac{F_i}{l_{obs}}$).

As for the large obstacle, the maximum force generally increases with the slope. When comparing F_{max}^{SO} to the hydrostatic and kinetic contributions, the behaviour is similar to that of F_{max}^{LO} for high slopes where maximum forces were found to be purely kinetic ($\frac{F_{max}^{SO}}{F_{kin}^{SO}} \simeq \frac{F_{max}^{LO}}{F_{kin}^{LO}} \simeq 1$). However, a difference was found at low slope angles where maximum forces exerted on the small obstacle were found to be much higher than those from the large obstacle ($\frac{F_{max}^{SO}}{l_{SO}} = 2 \frac{F_{max}^{LO}}{l_{LO}}$). At low slopes, the obstacle geometry influences the induced force. This is probably due to a network of forces acting along the transversal axis that reduce the force exerted on the structure (Janssen effect) in the presence of the large obstacle.

The residual force F_{res}^{SO} decreases rather constantly while increasing the slope and, as was the case for the large obstacle, the analytical model based on the equilibrium between the weight and the basal friction accurately describes the residual force behaviour, except for $\theta < 24^\circ$, when approaching the θ_{min} angle.

Dead zone to granular jump transition

Upon impact with an obstacle, a quasi-static zone forms directly uphill from the obstacle and an inertial layer starts flowing above and overflows the obstacle. These two parts compose the influence zone, a zone that plays an important role in the flow dynamics. The behaviour of this zone was investigated in detail, for a fixed slope of 31° , by studying the time evolution of three parameters: the influence zone angle α_{iz} , its length L_{iz} , and its surface S_{iz} . The results obtained through the laser technique and image processing exhibited a regime transition. Upon impact with the wall-like obstacle, a dead zone regime generates. A triangular quasi-static zone forms uphill from the obstacle and an inertial layer starts flowing above. Values of α_{iz} , L_{iz} and S_{iz} remain constant for several seconds and then the transition occurs. At $t^* \simeq 3.2$ s, values suddenly vary: α_{iz} starts decreasing, and L_{iz} and S_{iz} increase. The triangular quasi-static zone develops into more of a trapezoidal shape, increasing in volume and progressing upwards in the opposite direction of the flow (granular jump regime), until the motion stops. This dead zone to granular jump transition was found to influence force measurements. An analytical prediction showed that the time t^* at which the transition occurs would be rather constant for $\theta > \theta_{max}$, whereas the transition would not occur below θ_{max} .

Test on an analytical force model

A depth-averaged hydrodynamic analytical model was developed in tandem in order to calculate the normal force acting on a wall-like obstacle. The data obtained from laboratory experiments, in the presence of the large obstacle, were used to test the model. Results are qualitatively consistent. However, two different fit procedures were applied in order to further improve this consistency. The volume fraction $\bar{\phi}(t)$ was fitted for $\theta > \theta_{max}$, while the characteristic time for the influence zone formation, τ_{iz} , was adapted for slope angles close to θ_{min} ($\theta < 25^\circ$). Although improvements can still be implemented, the model predictions are in accordance with experimental small-scale results.

Density currents past an obstacle

In the design procedure of protection structures as catching dams, aerosol avalanches are supposed to overflow the obstacle in any given situation. The interest here lies in investigating the flow characteristics downhill from the obstacle in order to quantify the residual risk that the avalanche still represents.

Powder-snow avalanches were modelled by dyed salt solutions flowing in a channel immersed in a water tank.

Measurements were taken on the maximum flow height, front, and core velocity. Reference tests were first performed in order to characterise the flow dynamic parameters and to obtain reference values for comparison with the obstacle configurations.

Note that, in the following:

1. the main flow direction corresponds to the x -axis which is parallel to the channel axis and x_0 is set at the release gate of the reservoir;
2. measurements were taken up to a maximum distance of $x = 1.9$ m;
3. the clockwise and counter-clockwise rotations are considered with respect to a cloud flowing down from the right to the left;
4. the core velocity values for a given x -position correspond to:

$$U_i^+(z) = \frac{1}{n} \sum_1^n u_i^{max}(z) \quad (3.11)$$

with

$$u_i^{max}(z) = \max [u_i(z, t)] \quad (3.12)$$

where $i = x, z$, depending on which core velocity contribution is considered, and where n is the number of similar tests conducted for the same given (x, z) position ($n = 3 - 5$).

u_i can be positive or negative, thus, by analogy, it is possible to define

$$U_i^-(z) = \frac{1}{n} \sum_1^n u_i^{min}(z) \quad (3.13)$$

with

$$u_i^{min}(z) = \min [u_i(z, t)] \quad (3.14)$$

$U_i^+(z)$ and $U_i^-(z)$ are fictitious profiles of the flow velocity. They represent the profiles of maximum (and minimum) velocity.

$$U_i^{max} = \max (U_i^+(z)) = \max \left[\frac{1}{n} \sum_1^n u_i^{max}(z) \right] \quad (3.15)$$

$$U_i^{min} = \min (U_i^-(z)) = \min \left[\frac{1}{n} \sum_1^n u_i^{min}(z) \right] \quad (3.16)$$

U_i^{min} is defined only if $\min [U_i^-(z)] < 0$.

At $t = t_{U_i^{max}}$:

$$V_i^+(z) = \frac{1}{n} \sum_1^n u_i(z)_{(t=t_{U_i^{max}})} \quad (3.17)$$

And at $t = t_{U_i^{min}}$:

$$V_i^-(z) = \frac{1}{n} \sum_1^n u_i(z)_{(t=t_{U_i^{min}})} \quad (3.18)$$

$V_i^+(z)$ and $V_i^-(z)$ are real profiles as they represent the velocity profile at the time where the maximum (and minimum) value is observed.

5. the norm velocity was calculated according to

$$u_{xz}(z, t) = \sqrt{u_x(z, t)^2 + u_z(z, t)^2} \quad (3.19)$$

$$u_{xz}^{max}(z) = \max [u_{xz}(z, t)] \quad (3.20)$$

$$U_{xz}(z) = \frac{1}{n} \sum_1^n u_{xz}^{max}(z) \quad (3.21)$$

$$U_{xz}^{max} = \max [U_{xz}(z)] \quad (3.22)$$

6. the velocity norm is calculated from the time-dependent profiles of $u_x(z, t)$ and $u_z(z, t)$ according to:

$$\alpha_{xz}^*(z, t) = \arctan \left[\frac{u_z(z, t)}{u_x(z, t)} \right] \quad (3.23)$$

and, afterwards, this angle is always associated to the norm velocity value:

$$\alpha_{xz}^{*,max}(z) = \alpha_{xz} [u_{xz}^{max}(z)] \quad (3.24)$$

$$\alpha_{xz}(z) = \alpha_{xz} [U_{xz}(z)] \quad (3.25)$$

$$\alpha_{xz}^{max} = \alpha_{xz} [U_{xz}^{max}] \quad (3.26)$$

Reference flows

The density cloud is composed of 4 l of a dyed salt solution. When the reservoir gate is opened, the density cloud starts flowing downwards through the channel without hitting any obstacles. Reference flows flow down the channel with a velocity that appears to be rather constant. Their turbulent structure develops into a series of eddies rotating clockwise of different dimensions.

The maximum cloud height increases constantly up to a maximum value of $h_{max}^{REF} \simeq 0.24$ m at $x \simeq 1.4$ m and then remains rather constant.

The front velocity is rather constant and equal to $u_{fr}^{REF} \simeq 0.28$ m s⁻¹.

The maximum core velocity u_x^{max} decreases from $u_x^{max} \simeq 0.58$ m s⁻¹ ($x = 0.7$ m) to $u_x^{max} \simeq 0.47$ m s⁻¹ ($x = 1.9$ m). The maximum core velocity is generally higher than the front velocity and the ratio $\frac{U_x^{max,REF}}{u_{fr}^{REF}}$ ranges between 1.6 and 1.9.

The horizontal core velocity $V_x^+(z)$ reaches its maximum at the bottom of the flow and decreases, increasing the vertical coordinate z . Values of $V_x^-(z)$ correspond to the density cloud flowing uphill, in the opposite direction of the flow. Because of the turbulent structure of the powder avalanche, this happens at high values of z , at the top of the main turbulent eddy rotating clockwise. However, $|U_x^{min,REF}| \ll |U_x^{max,REF}|$ for the reference case.

Vertical core velocities $V_z^+(z)$ have a semi-elliptic profile with maximum values around $z = \frac{h_{max}}{2}$ and minimum values at $z \simeq 0$ and $z \simeq h_{max}$. Because of the turbulent structure of the density cloud, the vertical profiles of $V_z^+(z)$ and $V_z^-(z)$ are rather symmetric and values are lower than the horizontal contribution.

The maximum value of the core velocity norm was calculated for each x -position being investigated, and it was found to be up to 18% greater than the maximum horizontal core velocity. U_{xz}^{max} was found close to the bottom, for low values of z and, in reference conditions, is controlled by the maximum horizontal contribution U_x^{max} .

The angle related to the maximum norm value (α_{xz}^{max}) was calculated and, as the horizontal contribution is dominant, this angle was found to be rather low, $-5^\circ < \alpha_{xz}^{max} < 5^\circ$.

Effects of a catching dam with a vertical uphill face ($\alpha_{dam} = 90^\circ$)

After reference tests, a first obstacle (*OBS1*) was mounted on the channel at a distance of $x = 1$ m. In the *OBS1* configuration, the incoming flow hits the vertical wall of the dam and bursts. The cloud height rapidly increases, and the front of the flow separates into two main parts: an upper part rotating clockwise and expanding upward, and a second part generating new eddies turning counter-clockwise. The impact with the obstacle makes the cloud incorporate the ambient fluid, its surface increases and thus its density decreases. The effect of this obstacle is relevant to the three investigated parameters: the maximum flow height, front, and core velocity.

The maximum height, after the impact, increases rapidly up to a value of $h_{max}^{OBS1} \simeq 0.36$ m ($h_{max}^{OBS1} = 1.5h_{max}^{REF}$) at a distance of $x \simeq 1.7$ m. Values decrease afterwards due to the fact that the cloud, after bursting, comes down and continues to flow until reaching the end of the channel.

The flow front velocity drops after the impact. It reaches a minimum value of $u_{fr}^{OBS1} \simeq 0.14$ m s⁻¹ ($u_{fr}^{OBS1} = 0.5u_{fr}^{REF}$) at $x \simeq 1.3$ m and then it increases again to stabilise at a rather constant value of ($u_{fr}^{OBS1} = 0.78u_{fr}^{REF}$) until the end of the channel.

The maximum horizontal core velocity also drops at $x = 1$ m. $U_x^{max,OBS1}$ and reaches a minimum value of 0.35 m s⁻¹ ($U_x^{max,OBS1} = 0.69U_x^{max,REF}$) which remains constant up to the end of the channel. The ratio $\frac{U_x^{max,OBS1}}{u_{fr}^{OBS1}}$ ranges between 1.4 and 2.3.

Because of the impact, the turbulence inside the cloud increases and, consequently, vertical core velocities and upward horizontal core velocities increase too. Right after the obstacle, at $x = 1.15$ m, maximum uphill horizontal core velocities were found to be higher than the relative downhill maximum values: $|U_x^{min}| \simeq 2|U_x^{max}|$.

The increase of vertical core velocities u_z implies the increase of the maximum core velocity norm U_{xz}^{max} . In the presence of *OBS1*, the maximum norm was found to be up to almost 30% higher than the maximum horizontal contribution. The z -value, at which the maximum norm was registered, increases rapidly immediately after the impact, ($x = 1 - 1.2$ m) reaching up to $z = 0.18$ m because the cloud bursts. As a consequence, the angle related to the maximum norm (α_{xz}^{max}) increases to values approximately equal to 35° directly above the obstacle ridge ($x = 1$ m). It then decreases rapidly.

Effects of a catching dam with inclined uphill face ($\alpha_{dam} = 32^\circ$)

OBS1 was replaced by a second type of structure. *OBS2* consists of a catching dam, with the uphill face inclined at an angle $\alpha_{dam} = 32^\circ$ with respect to the terrain slope. In the presence of the second dam configuration, a different behaviour was observed. The flow does not hit the obstacle, but rather it keeps flowing on it by going up and down the uphill and downhill ramps. The obstacle seems to have a lower effect on the flow dynamics.

The maximum cloud height shows the same behaviour as that of reference conditions (increasing phase up to $h_{max}^{OBS2} \simeq h_{max}^{OBS1} \simeq 0.24$ m for $x = 1.4$ m and then constant value).

A small positive effect from the dam was measured on the front flow velocity. After the impact, the front velocity drops and reaches a value of $u_{fr}^{OBS2} \simeq 0.20$ m s⁻¹ ($u_{fr}^{OBS2} = 0.7u_{fr}^{REF}$). Afterwards, the cloud re-accelerates up to $u_{fr}^{OBS2} \simeq 0.25$ m s⁻¹ and, after $x = 1.3$ m, it remains constant.

Upon impact with the obstacle, the maximum horizontal core velocity starts decreasing at $x = 1.1$ m and decreases to a value close to that obtained for *OBS1* ($U_x^{max,OBS2} \simeq U_x^{max,OBS1} \simeq 0.7U_x^{max,REF}$) at $x = 1.7$ m. The ratio $\frac{U_x^{max,OBS2}}{u_{fr}^{OBS2}}$ ranges between 1.4 and 2.1. Uphill horizontal velocities are measured downhill from the obstacle but generally $|U_x^{min}| < |U_x^{max}|$.

Although the effects of the obstacle have a lower influence on the flow behaviour (with respect to *OBS1*), upon impact with *OBS2*, the difference between the maximum norm and the maximum horizontal contribution still remains significant, $U_{xz}^{max} \simeq 1.2U_x^{max}$. This means that u_x decreases however, and u_z increases (induced by the uphill obstacle ramp). The angle associated to the maximum norm remains rather low, $-10^\circ < \alpha_{xz}^{max} < 10^\circ$.

The full-scale experimental site of Taconnaz

A new experimental site was set on the already existing avalanche protection system of Taconnaz. This new site aims to collect data on the dynamics of naturally-released, full-scale avalanches. The design, the set-up, and the data interpretation were all a part of this research.

New equipment

Three breaking mounds ($H_{obs} = 7$ m) were equipped with two rows of pressure and velocity sensors at two different heights: ($\frac{1}{3}H_{obs}$ and $\frac{2}{3}H_{obs}$). Sensors had to resist temperatures between -30° and 30° , pressures up to 100 ton m^{-2} and to measure velocities up to 60 m s^{-1} . For safety reasons, the avalanche basin is not accessible during the winter and the three acquisition units therefore had to be linked together and connected to a central unit placed away from the protection system that would remain permanently accessible.

The entire acquisition system records continuously on a circular memory. When an event is detected on a sensor, a signal is sent to the mound $n^\circ 5$ (see the numbering of Fig.3.7.a) which releases the recording for all of the other mounds and provides the time t_0 , fundamental for the data synchronisation. The 120 s after t_0 , and the 60 s before, are finally stored in a specific memory device. A *GSM* router allows the consultation of the central unit from a distance and the downloading of the recorded data.

Preliminary results: the avalanche of December 29, 2010

The first avalanche was recorded December 29, 2010. The entire acquisition system and the majority of the sensors worked well. Mound $n^\circ 3$ provided both velocity and pressure data.

Velocity results concern only the avalanche tail, for $t > 5$ s, because before $t = 5$ s the correlation rate of the signal was found too low to be reliable. After some dispersed values with a maximum at $18 - 20 \text{ m s}^{-1}$, a continuous decreasing phase is exhibited.

A complete pressure signal was also recorded and allowed a detailed treatment.

The pressure maximum peak reached $P = 500$ kPa and it consisted of a continuous peak (not a single localised value) that reached half of the estimated design pressure ($P^{100} = 1000$ kPa). Three different wave surges successively struck the obstacle. Very high pressure gradients ($\frac{\Delta P}{\Delta t}$), up to 10000 kPa s^{-1} , were exerted by the avalanche and their values decrease throughout the three surges.

Resonance effects, due to the impact of single blocks, are visible in the pressure signal. Three main vibrating modes were found ($f_n \simeq 600$ Hz, $f_n \simeq 1000$ Hz and $f_n \simeq 1600$ Hz), probably depending on the impact application point with respect to the sensor centre. If these isolated impacts only affect the time-dependent pressure signal locally, their contribution to the total energy released by the avalanche is very significant ($\sim 65\%$).

For $t > 5$ s, where both velocity and pressure data were available, a preliminary interpretation showed that, at low velocity regimes, high pressures can still be exerted. Additionally, the drag coefficient C_d seems to increase when the Froude number Fr decreases. This confirms the observed behaviour from small-scale tests with grains and from full-scale tests at Col du Lautaret and Vallée de La Sionne.

Future perspectives

This thesis provided new results in terms of physical modelling of dense and powder-snow avalanches. A new full-scale experimental site was built and started collecting data on extremely large avalanche events.

Furthermore, this PhD research opens the path for various new challenges. Future perspectives are presented below.

Small-scale modelling of dense avalanches

The detailed study of the influence zone showed that a transition from a dead zone to a granular jump regime can occur during the flow-wall interaction. This result underscored the important role of the influence zone and the effect that the transition has on the flow behaviour as well as the force exerted on an obstacle. This study was conducted for a fixed slope of 31° , and it would be of great interest to extend this investigation to a larger range of slopes.

There are analytical models that calculate the force induced on an obstacle by a dense avalanche, but none of them take the dead zone to granular jump transition into account. More accurate analytical predictions could be obtained by implementing this new finding. Additionally, the influence of the obstacle geometry was investigated by using two different types of obstacles in laboratory experiments (catching-dam and breaking-mound-types). However, up until now, the analytical model developed to calculate the normal force acting on an obstacle is only valid in the case of a catching dam with a vertical uphill face. This model should be adapted to predict the force acting on a breaking-mound-like obstacle in order to compare the experimental results and the analytical prediction.

In order to adjust the model, a precise description of the influence zone shape is required. A laser technique was implemented on residual forces acting on the small obstacle. This technique provides a $3D$ reconstruction of the granular avalanche deposit. The preliminary results evidenced the potential of this method, although some discrepancies with experimental results still remain. Improvements should be made in order to obtain a powerful and reliable tool for measurements.

The data obtained were generally averaged and rounded, and the mean value was considered for the data interpretation. However, velocity and force signals in particular show fluctuations that were not analysed. Considering the discrete nature of granular flows, it would be interesting to carry out a specific analysis on the signal fluctuations. Finally, $2D$ discrete numerical simulations were conducted in order to reproduce a granular avalanche upon impact with a wall-like obstacle, and used for comparison with results obtained from the large obstacle. However, this type of modelling does not take into account lateral flows, as was the case for the small obstacle. Thus, discrete numerical simulations should be further developed in order to provide additional data for comparison and validation of the laboratory results.

Small-scale modelling of powder avalanches

The influence on the flow of two different types of obstacles was investigated. Two catching-dam-like obstacles were used: a dam with a vertical uphill face ($\alpha_{dam} = 90^\circ$ with respect to the terrain slope) and a dam with an inclined uphill face, $\alpha_{dam} = 32^\circ$. This angle corresponds to the natural angle of repose for an earth-filled dam and thus, from an engineering point of view, it represents a much simpler, low-cost solution for the construction of a dam. Results showed that the configuration with the inclined face has a lower influence on the dynamic of a

density current. We assume that there is a threshold angle, $32^\circ < \alpha_{dam}^{thr} < 90^\circ$, beyond which the obstacle's role becomes relevant (visible flow detachment from the surface). It would be interesting, for practical applications, to carry out more laboratory tests in order to identify this critical angle α_{dam}^{thr} . Attention should be focused on the influence that the uphill face angle, the local terrain slope, and the incoming flow velocity and density have on the threshold value.

We particularly stressed, throughout the entire thesis, the importance of the density parameter on the flow behaviour, on its dynamics and on all of the different types of snow avalanche modelling. A new method to measure the density of a small-scale aerosol avalanche was implemented, but it did not provide qualitatively reliable results. Although this type of measurement is precarious, density measurement techniques should be improved in order to provide models with proven values and to remove the significant assumptions influencing the accuracy of physical modelling. In fact, as previously discussed, the results issued from small-scale laboratory experiments are affected by a density distortion, due to the unmatched density requirement. As was previously done for prior research conducted in the water tank, numerical simulations of laboratory experiments should be implemented to correct this distortion and enable experimental results to be applied to reality.

Furthermore, the small-scale physical modelling of powder snow avalanches should continue and, in tandem to dense flows, a protection structure allowing lateral flows should be tested.

Lastly, as for the small-scale modelling of dense-snow avalanches, a mean-value approach was chosen for the study presented. Considering the turbulent nature of this type of flow, it could be of great interest to lead a different analysis focussing on the fluctuations of height and velocity signals to better understand the effects of turbulence on the flow dynamics.

The experimental site

The new full-scale experimental site of Taconnaz was equipped with pressure and velocity sensors on three breaking mounds, which are a part of the existing protection system. An avalanche occurred during the first winter season, but the system did not work. The second winter season provided the first recorded event. On December 29, 2010, the first data were recorded by sensors, showing that the acquisition system works. Last winter, two avalanches occurred but both of them stopped 1 m uphill from the first breaking mound, without reaching the obstacles. The first results were treated, but they remain scarce at the present time. Thus, the main perspective is based on the hope of having as many avalanches as possible throughout future seasons in order to expand the database. This would allow the research community to further the data interpretation.

Field height measurements on the incoming flow are not available at the current time. This parameter is crucial for calculating the Froude number and is thus also crucial for comparing the avalanches of Taconnaz to those observed on other full-scale experimental sites, as well as those obtained by small-scale laboratory experiments. Future site improvements should indeed provide for the installation of height sensors.

Application to the protection structure design

The force exerted on an obstacle remains a key parameter in the design process of avalanche protection structures. The present PhD work showed that this force is influenced by *(i)* a contribution proportional to the flow velocity (kinetic force), *(ii)* a contribution associated to the flow height (hydrostatic force), and *(iii)* a third contribution due to the weight of the quasi-static dead zone forming uphill from the obstacle and playing an important role in the overall force.

Even if this work provided some new results, the study of the dead zone, and on the influence zone associated with it, should continue. The role of the dead zone becomes important at low slopes, for low velocity regimes. The value of the C_d coefficient, introduced in Eq.(1.26), can greatly increase for low Froude numbers, which means high pressures despite the low velocities. Laboratory results showed this effect, and it was confirmed by data from the full-scale measurements. This must be taken into account when designing avalanche protection structures.

Another important process that must be considered consists of the dead zone to granular jump transition. At the moment, this transition was found experimentally for granular flows. Further works should investigate it through real-scale avalanches, and design procedures should include it.

A European guide published in 2009 provided some recent practical and theoretical developments aiming to update and enhance the protection design principles. Although this guide is based on a consistent dynamic representation of the flow behaviour, these two areas (role of the dead zone and dead zone to granular jump transition) are not taken into account and should therefore be included for future study.

Additionally, small-scale modelling of powder snow avalanches showed that a catching dam with an uphill face inclined at an angle $\alpha_{dam} = 32^\circ$ is less relevant to the dynamics of an aerosol flow than a dam with an uphill face normal to the terrain slope. This experimental configuration can easily occur in reality. As previously mentioned, this angle corresponds to the natural angle of repose for an earth-filled dam and thus represents an easier and less expensive design solution. Moreover, the deposit from a previous avalanche, stored uphill from the vertical wall, can form a ramp for a second incoming event. Thus, laboratory tests should study the influence of an inclined uphill face dam on the dynamics of a dense avalanche. From an engineering point of view, it would be also interesting to calculate the equivalent height of a dam with an inclined uphill face necessary for reaching the same effectiveness of a dam with a vertical uphill face.

Lastly, in order to apply the experimental results obtained in the small-scale water tank to real case studies, numerical simulations should be conducted to correct the density distortion affecting laboratory data.

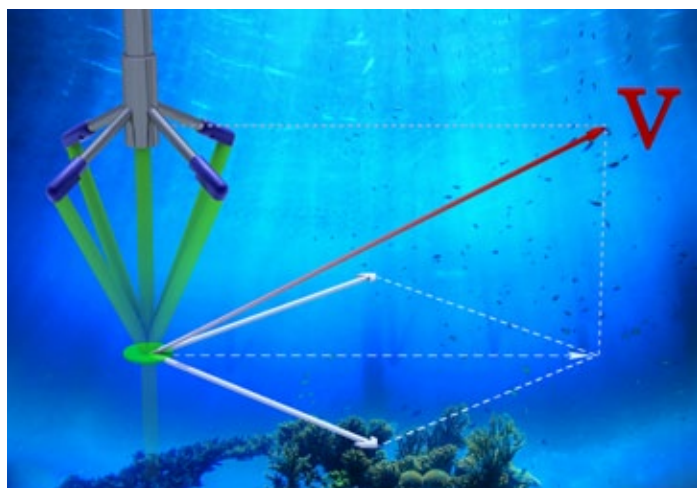
The initial aim of this thesis was to synthesise and reinforce the current understanding of the influence of an obstacle on the dynamics of an avalanche and the forces it induces. It is our hope that this work will contribute to furthering the improvement of future protection design against snow avalanches.

Annexe 1: Vectrino technical features

The Vectrino is a high-resolution acoustic velocimeter used to measure 3D water velocity in a wide variety of applications from the laboratory to the ocean in order to study rapid velocity fluctuations. The basic measurement technology is coherent Doppler processing, which is characterized by accurate data with no appreciable zero offset.

Vectrino

3D water velocity sensor
Lab Probe



The acoustic sensor has one transmit transducer and four receive transducers. The sampling volume is located away from the sensor to provide undisturbed measurements. Acoustic Doppler Velocimeters work by sending out a short acoustic pulse from the transmit element. When the pulse travels through the focus point for the receiver beams, the echo is recorded in each of the acoustic receiver elements. The echo is then processed to find the Doppler shift,



the scaling is adjusted with the measured speed of sound in the liquid (hence the temperature measurement), and the velocity vector is recorded or transmitted to a PC at a rapid rate. The Vectrino Lab Probe is used in a variety of laboratory applications for example in hydraulic laboratories to measure turbulence and 3D velocities in flumes and physical models.

CURRENT AND WAVE MEASUREMENTS IN THE OCEAN, LAKE AND LABORATORY

Nortek AS
Vangkroken 2
1351 Rud, Norway
Tel: +47 6717 4500
Fax: +47 6713 6770
E-mail: inquiry@nortek.no

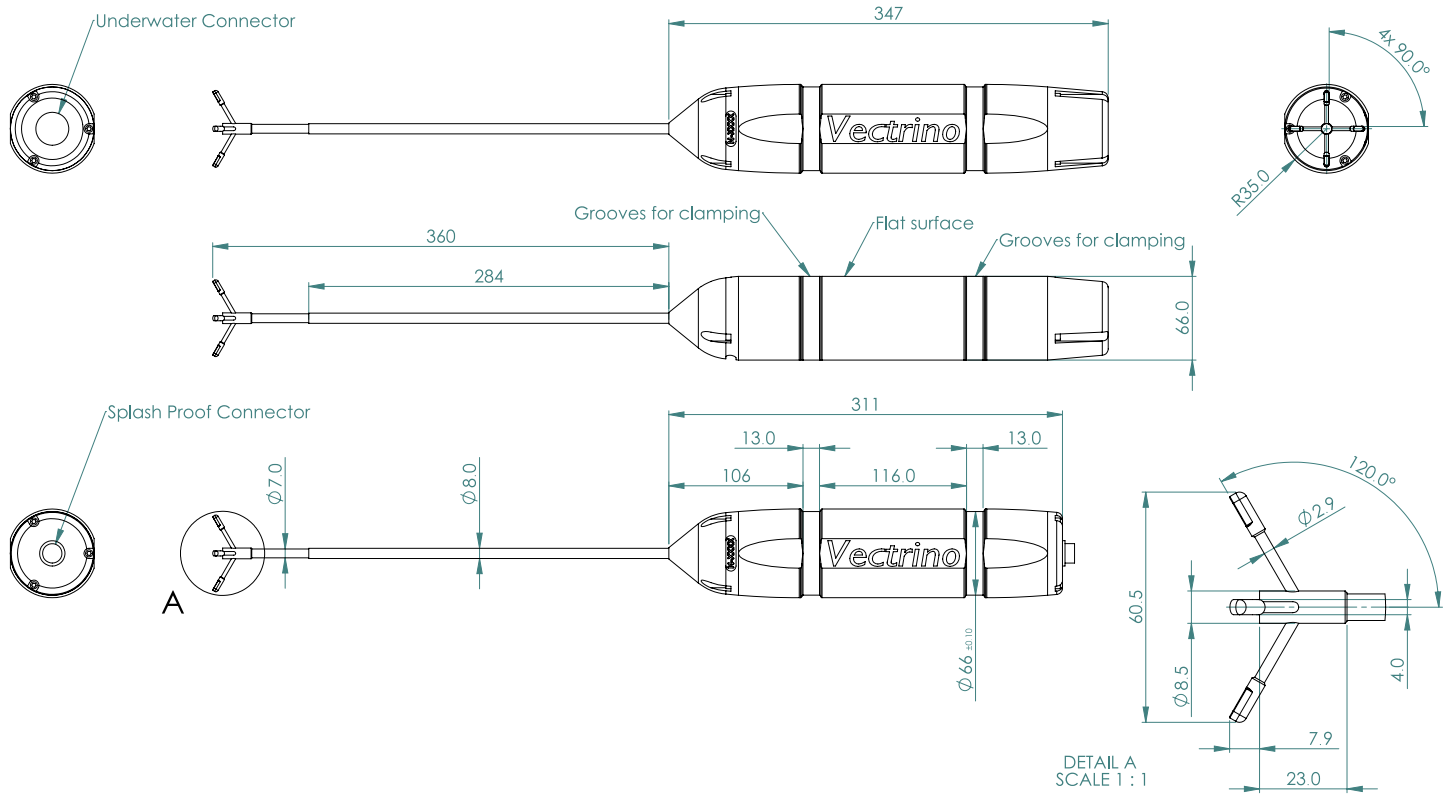


www.nortek-as.com

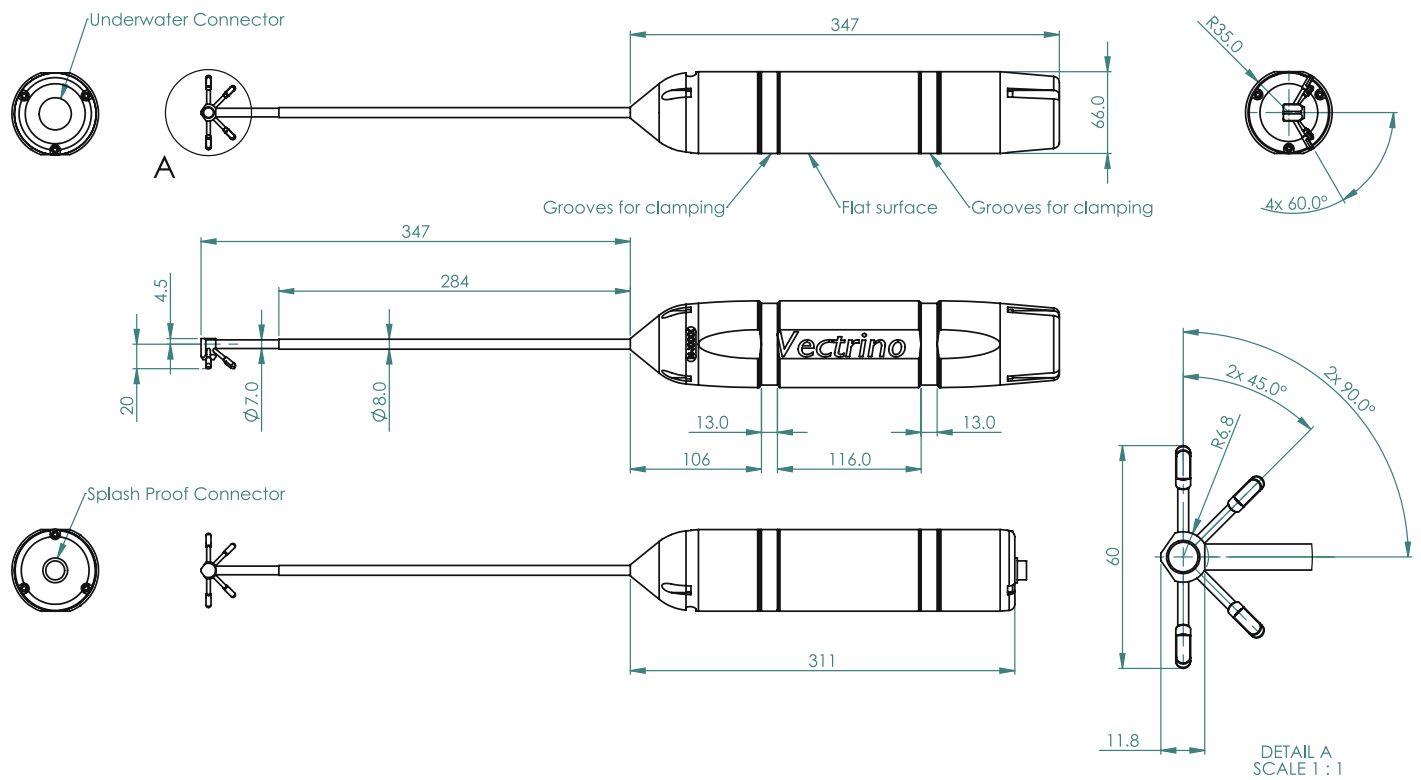
True innovation makes a difference



Vectrino 3D Downlooking, fixed stem



Vectrino 2D-3D Sideloooking, fixed stem



Water Velocity Measurements

Range:	±0.01, 0.1, 0.3, 1, 2, 4 m/s*(user selectable)
Accuracy:	±0.5% of measured value ±1 mm/s
Sampling rate (output):	1–25 Hz (standard firmware), 1–200 Hz (Plus firmware)

*) The velocity range is not the same in the horizontal and vertical direction. Please refer to the configuration software.

Sampling Volume

Distance from probe:	0.05 m
Diameter:	6 mm
Height (user selectable):	3–15 mm

Echo Intensity

Acoustic frequency:	10 MHz
Resolution:	Linear scale
Dynamic range:	25 dB

Sensors

Temperature:	Thermistor embedded in probe
Range:	–4°C to 40°C
Accuracy/Resolution:	1°C/0.1°C
Time response:	5 min

Data Communication

I/O:	RS 232. The software supports most commercially available USB–RS 232 converters.
Communication Baud rate:	300–115 200 Baud
User control:	Handled via Vectrino Win32® software, ActiveX® function calls, or direct commands.
Analog outputs:	3 channels standard, one for each velocity component.
Output range:	0–5 V, scaling is user selectable.
Synchronization:	SynchIn and SynchOut

Multi Unit Operation

Software:	Polysync
I/O:	RS 232–USB support for devices with 1, 2, 4, and 8 serial ports.

Software (“Vectrino”)

Operating system:	Windows®XP, Windows®7
Functions:	Instrument configuration, data collection, data storage. Probe test modes.

Power

DC Input:	12–48 VDC
Peak current:	2.5 A at 12 VDC (user selectable)
Max. consumption:	200 Hz 1.5 W



The Vectrino consists of two basic elements: the probe attached to a cylindrical housing and the processor inside the housing. From here the processed data is sent over a serial line or analog signals can be sent to an A/D converter.

Connectors

Bulkhead:	Splash proof connector or MCBH-12-FS, bronze (Impulse) – see also options below.
Cable:	Splash proof or PMCIL-12-MP – see also options below.

Materials

Standard model:	Delrin® housing, Stainles steel (316) probe and screws.
-----------------	---

Environmental

Operating temperature:	–4°C to 40°C
Storage temperature:	–15°C to 60°C
Shock and vibration:	IEC 721-3-2

Dimensions

See drawings on page 2-3 for dimensions	
Weight in air:	1.2 kg
Weight in water:	Neutral

Options

- Standard or Vectrino Plus firmware
- 4-beam down-looking probe or side-looking probe. Fixed stem or flexible cable
- 12-pin splashproof connector or Impulse 12-pin underwater connector
- 10, 20, 30 or 50 m cable with choice of splashproof or Impulse underwater connector
- RS 232–USB converter (one-to-one, four-to-one or eight-to-one)
- Combined transportation and storage case



NortekMed S.A.S.
Z.I. Toulon Est
BP 520
83 078 TOULON cedex 09
FRANCE
Tel: +33 (0) 4 94 31 70 30
Fax: +33 (0) 4 94 31 25 49
E-mail: info@nortekmed.com

NortekUK
Mildmay House, High St.
Hartley Wintney
Hants. RG27 8NY
Tel: +44- 1428 751 953
E-mail: inquiry@nortekuk.co.uk

NortekUSA
222 Severn Avenue
Building 14, Suite 102
Annapolis, MD 21403
Tel: +1 (410) 295-3733
Fax: +1 (410) 295-2918
E-mail: inquiry@nortekusa.com

青岛诺泰克测量设备有限公司
地址: 中国青岛香港西路65号
汇融广场1302
邮编: 266071
Tel: 0532-85017570, 85017270
Fax: 0532-85017570
E-mail: inquiry@nortek.com.cn

Nortek B.V.
Schipholweg 333a
1171PL Badhoevedorp
Nederland
Tel: +31 20 6543600
Fax: +31 20 6599830
email: info@nortek-bv.nl

Annexe 2: Caccamo et al., "Small-scale tests to investigate the dynamics of finite-sized dry granular avalanches and forces on a wall-like obstacle", Granular Matter (2012)

Small-scale tests to investigate the dynamics of finite-sized dry granular avalanches and forces on a wall-like obstacle

P. Caccamo · B. Chanut · T. Faug · H. Bellot ·
F. Naaim-Bouvet

Received: 9 March 2011
© Springer-Verlag 2012

Abstract Small-scale laboratory tests investigate the force from finite-sized granular avalanches on a wall. First, the reference flows, in absence of the wall, were analysed in a wide range of slopes from a minimum angle for which no flow is possible to a critical angle for which the flow becomes very dilute. The changes in thickness and velocity over time exhibit transitions at the minimum slope angle and at intermediate slopes. Then the normal force exerted on a wall spanning the flow was measured. It is notable that the transitions detected in reference flows had a direct effect on the force. The maximum force was equal to the kinetic force of the incoming flow at high slopes, whereas it scaled like hydrostatic force at lower slopes. This is the effect of the dense-to-dilute transition. Furthermore, the maximum force at low slopes was found to be several times greater than the hydrostatic force of the incoming flow. This finding is explained by the considerable contribution of the stagnant zone formed upstream of the wall. Furthermore, the jamming transition was highlighted at the avalanche standstill by the collapse of the residual force on the wall when approaching the minimum angle for which no flow is possible. These results are useful for the design of protection dams against rapid mass movements.

Keywords Granular · Avalanche · Obstacle · Force

P. Caccamo · B. Chanut · T. Faug (✉) · H. Bellot · F. Naaim-Bouvet
Irstea, UR ETGR, 2, rue de la Papeterie BP76,
38402 Saint Martin d'Hères, France
e-mail: thierry.faug@irstea.fr

P. Caccamo
e-mail: paolo.caccamo@irstea.fr

1 Introduction

The devastating effect of rapid mass movements such as dry landslides, rockfalls or snow avalanches can be reduced by placing protection structures that divert, slow down or stop the flow in the avalanche run-out zone. The design of such structures is still based on roughly accurate guides, based on practice rather than theory, even if recent practical and theoretical developments are available (see [1] for snow avalanches).

These full-scale natural flows generally involve granular materials. The granular behaviour of dry landslides or rock avalanches has already been emphasized and some quantitative studies have also proved that flowing snow is analogous to a granular material. First, the size distribution of snow aggregates in an avalanche deposit has been quantitatively analysed [2]. Second, it has been observed that steady and uniform snow flows are possible in a relatively wide range of slopes [3] and that the thickness of the deposit left by a snow avalanche strongly depends on the slope inclination [4], which is also typical of the behaviour of granular flows [5,6]. Finally, the velocity profiles over depth, measured in full-scale snow avalanches [7] or in controlled and steady snow chute flows [3], have a shape similar to those observed in granular mixtures [8].

Studies on the behaviour of gravity-driven granular flows using small-scale granular models (laboratory tests or numerical simulations) have been available for a long time [9–11]. The value of these studies for understanding this issue, and its perspectives [12–14], demonstrates the need for this growing research area [5,8,15,16]. Additionally, understanding the behaviour of such flows around obstacles [17–23] contributes to improving the design of protection structures in terms of shape, size and location in the avalanche run-out zone. Some studies have also investigated the force that granular flows

are likely to exert on obstacles (see, for example, [24–27]). The knowledge of this force is a crucial input in the design of resistant protection structures and reinforced buildings to prevent their collapse.

The present paper investigates small-scale laboratory tests on finite-sized granular avalanches overflowing a wall. For the sake of simplicity, and given the complexity of the flow-obstacle interaction, this study focuses on mono-disperse granular flows. Granular mixtures, involving various sizes of particles, interacting with an obstacle is a future challenge. The reference flows without obstacles are first investigated by measuring their thickness h and velocity U . In the second step, a wall spans the flow and the normal force F exerted on the obstacle is measured. A wide range of slopes is analysed from a minimum angle ϑ_{min} for which the avalanche flow comes to a standstill in absence of the wall up to a greater angle ϑ_c for which the avalanche flow becomes very dilute. This gaseous regime is characterized by the formation of a saltation layer making the definition of a continuous free-surface difficult. As a consequence, due to the features of the measurement techniques employed for this study, measurements on the flow thickness or velocity are not reliable for the saltation layer.

The detailed study of the $U(h)$ relation which governs the control flows, in absence of the wall, highlights two regime transitions: (i) when approaching the minimum angle ϑ_{min} , a jamming transition is clearly detected, and (ii) above the angle ϑ_{max} , relatively smaller than ϑ_c , a dense-to-dilute transition occurs. These two transitions are compatible with the three regimes classically observed for steady granular flow conditions: the quasi-static regime, the dense-liquid regime and the dilute-gaseous regimes [15,28]. It is then remarkable to observe the effect of the dense-to-dilute transition on the force exerted on the obstacle. The maximum force is equal to a purely kinetic force, proportional to the velocity squared, above ϑ_{max} for which the dense-to-dilute transition is observed. Below ϑ_{max} , it scales as the hydrostatic force, proportional to the flow thickness, but it remains several orders of magnitude greater than the typical hydrostatic force. Analysing the residual force allows us to highlight the crucial contribution of a stagnant zone formed upstream of the wall which depends on the incident flow regime. The results from channelized laboratory flows, presented in this paper, agree with previous 2D discrete numerical simulations of finite-sized avalanche flows past a wall [25].

The paper is organized into four parts. First, the experimental device is described. Section 3 gives details on the measurement techniques. Then the main experimental results are provided. The changes over time of the flow depth, the velocity and the force on the wall are analysed. In particular, the maximum values of these avalanche variables are considered to validate existing scaling laws and for data analysis.

Section 5 is devoted to data interpretation (in terms of regime transitions) and the conclusion.

2 Experimental approach

2.1 The device

The experimental device, as shown in Fig. 1, consists of an inclined plane on which a channel of variable width has been mounted. The side walls are made of plexiglas. The channel is 1.3 m long and the width is fixed at 0.25 m for the tests presented in this paper. On top of it, a reservoir stores the granular material which is released by opening a gate. The selected material consists of a constant mass of 9.2 kg of glass beads (the particle density is $\rho_P = 2,450 \text{ kg m}^{-3}$ and the mean diameter is $d = 1 \text{ mm}$). This material has been characterized with the function $h_{stop}(\vartheta)$, as done in [6]. Specific tests were carried out: a finite volume of granular material was released and a deposit was observed along the plane. The function $h_{stop}(\vartheta)$ (see Fig. 2) corresponds to the deposit height left by the avalanche which depends on

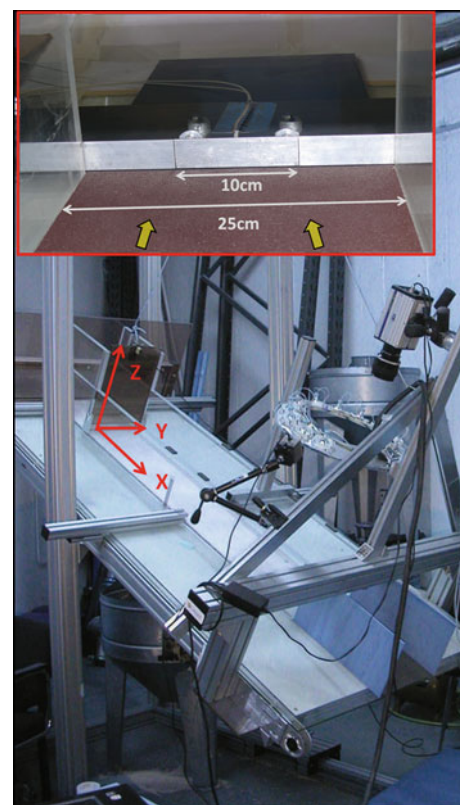


Fig. 1 Experimental device overview. The *insert* shows the wall-like obstacle: the central 10 cm are connected to the force sensors and not in contact with the rest of the structure. *Yellow arrows* indicate the direction of the incoming flow (colour figure online)

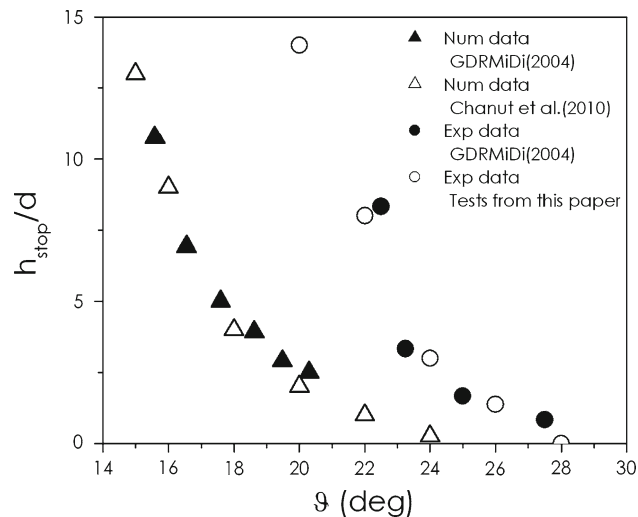


Fig. 2 Function h_{stop} : deposit thickness left by the avalanche versus the slope angle ϑ for 2D numerical (open triangle) and 3D experimental (open circle) flows [25,26]

the slope angle. ϑ_{min} is the angle for which h_{stop} tends to an infinite value and ϑ_{max} is the angle for which h_{stop} tends to zero. ϑ_{min} and ϑ_{max} refer to the effective friction coefficients associated with quasi-static deformation and rapid collisional flows, respectively. For experimental conditions (glass beads in motion and sandpaper bottom roughness), ϑ_{min} and ϑ_{max} were found to be close to 20° and 28° , respectively.

After the material was characterized, granular avalanches were investigated. The avalanche time-varying variables of interest are: the flow depth $h(t)$, the velocity $U(t)$ and the force $F(t)$ exerted on an obstacle. A laser and a high-speed video camera were used to measure the flow height. The video camera was also used to determine the velocity at the flow surface. An obstacle can be added at the end of the channel to measure the force induced by the granular avalanche. The obstacle, as shown in the insert in Fig. 1, consists in a flat steel beam, 2.5 cm high, normal to the bottom and to the main flow direction. The obstacle obstructed the whole width of the channel (25 cm). However, only the ten central centimetres were connected to force sensors in order to avoid problems related to vibrations and resonance frequencies. Details of the measurement techniques are given in Sect. 3.

2.2 Repeatability and experimental measurements

The repetition of the same test, in the same conditions, should theoretically give the same output. However, due to uncontrolled experimental conditions (air temperature, humidity, etc.), a random error constantly affects the results. To minimize this error, each test was repeated five to ten times at

constant parameters and the averaged value was retained and finally used for data treatment. This approach is reliable if the distribution of the data's standard deviation is Gaussian. Preliminary tests proved that the distribution was Gaussian. Henceforth, the values presented will always represent the average of five to ten tests performed in the same experimental conditions. However, particular attention was needed on the residual force measurement corresponding to when the flow stopped. In fact, it was noted that this configuration case was particularly sensitive to the above-cited uncontrolled experimental conditions.

3 Flow depth, velocity and force measurements

Tests on granular avalanches flowing down the channel without any obstacle were performed first. Measurements on this kind of flow will be called *reference measurements*. The evolution of flow depth and velocity over time was studied to characterize the avalanche dynamics. Then an obstacle was mounted and force measurements were taken. Both types of test were performed for a wide range of slope angles from 21° (close to ϑ_{min} , the angle below which no flow is possible) to 33° (larger than ϑ_{max}). The results will be presented in Sect. 4. This section describes the measurement techniques and their precision.

3.1 Flow depth

Flow depth measurement were taken using a laser line deflected by the incoming flow (a similar technique to that shown in [6]). A high-speed video camera, perpendicular to the channel bottom, recorded the line displacement at a frequency ranging from 150 fps (low slopes) to 350 fps (higher slopes). The laser line deflection Δ was proportional to the flow height h . An accurate calibration was needed to relate Δ and h , which was made using three standard plates of constant thickness (8 mm) combined together in order to calibrate in the thickness range of 0–24 mm, which corresponds to the typical depths of the released avalanches. The precision decreases with the dilution rate. It is difficult to evaluate this precision for very dilute flows. For rather dense flows, it was estimated at less than $0.5d$.

3.2 Flow velocity

Velocity measurements were taken using the particles image velocimetry (PIV), as previously done in [21,29]. Using a high-speed video camera (up to 350 fps) fixed normal to the flow surface, it is possible to analyse a selected view area (a $10 \times 10 \text{ cm}^2$) and to obtain the change over time of the surface velocity in this area. Image sequences were treated

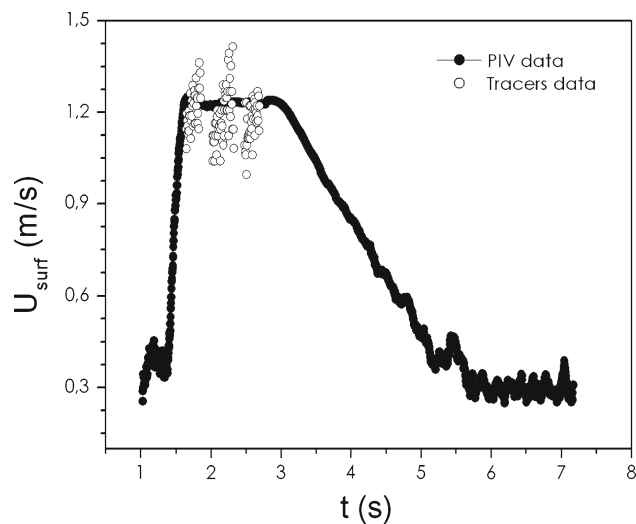


Fig. 3 Surface flow velocity versus time for $\vartheta = 28^\circ$. The black dotted line represents PIV measurements, whereas blank circles are the result of the tracer validation

using a Matlab routine which calculates the mean surface velocity field by finding the maximum of the cross-correlation between regions of the image. These velocity measurements were made at $1.3\text{ m} (=1,300d)$ downstream from the reservoir gate, central with respect to the channel axis. In order to validate values from the PIV method, tests were performed by adding tracers at the surface of the flow. The flows were recorded with a 25-fps video camera and the tracers' velocity derived with a simple image-processing program (Avistep). The results appear to be quantitatively consistent, as shown in Fig. 3 (an example is given for $\vartheta = 28^\circ$). The PIV method's precision was estimated at 0.01 m s^{-1} . The results obtained for flow velocity are presented in Sect. 4.2. They only concern the flow velocity over time along the x -axis. In fact, the tests showed that, with the experimental set-up adopted, the velocity component transversal to the main direction of the flow was negligible with respect to the longitudinal direction. This is probably due to the fact that the flow is canalized. Under certain circumstances, the formation of eddies was observed [30]. We did not note this type of phenomenon during the experiments.

A cross-channel velocity profile (y -axis direction) is additionally given in Fig. 4 for some of the investigated slopes. The curves show that, in the ten central centimetres, the velocity profile is nearly uniform and therefore the side-wall effect negligible.

3.3 Force

Normal force measurements were taken using two force sensors connected to the central part of the obstacle (10 cm wide). Preliminary tests with a 25-cm-wide obstacle showed that

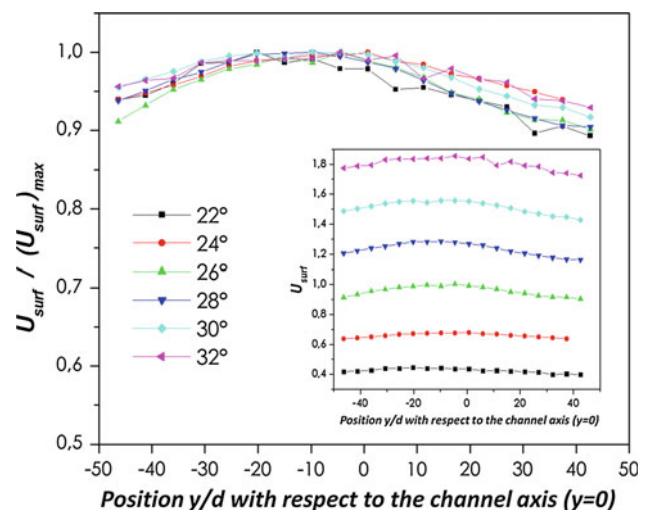


Fig. 4 Cross-channel velocity profiles (y -axis direction). The velocity profiles are nearly uniform and thus the side-wall effect is negligible. Note that the ten central centimetres of the channel correspond to the measurement area

the proper frequencies of the incoming flow could generate vibrations in the obstacle, preventing reliable measurements. Decreasing the width of the wall from 25 to 10 cm allowed us to increase the vibration frequency of the wall, preventing resonance problems. When the avalanche impacts the obstacle, the two *XFTC300* sensors measure a voltage value U_0 [V] at a frequency of 1 kHz. Load cells can exhibit residual voltage even without an applied force. This was systematically considered as an offset and removed in order to derive the actual force values. The offset was constant for all the tests at a given slope.

An accurate calibration is necessary to derive force values from voltages. Calibration consisted in applying well-known forces to the obstacle and relating them to the voltage values given by the sensors. First, the obstacle was positioned horizontally and six weights were loaded one on top of the other and off-loaded one by one. This procedure was repeated at six positions all along the upstream face of the obstacle. The load/unload cycle was tested to determine potential hysteresis effects. The results show that this kind of effect can be considered negligible (see Fig. 5). Two different types of validation tests were carried out to check the reliability of the calibration procedure. A well-known force was applied and we checked whether the force value given from the system corresponded to the expected value. Both methods are based on this principle. For the first one, the obstacle was removed from the channel and repositioned horizontally (as for the calibration procedure). For the second one, the obstacle was maintained in the position corresponding to the avalanche experiments, and the weights were hooked on it. The maximum gap obtained between the measured and expected value, for a minimum calibration force of 0.65 N, was 21 mN, corresponding to a 3% error.

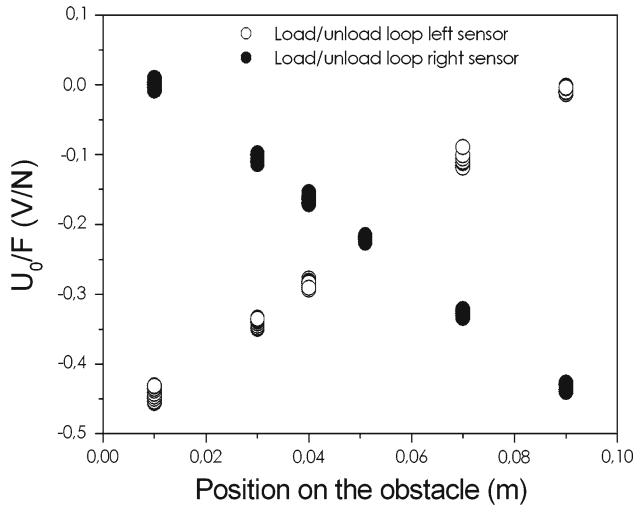


Fig. 5 Voltage U_0 over the force F versus the position on the obstacle. Load/unload cycles represent the calibration procedure for force sensors. No hysteresis effects are found

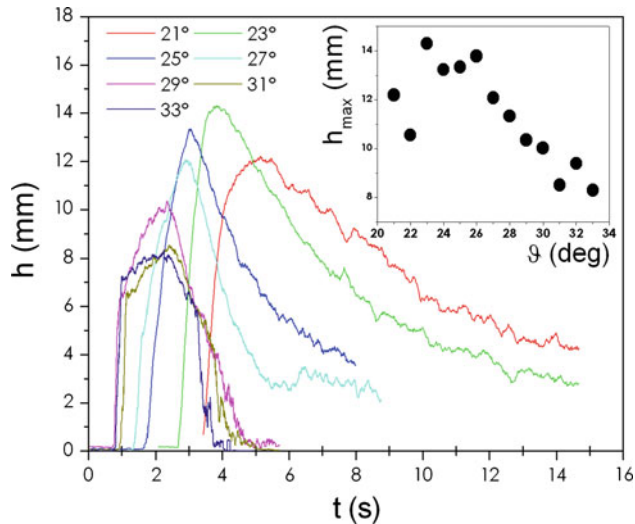


Fig. 6 Reference measurements: flow height h versus time t . The insert shows the maximum values of h versus the slope angle ϑ

4 Experimental results

4.1 Flow depth

Figure 6 shows the flow height h versus time t (moving average on 30 points). Generally the $h(t)$ signal displayed three main phases: (i) a rapid increase in height corresponding to the avalanche front, (ii) a maximum value and finally (iii) a relatively slow decrease corresponding to the avalanche tail.

The influence of the slope is clearly visible: the higher the slope the lower the maximum measured flow height (see insert in Fig. 6). Moreover, when ϑ increased, the increasing phase profile and the decreasing phase profile became

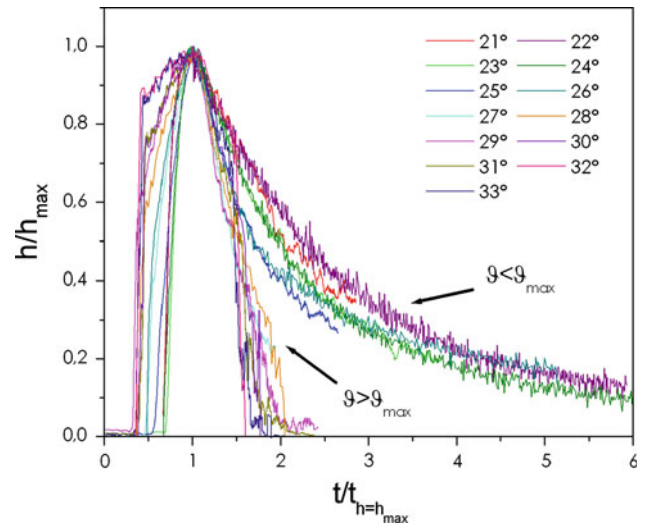


Fig. 7 Flow depth normalized by the maximum value h/h_{max} versus $t/t_{h=h_{max}}$. $t_{h=h_{max}}$ is the time corresponding to the maximum height

steeper, the avalanche arrival time shortened and the flow duration decreased. For $\vartheta = 21^\circ$, the trend was peculiar because the angle approached ϑ_{min} : the friction forces at the bottom of the channel (and side-wall effects) became significant which decreased the discharge when moving away from the reservoir gate (the material was stored upstream). This jamming transition explains the drop in maximum height when approaching ϑ_{min} and will be analysed in detail in Sect. 5.2.2.

Figure 7 shows the flow depth normalized by the maximum value h/h_{max} versus $t/t_{h=h_{max}}$, where $t_{h=h_{max}}$ is the time corresponding to the maximum height. The curves (particularly the decreasing phase) collapsed into two main groups, highlighting the transition between two regimes occurring at ϑ_{max} . This transition will be discussed in detail in Sect. 5.1.

4.2 Velocity

Figure 8 shows the surface velocity U versus time t (moving average on 30 points). $U(t)$ signals present three phases (increase, maximum and decrease) as is the case for the $h(t)$ signals. However, above a critical slope close to ϑ_{max} a plateau is observed.

The maximum velocity increases rather linearly with the slope, as shown in the insert in Fig. 8. Differently from the curve $h_{max}(\vartheta)$, the jamming transition is not visible here.

Figure 9 shows the flow velocity normalized by the maximum value U/U_{max} versus $t/t_{U=U_{max}}$, where $t_{U=U_{max}}$ is the time corresponding to the maximum velocity. As for flow depth results, two groups of curves are clearly identified for $\vartheta < \vartheta_{max}$ and $\vartheta > \vartheta_{max}$ (see Sect. 5.1).

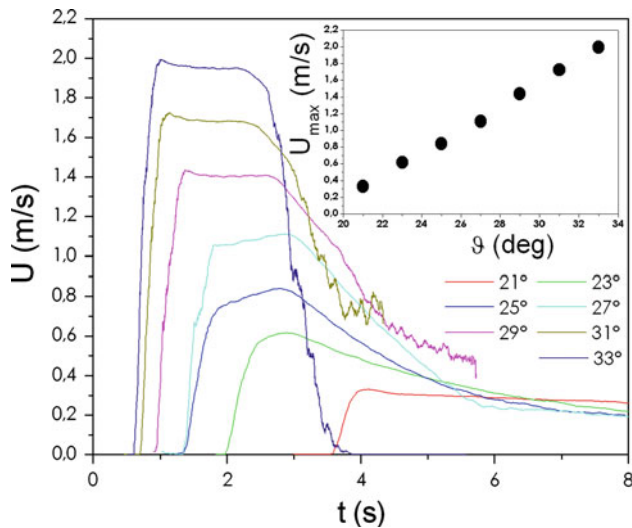


Fig. 8 Reference measurements: surface flow velocity U versus time t . The *insert* shows the maximum values of U versus the slope angle ϑ

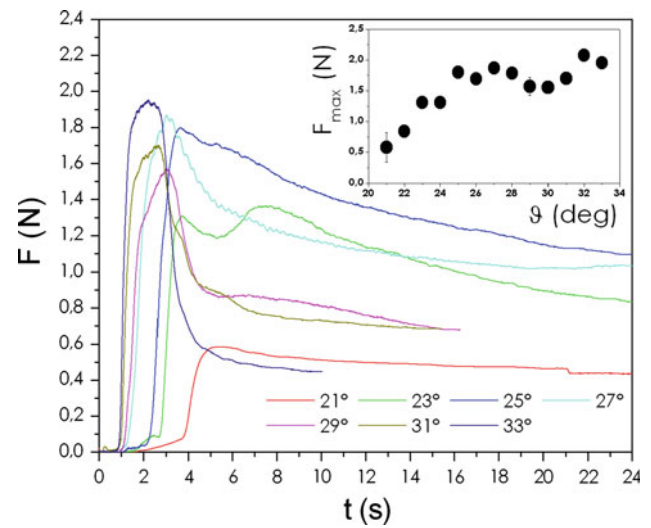


Fig. 10 Mean force F versus t . The *insert* shows maximum F values versus ϑ . Measurements were taken at a distance $x = 1,300d$ from the releasing gate

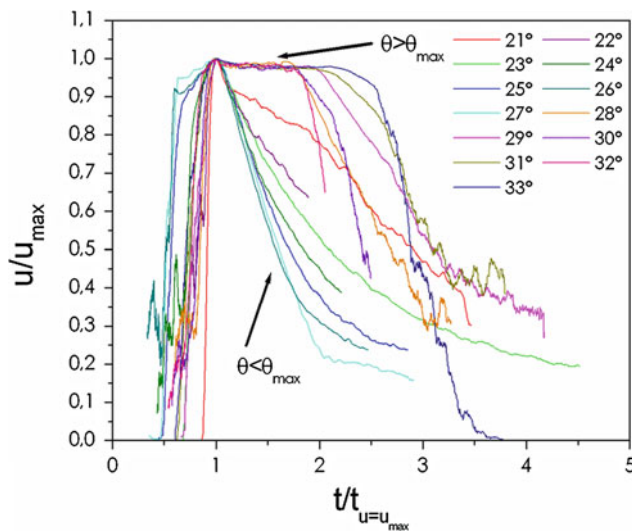


Fig. 9 Surface flow velocity normalized by the maximum value U/U_{max} versus $t/t_{U=U_{max}}$. $t_{U=U_{max}}$ is the time corresponding to the maximum height

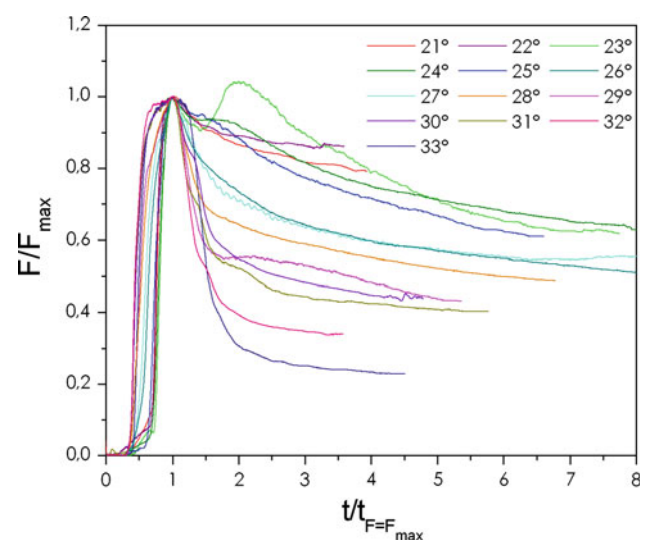


Fig. 11 Mean force normalized by the maximum value F/F_{max} versus $t/t_{F=F_{max}}$. $t_{F=F_{max}}$ is the time corresponding to the maximum height

4.3 Force

Figure 10 shows the force F versus t (moving average on 100 points representing 0.1 s). The $F(t)$ signals presented three phases (increase, maximum and decrease) as for the $h(t)$ and $U(t)$ signals. A residual force F_{res} , caused by the presence of the final deposit stored upstream the obstacle, was observed for all slope inclination values. This force F_{res} is the result of a complex competition between the material weight P (which tended to increase F_{res} when P increased) and the friction force F_f mobilized at the base (which tended to decrease F_{res} when F_f increased). Our data show that F_{res}

displays a maximum for intermediate slopes: this is an effect of the jamming transition (see Sect. 5.2.2).

The insert in Fig. 10 shows the maximum force F_{max} versus ϑ . The maximum force drops sharply when approaching ϑ_{min} .

Figure 11, shows the force normalized by the maximum value F/F_{max} versus $t/t_{F=F_{max}}$, where $t_{F=F_{max}}$ is the time corresponding to the maximum force. From these curves it is interesting to extract the values of F/F_{max} after the maximum. Figure 12 shows F/F_{max} at $t/t_{max} = 2$ and at $t/t_{max} = 3$. Both curves behave similarly and show that low slopes mobilize huge forces even after the maximum, whereas the force decreases sharply at higher slopes.

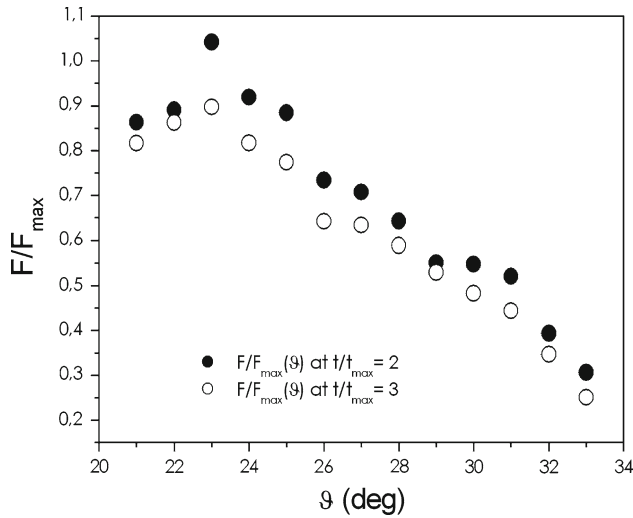


Fig. 12 The F/F_{max} signal versus the slope angle ϑ at different values of $t/t_{h=h_{max}}$

5 Discussion and conclusion

5.1 Flow-depth and velocity data interpretation

The finite-sized avalanche flows investigated in this paper are unsteady and non-uniform flows. A scaling law giving the depth-averaged velocity \bar{U} as a function of the flow depth h in steady and uniform flow conditions was formulated for dense flows [5,6]:

$$\bar{U} \propto h^{3/2}(\tan \vartheta - \tan \vartheta_{min}) \tag{1}$$

Only maximum values, which might correspond to a quasi-steady state, are taken into account. Figure 13 shows $U(h_{max})$ versus $h_{max}^{3/2}(\tan \vartheta - \tan \vartheta_{min})$. The scaling law is clearly verified for $\vartheta_{min} < \vartheta < \vartheta_{max}$. Above ϑ_{max} the regime changes completely and it cannot be reproduced by the scaling law. In the insert of Fig. 13 the Froude number Fr is drawn compared to h_{max}/h_{stop} . As found for the steady and uniform regime [6], Fr and h_{stop} are linearly correlated. However, the linear fit does not match the data very well. This discrepancy can be attributed to the unsteady flow state and the high Froude number values (with respect to the data in [6]).

The relation between flow depth and velocity data was analysed in greater detail by studying the behaviour of the $U(h)$ relation for each slope tested by hiding time t . A power-law relation $U = Ch^\alpha$ was considered to fit the flow velocity U as a function of its height h plotted in Fig. 14 (example for 23°). A hysteresis phenomenon can be clearly observed between the front and the tail. Figures 6, 7, 8, 9, 10, 11 and 14 show how an avalanche parameter (flow depth or velocity) evolves over time at a given position (Eulerian approach). These graphs show changes in behaviour corresponding to the horizontal structure of the avalanche flow: front, body and

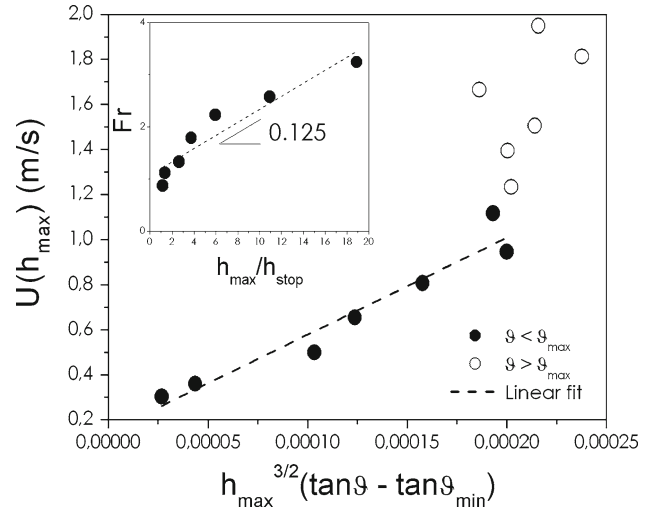


Fig. 13 A scaling law representation showing the maximum velocity $U(h_{max})$ versus $h_{max}^{3/2}(\tan \vartheta - \tan \vartheta_{min})$ for all the slopes investigated. The insert shows the Froude number Fr versus the maximum flow depth h_{max} normalized by the corresponding h_{stop} value within the range $[\vartheta_{min}; \vartheta_{max}]$. Note that the slope of the best-fit line is equal to 0.125, a value which is close to the value given in [6] for steady and uniform flows

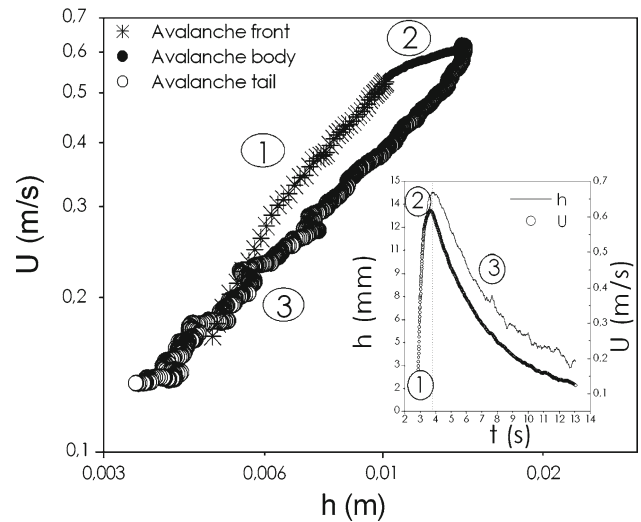


Fig. 14 Mean flow velocity U versus the flow depth h . An example case for $\vartheta = 23^\circ$. The insert reports U and h values versus time t

tail. The word *phase* will systematically define each of the three components of the avalanche. These phases are well represented in Fig. 14. As the avalanche front (phase 1 in Fig. 14) is very dilute, only the body (phase 2) and the tail (phase 3) were considered. For each slope tested, the α coefficient was systematically estimated. Figure 15 shows α versus the slope angle. Data from the avalanche body reached values close to $1/2$ for slopes lower than ϑ_{max} and, beyond this critical angle, the body became too dilute and the measurements were no longer reliable. Data from the avalanche tail highlight a transition occurring around ϑ_{max} : for lower

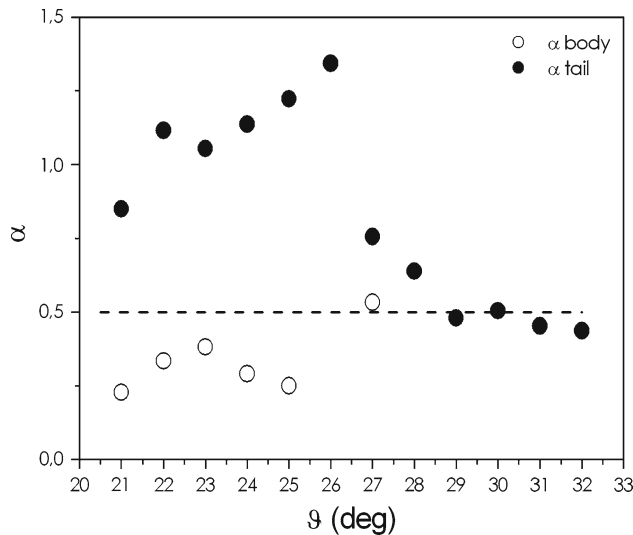


Fig. 15 α values from the power relation $U = Ch^\alpha$ for the avalanche body (open circle) and tail (filled circle) versus the slope angle ϑ . Note that for $\vartheta = 33^\circ$, the value of α for the avalanche tail was found to be equal to 2.7 (large value not shown here), which might indicate a transition to a dilute-gaseous regime

angles, α varies between 1 and 1.5, while it stabilizes around $\alpha = 1/2$ when ϑ exceeds ϑ_{max} . Even if the avalanche regime is unsteady and non-uniform, the α values obtained are reminiscent of well-known steady flow regimes.

On the one hand, a dense frictional regime can be described by a constant inertial number $I \propto Fr \frac{d}{h}$ implying $U \propto h^{3/2}$ as found for the avalanche tail at low slopes. On the other hand, a rapid dilute regime can be characterized by a constant Froude number implying $U \propto h^{1/2}$ which corresponds to the scaling found for the avalanche tail at high slopes and for the avalanche body. It should be noted that, near the flow bottom, above ϑ_{max} , the behaviour of a dense granular flow on a rough incline can resemble a flow on a flat base ($U \propto h^{1/2}$) [31]. However, if the latter case is associated with actual slipping, one may expect that the dilute flow on a rough bottom (above ϑ_{max}) will fluidize, leading to an apparent sliding velocity.

All these results highlight a transition from a dense frictional regime to a more dilute one. This transition has already been observed but its theoretical description remains a serious challenge ([15] and references therein). The next section presents the effect of this transition on the avalanche force induced on the wall-like obstacle.

5.2 Force data interpretation

5.2.1 Maximum force: dense-to-dilute transition

The two regimes mentioned above can be described by the following typical forces:

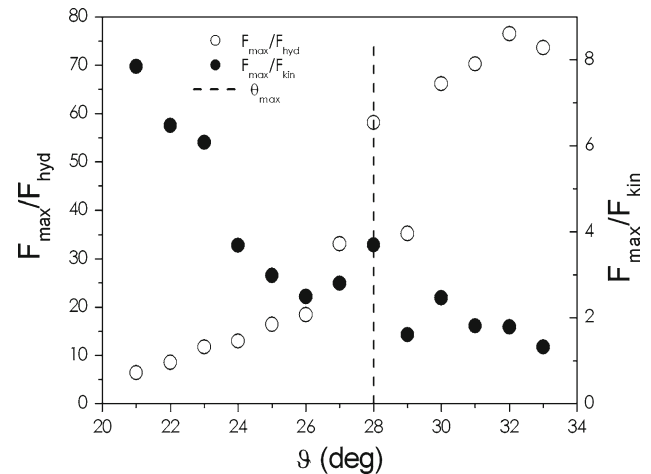


Fig. 16 F_{max}/F_{kin} and F_{max}/F_{hyd} ratios versus ϑ

$$F_{hyd} = \frac{1}{2} \phi(t) \rho_P g h^2(t) l_{obs} \cos \theta \tag{2}$$

$$F_{kin} = \frac{1}{2} \phi(t) \rho_P U^2(t) h(t) l_{obs} \tag{3}$$

where $\phi(t) \rho_P$ corresponds to the bulk density, l_{obs} is the obstacle length (y-axis direction) and all the time-dependent parameters have been considered at $t = t_{h=h_{max}}$. Equation (2) corresponds to the hydrostatic force, relevant in the dense frictional regime for which the force is likely to be driven by the flow weight related to its depth h . Equation (3) corresponds to the kinetic force, which is relevant in flow regimes for which the force is likely to be driven by the kinetic energy related to the velocity squared U^2 . This is the case for the dilute flows and also for dense flows at a high Froude number. To derive these two typical forces, it is necessary to estimate the depth-averaged volume fraction $\bar{\phi}$ (not measured in our experiments). The scaling law giving $\bar{\phi}$ versus I [5, 15] for stationary regimes was used as a first approximation:

$$\phi(I) = \phi_{max} + (\phi_{min} - \phi_{max}) I \sqrt{\bar{\phi}} \tag{4}$$

The depth-averaged volume fraction $\bar{\phi}$ was calculated by solving the above implicit equation considering the typical values $\phi_{min} = 0.4$ and $\phi_{max} = 0.6$, on the basis of the depth-averaged inertial number \bar{I} :

$$\bar{I} = \frac{5}{2\sqrt{\bar{\phi}}} \quad Fr \frac{d}{h} = \frac{5\bar{u}d}{2h\sqrt{gh\bar{\phi} \cos \vartheta}} \tag{5}$$

Figure 16 shows the normalized forces F_{max}/F_{kin} and F_{max}/F_{hyd} . Both curves depict the dense-to-dilute transition around ϑ_{max} . For high slopes, the F_{max}/F_{kin} ratio tends to 1, meaning that the force is purely kinetic: $F \simeq \frac{1}{2} \phi \rho_P U^2 h$. When approaching ϑ_{min} , the F_{max}/F_{hyd} ratio remains much greater than 1. At $\vartheta = 21^\circ$, the force is roughly five to six times the typical hydrostatic force of the incoming undisturbed flow. Another contribution plays a dominant role in

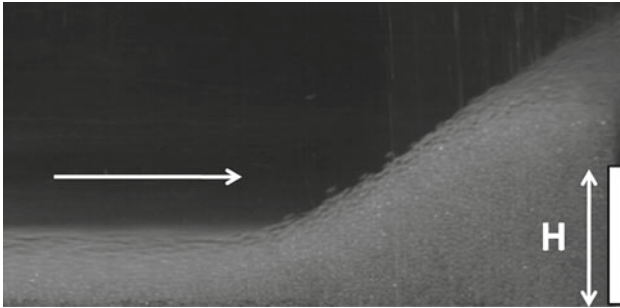


Fig. 17 Stagnant zone occurring upstream of the obstacle. The white horizontal arrow indicates the incoming flow direction. A quasi-static triangular zone forms and the inertial flow starts flowing above

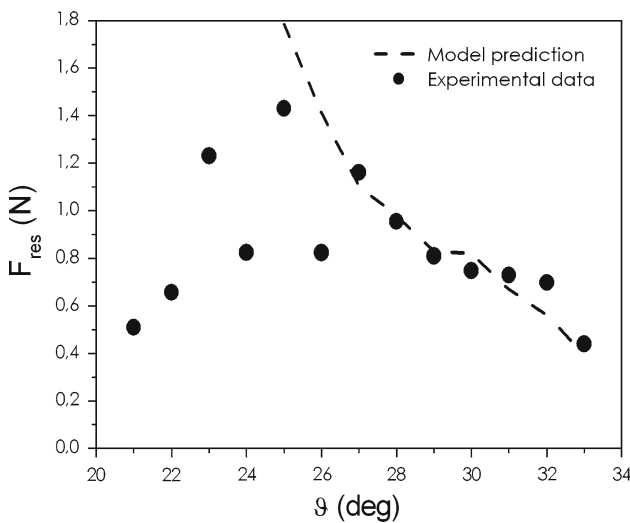


Fig. 18 Residual force F_{res} (measurements at $t = 10$ s) versus the slope angle ϑ . Black data points represent experimental results while the dashed line connects data obtained from Eq. (6) with $\mu = \tan \theta_{min}$ ($\mu \simeq 0.36$). Note that the measurement of F_{res} (average value of five to ten tests) is tedious because it is very sensitive to uncontrolled experimental conditions (day conditions) for angles below ϑ_{max}

the total force, caused by the presence of the stagnant zone upstream of the obstacle, as is shown in Fig. 17.

These results qualitatively fit well with those obtained in previous studies [25, 26] based on 2D discrete numerical simulations (see Fig. 7 in [25]). Cross-comparing in detail the discrete numerical simulations (2D) and the experiments presented here (confined 3D flow) is beyond the scope of this paper.

5.2.2 Residual force: jamming transition

In this section the residual force is discussed. The total signal duration strongly depends on the slope inclination. The lowest value is about 10 s for the highest slope (see Fig. 10). The residual force was arbitrarily assumed as the force at $t = 10$ s. Figure 18 shows the measured residual force F_{res}

versus the slope angle ϑ . F_{res} increases when decreasing the slope and it drops when approaching ϑ_{min} . A first qualitative explanation arises from the experimental observation. At low slope inclinations, the final deposit spreads across the channel up to the reservoir. Friction plays an important role, reducing the deposit weight acting on the obstacle. On the other hand, for high slopes, most of the bead volume goes past the structure, the final deposit is small and the force that it can exert decreases when increasing the slope. As a consequence, intermediate slopes exhibit a maximum of residual force.

A simple model based on the equilibrium between the weight $P = c\phi\rho_p g L H_{obs} \sin \vartheta$ and the basal friction $F_f = \mu c\phi\rho_p g L H_{obs} \cos \vartheta$ describes the decrease of the residual force with the slope angle beyond ϑ_{min} :

$$F_{res} = c\phi\rho_p g L H_{obs} (\sin \vartheta - \mu \cos \vartheta), \tag{6}$$

where c represents a shape coefficient, L the dead zone length experimentally measured, H_{obs} the obstacle height and μ the basal friction coefficient. The volume fraction for the deposit was assumed to be equal to $\phi_{max} = 0.6$.

The value of the shape coefficient c was derived from an accurate analysis of the stagnant zone behaviour at a fixed slope of 31° [32]. This analysis showed that the final deposit shape is trapezoidal. As a consequence, the shape coefficient was taken equal to 0.66. The basal friction coefficient μ was considered equal to $\tan(\vartheta_{min})$ ($\mu \simeq 0.36$), which typically characterizes a standstill condition (quasi-static deformation). This simple model predicts the residual force well for high slopes, whereas it fails close to ϑ_{min} . At angles close to ϑ_{min} , we observed a deposit all along the channel up to the reservoir and that almost no material had overflowed the obstacle. The length of this deposit, and the resulting residual force, appear to be very sensitive to certain uncontrolled experimental conditions. The velocity at which the gate is opened, the ambient humidity rate and the state of bottom roughness (due to its degradation) are some of these parameters influencing the residual force. Thus, the assumption is to attribute it to unstable states when approaching ϑ_{min} . As Eq. (6) is supposed to work in the case of geometrical catching due to the obstacle, it cannot take into account the additional friction effect related to h_{stop} , within the range $[\vartheta_{min}; \vartheta_{max}]$. The gap between the model prediction and experimental data emphasizes that this effect becomes dominant at the jamming transition.

5.3 Conclusion and outlook

The present paper investigated finite-sized granular avalanches over-topping a wall-like obstacle using small-scale laboratory tests. From reference flows in absence of obstacles, we highlighted the dense-to-dilute transition occurring at the angle ϑ_{max} , which is the critical angle for which

$h_{stop}(\vartheta)$ tends to zero. In particular, a change in the $U(h)$ relation was observed at ϑ_{max} . In the second step, the normal force on the wall was analysed and found to be driven by the incoming flow regime, as expected. Dilute avalanches above ϑ_{max} displayed a maximum force equal to a purely kinetic force proportional to the velocity squared, whereas dense avalanches below ϑ_{max} displayed a maximum force proportional to the typical flow depth, but several times greater than the hydrostatic force of the incoming undisturbed flow. This last finding was explained by the presence of a large stagnant zone formed upstream of the wall and enhancing the force on the wall. However, the physical process is complex because of a competition between the weight of the stagnant zone and its friction with the rough bottom and the channel lateral walls. As a consequence, the contribution of the weight of the stagnant zone can be reduced if the basal friction is significantly increased. This process typically occurred when the flow came to a standstill at low slope inclinations. Indeed, it is possible to observe that the residual force due to the motionless material stored upstream of the wall increases when decreasing the slope and sharply drops when approaching the minimum angle ϑ_{min} , which is the critical angle for which $h_{stop}(\vartheta)$ tends towards infinite (effect of the jamming transition).

Similar transient flows around a wall-like obstacle were previously studied using discrete numerical simulations [25] but in 2D dimensions. Cross-comparing the experimental data from the laboratory confined chute and the 2D numerical data from [25] was beyond the scope of the paper. However, it can already be noted that the results in terms of the maximum forces scaled by the typical forces of the incoming flow are qualitatively in very good agreement. The dense-to-dilute transition and its direct influence on the force scaling were also observed with discrete numerical simulations [25].

It is important to note that this study focused on the *granular dead zone* process. This consists of a quasi-static dead zone forming upstream of the obstacle (motionless grains), which coexists with an inertial layer flowing above. Here the free surface upstream of the obstacle varies smoothly, whereas a discontinuity in flow depth and velocity occurs in granular jumps, as observed in [19,22,33]. Such granular jumps were observed in our tests under certain circumstances. In particular, when the avalanche flow strikes the wall (impact of the front) and when the flow gets thinner, just before it stops (dilute tail). The transition between the dead zone and the granular jump regime is still an open question [32,34].

In this study, for the sake of simplicity, a wall-like obstacle spanning the chute was used. This obstacle simulates a catching dam overflowed by an avalanche as illustrated in [18], which focuses on the run-out shortening downstream of the obstacle. Future work will introduce more complex obstacle geometries for which lateral overflows are possi-

ble. This corresponds to the typical situation of dissipative structures, such as retarding mounds, used in avalanche engineering [35,36]. Also of interest are the granular mixtures which mimic more precisely the granular materials involved in natural avalanches, for which segregation processes occur (see, for example, [37–39]), and which may influence the flow-obstacle interaction.

Acknowledgments This study received financial support mainly from the European project Dynaval (INTERREG-ALCOTRA). Additional funding was provided by the French National Research Agency (ANR-MOPERA). The authors would like to thank Frederic Ousset for his crucial contribution to the design of the experimental device and Geoffrey Gaillard for his help in estimating the precision related to force sensor measurements.

References

1. Barbolini, M., Domaas, U., Faug, T., Gauer, P., Hákonardóttir, K.M., Harbitz, C.B., Issler, D., Jóhannesson, T., Lied, K., Naaim, M., Naaim-Bouvet, F., Rammer, L.: The design of avalanche protection dams. Recent practical and theoretical developments. Directorate-General for Research and Innovation, European Commission (2009)
2. Bartelt, P., McArdell, B.W.: Instruments and methods: granulometric investigation of snow avalanches. *J. Glaciol.* **55**, 829–833 (2009)
3. Rognon, P., Chevoir, F., Bellot, H., Ousset, F., Naaim, M., Coussot, P.: Rheology of dense snow flows: inferences from steady state chute-flow experiments. *J. Rheol.* **52**(3), 729–748 (2008)
4. Sovilla, B., McElwaine, J., Schaer, M., Vallet, J.: Variation of deposition depth with slope angle in snow avalanches: measurements from vallée de la sionne. *J. Geophys. Res.* **115**(F02016), 1–13 (2010)
5. GDRMiDi: On dense granular flows. *Eur. Phys. J. E* **1**, 341–365 (2004)
6. Pouliquen, O.: Scaling laws in granular flows down rough inclined planes. *Phys. Fluids* **11**(3), 542–548 (1999)
7. Dent, J.D., Burrell, K.J., Schmidt, D.S., Louge, M.Y., Adams, E.E., Jazbutis, T.G.: Density, velocity and friction measurement in a dry snow avalanche. *Ann. Glaciol.* **26**, 247–252 (1998)
8. Rognon, P., Roux, J.N., Naaim, M., Chevoir, F.: Dense flows of bidisperse assemblies of disks down an inclined plane. *Phys. Fluids* **19**(058101), 1–4 (2007)
9. Ridgway, K., Rupp, R.: Flow of granular materials down chutes. *Chem. Proc. Eng.* **51**, 82 (1970)
10. Savage, S.B., Jeffrey, D.: Gravity flow of cohesionless granular materials in chutes and channels. *J. Fluid Mech.* **92**, 53–96 (1979)
11. Wieghardt, K.: Experiments on granular flows. *Ann. Rev. Fluid Mech.* **7**, 89–114 (1975)
12. Campbell, C.S., Brennen, C.: Chute flows of granular material: Some computer simulations. *Trans. ASME* **52**, 172–178 (1985)
13. Johnson, P., Nott, P., Jackson, R.: Frictional-collisional equations of motion for particulate flows and their application to chutes. *J. Fluid Mech.* **210**, 501–535 (1990)
14. Patton, J., Brennen, C., Sabersky, R.: Shear flows of rapidly flowing granular materials. *J. Appl. Mech.* **54**, 801–805 (1987)
15. Forterre, Y., Pouliquen, O.: Flows of dense granular media. *Ann. Rev. Fluid Mech.* **40**, 1–24 (2008)
16. Hogg, A.J.: Two-dimensional granular slumps down slopes. *Phys. Fluids* **19**(093301), 1–19 (2007)
17. Chiou, M.C., Wang, Y., Hutter, K.: Influence of obstacles on rapid granular flows. *Acta Mechanica* **175**, 105–122 (2005)

18. Faug, T., Gauer, P., Lied, K., Naaim, M.: Overrun length of avalanches overtopping catching dams: cross-comparison of small-scale laboratory experiments and observations from full-scale avalanches. *J. Geophys. Res.* **113**(F03009), 1–17 (2008)
19. Gray, J.M.N.T., Tai, Y.C., Noelle, S.: Shock waves, dead zones and particle-free regions in rapid granular free-surface flows. *J. Fluid Mech.* **491**, 161–181 (2003)
20. Hákonardóttir, K.M., Hogg, A.J.: Oblique shocks in rapid granular flows. *Phys. Fluids* **17**(077101), 1–10 (2005)
21. Pudasaini, S.P., Hutter, K., Hsiau, S.S., Tai, S.C., Wang, Y., Katzenbach, R.: Rapid flow of dry granular materials down inclined chutes impinging on rigid walls. *Phys. Fluids* **19**(5), 053302 (2007)
22. Pudasaini, S.P., Kroener, C.: Shock-waves in rapid flows of dense granular materials: theoretical predictions and experimental results. *Phys. Rev. E* **78**(041308), 1–12 (2008)
23. Teufelsbauer, H., Wang, Y., Chiou, M.C., Wu, W.: Flow-obstacle interaction in rapid granular avalanches: Dem simulation and comparison with experiment. *Granul. Matter* **11**(4), 209–220 (2009)
24. Buchholtz, V., Pöschel, T.: Interaction of a granular stream with an obstacle. *Granul. Matter* **1**, 33–41 (1998)
25. Chanut, B., Faug, T., Naaim, M.: Time-varying force from dense granular avalanches on a wall. *Phys. Rev. E* **82**(041302), 1–12 (2010)
26. Faug, T., Beguin, R., Chanut, B.: Mean steady granular force on a wall overflowed by free-surface gravity-driven dense flows. *Phys. Rev. E* **80**(021305), 1–13 (2009)
27. Moriguchi, S., Borja, R., Yashima, A., Sawada, K.: Estimating the impact force generated by granular flow on a rigid obstruction. *Acta Geotech* **4**(1), 57–71 (2009)
28. Jaeger, H.M., Nagel, S.R., Behringer, R.P.: Granular solids, liquids, and gases. *Rev. Mod. Phys.* **68**, 1259–1273 (1996)
29. Schaefer, M., Bugnion, L., Kern, M., Bartelt, P.: Position dependent velocity profiles in granular avalanches. *Granul. Matter* **12**(3), 327–336 (2010)
30. Börzsönyi, T., Ecke, E., McElwaine, J.N.: Patterns in flowing sand: understanding the physics of granular flow. *Phys. Rev. L* **103**(178302), 1–4 (2009)
31. Louge, M., Keast, S.: On dense granular flows down flat frictional inclines. *Phys. Fluids* **13**, 1213–1233 (2001)
32. Caccamo, P., Faug, T., Bellot, H., Naaim-Bouvet, F.: Experiments on a dry granular avalanche impacting an obstacle: dead zone, granular jump and induced forces. In: *WIT Transactions on The Built Environment*, vol. 15, pp. 53–62 (2011)
33. Gray, J.M.N.T., Hutter, K.: Pattern formation in granular avalanches. *Contin. Mech. Thermodyn.* **9**, 341–345 (1997)
34. Hákonardóttir, K.M.: The Interaction Between Snow Avalanches and Dams. Ph.D. thesis, University of Bristol (2004)
35. Hákonardóttir, K.M., Hogg, A.J., Jóhannesson, T., Tomasson, G.G.: A laboratory study of the retarding effect of braking mounds. *J. Glaciol.* **49**, 191–200 (2003)
36. Naaim, M., Faug, T., Naaim-Bouvet, F., Eckert, N.: Return period calculation and passive structure design at the taconnaz avalanche path, france. *Ann. Glaciol.* **51**(54), 89–97 (2010)
37. Gray, J.M.N.T.: Particle size segregation in granular avalanches: a brief review of recent progress. In: *AIP, IUTAM-ISIMM Symposium on Mathematical Modeling and Physical Instances of Granular Flows* (2010)
38. Marks, B., Einav, I.: A cellular automaton for segregation during granular avalanches. *Granul. Matter* **13**(3), 211–214 (2011)
39. Savage, S.B., Lun, C.K.K.: Particle size segregation in inclined chute flow of dry cohesionless granular solids. *J. Fluid Mech.* **189**, 311–335 (1988)

Bibliography

- [1] www.anena.org
- [2] www.cnrm-game.fr
- [3] GUM, Guide to the expression of uncertainty in measurement. ISO/IEC Guide 98-3 (1998)
- [4] Ancey, C.: Guide neige et avalanches : connaissances, pratiques, sécurité. Edisud (1996)
- [5] Ancey, C.: Influence of particle entrainment from bed on the powder-snow avalanche dynamics. Tech. rep. (2003)
- [6] Ancey, C.: Powder snow avalanches: Approximation as non-boussinesq clouds with a richardson number-dependent entrainment function. *Journal of Geophysical Research* **109**(F01005), 1–14 (2004)
- [7] Ancey, C.: Dynamique des avalanches. Presses polytechnique et universitaires romandes (2006)
- [8] Ancey, C., Meunier, M.: Estimating bulk rheological properties of flowing snow avalanches from field data. *Journal of Geophysical Research* **109**(F01004), 1–15 (2004)
- [9] Armanini, A.: On the dynamic impact of debris flows. In: Recent developments in debris flows. *Lecture Notes in Earth Sciences* (1997)
- [10] Armanini, A., Scotton, P.: Experimental analysis on the dynamic impact of a debris flow on structures. In: Internationales Symposium INTERPRAEVENT 1992 (1992)
- [11] Auge, A., Ousset, F., Marco, O.: Effet d'une digue sur l'écoulement d'un aerosol. The contribution of scientific research to safety with snow, ice and avalanche pp. 235–240 (1995)
- [12] Azanza, E.: Ecoulements granulaires bidimensionnels sur un plan incliné. Ph.D. thesis, Ecole Nationale des Ponts et des Chaussées, Paris (1998)
- [13] Barbolini, M., Domaas, U., Faug, T., Gauer, P., Hákonardóttir, K.M., Harbitz, C.B., Issler, D., Jóhannesson, T., Lied, K., Naaim, M., Naaim-Bouvet, F., Rammer, L.: The design of avalanche protection dams. Recent practical and theoretical developments (2009)
- [14] Baroudi, D., Thibert, E.: An instrumental structure to measure avalanche impact pressure: Error analysis from monte carlo simulation. *Cold Regions Science and Technology* **59**, 242–250 (2009)
- [15] Bartelt, P., McArdell, B.W.: Instruments and methods: Granulometric investigation of snow avalanches. *Journal of Glaciology* **55**, 829–833 (2009)

- [16] Beghin, P.: Etude des bouffées bidimensionnelles de densité en écoulement sur pente avec application aux avalanches de neige poudreuse. Ph.D. thesis, Institut National Polytechnique de Grenoble (1979)
- [17] Beghin, P., Brugnot, G.: Contribution of theoretical and experimental results to powder-snow avalanche dynamics. *Cold Regions Science and Technology* **8**, 63–73 (1983)
- [18] Beghin, P., Closet, J.F.: Effet d’une digue sur l’écoulement d’une avalanche poudreuse. *Notes Techniques du Cemagref* **77** (1990)
- [19] Beghin, P., Hopfinger, E.J., Britter, R.E.: Gravitational convection from instantaneous sources on inclined boundaries. *Journal of Fluid Mechanics* **107**, 407–422 (1981)
- [20] Beghin, P., Olagne, X.: Experimental and theoretical study of the dynamic of powder snow avalanches. *Cold Regions Science and Technology* **19**, 317–326 (1991)
- [21] Bellot, H., Naaim-Bouvet, F., Faug, T., Naaim, M., Caccamo, P., Ousset, F.: Suivi du couloir avalancheux de taconnaz. mesures de pression et de vitesse sur des tas freineurs. *Grenoble 2012 Interpraevent International Research Society* **1**, 25–36 (2012)
- [22] Berthet-Rambaud, P., Limam, A., Baroudi, D., Thibert, E., Taillandier, J.M.: Characterisation of avalanche loading on impacted structures: a new approach based on inverse analysis. *Journal of Glaciology* **54**(185), 525–541 (2008)
- [23] Bouchet, A.: Etude expérimentale des avalanches denses de neige sèche. Ph.D. thesis, Université Joseph Fourier Grenoble (2003)
- [24] Bouchet, A., Naaim, M., Ousset, F., Bellot, H., Cauvard, D.: Experimental determination of constitutive equations for dense and dry avalanches: presentation of the set-up and first results. *Survey in Geophysics* **24**, 525–541 (2003)
- [25] Bozhinskiy, A.N., Losev, K.S.: The fundamentals of avalanche science. Mitteilung Nr. 55 des Eidg. Institutes für Schnee- und Lawinenforschung, Davos, Suisse (1998)
- [26] Bozhinskiy, A.N., Sukhanov, L.A.: Physical modeling of avalanches using an aerosol cloud of powder materials. *Annals of Glaciology* **26**, 242–246 (1998)
- [27] Brennen, C.E., Sieck, K., Paslaski, J.: Hydraulic jumps in granular material flow. *Powder Technology* **35**, 31–37 (1983)
- [28] Brewster, R., Grest, G., Landry, J., Levine, A.: Plug flow and the breakdown of bagnold scaling in cohesive granular flows. *Physical Review E* **72**(061301), 1–8 (2005)
- [29] Brossard, D.: Etude expérimentale de l’interaction entre un écoulement de gravité et son lit d’écoulement, application aux avalanches de neige en aérosol. Ph.D. thesis, Université Joseph Fourier, Grenoble (2010)
- [30] Börzsönyi, T., Ecke, E.: Rapid granular flows on a rough incline: phase diagram, gas transition, and effects of air drag. *Physical Review E* **74**(061301), 1–10 (2006)
- [31] Börzsönyi, T., Ecke, E., N., M.E.J.: Patterns in flowing sand: Understanding the physics of granular flow. *Physical Review L* **103**(178302), 1–4 (2009)
- [32] Caccamo, P.: Experimental assessment of the influence of a dam on powder snow avalanche impact: the case study of taconnaz. Master’s thesis, Politecnico of Milano (2008)

- [33] Caccamo, P., Chanut, B., Faug, T., Bellot, H., Naaim-Bouvet, F.: Small-scale tests to investigate the dynamics of finite-sized dry granular avalanches and forces on a wall-like obstacle. *Granular Matter on line* (2012)
- [34] Caccamo, P., Faug, T., Bellot, H., Naaim-Bouvet, F.: Experimental study on the behaviour of a dry granular avalanche impacting an obstacle and induced forces. In: *Fluid Structure Interaction, Orlando* (2011)
- [35] Chambon, G., Naaim, M.: Scaling relationships for constant-volume snow avalanches. *Annals of Glaciology* **50**(54) (2009)
- [36] Chanut, B.: Force exercée par une avalanche granulaire dense sur un obstacle. application aux digues de protection paravalanche. Ph.D. thesis, University of Grenoble (2010)
- [37] Chanut, B., Faug, T., Naaim, M.: Mean force on a wall overflowed by dense granular avalanches: Discrete numerical simulations. In: *AIP Conference Proceedings* (2009)
- [38] Chanut, B., Faug, T., Naaim, M.: Time-varying force from dense granular avalanches on a wall. *Physical Review E* **82**(041302), 1–12 (2010)
- [39] Chehata, D., Zenit, R., Wassgren, C.R.: Dense granular flow around an immersed cylinder. *Physics of Fluid* **15**(6), 1622–1631 (2003)
- [40] Chiou, M.C., Wang, Y., Hutter, K.: Influence of obstacles on rapid granular flows. *Acta Mechanica* **175**, 105–122 (2005)
- [41] Chu, T., Hill, G., Mc Lung, D.M., Ngun, R., Sherkat, R.: Experiments on granular flows to predict avalanche run up. *Can. Geotech. J.* **32**, 285–295 (1995)
- [42] Combe, G., Roux, J.N.: Quasi-static rheology and the origin of strain. *C. R. Physique* **3**, 131–140 (2002)
- [43] Cruz, F.: Ecoulement de grains secs: frottement et blocage. Ph.D. thesis, Ecole National des Ponts et des Chaussées, Paris (2004)
- [44] Cruz, F., Emam, S., Prochnow, M., Roux, J.N., Chevoir, F.: Rheophysics of dense granular materials: Discrete simulation of plane shear flows. *Physical Review E* **72**(021309), 1–17 (2005)
- [45] Cui, X., Gray, J.M.N.T., Jóhannesson, T.: Deflecting dams and the formation of oblique shocks in snow avalanches at flateyri, iceland. *Journal of Geophysical Research* **112**(F04012), 1–11 (2007)
- [46] Cundall, P., Strack, O.: A discrete numerical model for granular assemblies. *Geotechnique* **29**, 47–65 (1979)
- [47] De Biagi, V., Chiaia, B., Frigo, B.: Fractal grain distribution in snow avalanche deposits. *Journal of Glaciology* (2012)
- [48] Dent, J.D., Burrell, K.J., Schmidt, D.S., Louge, M.Y., Adams, E.E., Jazbutis, T.G.: Density, velocity and friction measurement in a dry snow avalanches. *Annals of Glaciology* **26**, 247–252 (1998)

- [49] Durand, Y., Laternser, M., Giraud, G., Etchevers, P., Lesaffre, B., Mérindol, L.: Re-analysis of 44 yr of climate in the french alps (1958-2002): methodology, model validation, climatology and trends for air temperature and precipitations. *J. Appl. Meteorol. Climatol.* **48**(3), 428–449 (2009)
- [50] Ertas, D., Grest, G., Halsey, T., Levine, D., Silbert, L.: Gravity-driven dense granular flows. *EPL* **56**, 214–218 (2001)
- [51] Faug, T., Beguin, R., Chanut, B.: Mean steady granular force on a wall overflowed by free-surface gravity-driven dense flows. *Physical Review E* **80**(021305), 1–13 (2009)
- [52] Faug, T., Caccamo, P., Chanut, B.: Equation for the force experienced by a wall overflowed by a granular avalanche: Experimental verification. *Physical Review E* **84**(051301), 1–7 (2011)
- [53] Faug, T., Caccamo, P., Chanut, B., Thibert, E.: A physically-sound scaling law for impact force of a finite-sized granular avalanche flowing past a wall. submitted to *Geophysical Research Letters* (2012)
- [54] Faug, T., Gauer, P., Lied, K., Naaim, M.: Overrun length of avalanches overtopping catching dams: cross-comparison of small-scale laboratory experiments and observations from full-scale avalanches. *Journal of Geophysical Research* **113**(F03009), 1–17 (2008)
- [55] Faug, T., Lachamp, P., Naaim, M.: Experimental investigation on steady granular flows interacting with an obstacle down an inclined channel: study of the dead zone upstream from the obstacle. application to interaction between dense snow avalanches and defence structures. *Natural Hazards and Earth System Sciences* **2**, 187–191 (2002)
- [56] Faug, T., Naaim, M.: Modelling a snow avalanche flowing past a protection dam: experimental investigations. In: *Kirovsk Conference* (2006)
- [57] Faug, T., Naaim, M., Bertrand, D., Lachamp, P., Naaim-Bouvet, F.: Varying dam height to shorten the run-out of dense avalanche flows: Developing a scaling law from laboratory experiments. *Survey in Geophysics* **24**, 555–568 (2003)
- [58] Faug, T., Naaim, M., Fourrière, A.: Dense snow flowing past a deflecting obstacle: an experimental investigation. *Cold Regions Science and Technology* **49**, 64–73 (2007)
- [59] Favier, L., Daudon, D., Donzé, F.V., Mazars, J.: Predicting the drag coefficient of a granular flow using the discrete element method. *Journal of Statistical Mechanics* (2009)
- [60] Forterre, Y., Pouliquen, O.: Flows of dense granular media. *The Annual Review of Fluid Mechanics* **40**, 1–24 (2008)
- [61] Fukushima, Y., Parker, G.: Numerical simulation of powder-snow avalanches. *Journal of Glaciology* **36**(123), 229–237 (1990)
- [62] Gauer, P., Issler, D., Lied, K., Kristensen, K., Iwe, H., Lied, E., Rammer, L., Schreiber, H.: On full-scale avalanche measurements at the ryggfonn test site, norway. *Cold Regions Science and Technology* **49**, 39–53 (2007)
- [63] GDRMiDi: On dense granular flows. *The European Physical Journal E* **14**, 341–365 (2004)
- [64] Goldhirsch, I.: Scales and kinetics of granular flows. *Chaos* **9**, 1–2 (1999)

- [65] Goujon, C.: *Écoulements granulaires bidisperses sur plans inclinés rugueux*. Ph.D. thesis, Université de Provence (2004)
- [66] Goujon, C., Thomas, N., Dalloz-Dubrujeaud, B.: Monodisperse dry granular flows on inclined planes: Role of roughness. *Eur. Phys. J. E.* **11**, 147–157 (2003)
- [67] Gray, J.M.N.T., Ancey, C.: Multi-component particle-size segregation in shallow granular avalanches. *Journal of Fluid Mechanics* **678**, 535–588 (2011)
- [68] Gray, J.M.N.T., Cui, X.: Weak, strong and detached oblique shocks in gravity-driven granular free-surface flows. *Journal of Fluid Mechanics* **579**, 113–136 (2007)
- [69] Gruber, U., Bartelt, P.: Study of the 1999 avalanches in the obergoms valley, switzerland, with respect to avalanche hazard mapping. In: *A Merging of Theory and Practice, Int. Snow Science Workshop* (2000)
- [70] Haff, P.K.: Grain flow as a fluid-mechanical phenomenon. *Journal of Fluid Mechanics* **134**, 401–430 (1983)
- [71] Hager, W.H.: *Energy dissipators and Hydraulic jump*. Kluwer Academic Publishers (1992)
- [72] Harter, M., Thibert, E., Vincent, C., Soruco, A.: A survey of taconnaz ice-fall from terrestrial photogrammetry: identification of precursor signs of serac falling events and associated discharged volumes. In: *12th Congress Interpraevent* (2012)
- [73] Hermann, F., Hutter, K.: Laboratory experiments on the dynamics of powder-snow avalanches in the run-out zone. *Journal of Glaciology* **37**(126), 281–295 (1991)
- [74] Hákonardóttir, K.M.: Retarding effects of braking mounds-avalanches. Master’s thesis, University of Bristol, School of Mathematics, Bristol, England (2000)
- [75] Hákonardóttir, K.M.: The interaction between snow avalanches and dams. Ph.D. thesis, University of Bristol (2004)
- [76] Hákonardóttir, K.M., Hogg, A.J., Jóhannesson, T., Kern, M., Tiefenbacher, F.: Large-scale avalanche braking mound and catching dam experiments with snow: a study of the airborne jet. *Survey in Geophysics* **24**, 543–554 (2003)
- [77] Hákonardóttir, K.M., Hogg, A.J., Jóhannesson, T., Tomasson, G.G.: A laboratory study of the retarding effect of braking mounds. *Journal of Glaciology* **49**, 191–200 (2003)
- [78] Hákonardóttir, K.M., Woods, W.: Flying avalanches. *Geophysical Research Letters* **30**(23), 1–4 (2003)
- [79] Hopfinger, E.J.: Snow avalanche motion and related phenomena. *Annual Review of Fluid Mechanics* **15**, 47–76 (1983)
- [80] Hopfinger, E.J., Tochon-Danguy, J.C.: A model study of powder-snow avalanches. *Journal of Glaciology* **19**(81), 343–356 (1977)
- [81] Irgens, F., Schieldrop, B., Harbitz, C.B., Domaas, U., Opdahl, R.: Simulations of dense-snow avalanches on deflecting dams. *Annals of Glaciology* **26**, 265–271 (1998)
- [82] Issler, D.: Experimental information on the dynamics of dry-snow avalanches. In: *Dynamic Response of Granular and Porous Materials under Large and Catastrophic Deformations*. Springer (2003)

- [83] Issler, D.: Dynamique et modélisation des avalanches. In: Université Européenne d'Eté (2010)
- [84] Iverson, R.M.: The physics of debris flow. *Reviews of Geophysics* **35**(3), 245–296 (1997)
- [85] Jaeger, H.M., Nagel, S.R., Behringer, R.P.: Granular solids, liquids, and gases. *Reviews of Modern Physics* **68**, 1259–1273 (1996)
- [86] Jenkins, J.T., Richman, M.W.: Kinetic theory for plane flows of a dense gas of identical, rough, inelastic, circular discs. *Physics of Fluids* **28**, 3485–3494 (1985)
- [87] Jóhannesson, T., Hákonardóttir, K.M.: Remarks on the design of avalanche braking mounds based on experiments in 3, 6, 9 and 34m long chutes. Tech. rep., Report 03024, IMO, Reykjavík (2003)
- [88] Jop, P., Forterre, Y., Pouliquen, O.: Crucial role of side walls for granular surface flows: consequences for the rheology. *Journal of Fluid Mechanics* **541**, 167–192 (2005)
- [89] Kawada, K., Nishimura, K., Maeno, N.: Experimental studies on a powder snow avalanche. *Annals of Glaciology* **13**, 129–134 (1989)
- [90] Keller, S.: Physikalische simulation von staublawinen - experimente zur dynamik im dreidimensionalem auslauf. VAW, ETH Zürich **141** (1996)
- [91] Keller, S., Issler, D.: Staublawinen über dämme und mauern im labor; zusammenstellung aller resultate und auswertung. Tech. rep., Swiss Federal Institute for Snow and Avalanches (1996)
- [92] Kern, M., Bartelt, P., Sovilla, B.: Velocity profile inversion in dense avalanche flow. *Annals of Glaciology* **51**, 27–31 (2010)
- [93] Kern, M., Tiefenbacher, F., N., M.J.: The rheology of snow in large chute flows. *Cold Regions Science and Technology* **39**, 181–192 (2004)
- [94] Kneller, B., Buckee, C.: The structure and fluid mechanics of turbidity currents: a review of some recent studies and their geological implications. *Sedimentology* **47**, 62–94 (2000)
- [95] Kulikovskiy, A.G., Sveshnikova, E.I.: A model for computing powdered snow avalanche motion (russian). *Data Glaciolog. Stud.* **31**, 74–80 (1977)
- [96] Levy, A., Sayed, M.: Numerical simulations of the flow of dilute granular materials around obstacles. *Powder Technology* **181**, 137–148 (2008)
- [97] Lied, E., Moe, A., Kristensen, K., Issler, D.: Snow avalanche research, programme sip-6. ryggfonn. full scale avalanche test site and the effect of the catching dam. Tech. rep., Norwegian Geotechnical Institute (2002)
- [98] Lied, K., Kristensen, K.: Snøskred. håndbok om snøskred. Tech. rep., Vett & Viten as., Oslo (2003)
- [99] Louge, M., Keast, S.: On dense granular flows down flat frictional inclines. *Physics of Fluids* **13**, 1213–1233 (2001)
- [100] Louge, M.Y., Carroll, C.S., Turnbull, B.: Role of pore pressure gradients in sustaining frontal particle entrainment in eruption currents - the case of powder snow avalanches. *Journal of Geophysical Research* **116**(4), 1–13 (2011)

- [101] Margreth, S.: Avalanche control structures. In: Grenoble, course material presented at the Université Européenne d'Eté, session 2004, Courmayeur:"Avalanches: Risque, zonage et protections" (2004)
- [102] Marks, B., Rognon, P., Einav, I.: Grainsize dynamics of polydisperse granular segregation down inclined planes. *Journal of Fluid Mechanics* **690**, 499–512 (2011)
- [103] McClung, D.M., Shaerer, P.: *The Avalanche Handbook*. The Mountaineers, Seattle (1993)
- [104] McClung, D.M., Shaerer, P.A.: Characteristics of flowing snow and avalanche impact pressures. *Annals of Glaciology* **6**, 9–14 (1985)
- [105] Naaïm, M., Eckert, N., Naaïm-Bouvet, F., Faug, T.: Amélioration du dispositif par-avalanche de taconnaz. etude quantitative de scénarii de référence. Rapport d'étude Cemagref (2007)
- [106] Naaïm, M., Faug, T., Naaïm-Bouvet, F., Eckert, N.: Return period calculation and passive structure design at the taconnaz avalanche path, france. *Annals of Glaciology* **51**(54), 89–97 (2010)
- [107] Naaïm-Bouvet, F., Naaïm, M., Bacher, M., Heiligenstein, L.: Physical modelling of the interaction between powder avalanches and defence structures. *Natural Hazards and Earth System Sciences* **2**, 193–202 (2002)
- [108] Naaïm-Bouvet, F., Naaïm, M., Faug, T.: Dense and powder avalanches: momentum reduction generated by a dam. *Annals of Glaciology* **38**(04/0555), 373–378 (2004)
- [109] Naaïm-Bouvet, F., Pain, S., Naaïm, M., Faug, T.: Numerical and physical modelling of the effect of a dam on powder avalanche motion: comparaison with previous approaches. *Surveys in Geophysics* **24**, 479–498 (2003)
- [110] Nishimura, K.: Studies on the fluidized snow dynamics. In: *The Institute of Low Temperature Science* (1991)
- [111] Nishimura, K., Keller, S., N., M.J., Nohguchi, Y.: Ping-pong ball avalanche at a ski jump. *Granular Matter* **1**, 51–56 (1998)
- [112] Nishimura, K., Maeno, N., Kawada, K., Izumi, K.: Structures of snow cloud in dry-snow avalanches. *Annals of Glaciology* **18**, 173–178 (1993)
- [113] Nishimura, K., Maeno, N., Sandersen, F., Kristensen, K., Norem, H., Lied, K.: Observations of the dynamic structure of snow avalanches. *Annals of Glaciology* **18**, 313–316 (1993)
- [114] Nishimura, K., Narita, H., Maeno, N., Kawada, K.: The internal structure of powder-snow avalanches. *Annals of Glaciology* **13**, 207–210 (1989)
- [115] Nishimura, K., Sandersen, F., Kristensen, K., Lied, E.: Measurements of powder-snow avalanche nature. *Surveys in Geophysics* **16**, 649–660 (1995)
- [116] Norem, H.: Snow engineering for roads. Tech. rep., Norwegian Public Roads Administration, Oslo (1994)
- [117] Norem, H., Irgens, F., Schieldrop, B.: A continuum model for calculating snow avalanche velocities. IAHS (1987)

- [118] Pazwash, H., Robertson, J.M.: Forces on bodies in bingham fluids. *Journal of Hydraulic Research* **13**(1), 35–55 (1975)
- [119] Pouliquen, O.: Scaling laws in granular flows down rough inclined planes. *Physics of Fluids* **11**(3), 542–548 (1999)
- [120] Pouliquen, O., Chevoir, F.: Dense flows of dry granular materials. *C. R. Physique* **3**, 163–175 (2002)
- [121] Pouliquen, O., Forterre, Y.: Friction law for dense granular flows: application to the motion of a mass down a rough inclined plane. *Journal of Fluid Mechanics* **453**, 133–151 (2002)
- [122] Rajchenbach: Granular flows. *Advanced in Physics* **49**, 229–256 (2000)
- [123] Rapin, F.: The french theory for the snow avalanches with aerosol. In: *Université Européenne d'Eté sur les risques naturels "Neige et Avalanches"*, Chamonix, 14-25 Septembre 1992, Editions Cemagref, pp. 149–154 (1995)
- [124] Rapin, F.: *Avalanche de taconnaz du 11 février 1999*. Tech. rep., Cemagref (2001)
- [125] Rastello, M., Hopfinger, E.J.: Sediment-entraining suspension clouds: a model of powder-snow avalanches. *Journal of Fluid Mechanics* **509**, 181–206 (2004)
- [126] Rastello, M., Rastello, F., Bellot, H., Ousset, F., Dufour, F., Meier, L.: Size of snow particles in a powder-snow avalanche. *Journal of Glaciology* **57**(201), 151–156 (2011)
- [127] Rastello, M.C.: *Etude de la dynamique des avalanches de neige en aérosol*. Ph.D. thesis, Université Joseph Fourier, Grenoble (2002)
- [128] Rognon, P.: *Rhéologie des matériaux granulaires cohésifs. application aux avalanches de neige dense*. Ph.D. thesis, Ecole Nationale des Ponts et des Chaussées (2006)
- [129] Rognon, P., Roux, J.N., Naaim, M., Chevoir, F.: Dense flows of bidisperse assemblies of disks down an inclined plane. *Physics of Fluids* **19**(058101), 1–4 (2007)
- [130] Rognon, P., Roux, J.N., Naaim, M., Chevoir, F.: Dense flows of cohesive granular materials. *Journal of Fluid Mechanics* **596**, 21–47 (2008)
- [131] Rognon, P.G., Chevoir, F., Bellot, H., Ousset, F., Naaim, M., Coussot, P.: Rheology of dense snow flows: inferences from steady state chute-flow experiments. *Journal of Rheology* **52**(3), 729–748 (2008)
- [132] Rusello, P.J., Lohrmann, A., Siegel, E., Maddux, T.: Improvements in acoustic doppler velocimetry. In: *Proceedings of the 7th International Conference on HydroScience and Engineering*, Philadelphia, USA (2006)
- [133] Salm, B.: *Lawinenkunde für den praktiker*. Bern, Verlag Schweizer Alpen-Club (1982)
- [134] Salm, B., Burkard, A., Gubler, H.: *Berechnung von fließlawinen: Eine anleitung fuer praktiker mit beispielen*. Tech. rep., Mitt. 47, Eidg. Inst. Schnee- und Lawinenforsch, Davos, Switzerland (1990)
- [135] Sampl, P., Naaim-Bouvet, F., Naaim, M.: Interaction between dams and powder avalanches: determination of simple friction laws for shallow water avalanche models. *Cold Regions Science and Technology* **39**, 115–131 (2004)

- [136] Savage, S.B., Hutter, K.: The motion of a finite mass of granular material down a rough incline. *Journal of Fluid Mechanics* **199**, 177–215 (1989)
- [137] Schaer, M., Issler, D.: Particle densities, velocities, and size distributions in large avalanches from impact-sensor measurements. *Annals of Glaciology* **32**, 321–327 (2001)
- [138] Schaerer, P.A., Salway, A.A.: Seismic and impact-pressure monitoring of flowing avalanches. *Journal of Glaciology* **26**, 179–187 (1980)
- [139] Scheiwiller, T., Hutter, K., Hermann, F.: Dynamic of powder snow avalanches. *Annales Geophysicae. Series B* **5**(6), 569–587 (1987)
- [140] Scotton, P., De Toni, S., Moro, F.: Passive defence structures against dense snow avalanches. experimental analysis. In: *Interpraevent 2008 - Conference Proceedings, Vol. 2* (2008)
- [141] Segor, V., Pitet, L., Chiaia, B., Frigo, B., Barbero, M., Barpi, F., Borri Brunetto, M., Bovet, E., De Biagi, V., Pallara, O., Zanini, E., Freppaz, M., Maggioni, M., Bruno, E., Ceaglio, E., Godone, D., Viglietti, D., Brulport, A.: Sito sperimentale della punta seehore. *Neve e Valanghe* **73**, 14–19 (2011)
- [142] Shimizu, H., Huzioka, E., Akitaya, E., Narita, H., Nakagawa, M., Kawada, K.: A study on high-speed avalanches in the kurobe canyon, japan. *Journal of Glaciology* **26**(94), 141–151 (1980)
- [143] Silbert, L., Ertas, D., Grest, G., Halsey, T., Levine, D., Plimpton, S.: Granular flow down an inclined plane: Bagnold scaling and rheology. *Physical Review E* **64**(051302), 1–14 (2001)
- [144] Silbert, L., Landry, J., Grest, G.: Granular flow down a rough inclined plane: transition between thin and thick piles. *Physics of Fluids* **15**, 1–10 (2003)
- [145] Soo, S.L.: *Fluid dynamics of multiphase systems*. Blaisdell Publishing CO. (1967)
- [146] Sovilla, B.: Field experiments and numerical modelling of mass entrainment and deposition processes in snow avalanches. Ph.D. thesis, Swiss federal institute of Technology, Zurich (2004)
- [147] Sovilla, B., N., M.J., Schaer, M., Vallet, J.: Variation of deposition depth with slope angle in snow avalanches: measurements from vallée de la sionne. *Journal of Geophysical Research* **115**(F02016), 1–13 (2010)
- [148] Sovilla, B., Schaer, M., Kern, M., Bartelt, P.: Impact pressure and flow regimes in dense snow avalanches observed at the vallé de la sionne test site. *Journal of Geophysical Research* **113**(F01010), 1–14 (2008)
- [149] Sovilla, B., Schaer, M., Rammer, L.: Measurements and analysis of full-scale avalanche impact pressures at the vallée de la sionne test site. *Cold Regions Science and Technology* **51**, 122–137 (2008)
- [150] Sovilla, B., Somnavilla, F., Tomaselli, A.: Measurements of mass balance in dense snow avalanche events. *Annals of Glaciology* **31**, 230–236 (2001)
- [151] Tai, Y.C., Gray, J.M.N.T., Hutter, K., Noelle, S.: Flow of dense avalanches past obstructions. *Annals of Glaciology* **32**, 281–284 (2001)

- [152] Thibert, E., Baroudi, D., Limam, A., Berthet-Rambaud, P.: Avalanche impact pressure on an instrumented structure. *Cold Regions Science and Technology* **54**, 206–215 (2008)
- [153] Turnbull, B., McElwaine, J.N.: Experiments on the non-boussinesq flow of self-igniting suspension currents on a steep open slope. *Journal of Geophysical Research* **113**(F01003), 1–12 (2008)
- [154] Turnbull, B., McElwaine, J.N.: Potential flow models of suspension current air pressure. *Annals of Glaciology* **51**(54), 113–122 (2010)
- [155] Turnbull, B., McElwaine, J.N., Ancey, C.: The kulikovskiy-sveshnikova-beghin model of powder snow avalanches: development and application. *Journal of Geophysical Research* **112** (2007)
- [156] Tüzün, U., Nedderman, R.M.: Gravity flow of granular materials round obstacles: Investigation of the effects of inserts on flow patterns inside a silo. *Chemical Engineering Science* **40**(3), 325–336 (1985)
- [157] UNESCO: Atlas des Avalanches. Paris (1981)
- [158] Voellmy, A.: Über die zerstörungskraft von lawinen. *Schweizerische Bauzeitung (Sonderdruck aus dem 73. Jahrgang)* **73**, 3–25 (1955)
- [159] Wassgren, C.R., Cordova, J.A.: Dilute granular flow around an immerse cylinder. *Physics of Fluids* **15**(11), 3318–3330 (2003)
- [160] Wieghardt, K.: Forces in granular flows. *Mech. Res. Comm.* **1**, 3–7 (1974)
- [161] Wieghardt, K.: Experiments on granular flows. *The Annual Review of Fluid Mechanics* **7**, 89–114 (1975)

List of symbols

α_{jet}^0	Jet deflecting angle (deg)
α_0	Free surface slope of the influence zone reached for the stationary regime (deg)
α_{dam}	Angle between the upstream side of the dam and the terrain (deg)
α_{dam}^{thr}	Uphill-ramp threshold angle (deg)
α_{dz}	Dead-zone angle (deg)
α_{fd}	Final deposit free surface slope (deg)
α_{iz}	Influence zone free surface slope (deg)
$\alpha_{xz}(z)$	Direction angle associated to $U_{xz}(z)$ (deg)
$\alpha_{xz}^{*,max}(z)$	Direction angle associated to $u_{xz}^{max}(z)$ (deg)
$\alpha_{xz}^*(z, t)$	Time-dependent profile of the direction angle associated to the velocity norm (deg)
α_{xz}^{max}	Direction angle associated to U_{xz}^{max} (deg)
β	Coefficient of the low-power relationship between u and h ()
β_n	Wave number ()
β_u	Boussinesq coefficient ()
ΔH_κ	Dam design height contribution due to the curvature of the dam axis (m)
ΔH_{θ_\perp}	Dam design height contribution due to the terrain normal to the dam axis leaning towards the dam (m)
Δt	Time lapse (s)
δ	Angle between the laser beam and the channel bottom (deg)
δ_h	Height ratio ()
Δr_o	Difference between the maximum and minimum avalanche run-out distances (m)
δ_u	Velocity ratio ()
$\dot{\gamma}$	Shear rate ()
η	Flow viscosity ()
η_d	Dynamic viscosity ($\text{kg m}^{-1} \text{s}^{-1}$)

η_{eq}	Equivalent flow viscosity ()
γ	Energy dissipation coefficient ()
κ	Velocity reduction factor ()
Λ	Empirical coefficient ()
μ	Friction coefficient ()
μ_{min}^*	Friction coefficient for quasi-static regime ()
μ_0	Friction coefficient of the avalanche close to the stand-still state ()
μ_c	Constant friction value ()
ν	Empirical coefficient ()
$\bar{\rho}$	Depth-averaged flow density (kg m^{-3})
\bar{u}	Depth-averaged flow velocity (m s^{-1})
ϕ	Volume fraction ()
ϕ_{max}	Maximum volume fraction ()
ϕ_{min}	Minimum volume fraction ()
Ψ	Momentum of inertia (kg m^2)
ρ	Density (kg m^{-3})
ρ_{beads}	Beads' density (kg m^{-3})
ρ_{dz}	Dead-zone density (kg m^{-3})
ρ_{low}	Density of the lower part of the aerosol flow (kg m^{-3})
ρ_{mean}	Mean flow density (kg m^{-3})
ρ_p	Particle density (kg m^{-3})
ρ_{ref}	Ambient fluid density (kg m^{-3})
σ	Standard deviation ()
σ_{xx}	Normal stress in the x direction ()
σ_{yy}	Normal stress in the y direction ()
τ	Strain rate ()
τ_c	Yield stress ()
τ_{iz}	Characteristic time for the formation of the influence zone (s)
θ	Slope angle (deg)
θ_{\perp}	Terrain slope in the direction normal to the dam axis (deg)

θ_c	Critical slope angle (deg)
θ_{max}	Characteristic angle for which $h_{stop}(\theta) \rightarrow 0$ (deg)
θ_{min}	Characteristic angle for which $h_{stop}(\theta) \rightarrow \infty$ (deg)
θ_{start}	Critical angle releasing the material flow (deg)
θ_{stop}	Critical angle arresting the material flow (deg)
Υ	Error parameter ()
φ	Deflecting angle (with respect to the flow direction) (deg)
φ_{max}	Maximum deflecting angle (deg)
ξ	Parameter related to the flow configuration and bottom roughness ()
ξ_{dam}	Distance along the dam axis measured from its upstream end (m)
a, b	General coefficients for linear fit ()
a_ϕ	Empirical coefficient ()
A_{obs}	Obstacle aspect ratio ()
B	Dimensionless value ()
b_μ	Empirical coefficient ()
C	Correlation rate ()
c	Shape coefficient ()
c_μ	Calibration parameter ()
C_d	Drag coefficient ()
c_{s0}	Speed of sound for pure water (m s^{-1})
c_s	Speed of sound (m s^{-1})
d	Diameter (mm)
d_{beads}	Beads' mean diameter (mm)
d_{laser}	Laser diameter (mm)
d_{plate}	Sensor plate diameter (m)
d_{rough}	Roughness mean diameter (mm)
D_r	Dimensionless number related to the areal proportion of large grains ()
E	Young modulus (Pa)
e	Restitution coefficient ()
E_{av}	Avalanche energy ()

F	Force (N)
f_{ac}	Acquisition frequency (Hz)
F_f	Basal friction (N)
F_{hyd}	Hydrostatic force (N)
F_{kin}	Kinetic force (N)
F_{max}	Maximum force (N)
F_n	Normal force acting on a wall (N)
f_n	Natural frequency (Hz)
F_{res}	Residual force (N)
F_w	Force due to the volume weight (N)
Fr	Froude number ()
Fr^{100}	Centennial Froude number ()
Fr_{\perp}	Froude number of the flow in the direction normal to the dam axis ()
Fr_d	Densimetric Froude number ()
Fr_{loc}	Local Froude number ()
Fr_{obs}	Obstacle Froude number ()
G	Dimensionless number highlighting the influence of the obstacle shape ()
g	Gravity acceleration (m s^{-2})
h	Flow height (m)
h_1	Incoming flow height (m)
h_2	Upstream shock height (m)
H_{cr}	Critical dam height (m)
h_{cr}	Critical flow height (m)
H_c	Critical obstacle height generating a jump (m)
h_{max}	Maximum flow height (m)
H_{obs_v}	Vertical dam height (m)
H_{obs}	Obstacle's height normal to the slope (m)
H_{ps}	Plane shear distance (m)
h_{rel}	Release height (m)
h_r	Run-up height (m)

h_{start}	Initial height (m)
h_{stop}	Final deposit height (m)
h_s	Height of the snow deposited upstream from the obstacle (m)
I	Inertial number ()
I_0	Constant value ()
K	Constant value ()
k	Earth pressure coefficient ()
$k(z)$	Coefficient considering the vertical profiles of horizontal velocity and density ()
k_{loss}	Momentum loss ()
k_s	Stiffness coefficient (N m ⁻²)
L	General length (m)
L_{dz}	Dead-zone length (m)
L_{iz}	Influence zone length (mm)
L_{laser}	Laser length (mm)
L_{line}	Laser line length (m)
l_{obs}	Obstacle length (m)
M	Bending momentum (N m)
m	Mass (kg)
MI	Module intensity ()
$n \times m$	Dimensions parameters
N	Shear force (N)
n	Slope of the power-fit
N_a	Attractive force (N)
N_c	Maximum value of the attractive force N_a (N)
P	Pressure (Pa)
P_h^0	Hydrostatic pressure contribution (Pa)
P_{kin}	Kinetic pressure (Pa)
P_u^0	Kinetic pressure contribution (Pa)
PW	Avalanche power ()
Q	Flow rate (m ³ s ⁻¹)

R_{κ}	Radius of curvature of the dam axis (m)
Re	Reynolds number ()
Re_{eq}	Equivalent Reynolds number
Ri	Richardson number ()
S_{iz}	Influence zone surface (mm ²)
S_r	Dimensionless number related to the surface ratio between the two sizes of disks ()
S_{st}	Storage volume per unit width (m ²)
St	Stokes number ()
T	Tension (V)
t	Time (s)
$T(t)$	Tension value measured by the pressure sensor (V)
t^*	Time at which the transition occurs (s)
t^0	Travel-time of an acoustic pulse in reference conditions (s)
t^{\diamond}	General characteristic time (s)
t_0	Time corresponding at $t = 0$ s (s)
$t_{\rho_{max}}$	Time at which the maximum density is recorded (s)
$t_{h=h_{max}}$	Time corresponding to the maximum flow height (s)
T_i	Time lapse from the flow release until the impact with the obstacle (s)
T_{offset}	Offset tension value affecting pressure measurements (V)
t_{pulse}	Travel-time of an acoustic pulse (s)
$t_{u=u_{max}}$	Time corresponding to the maximum flow velocity (s)
u	Flow velocity (m s ⁻¹)
u^*	General characteristic velocity (m s ⁻¹)
u_1	Incoming flow velocity (m s ⁻¹)
u_{fall}	Particle falling velocity (m s ⁻¹)
u_{fr}	Front velocity (m s ⁻¹)
$u_{h_{max}}$	Velocity corresponding at $t(h_{max})$ (m s ⁻¹)
$u_i(z, t)$	Time-dependent profile of the core i -velocity ($i = x, z$) (m s ⁻¹)
$U_i^+(z)$	Vertical profile of the positive core velocity in the i -direction ($i = x, z$). Each value of the profile represents the average of $u_i^{max}(z)$ over the 3 – 5 tests conducted in similar conditions (m s ⁻¹)

- $U_i^-(z)$ Vertical profile of the negative core velocity in the i -direction ($i = x, z$). Each value of the profile represents the average of $u_i^{min}(z)$ over the 3 – 5 tests conducted in similar conditions (m s^{-1})
- U_i^{max} Maximum value of the vertical profile $U_i^+(z)$ (m s^{-1})
- $u_i^{max}(z)$ Maximum value of the time-dependent core i -velocity profile ($i = x, z$) (m s^{-1})
- U_i^{min} Minimum value of the vertical profile $U_i^-(z)$ (m s^{-1})
- $u_i^{min}(z)$ Minimum value of the time-dependent core i -velocity profile ($i = x, z$) (m s^{-1})
- u_{max} Maximum flow velocity (m s^{-1})
- u_p Solid particle velocity (m s^{-1})
- u_{surf} Surface velocity (m s^{-1})
- $U_{xz}(z)$ Vertical profile of the core velocity norm. Each value of the profile represents the average of $u_{xz}^{max}(z)$ over the 3 – 5 tests conducted in similar conditions (m s^{-1})
- $u_{xz}(z, t)$ Velocity norm time-dependent profile ($i = x, z$) (m s^{-1})
- U_{xz}^{max} Maximum norm velocity value at a given x -position (m s^{-1})
- $u_{xz}^{max}(z)$ Maximum value of the time-dependent velocity norm profile ($i = x, z$) (m s^{-1})
- u_x Flow velocity in the x -direction (m s^{-1})
- u_x Velocity along the x -axis (m s^{-1})
- u_y Flow velocity in the y -direction (m s^{-1})
- u_y Velocity along the y -axis (m s^{-1})
- u_z Flow velocity in the z -direction (m s^{-1})
- u_z Velocity along the z -axis (m s^{-1})
- V Volume (m^3)
- V^{100} Centennial volume (m^3)
- V_0 Control volume (m^3)
- $V_i^+(z)$ Vertical profile of the positive core velocity in the i -direction ($i = x, z$). The vertical profile is taken at the time $t = t_{U_i^{max}}$ (m s^{-1})
- $V_i^-(z)$ Vertical profile of the negative core velocity in the i -direction ($i = x, z$). The vertical profile is taken at the time $t = t_{U_i^{min}}$ (m s^{-1})
- w Weight (N m^{-1})
- x Main direction of the flow
- x^* Position along the x -axis which has its origin at the position of the obstacle and is expressed in terms of obstacle height (m)

x_0	Position corresponding to $x = 0$ m (m)
x_{fr}	Front position along the x -axis (m)
x_{max}	Total length of the image (pix)
$x_{ref}; z_{ref}$	Reference coordinates for the influence zone analysis
y_{obs}	Obstacle coordinate
z	Vertical coordinate, normal to the bottom and the flow direction
z_l	Elevation of a straight line from the top of the dam towards the mountain with a slope in the range $0 - 10^\circ$ (m)
z_{sens}	Sensor height (m)
zU_{xz}^{max}	Z -value at which the maximum norm is recorded (m)

Experimental study of the influence of protection structures on avalanches and impact pressures

Abstract: In the frame of snow avalanche protection, the optimisation of defence structure design depends on the understanding of the flow dynamics and on an exhaustive knowledge of the flow-obstacle interaction. The study presented here utilises a mainly experimental approach. Small-scale laboratory tests were combined with field measurements and observations.

Dense snow avalanches are modelled by granular materials. Dry cohesionless and mono-dispersed glass beads are released down an inclined channel. Reference tests (with no obstacles) were carried out in order to characterise the flow dynamic properties, and an obstacle was then mounted and force measurements were taken. The geometry of two obstacles was tested: a large wall spanning the whole width of the flow and a narrower wall allowing lateral flows. Results showed that an influence zone forms uphill from the obstacle and plays an important role in the flow dynamics. An analysis of this zone was carried out, together with precise measurements of the flow depth (laser technique), surface velocity (PIV) and impact forces (force sensors).

In relation to density currents, powder snow avalanches are modelled by a dyed salt solution flowing down an inclined channel immersed in a water tank. We investigated the influence of two different catching-dam-type obstacles on the flow behaviour with respect to reference conditions. The maximum flow height and its front and core velocity were measured by means of image processing and ultrasound Doppler velocimetry. Results mainly showed the higher effectiveness of a dam with vertical uphill face rather than inclined and underscored the importance of the velocity norm in the computation of the total incoming flow velocity.

In-situ full-scale measurements complement small-scale laboratory tests. A new full-scale experimental site was implemented on the existing avalanche defence system of Taconnaz (Chamonix, France). Three breaking mounds were equipped with velocity and pressure sensors. The reference event, the rough site conditions, the need for data synchronization and remote access defined the design constraints. In December 2010, the first event was recorded, which proved that the conceived system works effectively and also provided the first set of data. Preliminary results showed very high pressure peaks with high impact pressures even for low velocity regimes and thus a drag coefficient which increases when the Froude number decreases. Isolated rocks or ice blocks struck the sensors, contributing significantly to the total energy released by the avalanche.

This work provided effective inputs for numerical and analytical models and enhanced the current knowledge of avalanche dynamics in order to optimise the future design guidelines for avalanche protection structures.

Keywords: Snow avalanches, impact pressure, laboratory experiments, dense avalanches, granular flows, influence zone, dead zone to granular jump transition, powder avalanches, density currents, ultrasound Doppler velocimetry, full-scale measurements.
